THE UNIVERSITY OF SHEFFIELD

Department of Electronic and Electrical Engineering
Electrical Machines and Drives Research Group

Thesis submitted in partial fulfilment of the requirements for the degree of

DOCTOR OF PHILOSOPHY

Magnetic Integration Techniques for Resonant Converters

by

Sajad Arab Ansari

Supervised by Dr Jonathan Neil Davidson and Prof Martin Paul Foster

July 2023

to the Women

of

Iran

تقدیم

به

زنان سرزمینم

That which you most need will be found where you least want to look.

- Carl Jung

Abstract

This thesis sets out a series of new transformer topologies for magnetic integration in different resonant converters. Resonant converters like LLC converters require a high number of magnetic components, leading to low power density and high cost. These magnetic components can usually be integrated into a single transformer to increase power density, efficiency, manufacturing simplicity and to reduce cost. This strategy is known as integrated transformer (IT). The work described in this thesis has sought to deliver improvements in implementing this strategy.

The benefits of resonant converters compared to pulse-width-modulated (PWM) converters are discussed. To show the drawbacks of PWM converters, two hard-switched DC-DC converters and two soft-switched DC-DC converters using state-of-the-art wide bandgap (WBG) gallium nitride devices are constructed and investigated.

The LLC resonant converter is fully discussed for unidirectional and bidirectional applications. The different techniques for magnetic integration that can be applied to the LLC resonant converter are reviewed. Amongst these techniques, the inserted-shunt integrated transformers, which have gained popularity recently, are made a focus of the thesis.

In general, the important challenges concerning the inserted-shunt integrated transformers are the need for bespoke material for the shunt, unwanted high leakage inductance on the secondary side, and that integrated magnetics are not usually suitable for bidirectional converters such as CLLLC converters.

Two new topologies (IT1 and IT2) for inserted-shunt integrated transformers are presented that do not need bespoke material for the shunt and can be constructed from materials available commercially in large and small quantities. However, the manufacturing of these proposed topologies is challenging since magnetic shunts are made by joining several smaller magnetic pieces to form a segmented piece.

A further new topology (IT3) is presented that not only does not need bespoke material for the shunt but also benefits from simple manufacturing. However, inserted-shunt integrated transformer, including all three proposed topologies (IT1-IT3), still suffer from increased leakage inductance on the secondary side, leading the control and design of the resonant converters to difficulty.

Another topology (IT4) is therefore proposed that can be constructed easily with commercially available materials and does not increase the leakage inductance on the secondary side. However, all four proposed topologies (IT1-IT4) and other topologies with an inserted-shunt are not suitable for use in bidirectional LLC-type resonant converters when different primary and secondary leakage inductances are needed, such as where variable gain is required.

Finally, a topology (IT5) is proposed that can be used in bidirectional LLC-type converters while it still benefits from simple manufacturing and using commercially available materials.

All the proposed topologies (IT1-IT5) are discussed in detail and their design guidelines and modelling are provided. The theoretical analysis is confirmed by finite-element (FEM) analysis and experimental results.

A unidirectional LLC resonant converter and a bidirectional CLLLC resonant converter are implemented to investigate the performance of the proposed integrated transformers (IT1-IT5) in practice. It is shown that the converters can operate properly while all their magnetic components are integrated into the proposed transformers.

Publications

Portions of the work contained in this thesis have been disseminated in the following internationally published works:—

Journal Publications

1. **Sajad A. Ansari**, Jonathan N. Davidson, Martin P. Foster "Fully-integrated Transformer with Asymmetric Primary and Secondary Leakage Inductances for a Bidirectional Resonant Converter", IEEE Transactions on Industry Applications, 2023.
2. **Sajad A. Ansari**, Jonathan N. Davidson, Martin P. Foster "Fully-integrated Planar Transformer with Low Secondary Leakage Inductance for LLC Resonant Converters", IEEE Transactions on Industrial Electronics, 2022.
3. **Sajad A. Ansari**, Jonathan N. Davidson, Martin P. Foster "Fully-Integrated Solid Shunt Planar Transformer for LLC Resonant Converters", IEEE Open Journal of Power Electronics, 2021.
4. **Sajad A. Ansari**, Jonathan N. Davidson, Martin P. Foster "Fully-integrated Planar Transformer with a Segmental Shunt for LLC Resonant Converters", IEEE Transactions on Industrial Electronics, 2021.
5. **Sajad A. Ansari**, Jonathan N. Davidson, Martin P. Foster "Evaluation of Si MOSFETs and GaN HEMTs in Soft-Switched and Hard-Switched DC-DC Converters for Renewable Energy Applications", IET Power Electronics, 2020.
6. Amirreza Mizani, **Sajad A. Ansari**, Abbas Shoulaie, Jonathan N. Davidson, Martin P. Foster "Single-Switch High Voltage Gain DC-DC Converter with Non-coupled Inductor", IET Power Electronics, 2020.

Conference Presentations

1. **Sajad A. Ansari**, Jonathan N. Davidson, Martin P. Foster, and David Stone " A Design Methodology for a CLLLC Bidirectional Resonant Converter with an Integrated Transformer", International Exhibition and Conference for Power Electronics, Intelligent Motion, Renewable Energy and Energy Management PCIM Europe, 2023.
2. **Sajad A. Ansari**, Jonathan N. Davidson, Martin P. Foster, and David Stone "Analysis of Test Methods for Measurement of Leakage and Magnetising Inductances in Integrated Transformers", The 24th European Conference on Power Electronics and Applications (EPE), 2022.
3. **Sajad A. Ansari**, Jonathan Davidson, and Martin Foster, "Fully-integrated Transformer with Asymmetric Leakage Inductances for a Bidirectional Resonant Converter", The 11th International Conference on Power Electronics, Machines and Drives (PEMD), 2022.
4. **Sajad A. Ansari**, Jonathan N. Davidson, Martin P. Foster, and David Stone "Analysis and Design of a Fully-Integrated Planar Transformer for LCLC Resonant Converters", The 23rd European Conference on Power Electronics and Applications (EPE), 2021.

5. **Sajad A. Ansari**, Jonathan N. Davidson, and Martin P. Foster "Analysis, Design and Modelling of Two Fully-Integrated Transformers with Segmental Magnetic Shunt for LLC Resonant Converters", The 46th Annual Conference of the IEEE Industrial Electronics Society (IECON), 2020.
6. **Sajad A. Ansari**, Jonathan Davidson, and Martin Foster, "A Comparative Evaluation of Si MOSFET-based Soft Switching DC-DC converters and GaN HEMT-based Hard Switching DC-DC converters", The 10th International Conference on Power Electronics, Machines and Drives (PEMD), 2020.

Acknowledgements

As I approach the end of my PhD, it gives me great pleasure to reflect on all the invaluable help and support I have received, and to show my appreciation for it. So many people made this PhD the pleasant journey it was. In this small space I wish to offer thanks to those special people who have had a great impact on my work.

I would firstly like to acknowledge the support and encouragement of my academic supervisors, Jonathan Davidson and Martin Foster, who have helped me both for my professional and personal development. The friendly and supportive environment provided by the EMD group colleagues and staff has been crucial in making my time at the university enjoyable and productive.

A sincere acknowledgement to E&C lab teachers and staff, especially Panos Lazari, for giving me the opportunity to gain teaching experience and their prestigious support through my Fellowship of the Higher Education Academy (FHEA) application which I would not have been awarded without their support.

To my family, who have always stood by me with their love, encouragement, and advice, I owe a debt of gratitude. Their unrelenting efforts have made this thesis readable and achievable.

Lastly, I extend my heartfelt thanks to my dear friends, Kimia, Mahmoud, Yousef, Toby, Hossein, Ellie, Eloise, Hubert, Chris, Hamid, Navid and Amirreza who have had to endure me the most during my studies in Sheffield and to whom I owe so much. Their unwavering support, time, safe space, and love have made the arduous journey of completing this PhD possible.

Contents

Nomenclature

B	magnetic flux density
C_{o}	output capacitance
C_{r}	resonant capacitor
C_{r1}	primary resonant capacitance
C_{r2}	secondary resonant capacitance
C_{oss}	output capacitance of MOSFET
C_{St}	stray capacitance of the circuit
C_{ZVS}	summation of C_{oss} and C_{St}
D	diode
D	duty cycle (ratio)
D_{a}	auxiliary diode
D_{o}	output diode
$\mathrm{D_{a.sb}}$	antiparallel diode of $\mathrm{S_{a.sb}}$
E	energy
E_{air}	energy stored within the air area of E-cores
E_{fair}	energy stored within the air area of E-cores of five-segment shunt topology
E_{tair}	energy stored within the air area of E-cores of two-segment shunt topology
E_{P}	energy stored in the primary winding
E_{S}	energy stored in the secondary winding
E_{Sh}	energy stored in the shunt
f_{r}	resonance frequency
f_{s}	switching frequency
$f_{\mathrm{r\_NL}}$	resonance frequency of the LLC converter at no-load
f_{N}	normalised frequency
$f_{\mathrm{N\_Cr}}$	normalised crossing frequency of the LLC converter
$f_{\mathrm{N\_Bo}}$	normalised boundary frequency of the LLC converter
$f_{\mathrm{N\_NL}}$	normalised frequency of the LLC converter at no-load
$f_{\mathrm{N\_max}}$	maximum normalised switching frequency
$f_{\mathrm{N\_min}}$	minimum normalised switching frequency
$f_{\mathrm{N\_CTM}}$	normalised frequency of complete transformer model
$\mathfrak{F}_{\mathrm{P}}$	MMF of each layer of the primary winding
$\mathfrak{F}_{\mathrm{S}}$	MMF of each layer of the secondary winding
h_{P}	primary winding conduction thickness
h_{S}	secondary winding conduction thickness
H_{air}	magnetic field intensity within the air area of E-cores
$h_{\Delta\mathrm{P}}$	primary winding insulation thickness
$h_{\Delta\mathrm{S}}$	secondary winding insulation thickness
i_{ds}	drain-source current
i_{P}	primary current

i_{S}	secondary current
$i_{C_{\mathrm{r}}}$	resonant capacitor current
$i_{L_{\mathrm{r}}}$	resonant inductor current
$i_{\mathrm{S_a}}$	current of auxiliary switch
$i_{\mathrm{S_m}}$	current of main switch
i_{AC}	secondary current of the LLC converter
I_{o}	DC output current
I_{r}	RMS of resonant current of the LLC converter
I_{In}	DC input current
$I_{\mathrm{S_m}}$	average current of the main switch
$I_{\mathrm{C(rms)}}$	capacitor RMS current
$I_{\mathrm{D(avg)}}$	diode average current
$I_{\mathrm{D(rms)}}$	diode RMS current
$I_{\mathrm{L(rms)}}$	inductor RMS current
$I_{\mathrm{D_o(avg)}}$	average current of the output diode
$I_{\mathrm{D_o(rms)}}$	RMS current of the output diode
$I_{\mathrm{D_{a.sb}(rms)}}$	RMS current of $\mathrm{D_{a.sb}}$
$I_{\mathrm{D_{a.sb}(avg)}}$	Average current of $\mathrm{D_{a.sb}}$
$I_{\mathrm{S_{a.sb}(rms)}}$	RMS current of the auxiliary switch of soft-switched boost converter
$I_{\mathrm{S_{m.b}(rms)}}$	RMS current of the main switch of boost converter
$I_{\mathrm{S_{m.sb}(rms)}}$	RMS current of the main switch of soft-switched boost converter
$I_{\mathrm{ds(rms},i_{\mathrm{ds}}>0)}$	RMS current of the switch when the drain current is positive
k_{P}	number of turns in each layer of the primary winding
k_{S}	number of turns in each layer of the secondary winding
L_{r}	resonant inductor
L_{r1}	primary resonant inductance
L_{r2}	secondary resonant inductance
$L_{\mathrm{r\_CTM}}$	resonant inductance of complete transformer model
L_{m}	magnetising inductance
$L_{\mathrm{m\_P}}$	primary magnetising inductance
$L_{\mathrm{m\_S}}$	secondary magnetising inductance
$L_{\mathrm{m\_STM}}$	magnetising inductance of simplified transformer model
L_{fm}	magnetising inductance of five-segment shunt topology
L_{tm}	magnetising inductance of two-segment shunt topology
L_{min}	minimum inductance
L_{fPP}	primary self-inductance of five-segment shunt topology
L_{fSS}	secondary self-inductance of five-segment shunt topology
L_{tPP}	primary self-inductance of two-segment shunt topology
L_{tSS}	secondary self-inductance of two-segment shunt topology
L_{PP}	primary self-inductance
L_{SS}	secondary self-inductance

L_{PS}	mutual inductance
L_{SP}	mutual inductance
L_{Sh}	shunt inductor
L_{Lk}	leakage inductance
L_{fLk}	leakage inductance of five-segment shunt topology
L_{tLk}	leakage inductance of two-segment shunt topology
$L_{\mathrm{fLk\_Sh}}$	leakage inductance caused by the shunt of five-segment shunt topology
$L_{\mathrm{tLk\_Sh}}$	leakage inductance caused by the shunt of two-segment shunt topology
$L_{\mathrm{Lk\_P}}$	primary leakage inductance
$L_{\mathrm{Lk\_S}}$	secondary leakage inductance
$L_{\mathrm{Lk\_S(P)}}$	$L_{\mathrm{Lk\_S}}$ referred to the primary side
$L_{\mathrm{Lk\_S\_STM}}$	secondary leakage inductance of simplified transformer model
$L_{\mathrm{Lk\_P\_STM}}$	primary leakage inductance of simplified transformer model
$L_{\mathrm{Lk\_P\_Sh}}$	primary leakage inductance caused by the shunt
$L_{\mathrm{Lk\_S\_Sh}}$	secondary leakage inductance caused by the shunt
ℓ_{G}	air gap length between two E-cores
ℓ_{GP}	distance between the primary shunt and primary E-core
ℓ_{GS}	distance between the secondary shunt and secondary E-core
ℓ_{Sh}	distance between shunt and E-cores
ℓ_{fG1}	horizontal air gap length of five-segment shunt topology
ℓ_{tG1}	horizontal air gap length of two-segment shunt topology
ℓ_{fG2}	vertical air gap length of five-segment shunt topology
ℓ_{tG2}	vertical air gap length of two-segment shunt topology
M	voltage gain
M_{Nom}	nominal voltage gain of the LLC converter
M_{max}	maximum gain of the LLC converter
M_{min}	minimum gain of the LLC converter
M_{AC}	gain of AC circuit (AC voltage gain) of the LLC converter
$M_{\mathrm{AC\_Bo}}$	boundary gain of AC circuit of the LLC converter
$M_{\mathrm{AC\_NL}}$	no-load AC voltage gain of the LLC converter
$M_{\mathrm{AC\_NL\_\infty}}$	$M_{\mathrm{AC\_NL}}$ when operating frequency is infinity
$M_{\mathrm{AC\_Ind\_max}}$	maximum AC gain of the LLC converter for a fixed λ and a fixed Q
n	turns ratio
n_{P}	number of layers of the primary winding
n_{S}	number of layers of the secondary winding
N_{P}	primary turns number
N_{S}	secondary turns number
P_{d}	losses of the device
P_{o}	output power
$P_{\mathrm{o\_max}}$	maximum output power
P_{Loss}	total power loss
$P_{\mathrm{Loss}}^{\mathrm{C}}$	capacitor losses

$P_{\mathrm{Loss}}^{\mathrm{D}}$	diode losses
$P_{\mathrm{Loss}}^{\mathrm{L}}$	inductor losses
$P_{\mathrm{Loss}}^{\mathrm{S}}$	switch losses
$P_{\mathrm{Loss}}^{\mathrm{L,ohmic}}$	ohmic losses of the inductor
$P_{\mathrm{Loss}}^{\mathrm{S,gate}}$	gate losses of the switch
$P_{\mathrm{Loss}(i_{\mathrm{ds}}<0)}^{\mathrm{D}}$	losses of the antiparallel diode of switch when the drain current is negative
$P_{\mathrm{Loss}}^{\mathrm{S,switching}}$	switching losses of the switch
$P_{\mathrm{Loss}}^{\mathrm{S,conduction}}$	conducting losses of the switch
Q	quality factor
Q_{g}	total input gate charge of the switch
Q_{max}	maximum quality factor
Q_{Bo}	boundary quality factor of the LLC converter
Q_{CTM}	quality factor of complete transformer model
r_{C}	capacitor equivalent series resistance
$r_{\mathrm{C_o}}$	output capacitor series resistance
$r_{\mathrm{C_r}}$	resonant capacitor series resistance
r_{L}	inductor equivalent series resistance
$r_{\mathrm{L_r}}$	resonant inductor series resistance
R_{cs}	case-to-heatsink thermal resistance
R_{jc}	junction-to-case thermal resistance
R_{sa}	thermal resistance of heatsink
$R_{\mathrm{ds(on)}}$	on-state resistance of switch
R_{D}	series resistances of the diode
$R_{\mathrm{L\_AC}}$	AC equivalent load resistance of the LLC converter
$R_{\mathrm{L\_AC(P)}}$	$R_{\mathrm{L\_AC}}$ referred to the primary side
$\mathcal{R}$	reluctance
$\mathcal{R}_{\mathrm{C}}$	reluctance of core
$\mathcal{R}_{\mathrm{G}}$	reluctance of air gap
$\mathcal{R}_{\mathrm{Sh}}$	reluctance of shunt
$\mathcal{R}_{\mathrm{T\_P}}$	reluctance experienced by the primary winding
$\mathcal{R}_{\mathrm{T\_S}}$	reluctance experienced by the secondary winding
S	switch
$\mathrm{S_a}$	auxiliary switch
$\mathrm{S_{a.sb}}$	auxiliary switch of soft-switched boost converter
$\mathrm{S_m}$	main switch
$\mathrm{S_{m.b}}$	main switch of boost converter
$\mathrm{S_{m.sb}}$	main switch of soft-switched boost converter
S_{P}	primary switch
S_{S}	secondary switch
t_{on}	turn-on time
$t_{\mathrm{off.s}}$	current fall time plus voltage rise time of switch

$t_{\mathrm{on.s}}$	current rise time plus voltage fall time of switch
T_{a}	ambient temperature
T_{c}	case temperature
T_{j}	junction temperature
T_{r}	resonant period
T_{s}	switching period
T_{D}	dead time
t_{Sh}	shunt thickness
t_{ShP}	primary shunt thickness
t_{ShS}	secondary shunt thickness
v_{o}	AC output voltage
v_{P}	primary voltage
v_{S}	secondary voltage
$v_{L_{\mathrm{r}}}$	resonant inductor voltage
$v_{\mathrm{In\_Fu}}$	fundamental component of $v_{\mathrm{In\_Pu}}$
$v_{\mathrm{In\_Pu}}$	input pulse voltage of the LLC converter
V_{gg}	voltage applied to the gate driver of switch
$V_{\mathrm{In\_max}}$	maximum input voltage
$V_{\mathrm{In\_min}}$	minimum input voltage
$v_{\mathrm{Re\_Fu}}$	fundamental component of $v_{\mathrm{Re\_Pu}}$
$v_{\mathrm{Re\_Pu}}$	secondary pulse voltage of the LLC converter
$v_{\mathrm{Re\_Fu(P)}}$	$v_{\mathrm{Re\_Fu}}$ referred to the primary side
V_{f}	diode forward voltage drop
V_{o}	DC output voltage
V_{ds}	Drain-source voltage
$V_{\mathrm{gs.S_m}}$	gate-source voltage of the main switch
$V_{\mathrm{ds.S_m}}$	drain-source voltage of the main switch
$V_{\mathrm{gs.S_a}}$	gate-source voltage of the auxiliary switch
$V_{\mathrm{ds.S_a}}$	drain-source voltage of the auxiliary switch
V_{In}	DC input voltage
V_{L}	average current of the inductor
w_{Sh}	Shunt wideness
x_{P}	distance between primary winding and shunt
x_{fP}	distance between primary winding and five-segment shunt
x_{tP}	distance between primary winding and two-segment shunt
x_{S}	distance between secondary winding and shunt
x_{fS}	distance between secondary winding and five-segment shunt
x_{tS}	distance between secondary winding and two-segment shunt
Z_{n}	characteristic impedance of soft-switched boost converter
Z_{o}	characteristic impedance of the LLC converter
$Z_{\mathrm{In\_N}}$	normalised input impedance of the LLC converter

$Z_{\mathrm{In\_AC}}$	input impedance of the AC circuit of the LLC converter
Δi_{L}	inductor current ripple
ΔV_{o}	output voltage ripple
ΔV_{ds}	change of drain-source voltage
λ	inductance ratio
λ_1	primary inductance ratio of complete transformer model
λ_2	secondary inductance ratio of complete transformer model
μ_0	permeability of the air
μ_{r}	relative permeability of the core
μ_{Sh}	relative permeability of the shunt
μ_{ShP}	relative permeability of the primary shunt
μ_{ShP}	relative permeability of the secondary shunt
ϕ_{PS}	mutual flux generated by the primary winding
ϕ_{SP}	mutual flux generated by the secondary winding
Φ	phase difference between $v_{\mathrm{In\_Fu}}$ and i_{r}
Ψ	phase difference between $v_{\mathrm{In\_Fu}}$ and i_{AC}
ω	angular frequency
η	efficiency

List of figures

List of tables

Chapter 1

Introduction

This Chapter introduces the body of work which forms this thesis. It explains the motivation for the presented research and introduces the issues surrounding integrated transformers in a practical context, describing the challenges facing modern power electronics designers. Finally, it sets out the structure of the thesis and states the contribution made by each chapter.

1.1 Motivation

Power electronics bridges the gap between traditional analogue small-signal technologies, such as amplifiers, and traditional power technologies, such as transformers and power generators, by enabling the voltage-current transformation of all categories of electrical waveform [3].

Power electronics systems can fine-tune the technology and enable it to perform at the top of its ability. They are a vital part of every electronic device, from tiny voltage regulators inside microprocessors to battery chargers, renewable energy systems, power regeneration capture in braking systems and motor drives in electric vehicles. In the future, not only is this highly unlikely to change but also the attention will increase as our lives are enriched with more and more electronic devices and renewable energy demand grows. In other words, it is an exciting period in power electronic technology, as each new electrical device poses new challenges for power electronics engineers, and they require a wide range of specifications.

Power electronics is the workhorse that has underpinned most of our electrical and electronic systems. One of the interesting topics for power electronics experts is improving the existing systems in terms of efficiency, power density, reliability, and cost. This field requires an ever-improving arsenal of circuit designs, control techniques and filters as well as developing new physical arrangements of components (especially magnetic devices) to improve the overall

Fig. 1.1 Power electronics inside a SAMSUNG mobile phone charger [1].

efficiency, power density and cost of the power electronics systems. This thesis aims to further the state-of-the-art in this field.

1.2 Design constraints for power electronics

Power electronics devices have different constraints depending on their applications. In mobile phone chargers, for example, the electric design is limited by the small volume inside the charger cube, power, mobile phone battery's characteristics and required charging speed. In **Fig. 1.1**, a mobile phone charger sold by SAMSUNG is shown. As shown, the available space inside the charger cube is clearly limited while the charger needs to rectify the grid voltage to a DC voltage and then drop the voltage to 5 V. In addition, the charger must regulate the output voltage at 5 V while the grid voltage is not stable and despite the battery charging demand being non-linear. Furthermore, for mobile phones, tablets and laptop chargers in particular, the mass of power electronics (weight and size) is an issue because people are always carrying them. Therefore, there is an increasingly strong impetus to produce smaller and lighter power electronics.

Reductions in size and weight have been an interesting topic through all branches of power electronics. In **Fig. 1.2**, for example, the size change of computer power supplies from 1990 to 2000 is presented. As shown in **Fig. 1.2**, since there has been a demand for smaller computers, the newer computer power supply has a power density almost double of its predecessor.

circa 1990 (1.8 kg) circa 2000 (0.9 kg)

Fig. 1.2 Size comparison of two computer power supplies with identical electrical characteristics (power, input, and output voltages) from different period [2].

Additionally, as a rule of thumb, a smaller device needs less materials and therefore reduction of size eventually results in reduction of cost as well.

There are several ways to reduce the size of a power electronics converter, *viz* changing the topology of the converter for fewer components [4], switching the converter at higher frequencies [5] and magnetic integration [6]. Changing the topology is not always possible and higher switching frequency has its own limitation due to switching losses and the inability of semiconductor devices. However, magnetic integration (when it is possible) can increase the power density of the converter noticeably and reduce the cost. Magnetic integration is therefore a vital area of research and one to which this thesis intends to offer a contribution.

In the world of power electronics converters, capacities range from a few watts to several gigawatts, catering to diverse applications and technological advancements. This thesis focuses on investigating power levels below 50W, targeting desktop computer applications for enhanced efficiency.

Additionally, the research explores size reduction in bidirectional converters for electric vehicles, operating at a few kilowatts. Due to safety and hardware limitations, experimentation is conducted in a laboratory set-up at a few hundred watts. However, the findings could be poised to impact real-world applications up to a few kilowatts.

1.3 Novelty and Contribution

This thesis aims to develop technologies that increase power density and decrease the cost of power electronics DC-DC converters without decreasing their efficiency. Pulse-width-modulated (PWM) DC-DC converters are investigated for high switching frequencies, and it is shown that achieving high power density alongside high efficiency is difficult in these converters. On the other hand, resonant converters have good efficiency because of their soft-switching capability, and they can also benefit from high power density through magnetic integration. Therefore, the main focus of this thesis is addressing the issues of integrated transformers used in resonant converters. The novelty presented in this thesis covers five broad areas, which are discussed in the following subsections.

1.3.1 Evaluation of Si MOSFETs and GaN HEMTs in soft-switched and hard-switched DC-DC boost converters

The PWM converters, such as buck and boost, suffer from high switching losses and cannot provide high efficiency at high switching frequencies. Hence, in these converters, high power density cannot be obtained since the switching frequency is limited. Even though soft-switching capability can be achieved by adding an auxiliary circuit to the conventional topology of the PWM converters, the auxiliary circuit adds complexity and cost [7, 8]. Using wide bandgap (WBG) devices, such as gallium nitride (GaN), results in lower switching losses than using silicon (Si), and can be used while retaining the simple structure of a hard-switched topology. However, the high cost of these devices is problematic for what are frequently cost-sensitive applications. Additionally, capacitor-discharge switching losses remain.

To quantify the cost and efficiency, this thesis compares soft-switching techniques and WBG-based switches for a DC-DC boost converter in the application range of hundred watts. The performance of four prototypes including the soft-switched and hard-switched DC-DC converters with both state-of-the-art Si and GaN switches are evaluated in terms of cost, power

density, efficiency, and reliability using theoretical analysis, simulation and experimental results. It is shown that the GaN-based hard-switched converter provides higher efficiency and power density but is more expensive than its Si-based counterpart and yet is still cheaper than soft-switched converters. Therefore, adding an auxiliary circuit to obtain soft switching leads to a more expensive and complicated circuit and does not always guarantee a higher efficiency.

1.3.2 Fully-integrated planar transformer with a segmental shunt for LLC resonant converters

As mentioned in subsection 1.3.1, PWM converters suffer from high switching losses and cannot provide high efficiency at high switching frequencies. In addition, it is shown in Chapter 4 that adding soft-switching capability to PWM converters is usually with the penalty of a more complicated circuit and more expensive converter, and it does not always guarantee a higher efficiency. On the other hand, resonant converters provide soft-switching capability inherently and they can achieve high efficiency at high switching frequencies [9, 10]. Therefore, the remaining chapters of this thesis focus on resonant converters since they are more likely to achieve both high efficiency and power density.

To decrease the volume and cost, and increase the efficiency of resonant converters, such as LLC topology, the magnetic elements should be integrated into a magnetic transformer, known as integrated transformer (IT) [11]. Amongst different techniques for magnetic integration, the inserted-shunt integrated planar transformer (presented later in **Fig. 3.12**, page 67) is an attractive technique for integrating magnetic components of the LLC topology in a single transformer.

This thesis presents two topologies (termed IT1 and IT2) which provide high leakage inductance in shunt-inserted integrated magnetic planar transformers designed for magnetic integration in LLC topology. These differ from conventional designs by replacing the low-permeability magnetic shunt of a planar transformer with high-permeability magnetic shunt segments, separated by many small air gaps. This approach results in a shunt with the same bulk permeability as the conventional design, while using lower cost and readily available magnetic materials such as ferrite. A modelling and design approach which can estimate the leakage and magnetising inductances precisely is provided for each topology. Theoretical analysis is presented and verified using finite-element analysis and experimental

implementation. AC resistance analysis for both transformer topologies is also presented. In addition, an LLC resonant converter is built to verify the performance of the proposed fully-integrated magnetic transformers in practice. It is shown that the proposed topologies can integrate all three magnetic components of an isolated LLC resonant converter in a single planar transformer, which reduces the converter's volume and cost.

1.3.3 Fully-integrated solid shunt planar transformer for LLC resonant converters

Although the structures (IT1 and IT2) proposed in subsection 1.3.2 (Chapter 5) eliminate the need for shunts with specific permeabilities and dimensions, the inserted shunt has multiple segments and has to be placed between two E-cores which makes the implementation difficult. Therefore, to address this issue, a new shunt topology (termed IT3) for achieving high leakage inductance in inserted-shunt integrated magnetic planar transformers is proposed.

In the proposed topology, two one-segment shunts are placed across the planar E-core air gap and between the primary and secondary windings. The proposed topology benefits from using solid inexpensive ferrite shunts, making manufacturing easier. A detailed mathematical model is derived from which a design methodology is developed, providing accurate estimation for the leakage and magnetising inductances. The theoretical analysis has been verified using finite-element analysis and experimental implementation.

1.3.4 Inserted-shunt integrated planar transformer with low secondary leakage inductance for LLC resonant converters

The leakage inductance of an inserted-shunt integrated transformer is usually utilised as the series inductor of an LLC topology. However, leakage inductance exists on both the primary and secondary sides of an inserted-shunt integrated transformer and secondary leakage inductance leads the control and design of the converter to difficulty [12].

In this thesis, a novel topology (termed IT4) for inserted-shunt integrated transformers is proposed which has low secondary leakage inductance. The inserted shunt of the proposed topology is not segmental and can be located conveniently within the transformer. In addition, the inserted shunt does not require low permeability core material, simplifying its manufacture.

The design and modelling of the proposed transformer topology are presented and verified by finite-element analysis and experimental implementation.

1.3.5 Fully-integrated transformer with asymmetric primary and secondary leakage inductances for a bidirectional resonant converter

Typically, inserted-shunt integrated transformers have symmetric primary and secondary leakage inductances [13]. However, bidirectional resonant converters typically could operate more efficiently with different primary and secondary series inductances.

In this thesis, a new shunt topology (termed IT5) for an inserted-shunt integrated transformer which can provide tuneable, asymmetric leakage (series) inductances on the primary and secondary sides is presented. Two magnetic shunts, with appropriate air gaps, are inserted between two E-cores and the primary and secondary windings are separated by being placed at opposite sides of the shunts. The proposed transformer is analysed in detail and modelling and design guidelines are provided. It is shown that the magnetising inductance and the primary and secondary leakage inductances are decoupled from each other, and they can be determined separately. The design has the advantage of using planar E-cores and magnetic sheets that are readily available in the market. The theoretical analysis is verified by simulation and experimental results. In addition, to demonstrate the performance of the proposed integrated transformer in practice, an exemplar bidirectional CLLLC resonant converter is designed, constructed and tested using the new integrated transformer.

1.4 Thesis structure

The thesis structure is presented diagrammatically in **Fig. 1.3**. The thesis has 9 chapters, and it has a predominantly linear structure, with each chapter expanding and improving on the previous. A brief description of each chapter is provided below and the publications corresponding to each chapter are presented in section 1.5 (see **Fig. 1.4**).

Chapter 1 introduces current topics in modern power electronics engineering and the motivation for this thesis which is increasing the power density of power electronics converters without negatively affecting their cost and efficiency. In addition, the breakdown of the thesis

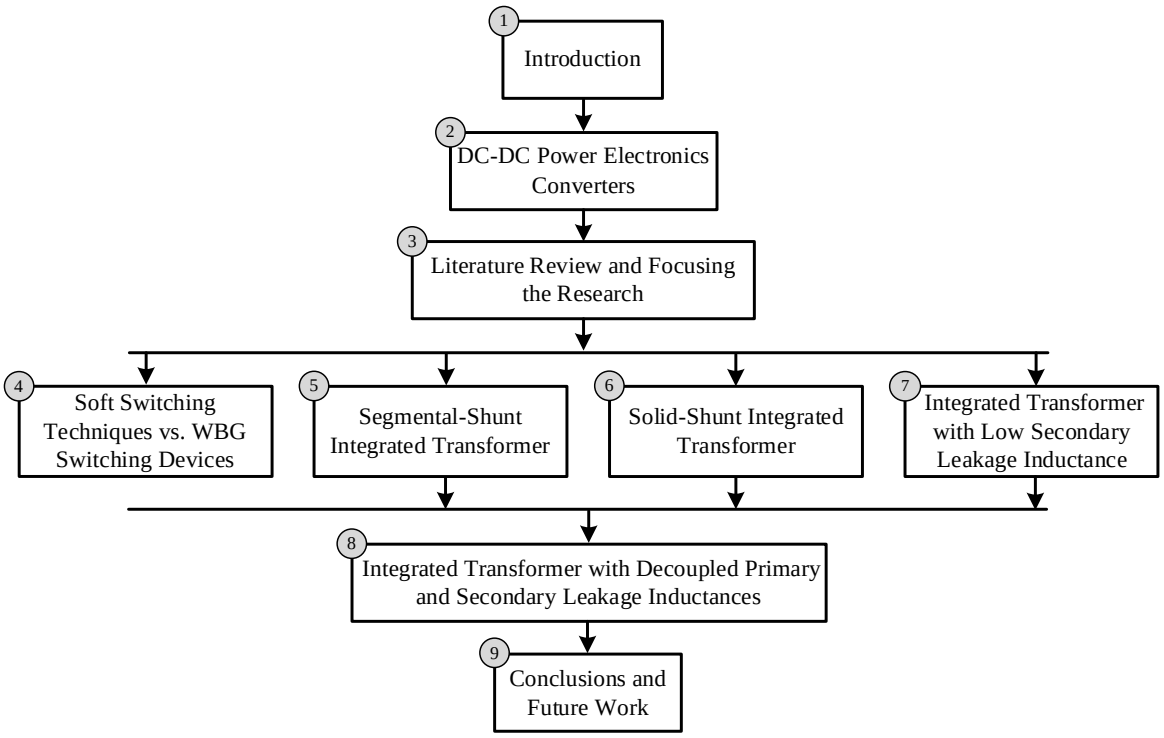

Fig. 1.3 Thesis structure.

structure is presented in this Chapter. Finally, the links between the papers generated by this thesis and its chapters are discussed.

Chapter 2 discusses different types of DC-DC converters and explains why switched-mode power supplies are preferred compared to linear power supplies. PWM converters and their limitation for achieving high power density are discussed. In addition, Chapter 2 investigates the LLC converter for achieving high power density and presents the theoretical analysis and design guidelines of this converter. The benefits of magnetic integration for the LLC topology are also presented.

Chapter 3 discusses reducing switching losses of DC-DC PWM converters. It discusses the advantages and disadvantages of soft-switching techniques and new semiconductor devices. This introduces the first research focus of this thesis, further investigating the PWM converters which either use soft-switching techniques or new WBG semiconductor devices or both or

neither of them, to find the most beneficial method for limiting the switching losses. This question will be investigated in Chapter 4.

The chapter also highlights the benefits of resonant converters, particularly the LLC topology, for achieving high efficiency and power density. To achieve both, integrated magnetic components are essential, and the inserted-shunt integrated transformer's topology is selected for further investigation. Several issues with this transformer type are discussed, leading to four additional research focuses in Chapters 5-8 to address these challenges.

Chapter 4 evaluates the performance of four prototypes including the soft-switched and hard-switched DC-DC converters with both state-of-the-art Si and GaN switches in terms of cost, power density, and efficiency using theoretical analysis, simulation and experimental results..

Chapter 5 presents two new transformer topologies (termed IT1 and IT2) which provide high leakage inductance in shunt-inserted integrated magnetic transformers. The proposed topologies are modelled and investigated in detail. Simulation and experimental results are presented to verify the theoretical analysis.

Chapter 6 discusses the issue of the topologies presented in Chapter 5 (IT1 and IT2) and proposes a new topology (termed IT3) which addresses their issue. Again, the proposed topology is modelled and investigated in detail and verified by a simulation study and experimental investigation.

Chapter 7 mentions an important issue of inserted-shunt integrated transformers which is increasing the leakage inductance on the secondary side. To address this issue, a new topology (termed IT4) for inserted-shunt integrated transformers is presented and investigated in this Chapter.

Chapter 8 introduces an inserted-shunt integrated transformer which can be suitable for bidirectional LLC-type resonant converters. The proposed topology is modelled and investigated in detail and verified by a simulation study and experimental investigation.

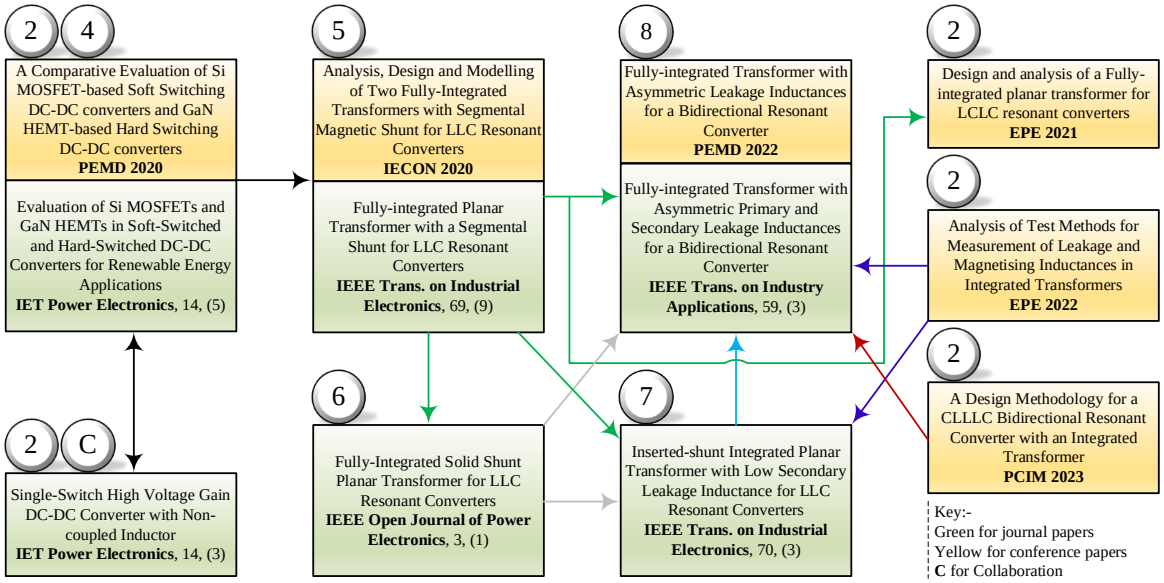

Fig. 1.4 Links between the papers and chapters (numbers) of this thesis.

Finally, in ***Chapter 9***, a brief conclusion of the work and its achievements are presented. In addition, it suggests further work which could be undertaken following from the work presented in this thesis, and which will increase the thesis' impact on the field of magnetic integration for resonant converters.

1.5 Publication interconnections

Several parts of this thesis have been published in internationally recognised journals and conference proceedings. The links between the papers generated by this thesis and its chapters are presented in **Fig. 1.4**. In addition, the link between different papers is indicated too.

In summary, five journal papers [14-18] and six conference proceedings [19-24] have been generated directly from this thesis. In addition, I have had a collaboration with a Master's student for his main project and the results of this collaboration, which is in line with the content of Chapter 2, have been published in a journal paper [25].

Chapter 2

DC-DC Power Electronics Converters

This Chapter introduces PWM DC-DC converters and discusses their advantages and disadvantages. It explains the switching losses of traditional hard-switched PWM converters and soft-switching techniques that can be applied to reduce switching losses of these DC-DC converters.
Resonant converters are then introduced, and it is discussed that resonant converters, such as LLC topology, could be a better option compared to the PWM converters for achieving both high efficiency and power density. The LLC topology is presented and analysed in detail. In addition, design guidelines of an LLC-type resonant converter are provided. Finally, the benefits of magnetic integration for the LLC resonant converter are discussed.

2.2 Introduction to switched-mode power supplies

A power supply is an electrical device that provides electrical power to an electronic load such as laptop, computer, server, or other electronic devices. The main design specification of a power supply is to provide the correct voltage, current and frequency to power the load. The energy conversion could be AC to DC, DC to DC, DC to AC or AC to AC. Consequently, power supplies are sometimes regarded as electrical power converters.

Applications of power supplies cover high-power conversion equipment such as DC power transmission to everyday appliances, *viz* mobile phone chargers, electric vehicles and computer power supplies.

Every power supply has a power input connection, which obtains energy from an energy source, and a single or multiple power output connections that transmit current to the electrical load. The energy source could be from the AC electric power grid, such as an electrical outlet, or could be from DC energy storage devices, such as batteries.

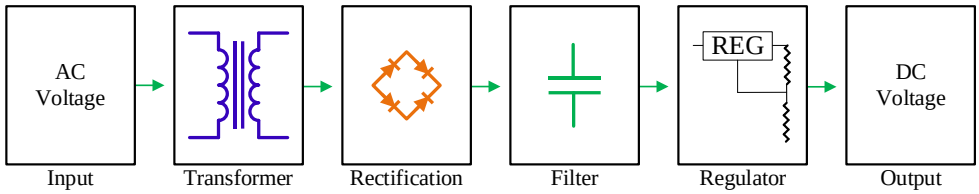

Fig. 2.1 Block diagram example of a typical AC-to-DC linear power supply.

The power-supplies are often categorised in two different types: linear and switched-mode power supplies [26].

2.2.1 Linear power supplies

Linear power supplies have been around for over 100 years, long before the advent of semiconductors. A linear power supply does not contain any switching or digital components and operates at low frequency or DC. In **Fig. 2.1** , the block diagram example of a typical AC-to-DC linear power supply is presented. This power supply includes four blocks. In the first block, the transformer changes the voltage level towards the required voltage level. There is then a rectifier to convert the new AC voltage to a DC voltage. A capacitor smooths the DC voltage and supresses ripple by holding energy when the transformer output voltage drops. Finally, there is a linear regulator that helps ensure that the DC output voltage is steady regardless of any variation in the input voltage, which enables the load to operate properly.

A linear power supply has some outstanding characteristics such as very low noise and ripple, immunity from mains-borne noise, simplicity, robustness, ease of design and repair. They can also generate very high voltages (thousands of volts) and very low voltages (less than 1V) from mains supplies with an appropriate transformer selection.

Along with the many advantages of linear power supplies, there are some disadvantages. Linear regulators are ideal for low-power applications; disadvantages appear when higher power is required. In a high-power application, linear power supplies require a large transformer and other large components to handle the power as the frequency of operation is low (typically 50-60 Hz). Using larger components increases the overall size and weight of the power supply. It also makes the power supply bulky and less portable. Linear power supplies use power

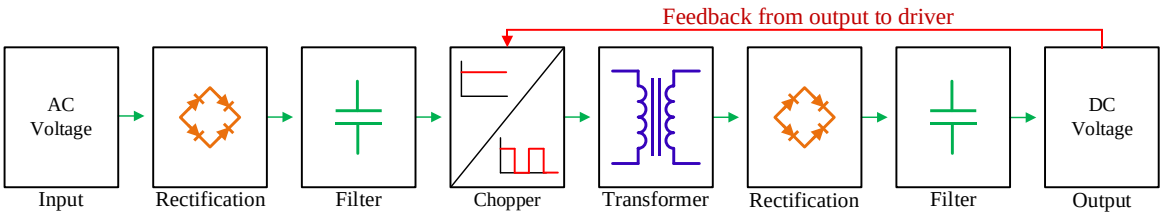

Fig. 2.2 Block diagram example of a typical AC-to-DC switched-mode power supply.

dissipation to achieve voltage regulation. Therefore, high heat loss occurs while regulating a high power demand by the load, making the process inefficient.

2.2.2 Switched-mode power supplies

Switched-mode power supplies address many of the issues associated with linear power supply design, such as transformer size and the need for lossy linear voltage regulation. A switched-mode power supply is designed using a different technique as presented in **Fig. 2.2**. The low-frequency transformer is eliminated and the input voltage is rectified and filtered directly. The voltage is then passed through a chopper, an electronic switch (e.g. a MOSFET), that regulates the voltage and produces a high-frequency pulse train. A magnetic transformer can be used for reduction/increase of the voltage level and to provide electric isolation. Before reaching the output, the voltage is filtered and rectified once more [27].

The transformation into a high frequency pulse train helps reduce the size of the components, leading to reduced volume. In addition, an inefficient linear regulator circuit is not needed since the final output is used to send feedback to the chopper block, which makes a feedback loop that regulates output voltages regardless of any variation in the input voltage and load.

2.2.3 DC-DC converters

There are many applications in which the input supply is DC and therefore the input rectification and smoothing filter blocks (presented in **Fig. 2.2**) are not needed anymore. DC-DC converters are widely used to transform and distribute DC power in systems and instruments. A DC-DC converter is a subset of power supplies that specializes in regulating and converting DC voltages to different levels as required by the specific application. DC

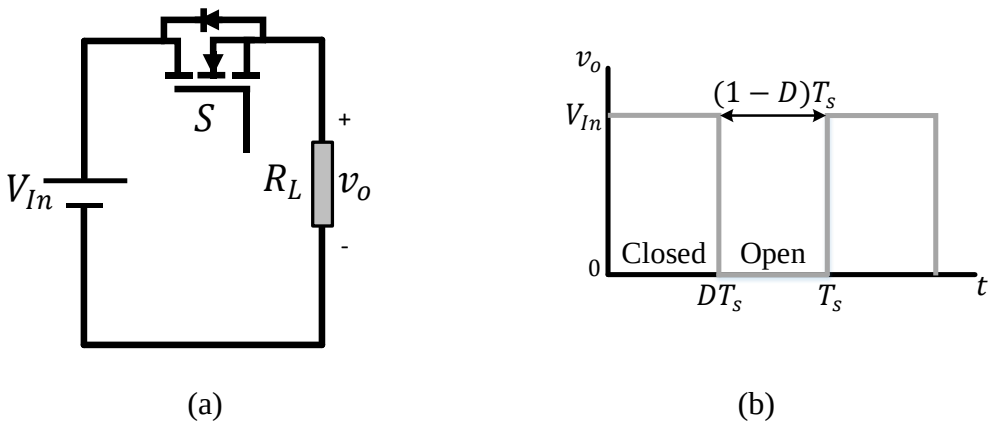

(a) (b)

Fig. 2.3 A basic DC-DC switching converter (DC chopper). (a) Schematic. (b) Switching waveforms.

power is usually available to a system in the form of a system power supply or battery. This power may be in the form of 5V, 28V, 48V or other DC voltages.

2.2.3.1 DC-DC PWM converters

One way to control the average power to a load is to control the average pulse-train voltage. This can be done by opening and closing an electronic switch in rapid fashion. This method of control is referred to as pulse width modulation (PWM).

In PWM, the overall switching period is kept constant while the on time of the electronic switch is varied. In a PWM converter, the transistor operates as an electronic switch by being completely on (closed) or completely off (open). For example, in a basic switching circuit presented in **Fig. 2.3(a)**, which is known as a DC chopper, the output is the same as the input when the switch is closed, and the output is zero when the switch is open.

If we assume all the elements of this DC chopper are ideal, periodic switching results in having a pulse in the output as shown in **Fig. 2.3(b)**. The average of the output voltage may be obtained by (2-1).

$$V_{\mathrm{o}} = \frac{1}{T_{\mathrm{s}}}\int_0^{T_{\mathrm{s}}} v_{\mathrm{o}}(t)\mathrm{d}t = \frac{1}{T_{\mathrm{s}}}\int_0^{DT_{\mathrm{s}}} V_{\mathrm{In}}\mathrm{d}t = V_{\mathrm{In}}D \qquad (2\text{-}1)$$

As shown in **Fig. 2.3**, the output DC voltage can be set by adjusting the fraction of the switching period, T_s, in which the switch is closed. This fraction can be named as duty ratio, D, which may be defined as (2-2).

$$D = \frac{t_{on}}{t_{on} + t_{off}} = \frac{t_{on}}{T_s} = t_{on} f_s \quad (2\text{-}2)$$

where f_s is the switching frequency, t_{on} is the period in which the switch is closed and t_{off} is the period in which the switch is open.

The converter presented in **Fig. 2.3** can reduce the voltage level by chopping the input voltage while often the requirement is to produce a purely DC voltage, and the converter may need to boost the voltage level for some applications. In addition, in this topology, switching losses may be high when the load is not purely resistive (as it is not for most of the applications). Therefore, many more complicated PWM converters have been proposed to address these issues such as buck, boost, buck-boost, SEPIC, Ćuk, forward and flyback converters. Amongst these converters, only the step-down (buck) and the step-up (boost) are the basic converter topologies and are briefly discussed in this thesis and the reader can be referred to [26, 27] to study other topologies.

The buck converter, which is presented in **Fig. 2.4(a)**, reduces the voltage of a power supply. The buck converter is a power electronics circuit that steps down the DC voltage to a level determined by the choice of components in your circuit. As shown in **Fig. 2.4(a)**, along with the power electronics solid-state device which acts as a switch for the circuit, there is another switch in the circuit which is a freewheeling diode. The diode provides a path for the inductor current when the switch is open and is reverse-biased when the switch is closed. The combination of these two switches forms a connection with a low-pass LC filter in order to reduce current or voltage ripples.

The whole operation of the buck circuit takes place in two modes, presented in **Fig. 2.4(b)**. In the first mode, the power MOSFET (main switch) is closed (turned on) and the diode is off (reverse-biased). Therefore, the current flows through the inductor and the output capacitor, and the inductor starts charging by the input source. In the second mode, the switch is turned

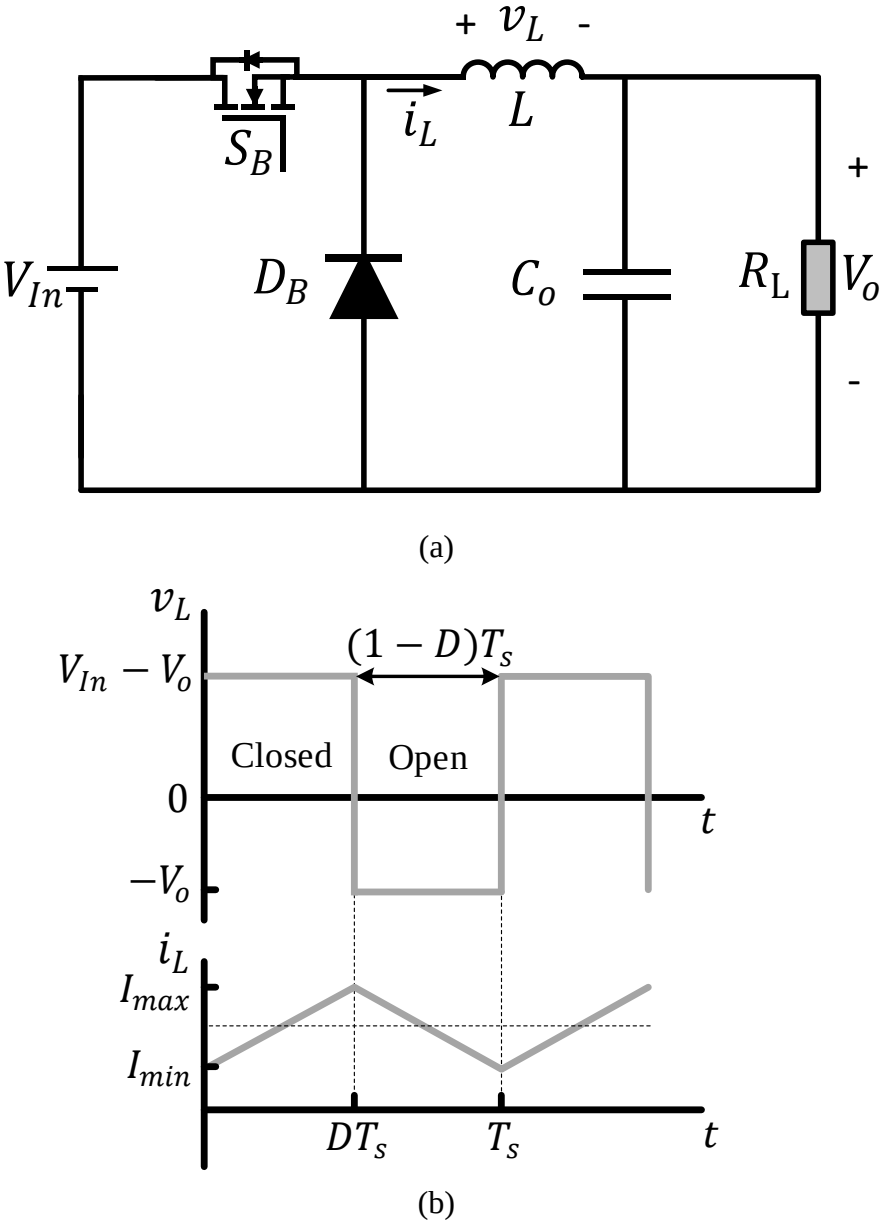

Fig. 2.4 Buck converter. (a) Schematic. (b) Switching waveforms.

off (open) and the diode turns on. Therefore, the inductor starts discharging to the load and the output capacitor through the diode.

The average voltage across the inductor is zero for periodic operation, assuming ideal components, continuous current in the inductor and a purely resistive load. Therefore, from **Fig. 2.4**,

$$V_{\mathrm{L}} = (V_{\mathrm{In}} - V_{\mathrm{o}})DT_{\mathrm{s}} + (-V_{\mathrm{o}})(1 - D)T_{\mathrm{s}} = 0 \quad (2\text{-}3)$$

Solving the preceding equation for V_{o} gives

$$V_{\mathrm{o}} = V_{\mathrm{In}}D \quad (2\text{-}4)$$

Therefore, the buck converter produces an output voltage which is less than or equal to the input voltage and its output voltage can be controlled by adjusting the duty ratio, D.

A buck converter and other DC-DC PWM converters may operate in three conduction modes which are presented as follows:-

- Continuous conduction mode (CCM): the inductor always has a non-zero current. In other words, the inductor current from the beginning to the end of a switching cycle is non-zero.
- Boundary conduction mode (BCM): the inductor current switches on (increases) as soon as the inductor current drops to zero. In other words, in each switching cycle, the inductor current increases from zero at the beginning of the switching period and drops to zero again at the end of the switching period. A specific duty cycle is needed in this method for each load.
- Discontinuous conduction mode (DCM): the inductor current drops to zero and remains zero until the start of the next switching period. In other words, in each switching cycle, the inductor current increases from zero at the beginning of the switching period and drops to zero before the end of the switching period. This can happen if the duty cycle is too short or the load is too small.

2.2.3.2 Soft-switched DC-DC PWM converters

In the topology of PWM converters, the controllable switches are required to turn on and turn off the entire load current during each switching. Switching devices absorb energy when they turn on or off if they go through a transition when both voltage and current are nonzero, presented in **Fig. 2.5(a)**. In this type of switching, which is known as hard switching, the switches are subjected to high switching stress and high switching power loss that increases linearly with the switching frequency of the PWM. Another significant drawback of this type

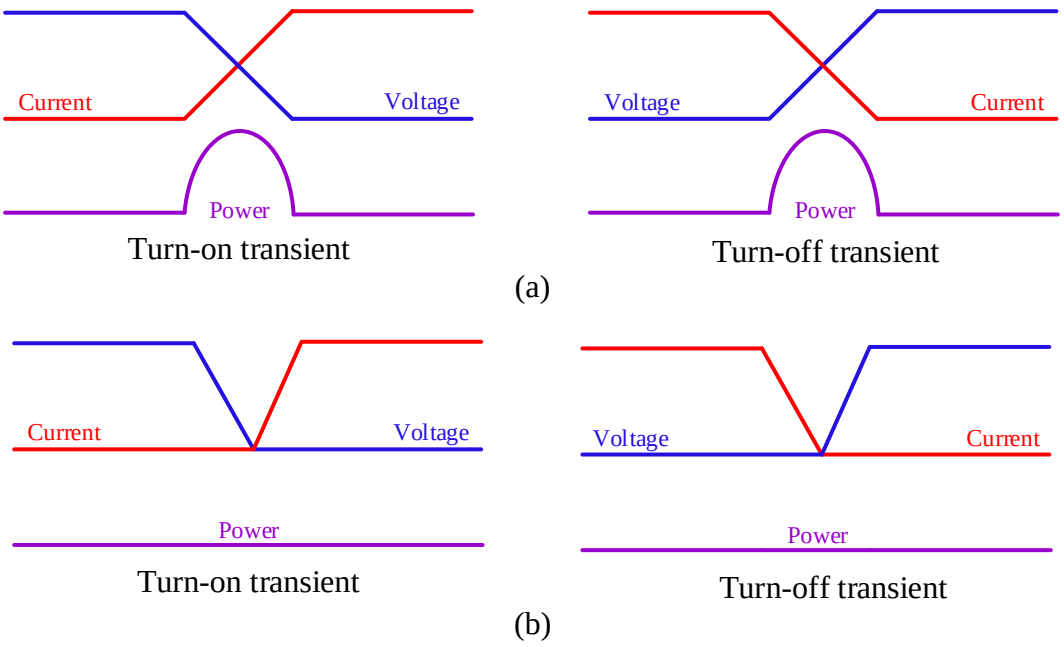

Fig. 2.5 Different switching conditions. (a) Hard switching. (b) Soft switching.

of switching is the EMI produced due to large d*i*/d*t* and d*v*/d*t* caused by hard switching condition.

High switching frequencies are desirable because of the reduced size of filter components and transformers, which eventually reduces the size and weight of the converter (and increases the power density). However, increases to switching frequency are limited due to switching device availability (and cost), and also because high frequency operation increases switching losses considerably (because a set amount of energy is lost per cycle). Therefore, resonant switching circuits have been introduced to provide the PWM converters with soft switching capability. Under soft switching condition, switching takes place when voltage or current of the switch is zero to avoid simultaneous transition of voltage and current which eliminates switching losses, presented in **Fig. 2.5(b)**.

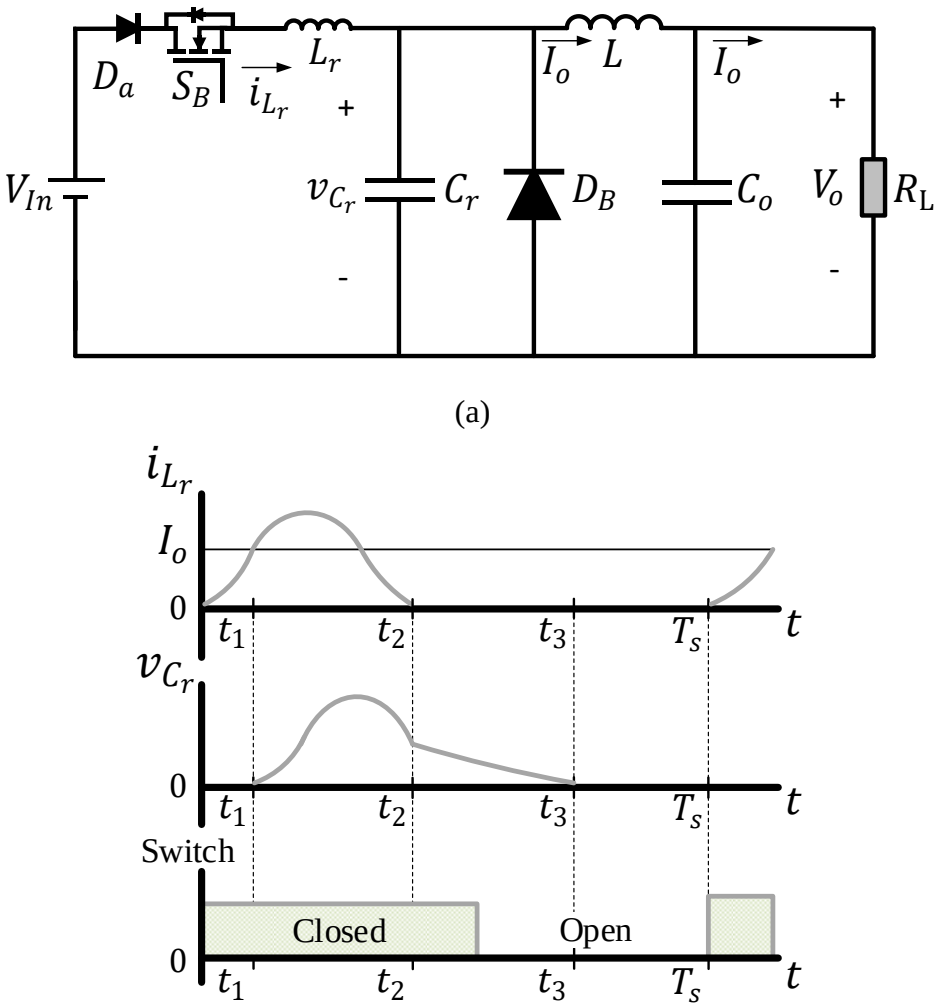

Fig. 2.6 Soft-switched buck converter. (a) Schematic. (b) Switching waveforms.

The DC-DC PWM converters (buck, boost, etc.) can be reconfigured by adding different auxiliary circuits to adopt them for soft switching capability [28]. For example, one of the methods for taking advantages of oscillation caused by LC circuit to reduce switching losses is shown in **Fig. 2.6**. As shown, this topology is very similar to buck converter, but there is an extra capacitor, C_{r}, an extra inductor, L_{r}, and an extra diode, D_{a}.

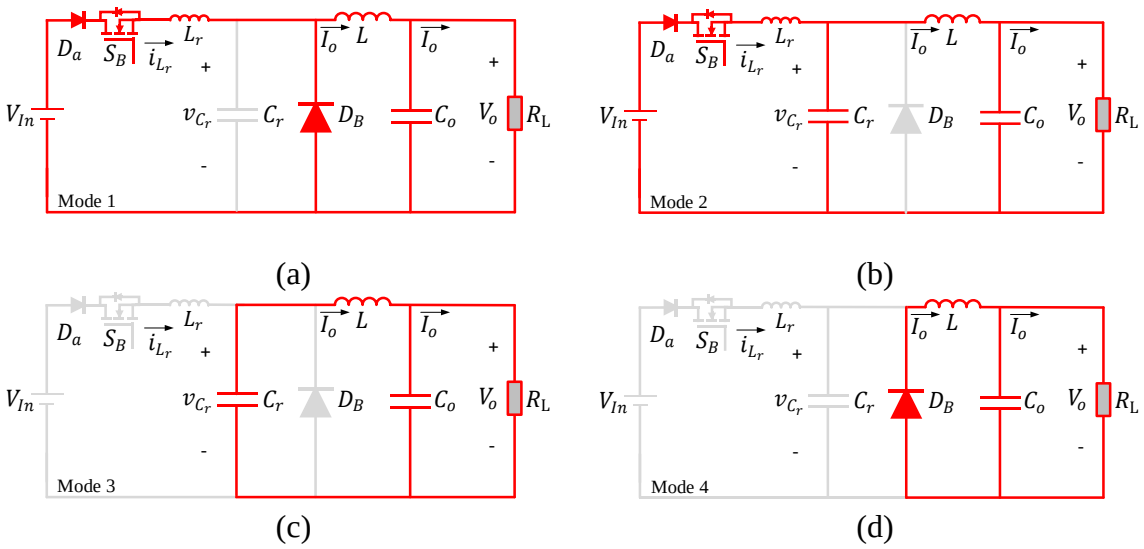

Fig. 2.7 Different modes of soft-switched buck converter. (a) Mode 1. (b) Mode 2. (c) Mode 3. (d) Mode 4.

Assuming that the output inductor current is ripple-free and equal to the load current, I_o, the converter operates in four modes. The converter important waveforms in each mode are presented in **Fig. 2.6(b).** Before first mode begins, the switch is open, the diode D_B is forward-biased to carry the output inductor current and the resonant capacitor voltage, V_{C_r}, is zero. At the beginning of the first mode, the switch is turned on, D_B is still forward-biased to carry I_o and the resonant inductor voltage, v_{L_r}, is equal to the input voltage, V_{In} (**Fig. 2.7(a)**). The resonant inductor current, i_{L_r}, increases linearly and the diode D_B remains on until i_{L_r} reaches I_o. When i_{L_r} reaches I_o, the diode D_B becomes reverse-biased, and the second mode starts (**Fig. 2.7(b)**). If I_o is constant, the load appears as a current source. Therefore, the LC circuit oscillates and the switch current, i_{L_r}, drops to zero. In the third mode (**Fig. 2.7(c)**), i_{L_r} is zero and the switch can be turned off at zero current condition, resulting almost no switching loss. In this mode, the positive resonant capacitor voltage (v_{C_r}>0) keeps the diode D_B reverse-biased and load current flows through resonant capacitor (i_{C_r}=-I_o). Therefore, the capacitor voltage decreases linearly in the third mode. When v_{C_r} drops to zero, the fourth mode starts (**Fig. 2.7(d)**), and the diode D_B becomes forward-biased to carry the inductor current (I_o). The circuit is then back to the starting point.

In recent years, several other soft-switching techniques have been introduced to augment traditionally hard-switched DC-DC converters thereby limiting switching losses [28-34], by commutating the devices during their zero-current or zero-voltage transitions.

2.3 Introduction to LLC resonant converters

With the increased power capability, improved control and reduced cost of modern power semiconductor devices, designers of electronic equipment, computers and electronic instrumentation are increasingly demanding higher energy density and efficient power sources to supply their equipment.

To date, most commercial switched-mode power supplies on the market operate in the range of tens to hundreds of kilohertz [35], and are found in many commercial products and white goods *viz* computers, television receivers, battery chargers and renewable energy systems, *etc*. For domestic applications, switching frequencies in excess of 20 kHz are usually employed to reduce the impact of acoustic noise emissions. However, the trend towards miniaturisation of electronic systems, particularly for communication and entertainment products, and the emergence of enhanced power switch technologies based on WBG semiconductors, is leading to the use of switching frequencies in the range of MHz [36].

Although the use of higher switching frequencies allows smaller reactive components to be employed in designs, in turn leading to systems with lower volume envelope and reduced cost, the resulting supplies are often more susceptible to the effects of parasitic capacitance and leakage inductance such as higher peak current stress and higher switching losses. In conventional PWM converters, such effects manifest as high-frequency ringing and large current spikes, which are generated by the rapid charging and discharging of device capacitances, and unwanted electromagnetic interference (EMI). In addition, in PWM converters, high switching frequencies cause high switching losses. An auxiliary circuit can usually be added to the conventional topology of the PWM converters to achieve soft switching capability for them. However, this auxiliary circuit leads to a more complex and expensive circuit, and it cannot always guarantee higher efficiency of the converter for different applications [5-7].

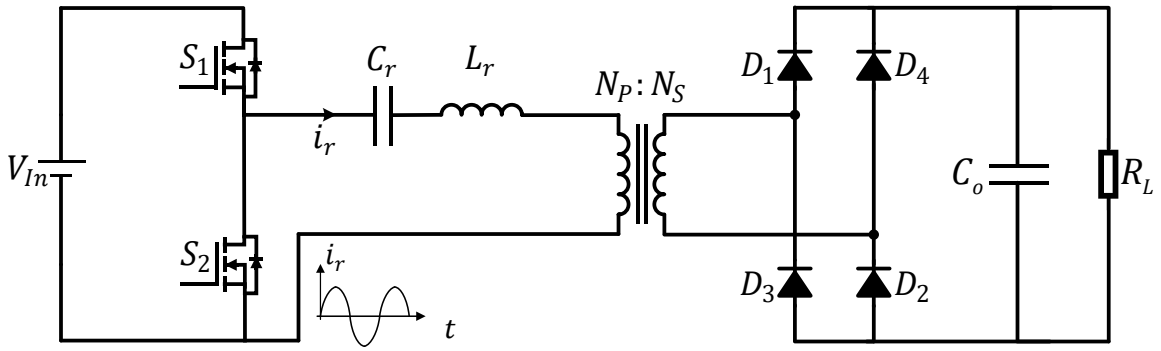

Fig. 2.8 Topology of a series resonant converter.

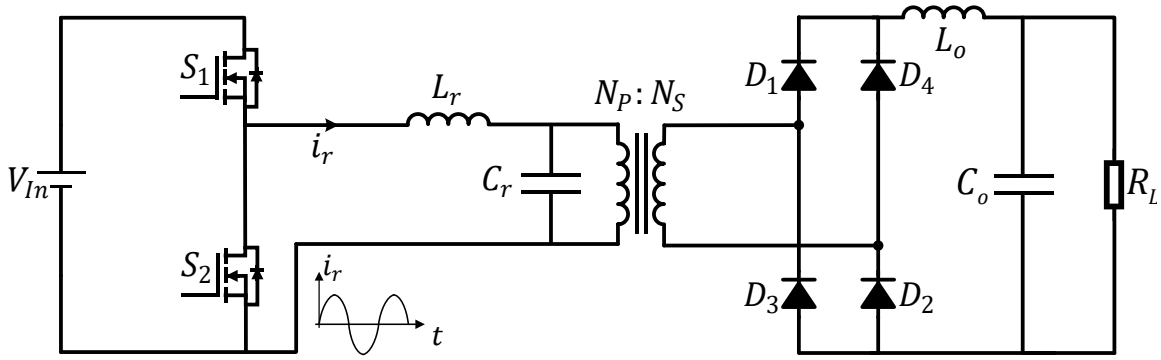

Fig. 2.9 Topology of a parallel resonant converter.

The switching devices of resonant converters, as opposed to hard-switched PWM converters, can be configured to operate in either 'zero-current' (ZCS) or 'zero-voltage' (ZVS) switching modes [37], thereby greatly reducing electrical stresses on devices and minimising switching losses. Furthermore, the sine-wave characteristics of resonant tank voltages and currents reduce the generation of high frequency harmonics (see **Fig. 2.8** and **Fig. 2.9** for series and parallel resonant converters, respectively). Another advantage is the reduction of EMI normally associated with applying high-bandwidth switching transients to internal capacitances of devices. Converters designed to exhibit ZVS, for instance, do not generate this type of EMI [38]. Generally, the resonant tank is switched above the resonance frequency (this will be defined later by (2-17)), thereby imparting ZVS to minimise turn-on losses. Therefore, for higher power applications where efficiency and EMI are critical considerations, resonant converters may be a better option. A variable frequency control is typically used to regulate the

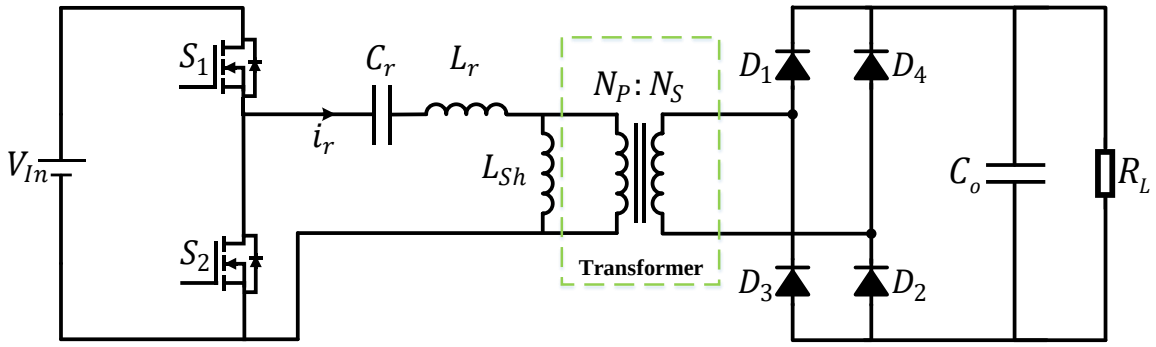

Fig. 2.10 Topology of the half-bridge LLC resonant converter.

output voltage in a resonant converter. However, a disadvantage of this method is that the transfer characteristic is non-linear and generally changes with load.

Many variants of resonant converters have emerged and amongst them, the simplest topologies are series-resonant or parallel-resonant tank networks [39-42]. The topologies of series and parallel resonant converters are shown in **Fig. 2.8** and **Fig. 2.9**, respectively. Owing to C_{r} shunting the load, the parallel resonant converter is able to control the output voltage at no-load but the current into the resonant circuit stays relatively constant for different loads, leading to low efficiency at light loads. In the series resonant converter, in contrast with the parallel resonant converter, the resonant current changes with load. However, at light-load conditions, because the impedance of the load is far higher than the impedance of the resonant circuit (LC tank), all the input voltage is imposed on the load and this makes it difficult to regulate the output voltage at light loads [37].

Higher-order resonant converters are constructed from resonant tank networks typically employing three or four reactive components, contained in two resonant branches (a series branch and a parallel branch). By appropriate selection of component values, it is possible to obtain converters with the combined advantages of both the series- and parallel-tank variants. For example, to overcome the limitation of series resonant converters, the LLC resonant converter has been proposed. The LLC resonant converter is a modified LC series resonant converter implemented by placing a shunt inductor L_{Sh} across the primary winding of the transformer as shown in **Fig. 2.10** [43].

An LLC resonant converter has many advantages compared to a series LC resonant converter. It can control the output voltage over a wider input voltage and load variations with a smaller variation of switching frequency while it still benefits from ZVS over the entire operating range. In addition, the LLC converter is also able to usefully 'absorb' circuit parasitic elements such as leakage and magnetising inductances of the transformer, as designed components which is an important feature for switching frequencies in the MHz range.

2.3.1 Analysis of LLC resonant converter

The topology of the LLC resonant converter is shown in **Fig. 2.10**. As shown, an LLC converter includes four stages: the power switches, resonant tank (including resonant capacitor, C_{r}, resonant inductor, L_{r}, and shunt inductor, L_{Sh}), transformer, and diode rectifier. Even though the LLC topology has many advantages, it uses three magnetic components which makes the converter large and expensive. Therefore, to decrease the volume and cost, and increase the efficiency of the LLC resonant converter, all three magnetic elements are often integrated into a single magnetic device (an “integrated transformer” or “integrated magnetic”) as presented in **Fig. 2.11(a)** [44]. The magnetising inductance, L_{m}, of a transformer can be realised by introducing an air gap to decrease the transformer’s normally very high magnetising inductance, so that it can be used as the shunt inductance, L_{Sh}. In addition, there are many techniques for increasing and adjusting the leakage inductance, L_{Lk}, so that it can be used as the resonant (series) inductance.

The operation of the LLC resonant converter is discussed below, but to see a detailed discussion, it can be referred to [45, 46].

The main waveforms of the LLC resonant converter when the operating frequency is the same as the resonance frequency, determined by C_{r} and L_{r} (or L_{Lk} in an integrated transformer), are shown in **Fig. 2.11(b).** In general, the LLC resonant topology consists of three stages, which are presented below.

- First, the power switches convert the input DC voltage, V_{In}, into a high-frequency square wave (pulse voltage), $v_{\mathrm{In\_Pu}}$, by driving switches $S_1$and S_2 alternately with 50% duty cycle for each switch. A small dead time, T_{D}, is usually introduced to avoid short-

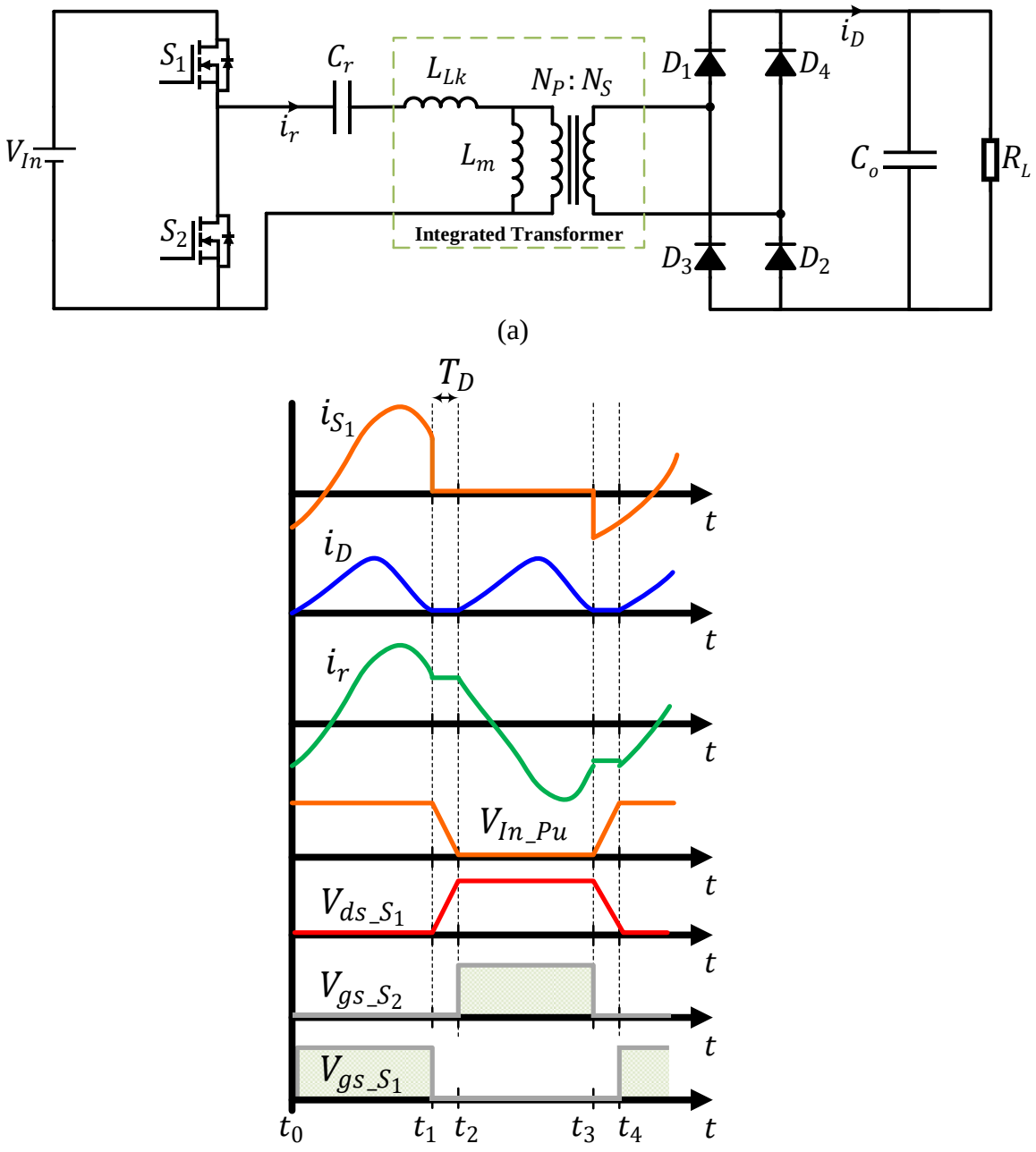

Fig. 2.11 LLC resonant converter with magnetic integration. (a) Schematic. (b) Waveforms.

circuit between consecutive transitions. The square wave generator stage can be built as a full-bridge or half-bridge type (e.g., **Fig. 2.11(a)**).

- The square wave ($v_{\text{In\_Pu}}$) then enters the resonant tank, which eliminates the square wave's harmonics and outputs a sinusoidal current at the switching frequency, named the resonant current, i_{r}. The resonant current lags the pulse voltage applied to the resonant network, $v_{\text{In\_Pu}}$, and the switch (S_1 or S_2) turns on while the voltage across it

is zero since the resonant current flows through anti-parallel diode of the switch. Therefore, the switch is turned on under zero-voltage switching (ZVS) conditions.

- The sine wave current is transferred to the secondary side of the converter through a high-frequency transformer, which scales the voltage up or down, according to the application. Lastly, the diode rectifier converts the sine wave into a purely DC voltage. The rectifier network can be implemented as a full-wave bridge or centre-tapped configuration with a capacitive output filter.

The LLC converter is usually operated in the vicinity of resonance frequency. This means that the main harmonic of circulating current in the resonant network is at or close to the series resonance frequency (will be defined later by (2-17)); other harmonics are heavily attenuated. It is possible to ignore other harmonics, especially when the square wave's switching cycle is close to the series resonance frequency. Analysis making this assumption is called the fundamental harmonic approximation (FHA) method, widely used for resonant-converter analysis, and is used to analyse the LLC resonant converter.

In the FHA method, the dead time, T_{D}, and parasitic components are neglected. Therefore, the input pulse voltage, $v_{\mathrm{In\_Pu}}$, for a half-bridge LLC resonant converter (**Fig. 2.11(a)**) can be expressed as (2-5).

$$v_{\mathrm{In\_Pu}} = \begin{cases} V_{\mathrm{In}} & \sin(\omega t) > 0 \\ 0 & \sin(\omega t) < 0 \end{cases} \tag{2-5}$$

The fundamental component of the input pulse voltage, $v_{\mathrm{In\_Fu}}$, may be obtained as (2-6) [46].

$$v_{\mathrm{In\_Fu}} = \frac{2V_{\mathrm{In}}}{\pi} \sin(\omega t) \tag{2-6}$$

As a consequence of the above mentioned assumptions, the resonant tank current, i_{r}, is sinusoidal, with a certain RMS value I_{r} and a phase shift Φ with respect to the fundamental component of the input pulse voltage, $v_{\mathrm{In\_Fu}}$, and can be expressed as (2-7).

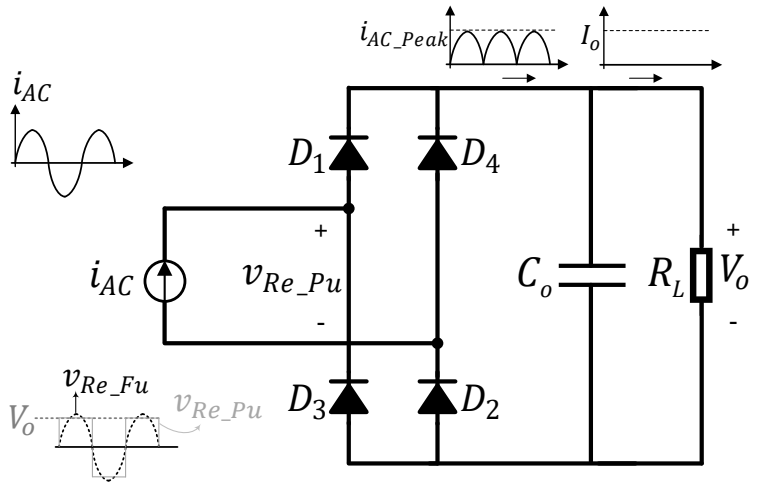

Fig. 2.12 Derivation of Equivalent Load Resistance.

$$i_{\mathrm{r}} = \sqrt{2} I_{\mathrm{r}} \sin(\omega t - \Phi) \tag{2-7}$$

The resonant current lags or leads the voltage, depending on whether inductive reactance or capacitive reactance dominates the behaviour of the resonant tank in the frequency region of interest.

There is a rectifier stage and an output capacitive filter on the secondary side of the transformer. Therefore, the equivalent load resistance is different from the actual load resistance. This equivalent resistance of the load transferred to the primary side of the rectifier can be derived from **Fig. 2.12.** As shown, the secondary side of the transformer is represented by a sinusoidal current source, i_{AC}, and the voltage on the primary side of the rectifier, $v_{\mathrm{Re\_Pu}}$, is square waves. The output current, I_{o}, is the average of the current source after rectification, $|i_{\mathrm{AC}}|$. Therefore, i_{AC} may be obtained from I_{o} by (2-8) [46].

$$i_{\mathrm{AC}} = \frac{\pi I_{\mathrm{o}}}{2} \sin(\omega t - \Psi) \tag{2-8}$$

where Ψ is a phase shift with respect to the fundamental component of the input voltage, $v_{\mathrm{In\_Fu}}$. The voltage on the primary side of rectifier, $v_{\mathrm{Re\_Pu}}$, can be expressed as follows:

$$v_{\text{Re\_Pu}} = \begin{cases} +V_{\text{o}} & \sin(\omega t - \Psi) > 0 \\ -V_{\text{o}} & \sin(\omega t - \Psi) < 0 \end{cases} \tag{2-9}$$

The fundamental component of $v_{\text{Re\_Pu}}$ may be obtained by (2-10) [46].

$$v_{\text{Re\_Fu}} = \frac{4V_{\text{o}}}{\pi} \sin(\omega t - \Psi) \tag{2-10}$$

In FHA, it is assumed that overtones of $v_{\text{Re\_Pu}}$ do not play a role in power transfer. Therefore, the AC equivalent load resistance may be calculated as follows:

$$R_{\text{L\_AC}} = \frac{v_{\text{Re\_Fu}}}{i_{\text{AC}}} = \frac{8}{\pi^2}\frac{V_{\text{o}}}{I_{\text{o}}} = \frac{8}{\pi^2}R_{\text{L}} \tag{2-11}$$

The transformer turns ratio can be defined as $n = N_{\text{P}}/N_{\text{S}}$ and therefore the equivalent AC load resistance referred to the primary side of the transformer can be obtained by (2-12).

$$R_{\text{L\_AC(P)}} = \frac{8n^2}{\pi^2}R_{\text{L}} \tag{2-12}$$

From the above AC analysis technique, the equivalent AC circuit of the LLC converter may be obtained as **Fig. 2.13**. In **Fig. 2.13**, $v_{\text{Re\_Fu(P)}}$ is $v_{\text{Re\_Fu}}$ referred to the primary side which may be obtained by (2-13).

$$v_{\text{Re\_Fu(P)}} = nv_{\text{Re\_Fu}} \tag{2-13}$$

From **Fig. 2.13**, the characteristics of the LLC resonant converter can be derived. Input impedance of the AC circuit, $Z_{\text{In\_AC}}$, may be obtained as (2-14).

$$Z_{\text{In\_AC}} = \frac{v_{\text{In\_Fu}}}{i_{\text{r}}} = j\omega L_{\text{Lk}} + \frac{1}{j\omega C_{\text{r}}} + j\omega L_{\text{m}} || R_{\text{L\_AC(P)}} \tag{2-14}$$

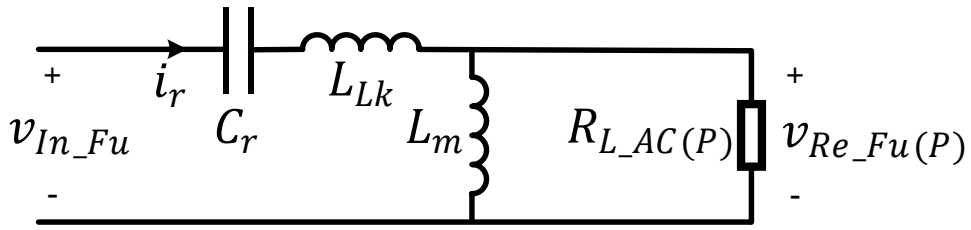

Fig. 2.13 AC equivalent circuit for LLC resonant converter.

The voltage gain of the AC circuit, M_{AC}, may be obtained as (2-15).

$$M_{\mathrm{AC}} = \frac{\left|v_{\mathrm{Re_{Fu(P)}}}\right|}{\left|v_{\mathrm{In_{Fu}}}\right|} = \frac{2nV_{\mathrm{o}}}{V_{\mathrm{In}}} \tag{2-15}$$

The gain of AC circuit may be also derived from the circuit analysis as:

$$M_{\mathrm{AC}} = \left| \frac{j\omega L_{\mathrm{m}} || R_{\mathrm{L\_AC(P)}}}{j\omega L_{\mathrm{m}} || R_{\mathrm{L_{AC(P)}}} + j\omega L_{\mathrm{Lk}} + \frac{1}{j\omega C_{\mathrm{r}}}} \right| \tag{2-16}$$

The following parameters are defined:

Series resonance frequency:

$$f_{\mathrm{r}} = \frac{1}{2\pi\sqrt{L_{\mathrm{Lk}} C_{\mathrm{r}}}} \tag{2-17}$$

Characteristic impedance:

$$Z_{\mathrm{o}} = \sqrt{\frac{L_{\mathrm{Lk}}}{C_{\mathrm{r}}}} = 2\pi f_{\mathrm{r}} L_{\mathrm{Lk}} = \frac{1}{2\pi f_{\mathrm{r}} C_{\mathrm{r}}} \tag{2-18}$$

Quality factor:

$$Q = \frac{Z_{\mathrm{o}}}{R_{\mathrm{L\_AC(P)}}} \tag{2-19}$$

Inductance ratio:

$$\lambda = \frac{L_{\mathrm{Lk}}}{L_{\mathrm{m}}} \tag{2-20}$$

Normalised frequency:

$$f_{\mathrm{N}} = \frac{f_{\mathrm{s}}}{f_{\mathrm{r}}} \tag{2-21}$$

where f_{s} is the operating switching frequency of the converter. From (2-16)-(2-21) and after some simplification, the AC voltage gain. M_{AC}, may be obtained as

$$M_{\mathrm{AC}}(f_{\mathrm{N}}, \lambda, Q) = \frac{1}{\sqrt{\left(1 + \lambda - \frac{\lambda}{f_{\mathrm{N}}^2}\right)^2 + Q^2\left(f_{\mathrm{N}} - \frac{1}{f_{\mathrm{N}}}\right)^2}} \tag{2-22}$$

The AC voltage gain can be simplified as (2-23) under the no-load condition (i.e., Q=0).

$$M_{\mathrm{AC\_NL}} = \frac{1}{\left|1 + \lambda - \frac{\lambda}{f_{\mathrm{N}}^2}\right|} \tag{2-23}$$

The no-load AC voltage gain, $M_{\mathrm{AC\_NL}}$, can be simplified as (2-24) for normalised frequency going to infinity.

$$M_{\mathrm{AC\_NL\_}\infty} = \frac{1}{1+\lambda} \tag{2-24}$$

There is another resonance frequency at no-load condition which can be defined as (2-25).

$$f_{\mathrm{r\_NL}} = \frac{1}{2\pi\sqrt{(L_{\mathrm{Lk}}+L_{\mathrm{m}})C_{\mathrm{r}}}} = f_{\mathrm{r}}\sqrt{\frac{\lambda}{1+\lambda}} \tag{2-25}$$

and in the normalised form:

$$f_{\mathrm{N\_NL}} = \frac{f_{\mathrm{r\_NL}}}{\mathrm{f_r}} = \sqrt{\frac{\lambda}{1+\lambda}} \tag{2-26}$$

$M_{\mathrm{AC\_NL}}$ tends to infinity at the no-load resonance frequency, $f_{\mathrm{r\_NL}}$.

The gain of AC circuit for different switching frequencies, inductance ratios and quality factors are presented in **Fig. 2.14(a) and (b)**. As shown, the gain is independent of the load at the resonance frequency (f_{N}=1). Therefore, it is natural to operate the converter around the resonance frequency to minimise the switching frequency variation. In addition, in the LLC resonance converter as the quality factor, Q, increases (or load increases), the peak voltage gain decreases and moves toward series resonance frequency, f_{r}. Therefore, the full load condition should be the worst case for the design of voltage gain and then the resonant network's components. In other words, the required maximum gain is needed for the full load condition (maximum Q).

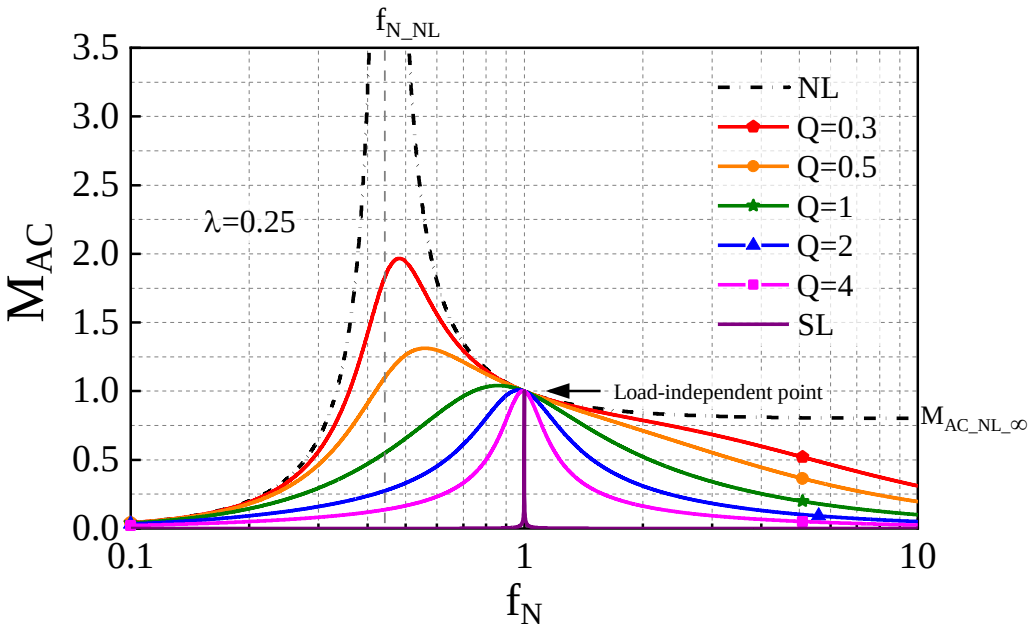

(a)

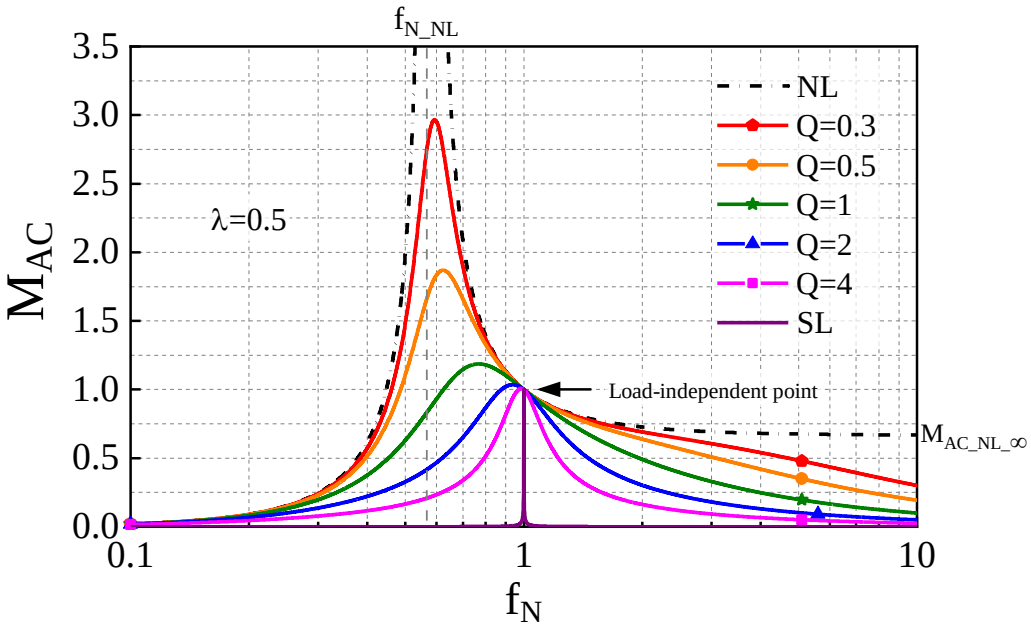

(b)

Fig. 2.14 AC circuit gain of the LLC resonant converter. (a) λ=0.25. (b) λ=0.5.

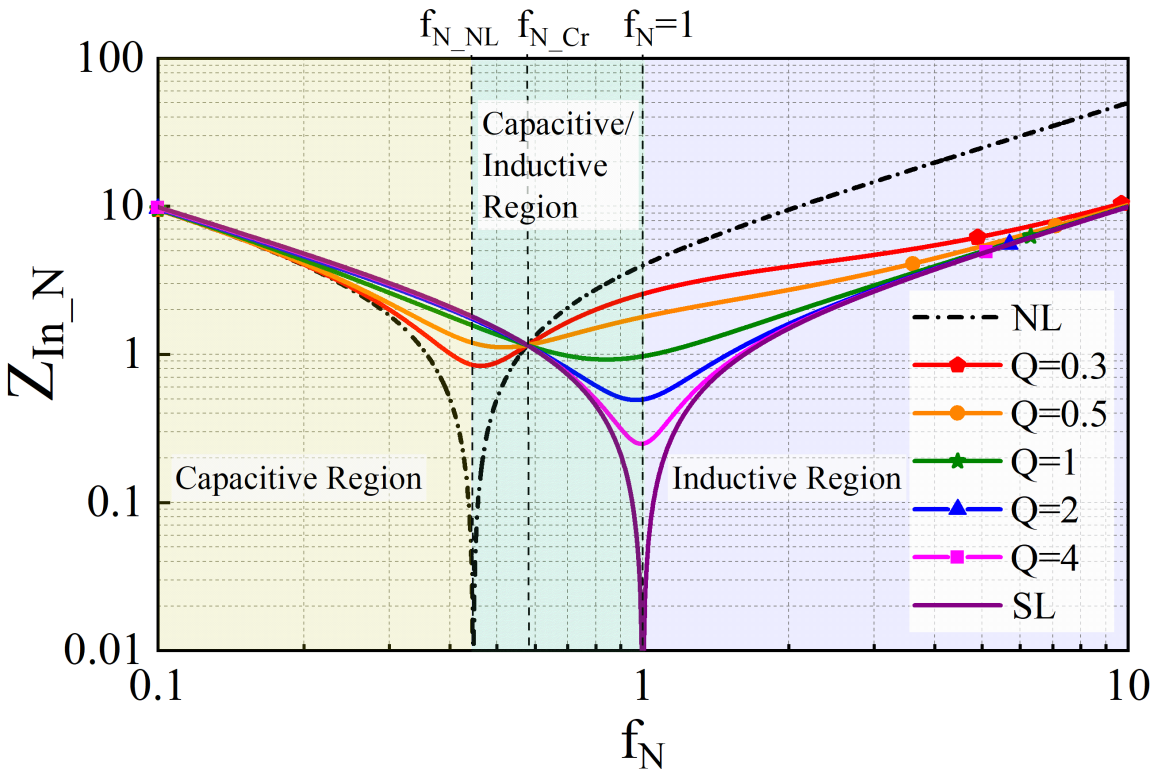

Fig. 2.15 Normalised input impedance magnitude of the LLC resonant converter. λ=0.25, no-load (NL) and shorted-load (SL).

From **Fig. 2.14**, increasing the inductance ratio, λ, shrinks the AC gain curves toward the resonance frequency (which means the no-load resonance frequency, $f_{\mathrm{r\_NL}}$, moves toward resonance frequency). In addition, the increase of λ reduces $M_{\mathrm{AC\_NL\_}\infty}$ while it increases the peak gain of each curve.

From (2-15) and (2-18), the expression of the normalised input impedance, $Z_{\mathrm{In\_AC}}$, may be obtained as (2-27).

$$Z_{\mathrm{In\_N}} = \frac{Z_{\mathrm{In\_AC}}}{Z_{\mathrm{o}}} = \frac{jf_{\mathrm{N}}}{\lambda + jf_{\mathrm{N}}Q} + \frac{1 - f_{\mathrm{N}}^2}{jf_{\mathrm{N}}} \tag{2-27}$$

The magnitude of $Z_{\mathrm{In\_N}}$ for different values of Q and with λ=0.25 are presented in **Fig. 2.15**. As shown, all curves intercept at normalised crossing frequency, $f_{\mathrm{N\_Cr}}$, which can be obtained by (2-28). In addition, at frequencies higher than the crossing frequency, the input impedance

decreases by increasing the quality factor, Q. However, at frequencies lower than the crossing frequency, the input impedance increases by increasing the quality factor.

$$f_{\mathrm{N\_Cr}} = \sqrt{\frac{2\lambda}{1+2\lambda}} \tag{2-28}$$

The region on the left-hand side of the diagram in **Fig. 2.15** (i.e., $f_{\mathrm{N}}<f_{\mathrm{r\_NL}}$) is the capacitive region, where the resonant current, i_{r}, leads the half-bridge square voltage, $v_{\mathrm{In\_Pu}}$; at frequencies higher than the resonance frequency (i.e., $1<f_{\mathrm{N}}$), on the right-hand side region, the input impedance is inductive, and i_{r} lags $v_{\mathrm{In\_Pu}}$. In the region between the two resonance frequencies the impedance can be either capacitive or inductive, depending on the value of the impedance phase angle. Therefore, the load-independent point occurs in the inductive region of the voltage gain characteristic, in which the resonant current lags the pulse voltage applied to the resonant network, resulting ZVS for the switches.

The LLC resonant converter usually operates in the inductive region to achieve ZVS for the switches. Therefore, the boundary operating frequency needs to be obtained for a fixed inductance ratio and fixed quality factor. By imposing that the imaginary part of $Z_{\mathrm{In\_N}}$ is zero (meaning that $Z_{\mathrm{In\_AC}}$ has zero phase angle, because Z_{o} is real and does not affect the phase), the boundary condition between capacitive and inductive mode operation of the LLC resonant converter can be calculated. Therefore, from (2-27), the normalised boundary switching frequency, $f_{\mathrm{N\_Bo}}$, at which the phase angle of the input impedance is zero may be calculated as (2-29). In addition, the boundary quality factor, Q_{Bo}, at which the phase angle of the input impedance is zero may be calculated as (2-30).

$$f_{\mathrm{N\_Bo}}(\lambda, Q) = \sqrt{\frac{Q^2 - \lambda(1+\lambda) + \sqrt{\left(Q^2 - \lambda(1+\lambda)\right)^2 + 4Q^2\lambda^2}}{2Q^2}} \tag{2-29}$$

$$Q_{\mathrm{Bo}} = \sqrt{\frac{\lambda}{1 - f_{\mathrm{N}}^2} - \left(\frac{\lambda}{f_{\mathrm{N}}}\right)^2} \tag{2-30}$$

At a fixed normalised frequency and inductance ratio, when the quality factor is below Q_{Bo}, the tank impedance is inductive. Considering that the LLC converter only operates in the inductive region and from (2-22) and (2-29), the maximum voltage gain available for a fixed inductance ratio (λ_1) and fixed quality factor (Q_1) may be achieved by (2-31).

$$M_{\mathrm{AC\_Ind\_max}}(\lambda_1, Q_1) = M_{\mathrm{AC}}\left(f_{\mathrm{N\_Bo}}(\lambda_1, Q_1), \lambda_1, Q_1\right) \tag{2-31}$$

By plotting the locus of operating points $[M_{\mathrm{AC\_Ind\_max}}(\lambda, Q), f_{\mathrm{N\_Bo}}(\lambda, Q)]$, the boundary gain which shows a borderline between the capacitive and inductive mode in the region between the two resonance frequencies, may be obtained as (2-32) [46]. In **Fig. 2.16**, the AC circuit gain of the LLC converter alongside the borderline separating the capacitive and inductive regions is shown.

$$M_{\mathrm{AC\_Bo}}(f_{\mathrm{N}}, \lambda) = \frac{f_{\mathrm{N}}}{\sqrt{f_{\mathrm{N}}^2(1 + \lambda) - \lambda}} \tag{2-32}$$

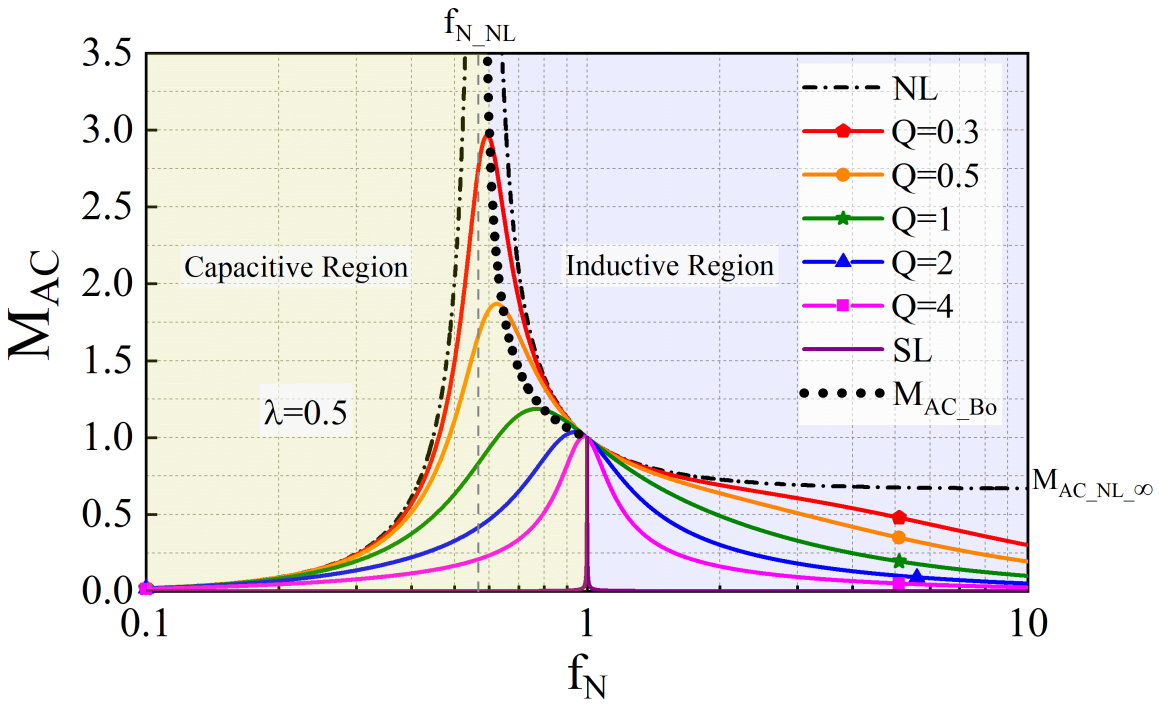

Fig. 2.16 AC circuit gain of the LLC resonant converter and borderline between capacitive and inductive regions. λ=0.5, no-load (NL) and shorted-load (SL).

2.3.2 Design of an LLC resonant converter

If an LLC converter operates in the capacitive region, the LLC converter suffers from turn-on switching losses in its power switches and diode losses (requiring high-speed diodes), energy stored in device capacitances is discharged and lost internal to the power switches, and the input and output filters must be designed for the minimum switching frequency (leading to the larger size of the filters) [37]. Therefore, the LLC resonant converter is usually designed to operate in the inductive region. In the following of this section, the design guidelines for an LLC resonant converter operating in the inductive region is presented.

As shown in **Fig. 2.16**, when the converter is in inductive region, the output voltage increases by decreasing the operating frequency, and the output voltage decreases by increasing the operating frequency. Therefore, the output voltage of an LLC resonant converter can be controlled by adjusting its operating frequency.

The LLC resonant converter can be designed to increase (step-up mode) and decrease (step-down mode) the output voltage. Therefore, when the input voltage varies, the LLC resonant

converter should be designed to operate at the resonance frequency (where M_{AC}=1) under nominal input voltage condition and if the input voltage decreases, the converter operates in step-up mode ($f_s<f_r$) and if the input voltage increases the converter operates in step-down mode ($f_s>f_r$).

2.3.2.1 Maximum and minimum gains

The nominal voltage gain, M_{Nom}, is required at the nominal input voltage which may be obtained by (2-33).

$$M_{Nom} = \frac{2nV_o}{V_{In}} \tag{2-33}$$

The maximum required gain, M_{max}, is required at the minimum input voltage, V_{In_min}, and for maximum load (maximum Q). Therefore, M_{max} may be obtained from (2-34).

$$M_{max} = \frac{2nV_o}{V_{In\_min}} \tag{2-34}$$

The minimum required gain, M_{min}, is required at the maximum input voltage, V_{In_max}, which may be obtained as (2-35).

$$M_{min} = \frac{2nV_o}{V_{In\_max}} \tag{2-35}$$

2.3.2.2 Maximum and minimum operating frequencies

In a design process, the minimum, f_{min}, and maximum, f_{max}, operating frequencies may be limited based on the capability of the hardware of the control system and they are needed for designing the input and output filters. The converter should operate at f_{min} when the maximum gain is needed, and it operates at f_{max} when the minimum gain is required.

The minimum operating frequency can be chosen as the boundary frequency between capacitive and inductive regions. In other words, M_{AC_Bo} is considered as the maximum

required gain, $M_{\max}$, to define the minimum operating frequency, $f_{\min}$. Therefore, solving (2-32) for f_{N}, the minimum normalised operating frequency which allows the required maximum voltage gain at the boundary between capacitive and inductive mode can be calculated as follows:

$$f_{\mathrm{N\_min}} = \sqrt{\frac{\lambda}{\lambda + 1 - \frac{1}{M_{\max}^2}}} \tag{2-36}$$

In order to make sure that the converter can control the output voltage under no-load condition at a finite operating frequency (which is $f_{\max}$), the minimum required gain (at the maximum input voltage, $V_{\mathrm{In\_max}}$), $M_{\min}$, should be greater than (2-24).

$$M_{\min} = \frac{2nV_{\mathrm{o}}}{V_{\mathrm{In\_max}}} > \frac{1}{1+\lambda} \tag{2-37}$$

Finally, by equating the second term of the no-load transfer function (2-23) to the minimum required voltage gain $M_{\min}$, the expression of the maximum normalised frequency, $f_{\mathrm{N\_max}}$, may be obtained as follows:

$$f_{\mathrm{N\_max}} = \sqrt{\frac{1}{1 + \frac{1}{\lambda}\left(1 - \frac{1}{M_{\min}}\right)}} \tag{2-38}$$

2.3.2.3 Maximum quality factor

By substituting the minimum frequency (2-36) into (2-30), the maximum quality factor, $Q_{\max}$, which allows the required maximum voltage gain at the boundary between the capacitive and inductive mode, may be obtained as (2-39).

$$Q_{\max} = \frac{\lambda}{M_{\max}} \sqrt{\frac{1}{\lambda} + \frac{M_{\max}^2}{M_{\max}^2 - 1}} \tag{2-39}$$

Operating in the inductive region for the LLC topology is a necessary condition for the ZVS, but it is not sufficient. In the FHA, the dead time and parasitic capacitance of the half-bridge's switches are neglected. However, the parasitic capacitors of the half-bridge's switches need to be charged and discharged during turn-on and -off transients, respectively.

To allow ZVS, the half-bridge's driving circuit is such that a dead time, T_{D}, is inserted between the end of the on-time of either power switch and the beginning of the on-time of the other one so that both are not conducting during T_{D}. Due to the phase lag of the input current with respect to the input voltage, at the end of the first half cycle the resonant current is still flowing into the circuit and, therefore it can deplete the parasitic capacitor so that its voltage swings from V_{In} to zero (it will be vice versa during the second half cycle).

The analysis for achieving ZVS while the dead time and parasitic capacitors are considered is out of the scope of this thesis and the final conditions are only presented here. Reference [46] has a detailed discussion for the interested reader. In [46], it is shown that the maximum quality factor, $Q_{\max}$, should satisfy both conditions (2-40) and (2-41) to guarantee ZVS over the whole operating range of the LLC resonant converter.

$$Q_{\max} < \left(0.95 \frac{\lambda}{M_{\max}} \sqrt{\frac{1}{\lambda} + \frac{M_{\max}^2}{M_{\max}^2 - 1}} \right) \tag{2-40}$$

$$Q_{\max} < \frac{2}{\pi} \frac{\lambda f_{\mathrm{N\_max}}}{(\lambda + 1) f_{\mathrm{N\_max}}^2 - \lambda} \; \frac{T_{\mathrm{D}}}{R_{\mathrm{L\_AC(P)}} C_{\mathrm{ZVS}}} \tag{2-41}$$

where C_{ZVS} is the summation of output capacitance of the MOSFET switches, C_{oss}, and stray capacitance, C_{St}, of the circuit.

$$C_{\mathrm{ZVS}} = 2C_{\mathrm{oss}} + C_{\mathrm{St}} \tag{2-42}$$

2.3.2.4 Design procedure

Based on the presented analysis, a step-by-step design procedure of an LLC resonant converter is presented in the following of this subsection.

Step 1: Design specification listed below should be considered in the first step.

- Input voltage range: $V_{\mathrm{In\_min}}$ to $V_{\mathrm{In\_max}}$
- Nominal input voltage: V_{In}
- Regulated output voltage: V_{o}
- Maximum output power: $P_{\mathrm{o\_max}}$
- Resonance frequency: f_{r}
- Maximum operating frequency: f_{max}
- Parasitic capacitance: C_{ZVS}
- Dead time: T_{D}

Step 2: The converter should be designed to work at resonance frequency at nominal input voltage. Therefore, the required gain at nominal input voltage equals unity and from (2-33), the transformer turns ratio may be calculated as:

$$n = \frac{V_{\mathrm{In}}}{2V_{\mathrm{o}}} \tag{2-43}$$

Step 3: The maximum and minimum gains need to be calculated from (2-34) and (2-35), respectively.

Step 4: The maximum normalised operating frequency can be calculated as (2-44).

$$f_{\mathrm{N\_max}} = \frac{f_{\max}}{f_{\mathrm{r}}} \tag{2-44}$$

Step 5: The effective load resistance reflected to the transformer primary side may be obtained as (2-45).

$$R_{\mathrm{L\_AC(P)}} = \frac{8n^2}{\pi^2}\frac{V_{\mathrm{o}}^2}{P_{\mathrm{o\_max}}} \tag{2-45}$$

Step 6: From (2-38) and imposing that the converter operates at the maximum frequency at zero load and maximum input voltage, the inductance ratio may be obtained by (2-46).

$$\lambda = \frac{1 - M_{\min}}{M_{\min}}\frac{f_{\mathrm{N\_max}}^2}{f_{\mathrm{N\_max}}^2 - 1} \tag{2-46}$$

Step 7: A maximum quality factor, $Q_{\max}$, that satisfies both conditions (2-40) and (2-41) should be considered.

Step 8: The minimum operating frequency, $f_{\min}$, at full load and minimum input voltage may be obtained as (2-47).

$$f_{\min} = f_{\mathrm{r}}\sqrt{\frac{1}{1 + \frac{1}{\lambda}\left(1 - \frac{1}{M_{\max}^2}\right)}} \tag{2-47}$$

Step 9: The resonant components of the LLC topology can be obtained as follows:

$$Z_{\mathrm{o}} = Q_{\max}\, R_{\mathrm{L\_AC(P)}} \tag{2-48}$$

$$C_{\mathrm{r}} = \frac{1}{2\pi f_{\mathrm{r}} Z_{\mathrm{o}}} \tag{2-49}$$

$$L_{\mathrm{Lk}} = \frac{Z_{\mathrm{o}}}{2\pi f_{\mathrm{r}}} \tag{2-50}$$

$$L_{\mathrm{m}} = \frac{L_{\mathrm{Lk}}}{\lambda} \tag{2-51}$$

Step 10: Finally, an integrated transformer with a leakage inductance of L_{Lk}, magnetising inductance of L_{m} and turns ration of n needs to be designed.

It should be mentioned that while the LLC resonant converter benefits from higher power density and efficiency, better EMI performance, and more flexibility in voltage range compared to PWM converters, there are also some disadvantages associated with this converter. Firstly, the design process of a resonant converter is more time-consuming and complicated than that of a PWM converter. Secondly, the output voltage could be affected by the load, making it challenging to regulate the output voltage for different loads. Additionally, the duty cycle is usually constant in resonant converters, and the output voltage is controlled by the switching frequency. Therefore, achieving efficient and stable control over the resonant tank, switching devices, and feedback loops requires sophisticated control algorithms and careful implementation. Lastly, the LLC topology either requires three magnetic components, leading to low power density, or an integrated transformer, which adds complexity to the design process of the converter. This is further discussed in the next section.

2.4 Magnetic integration for LLC resonant converter

Magnetic integration can be applied to a converter to combine the inductors and the transformer into a single magnetic device. Integrating magnetic components of an LLC topology into a single magnetic device enhances the power density and efficiency and decreases the cost. In addition, when all of a circuit's inductive elements are placed in the same structure,

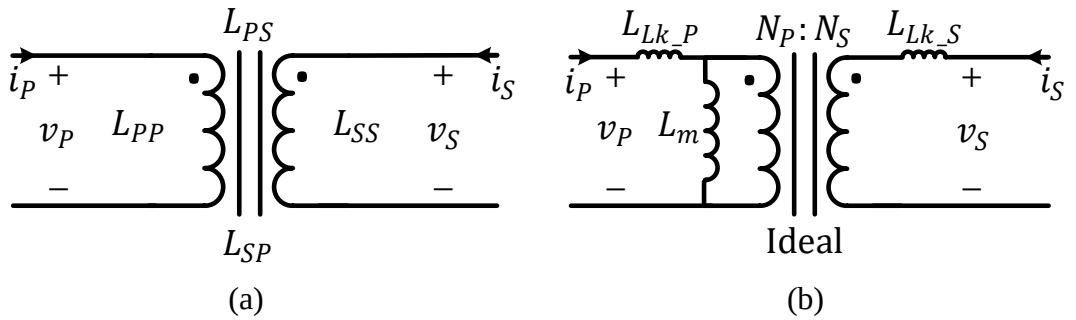

Fig. 2.17 The equivalent circuit of a coupled inductor. (a) First model. (b) Second model.

electromagnetic compatibility is improved, since it is easier and cheaper to shield one structure than three.

There are many methods to integrate the magnetic components of an LLC converter into a single magnetic device by manipulation of the cores and windings of the transformer and inductor, which will be reviewed in Chapter 3. In addition, the leakage inductance of a typical high frequency transformer can be selected by design and used as the series inductor of the LLC tank as presented in **Fig. 2.11(a)**.

The equivalent circuit of a coupled inductor is shown in **Fig. 2.17(a)**. This equivalent circuit can be expressed as (2-52) [5, 12].

$$\begin{bmatrix} v_{\mathrm{P}} \\ v_{\mathrm{S}} \end{bmatrix} = \begin{bmatrix} L_{\mathrm{PP}} & L_{\mathrm{PS}} \\ L_{\mathrm{SP}} & L_{\mathrm{SS}} \end{bmatrix} \frac{\mathrm{d}}{\mathrm{d}t} \begin{bmatrix} i_{\mathrm{P}} \\ i_{\mathrm{S}} \end{bmatrix} \tag{2-52}$$

where L_{PP} and L_{SS} are primary and secondary self-inductances, respectively, L_{PS} and L_{SP} are mutual inductances and i_{P} and i_{S} are the primary and secondary currents, respectively.

The coupled inductor can also be represented by the three-inductor model shown in **Fig. 2.17(b)**. This equivalent circuit can be expressed as (2-53). In (2-53), N_{P} and N_{S} are the number of primary and secondary turns, respectively, $L_{\mathrm{Lk\_P}}$ and $L_{\mathrm{Lk\_S}}$ are primary and secondary leakage inductances, respectively and L_{m} is magnetising inductance which may be obtained as shown in (2-54).

$$\begin{bmatrix} v_{\mathrm{P}} \\ v_{\mathrm{S}} \end{bmatrix} = \begin{bmatrix} L_{\mathrm{Lk\_P}} + L_{\mathrm{m}} & \frac{N_{\mathrm{S}}}{N_{\mathrm{P}}} L_{\mathrm{m}} \\ \frac{N_{\mathrm{S}}}{N_{\mathrm{P}}} L_{\mathrm{m}} & L_{\mathrm{Lk\_S}} + \frac{N_{\mathrm{S}}^2}{N_{\mathrm{P}}^2} L_{\mathrm{m}} \end{bmatrix} \frac{\mathrm{d}}{\mathrm{d}t} \begin{bmatrix} i_{\mathrm{P}} \\ i_{\mathrm{S}} \end{bmatrix} \tag{2-53}$$

$$L_{\mathrm{m}} = \frac{N_{\mathrm{P}}}{N_{\mathrm{S}}} L_{\mathrm{PS}} \tag{2-54}$$

To calculate the magnetising inductance, the mutual inductance, L_{PS}, needs to be obtained. L_{PS} may be obtained as

$$L_{\mathrm{PS}} = \frac{N_{\mathrm{S}}}{i_{\mathrm{P}}} \phi_{\mathrm{PS}} \tag{2-55}$$

where ϕ_{PS} is the mutual flux generated by the primary winding. By substituting (2-55) into (2-54), the magnetising inductance can be obtained as

$$L_{\mathrm{m}} = \frac{N_{\mathrm{P}}}{i_{\mathrm{P}}} \phi_{\mathrm{PS}} \tag{2-56}$$

The primary self-inductance may be obtained from (2-57), where $\mathcal{R}_{\mathrm{T\_P}}$ is the total core reluctance experienced by the primary winding (including the air gaps).

$$L_{\mathrm{PP}} = \frac{N_{\mathrm{P}}^2}{\mathcal{R}_{\mathrm{T\_P}}} \tag{2-57}$$

And the secondary self-inductance can be obtained by (2-58), where $\mathcal{R}_{\mathrm{T\_S}}$ is the core reluctance (evaluated from the secondary side).

$$L_{\mathrm{SS}} = \frac{N_S^2}{\mathcal{R}_{\mathrm{T\_S}}} \tag{2-58}$$

From (2-52) and (2-53), the primary, $L_{\mathrm{Lk\_P}}$, and secondary, $L_{\mathrm{Lk\_S}}$, leakage inductances can be obtained as (2-59) and (2-60), respectively.

$$L_{\mathrm{Lk\_P}} = L_{\mathrm{PP}} - L_{\mathrm{m}} \tag{2-59}$$

$$L_{\mathrm{Lk\_S}} = L_{\mathrm{SS}} - \frac{N_S^2}{N_{\mathrm{P}}^2} L_{\mathrm{m}} \tag{2-60}$$

When it is assumed that flux linkage is exactly the same for both primary and secondary windings, the primary and secondary leakage inductances can be considered identical. Therefore, the secondary leakage inductance can be referred to the primary side of the simplified equivalent circuit according to transformer turns ratio. Assuming magnetising inductance is much greater than the primary leakage inductance, the total leakage inductance may be estimated as (2-61).

$$L_{\mathrm{Lk}} = L_{\mathrm{Lk\_P}} + \frac{N_{\mathrm{P}}^2}{N_S^2} L_{\mathrm{Lk\_S}} = 2L_{\mathrm{Lk\_P}} \tag{2-61}$$

It should be mentioned that while magnetic integration provides many advantages, it also makes the design of the converter more complex and time-consuming. Magnetic integration involves combining multiple passive elements, such as inductors and transformers, into a single magnetic component. The limitation of this magnetic component can lead to a more intricate and restricted design process, which may impact overall converter performance in specific operating conditions. For example, the transformer may not be able to provide the required leakage inductance, and therefore, the converter needs to be redesigned, with its series resonant inductance limited to the maximum value that the integrated transformer can provide. In section 3.2, the limitations of different topologies of integrated transformers are discussed.

2.5 Conclusion

This Chapter introduced different types of power electronics DC-DC converters. In addition, the PWM technique for switching of switched-mode power supplies was investigated. PWM converters, like the boost converter, suffer from a lack of soft-switching capability and thus have high switching losses under high-frequency operation. Losses are limited by constraining the operating frequency, leading to lower power density. It is discussed that the switching losses can be limited by adding soft switching capability to the traditional PWM converters.

Even though soft-switching capability can be achieved by adding an auxiliary circuit to the conventional topology of the PWM converters, the auxiliary circuit adds complexity and cost (will be shown in Chapter 4). On the other hand, the resonant converters benefit from soft-switching capability inherently and therefore they could be a more suitable choice for high frequency and high power density converters.

Resonant converters were discussed and, amongst different resonant converters, the LLC converter was chosen to be further investigated due to its unique advantages. The LLC converter was analysed and it was pointed out that this topology needs three magnetic components which make the converter's volume large. However, the LLC resonant converter can provide a higher power density when its magnetic components are integrated into the transformer. It is discussed how the leakage inductance of a typical high frequency-transformer can be selected by design and used as the series inductor of the LLC tank.

Chapter 3

Literature Review and Focusing the Research

This Chapter discusses the advantages and disadvantages of soft-switching techniques that can be applied to reduce switching losses of DC-DC converters. In addition, it discusses the costs and benefits of new state-of-the-art semiconductor devices that can be used to decrease switching losses. Finally, it introduces the first research focus of this thesis to further investigate the PWM converters which either use soft-switching techniques or new wide bandgap (WBG) semiconductor devices or both or neither of them to find the most beneficial method for achieving lower switching losses.
In the following of this Chapter, a full review of integrated transformers suitable for LLC-type topologies and their issues is provided. Finally, the main issues of inserted-shunt integrated transformers are discussed and four research focuses to address these issues are proposed.

3.1 Limiting switching losses in DC-DC converters

It is well-known that the volume of passive components is inversely proportional to the switching frequency. At higher switching frequencies, in addition to reduced passive component volume, a low-capacitance and low-inductance filter can be used which also enhances the dynamic response of the system. However, increases to switching frequency are limited due to switching device availability (and cost), and also because high frequency operation increases switching losses considerably [47]. There are different methods that can be used to decrease the switching losses which are discussed in the following of this subsection.

3.1.1 Soft switching techniques

The switching frequency of a DC-DC converter can be changed based on load so that the converter operates in boundary condition mode (BCM) or discontinuous condition mode (DCM) for a wide load range [48]. The DC-DC converter's switches can be turned on at zero current switching (ZCS) condition under BCM and DCM switching strategies. However, this technique needs complicated control strategies, and has a large peak-to-peak and RMS currents

across the main inductor and the semiconductors, leading to higher core and conduction losses. In addition, the DC-DC converter's switches still suffer from high turn-off switching losses.

DC-DC PWM converters in continuous conduction mode (CCM) suffer from high switching losses and cannot be switched at high switching frequencies, leading to low power density. However, by adding an auxiliary circuit to the conventional topology of DC-DC PWM converters, their switches can be turned on or off (or both) under soft-switching conditions to limit (or eliminate) switching losses.

In recent years, several soft-switching techniques have been introduced to augment traditionally hard-switched DC-DC converters thereby limiting switching losses [28-34], by commutating the devices during their zero-current or zero-voltage transitions. In these techniques, an auxiliary circuit is usually added to the conventional topology of the DC-DC converters. This auxiliary circuit can have an active device such as MOSFET and IGBT or cannot have it [49].

The techniques that do not use an active device include quasi-resonant converters, passive snubber converters and auxiliary commutation converters. Quasi-resonant converters often use small inductors and capacitors connected with the switching unit in series or parallel to obtain zero-current switching (ZCS) or zero-voltage switching (ZVS) conditions [50-52]. For example, the topology shown in **Fig. 2.6** (page 19) is a ZCS quasi-resonant converter. Passive snubber converters use a snubber circuit consisting of inductors, diodes, and capacitors to achieve ZVS or ZCS conditions [53-55]. For example in **Fig. 3.1**, a passive snubber buck converter is shown, which is proposed in [56]. Auxiliary commutation converters use auxiliary circuits to generate an additional auxiliary current between two semiconductor devices to composite current waveforms needed by ZCS or ZVS conditions [57, 58].

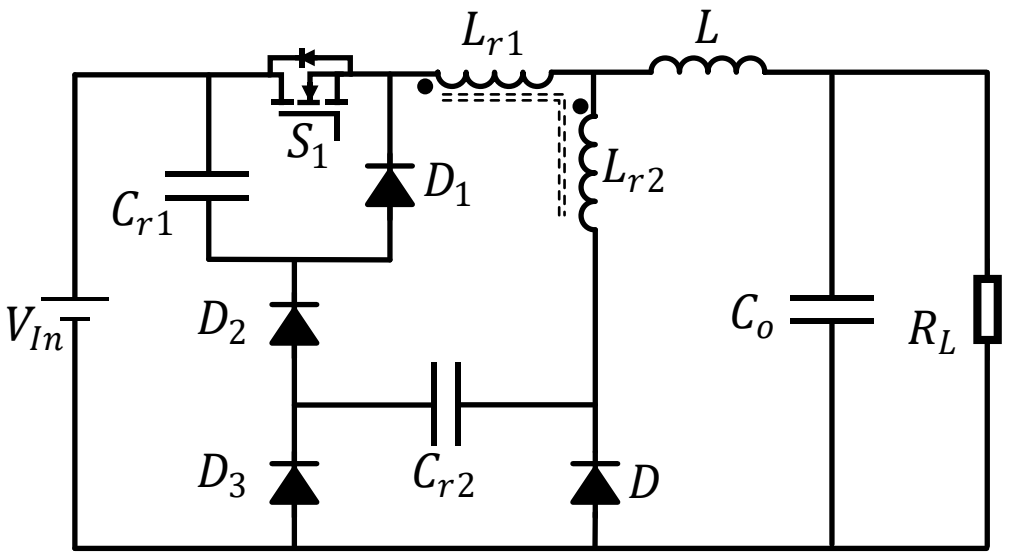

Fig. 3.1 Passive snubber buck converter presented in [56].

The techniques that need an active device include zero-voltage transition converters, zero-current transition converters, active resonant converters and active snubber converters. The zero voltage transition and zero current transition converters use auxiliary power transistors to create ZVS or ZCS conditions for turning on or off the main switches [59-61]. Zero voltage transition auxiliary circuits are composed of power transistors with an inductor in series, but a zero current transition auxiliary circuit is composed of power transistors with a capacitor in series. The active resonant converters are quasi-resonant converters with active switches added in the auxiliary circuit to obtain a fixed frequency control characteristics (such as the topology shown in **Fig. 4.2** in Chapter 4, page 86) [62, 63]. Finally, an active snubber converter is a passive snubber converter with an active switch added in the auxiliary circuit to control the resonant process [64, 65]. For example, in **Fig. 3.2**, the topology of an active snubber buck-boost converter is shown which is presented in [66].

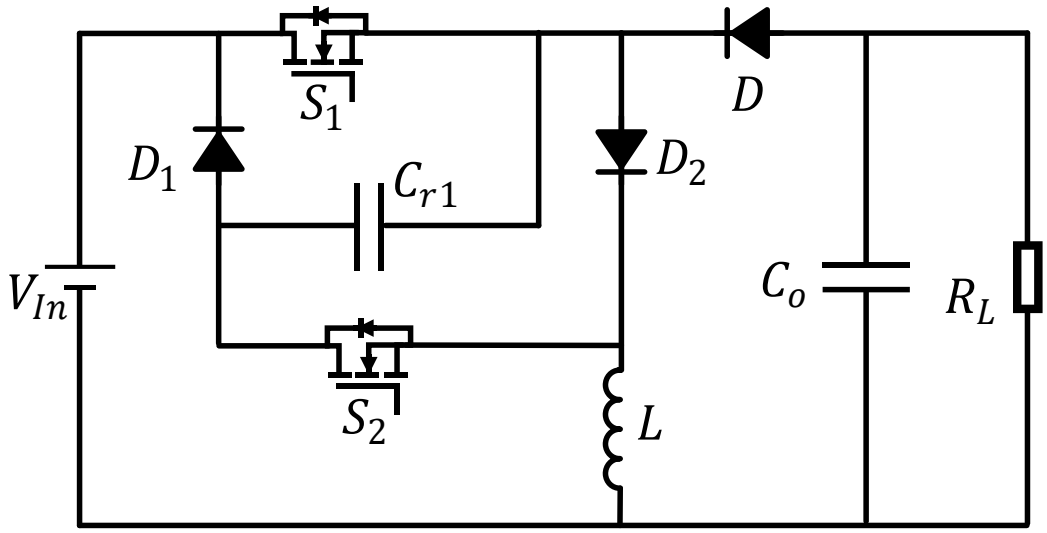

Fig. 3.2 Active snubber buck-boost converter presented in [66].

The switching losses are limited (or eliminated) in soft-switched DC-DC PWM converters. However, the soft-switching techniques usually require an auxiliary circuit consisting of inductors, capacitors, diodes and switches, which increases the complexity and cost of the converter [7]. The complexity could involve more passive and active components, and the control systems may need to manage an auxiliary switch alongside the main switch, making compensation a bit more challenging due to the higher order of the new circuit. This ultimately leads to a higher price. In addition, the soft-switching techniques cannot provide high efficiency for all load ranges and, sometimes, they only can be used for a narrow voltage and power range.

Therefore, soft-switching techniques can only enhance the efficiency in the vicinity of the nominal operating conditions and for the designed applications [47].

Several authors have proposed soft-switched converters to increase efficiency for a range of applications [29-34, 47, 67]. However, there has been no rigorous analysis to confirm, once all implications of implementing a soft-switched approach have been considered, that the solution is more meritorious than a traditional hard-switched approach. Therefore, a comparison in terms of cost, power density and efficiency for hard- and soft-switched DC-DC converters is needed.

3.1.2 Wide-bandgap semiconductors

The quality of the semiconductor devices has a significant influence on the performance of the DC-DC converters. Recently, significant efforts have been applied to decrease the switching losses (chiefly by reducing parasitic capacitance) and conduction losses (by reducing on-state resistance) of the switching devices [68].

The present silicon (Si) technology is reaching the material's theoretical limit and it is becoming more difficult to meet all the requirements of the next generation's industrial applications. However, a breakthrough has been achieved by using wide-bandgap (WBG) materials, such as silicon carbide (SiC) and gallium nitride (GaN) and they are becoming gradually more popular because of their improved electrical, mechanical, and thermal performance [13].

SiC diodes such as Schottky diode [69], PiN diode [70] and junction barrier Schottky diode [71] and, SiC electronic switches such as metal oxide semiconductor field effect transistors (MOSFETs) [72], junction field-effect transistors (JFETs) [73] and insulated gate bipolar transistors (IGBTs) [73] have been developed for commercial use during the last two decades. High-power SiC Schottky diodes have almost zero reverse recovery charge, and the reverse recovery current is low, which makes them popular for industrial use. The SiC PiN diode has low specific resistance but the reverse recovery current during switching and the forward voltage drop are high. The junction barrier Schottky diode combines the advantages of the Schottky and PiN diodes. The SiC MOSFETs are the main switching devices and are widely used. The SiC JFETs are usually on devices and have advantages such as resistive forward characteristics. To overcome the increasing on-resistance under high blocking voltage, bipolar devices such as SiC IGBTs are developed for high-power and high-voltage use [74].

GaN power diodes such as Schottky diode [75] and PiN diode [76] and, GaN electronic switches such as JFETs [77] and MOSFETs [78] have similar characteristics to the SiC devices. GaN high electron mobility transistor (HEMT) [79] is the most famous GaN device in the market. Several modified structures have been developed to improve the performance of the GaN HEMT such as the enhancement of the GaN transistor (eGaN) [80].

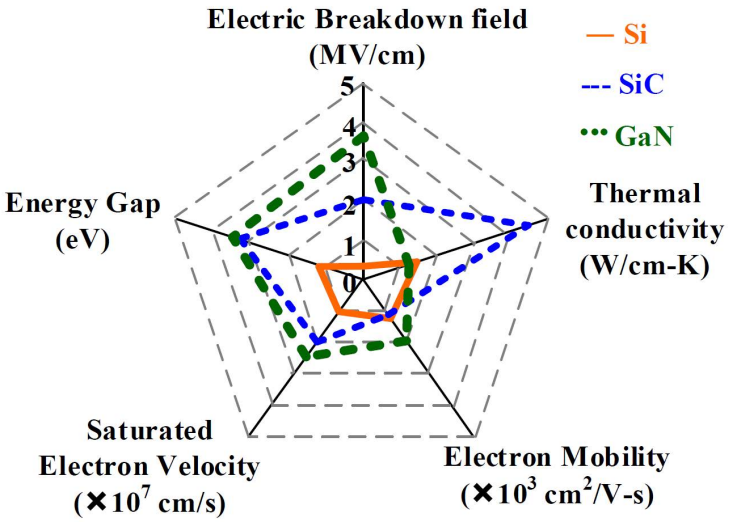

Fig. 3.3 Comparison of Si, SiC, and GaN for power semiconductor applications [13].

The superior performance of WBG-based switches over Si-based switches in terms of switching losses and switching speed has already been confirmed in the literature [81, 82]. In general, the advantages of SiC and GaN could be summarised as presented in **Fig. 3.3**. The switching devices based on WBG materials cannot only be switched with greater speed (MHz range), but also have lower switching losses compared to traditional silicon (Si) switches. In addition, they benefit from higher maximum junction temperature (if appropriately packaged) and lower conduction losses due to increased carrier mobility [83]. This allows higher efficiency to be achieved at high switching frequencies with the help of WBG-based switches while the conventional simple structure of the DC-DC converter does not need to be changed (in contrast with soft switching techniques).

WBG devices such as SiC and GaN have shown improvements in the design of highly efficient and compact DC-DC converters [84]. An efficiency comparison between a Si-IGBT-based switch and a GaN-based switch in a motor drive application is provided in [85]. It is shown that the GaN-based drive has a better efficiency. In [86], the efficiency of Si and SiC-based switches in a high gain DC–DC boost converter for high-voltage low-power applications has been investigated. It was shown that the highest efficiency is obtained when the power transistor is implemented by a normally-off junction field-effect transistor and the diode by a

SiC Schottky device with a small parasitic capacitance. In [87], the common-mode EMI characteristics of GaN high-electron-mobility transistor (HEMT) and Si MOSFET power converters in (hybrid-) electric vehicle applications have been studied. By parametrically increasing the gate resistance of switches, the tradeoff between converter efficiency and common-mode noise generation is quantified. In [88], a 360 V/180 W boost converter was proposed using GaN FET and SiC Schottky diodes at 200-kHz switching frequency, with an efficiency of >92%. In addition, a 10-MHz GaN 16-34 V boost converter with above-90% efficiency is presented to show the capability of GaN devices at high frequencies [89].

In [90], an overview of the classical and recent development in DC–DC converter topologies based on WBG semiconductor devices is presented. The properties of WBG devices motivate a new generation of high-efficiency converters in applications where classical power converters present significant limitations, such as high-voltage, high-temperature and high-frequency operation.

Even though WBG devices have many advantages compared to silicon switching devices and may be considered as an alternative for soft switching techniques, the use of WBG devices has still some drawbacks. First, WBG-based hard-switched converters still suffer higher switching loss than full soft-switched converters, where soft switching is applied to all commutations. Second, WBG-based switches have shown considerable progress, but they have not yet achieved the same level of technological advancement for their production as silicon switches in terms of production and manufacturing. Therefore, due to the complexities in manufacturing WBG materials and limited economies of scale, WBG-based switches are often more costly. Furthermore, they suffer from sensitivity to parasitic components in the high-speed gate drive, high reverse-conducting voltage drop and high electromagnetic interference (EMI) [91]. The fast switching speeds of WBG devices lead to sharp voltage and current transitions, which in turn generate significant EMI.

The point at which parasitics become problematic for hard-switched PWM converters depends on various factors, including the specific converter design, the quality of components used, and the parasitic values themselves. Generally, as the power level and switching frequency increase, the impact of parasitics becomes more pronounced. In **Fig. 4.12**, for example, it can be observed that increasing the power level and switching frequency impacts the efficiency.

3.1.3 First research focus of the thesis: soft switching circuits vs. WBG switching devices

Considering soft switching techniques discussed in 3.1.1 and given studies in 3.1.2, one of the aims of this thesis is answering the important question they raise: in general, are silicon-based soft-switched DC-DC converters more efficient and/or more convenient than WBG-based hard-switched DC-DC converters, or is the reverse true? For completeness and to set benchmarks, this thesis also should investigate WBG-based soft-switched converters and Si-based hard-switched converters.

Similar previous work has not covered the same scope. Reference [92], for example, presents only a comparison of silicon-based soft-switched and SiC-based hard-switched inverters. However, a comprehensive performance comparison was not presented in [92]; only cost and power losses were compared. It should be noted the characteristics of DC-AC inverters studied in [92] and DC-DC converters can be significantly different. Moreover, each technique (soft switching and state-of-the-art WBG switches) can have different results for different applications. A method can be more efficient in a particular application such as battery charger while it might be less suitable for another application such as in PV systems. This presents an opportunity to explore the space between the use of soft-switching techniques and state-of-the-art WBG semiconductors in low-voltage (<650V) hard-switched DC-DC converters for renewable energy applications comprehensively. We therefore present a case study which supplements existing literature and expands the scope of knowledge to encompass DC-DC converters in the application range of hundred watts. This case study is investigated in Chapter 4. As previously stated, this thesis primarily focuses on DC-DC converters. Therefore, the findings and contributions of this study may not necessarily be applicable to inverters.

3.1.4 Resonant converters

In PWM converters, high switching frequencies cause high switching losses. An auxiliary circuit can be usually added to the conventional topology of a PWM converter to provide soft-switching capability for the converter. However, this auxiliary circuit leads to a more complex and expensive circuit, and it cannot always guarantee higher efficiency of the converter for different applications [5-7]. In Chapter 4, it is, for example, shown that the soft-switched version of the boost converter is more expensive and complex than the conventional hard-switched boost converter. On the other hand, as discussed in Chapter 2, resonant converters

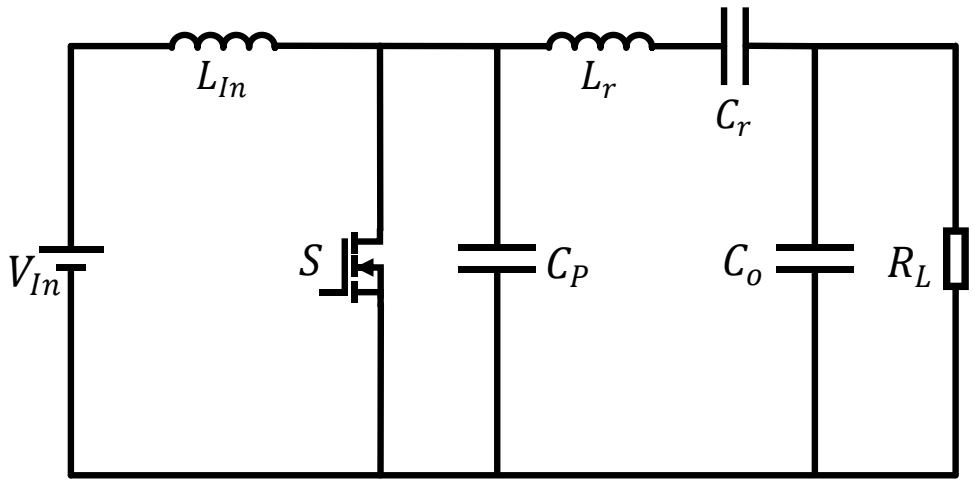

Fig. 3.4 The schematic of class E converter.

benefit from soft-switching capability inherently and therefore by using the new WBG semiconductors, they can be switched at high frequencies to achieve high power density [93].

The soft-switching nature has been previously studied in resonant converters such as class-E inverters [94] and class-D inverters [95]. As a result, resonant converters have been investigated for use in many applications such as LED drivers [96], LCD TV [97], electric vehicles charging station [98] and photovoltaic systems [99], for converting AC to DC [100, 101], DC to DC [102, 103], or both [104, 105]. However, resonant topologies require extra reactive components which decrease the positive effect of the high switching frequency on the power density. It is often argued that the extra reactive elements of resonant converters are of small physical size at high frequencies and therefore the penalty is not serious. Besides, since the required resonant inductor is normally of small inductance value due to high operating frequency, the possibility of applying parasitic component, such as leakage inductance of the transformer, is frequently discussed [44, 106].

Class E converter, shown in **Fig. 3.4**, is simple with only one active power switch and is efficient at high frequencies [107]. Even though this converter has a great potential for high frequency DC-DC converters, it also increases the voltage stress over the switch, greatly

limiting its application. Moreover, its ZVS performance is sensitive to the load variation and additional compensation circuit need to be designed to improve this sensitivity [108].

Class D series resonant converter and class D parallel resonant converter (**Fig. 2.8** and **Fig. 2.9**, respectively, page 22) have been used for designing AC power supplies [109, 110]. However, they have their limitation such as difficulty in regulating the output voltage at low-load conditions (series topology) and low efficiency at light loads (parallel topology) [37]. As discussed in section 2.3, the LLC resonant converter, which is still one of the derivatives of class D series resonant converter, can overcome the limitation of the series resonant converter.

The LLC converter is one of the most popular topologies amongst resonant converters and has been used in many applications because of its unique advantages. The LLC converter benefits from ZVS capability from zero to full load range, low voltage stress on secondary rectifier, no-load voltage regulation, high efficiency and can be designed to obtain high voltage gain at a narrow range of operating frequencies [111, 112]. Therefore, the focus of this thesis is on the LLC converter for achieving high efficiency and power density converters.

An isolated LLC resonant converter, shown in **Fig. 2.10** (page 23), uses three magnetic components: a parallel inductor, a series (or resonant) inductor and a transformer, which makes it large. However, to further increase the efficiency and power density of the LLC resonant converter, all three magnetic elements can be integrated into a single magnetic component. Even though a lot of research for integrating magnetic components of LLC converters has been conducted in recent years, there are still some issues in this area [12], which are discussed in subsection 3.2.1. Therefore, the main focus of this research is on improving magnetic integration for the LLC topology.

3.2 Magnetic integration

3.2.1 A review on different techniques for magnetic integration

A lot of research on integrating magnetic components of LLC converters and other resonant converters such as push-pull class E topology [113], LCC topology [114], LCLC topology [21], and, other converters such as phase-shifted full-bridge converters [115], interleaved converters [116] and dual active bridge converters [117] has been conducted in recent years. In the this section, the techniques which may be suitable for magnetic integration in resonant converters, especially the LLC topology, are presented and their advantages and disadvantages are discussed, then one of them is chosen to be the focus of this thesis and finally, four research focuses to address its current issues are proposed.

3.2.1.1 Three windings with a single transformer core

The structure of this technique in which the transformer has three windings—two windings for the transformer looped around one leg and one winding looped around another leg of cores for the series inductor—can be used to integrate the transformer and series (resonant) inductor into a single transformer core. For example, **Fig. 3.5(a)** shows the structure presented in [118]. In this structure, the transformer windings are placed on the left outer leg and the resonant inductor winding is placed on the right outer leg of the magnetic core. In addition, there are air gaps on both outer legs and no air gap on the centre leg. The left air gap can regulate the magnetising inductance and the right air gap can be used to adjust the resonant (series) inductance. The fluxes generated by the transformer and the resonant inductor are shorted through the centre leg and the fluxes on the centre leg can be cancelled.

Even though this structure does not need a bespoke transformer core, it is mechanically unstable (outer leges' airgaps are not the same), leading to imbalances in the magnetic flux within the outer legs, which in turn affects the transformer's overall performance and efficiency. In addition, the flux density on the left outer leg is doubled compared to the discrete transformer because the cross-sectional area of the left outer leg is only half of the centre leg (leading to higher core loss).

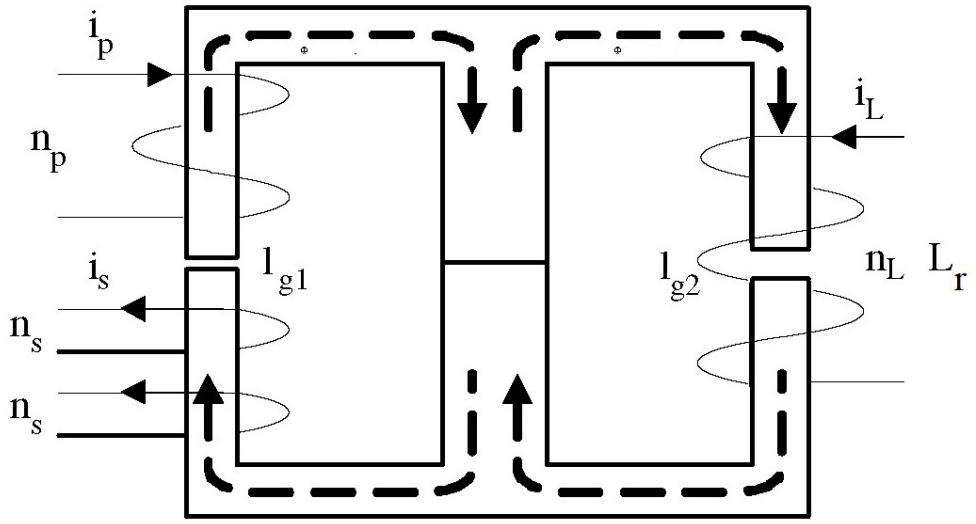

(a)

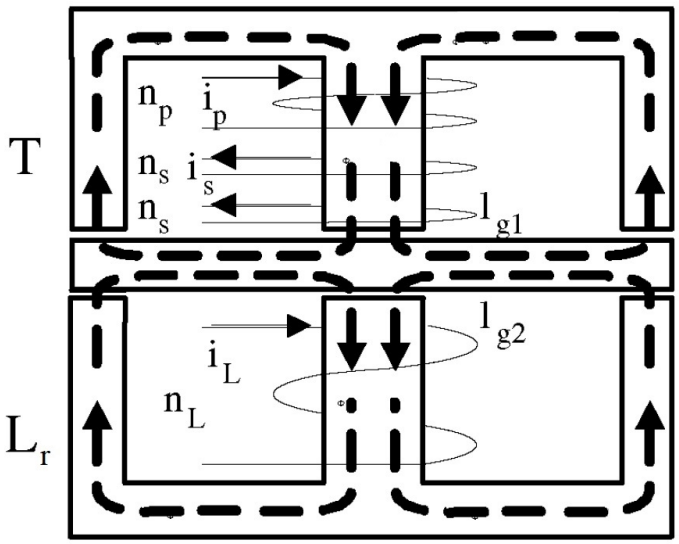

(b)

Fig. 3.5 The structures of the integrated transformers presented in [118]. Resonant inductor winding on the outer leg. (b) Resonant inductor winding on another E core.

3.2.1.2 Three windings with a single transformer core

To make the flux density of the integrated transformer the same as the discrete transformer, the topology shown in **Fig. 3.5(b)** has been proposed [118, 119]. In this structure, the transformer winding is on the upper E-core and the resonant inductor winding is on the lower E-core. There are air gaps on both the upper and lower centre legs and outer legs. The fluxes generated by

the transformer and the resonant inductor are combined through the middle I-core and the flux on the I-core can be cancelled.

This topology is a mechanically stable structure because the air gap is on all the legs. However, the window area in this structure is decreased compared to a discrete transformer. In addition, the power density still does not increase noticeably compared to using a separate transformer and inductor. In other words, for identical power and voltage, similar volumes for the inductor and transformer are needed and combining them does not change the total power density compared to using a separate transformer and inductor (since they both have the same size).

3.2.1.3 Outer legs decoupling and integration of windings

The winding of the resonant inductor can be integrated into the primary winding of the transformer. For example, as presented in **Fig. 3.6** [120], the resonant inductor is distributed on both sides of the outer legs and the transformer's primary and secondary windings are looped around the centre leg. The two windings of the resonant inductor are connected in series with the primary winding of the transformer.

By adjusting the winding direction of the resonant inductor, this method can make the flux on the centre column generated by the two sides windings cancel each other and realize the decoupling of the resonant inductor and transformer windings. However, this technique results in a magnetic bias problem and increases the core loss greatly. In addition, this structure suffers from higher conduction losses due to the auxiliary winding and eddy-current effect and has low flexibility in the design.

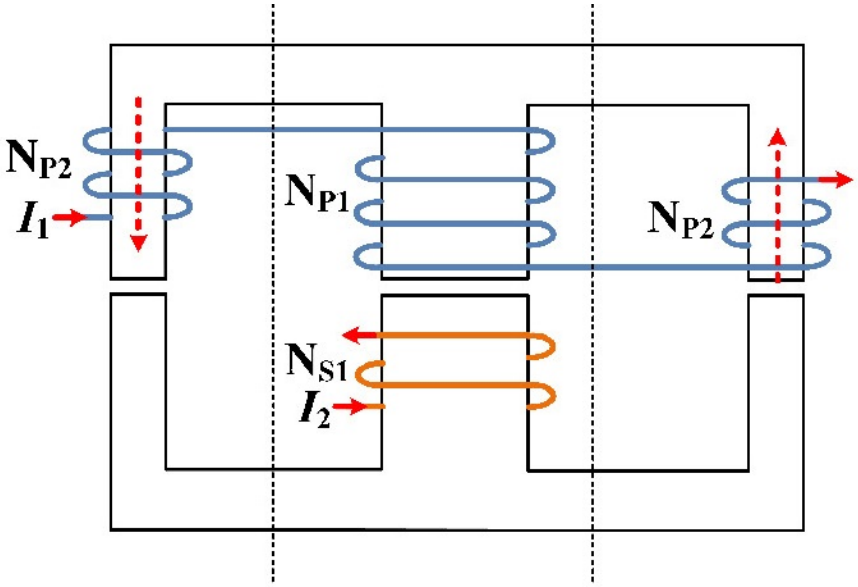

Fig. 3.6 The structure of the integrated transformer presented in [120].

3.2.1.4 Manipulation of the transformer core or adding auxiliary core for magnetic integration

Another way to integrate the required series inductance into the transformer is to produce a design-specific core geometry or add an auxiliary core to a standard-geometry transformer and merge either the primary winding or secondary winding with the winding of the series inductor [44, 120-125].

In [44, 120], a structure for magnetic integration is proposed which uses two pairs of cores (one for the transformer and one for the resonant inductor) and the primary winding is merged with the resonant inductor winding. This structure is presented in **Fig. 3.7**. As shown, the primary winding is looped around the centre leg of the two pairs of cores at the same time, while the secondary winding is only looped around the centre leg of the transformer core. The gap between the two pairs of cores can be adjusted separately. The transformer core has a smaller air gap to increase the coupling between the primary and secondary sides and reduce the leakage inductance of the secondary side, while the inductor core has a larger gap to provide a larger resonant inductance.

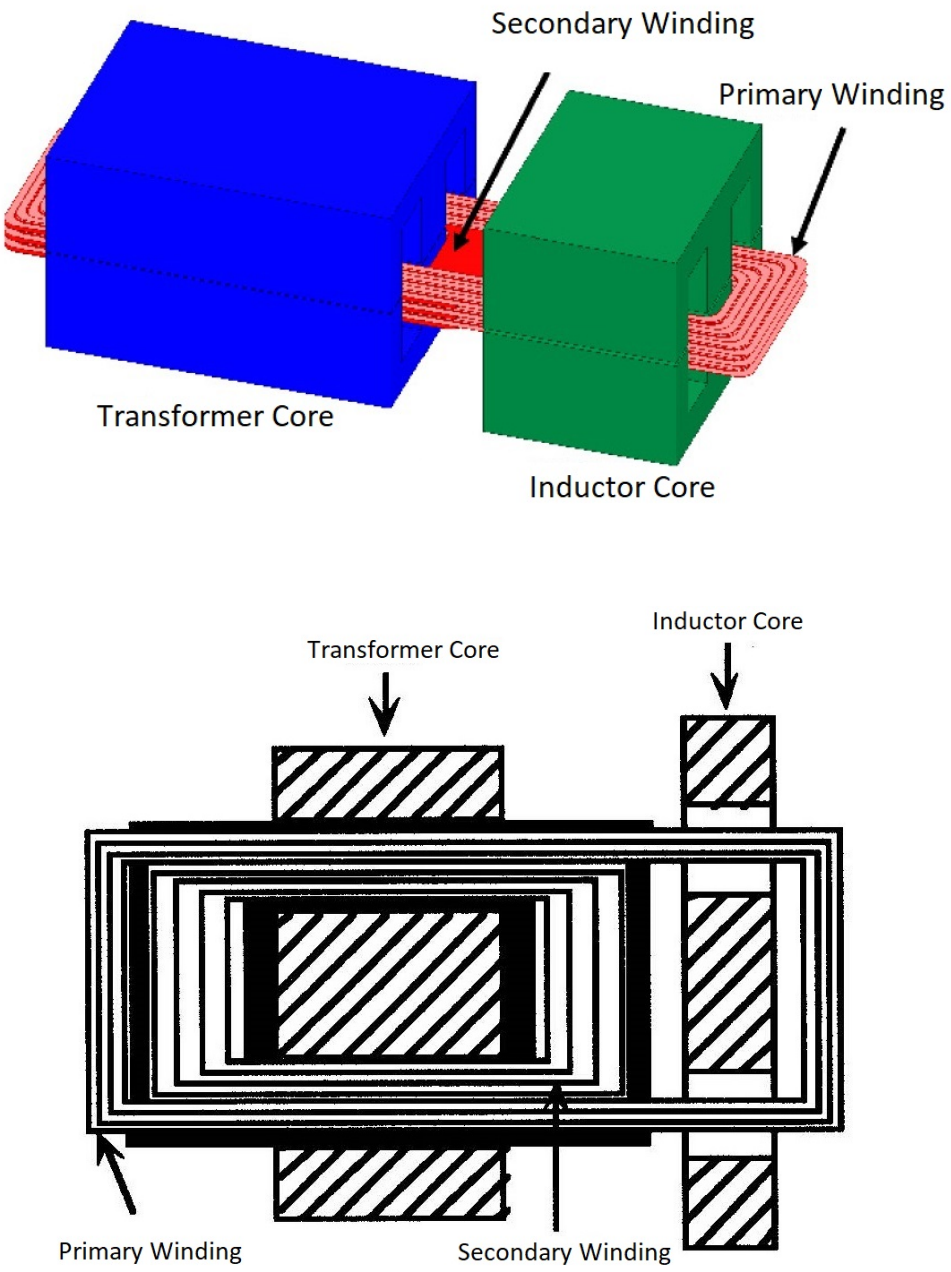

Fig. 3.7 The structure of the integrated transformer presented in [44, 120].

This scheme of using two pairs of cores increases the volume and the power density does not improve noticeably compared to using a single transformer and a single inductor. The core structures can be modified to achieve flux cancellation and lower volume [121-123], but as presented in **Fig. 3.8**, this approach requires a new bespoke transformer core for each design.

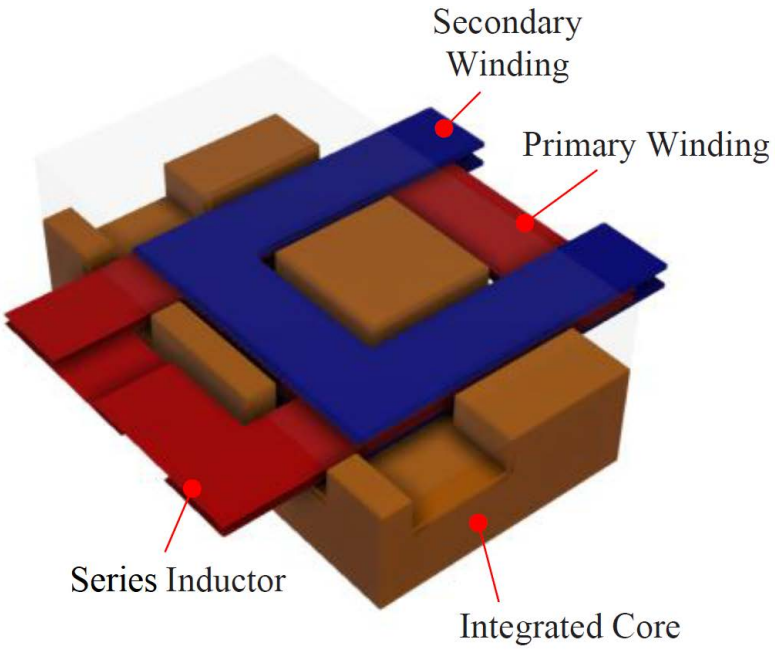

Fig. 3.8 The structure of the integrated transformer presented in [123].

3.2.1.5 Utilisation of the leakage inductance as the resonant inductance

As discussed in Chapter 2, to eliminate the need for an auxiliary core or winding for magnetic integration, the leakage inductance of a typical high frequency-transformer can be selected by design and used as the series inductor of the LLC tank as presented in **Fig. 2.11(a)** [5, 46, 126, 127].

The planar transformer can achieve a high leakage inductance which can be estimated precisely when the primary and secondary windings are placed separately as shown in **Fig. 3.9**. In [128, 129], a detailed analysis for more precise estimation and adjustment of the leakage inductance of a planar transformer is presented.

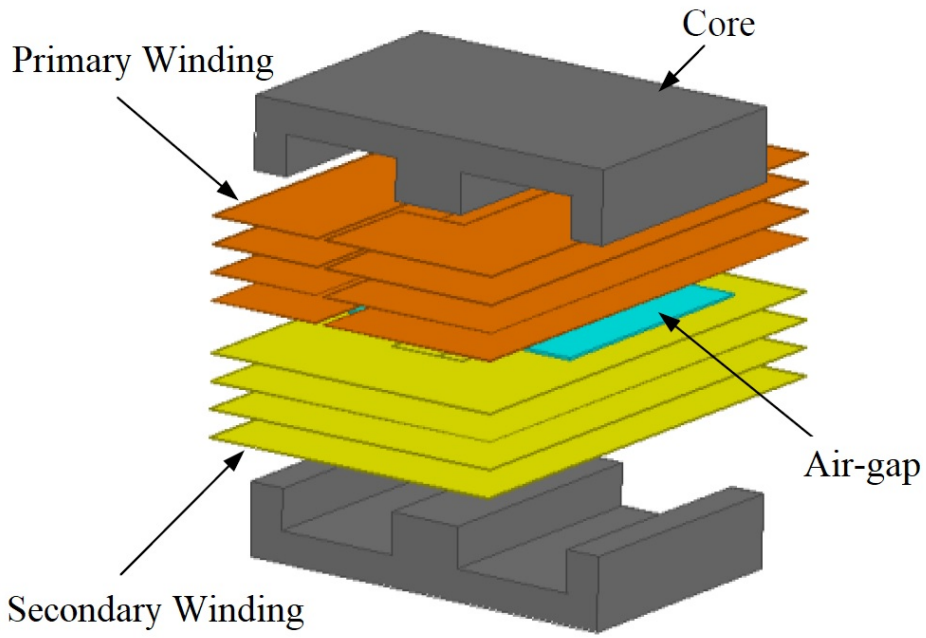

Fig. 3.9 Planar transformer with separated primary and secondary windings [130].

Using the leakage inductance of a typical wound-core or planar transformer benefits from low cost and simplicity in manufacturing because it does not need any manipulation in the transformer structure and an auxiliary winding for the inductor is not required. However, in this approach, the leakage inductance can be only adjusted for a limited variation since it is determined based on the geometry of the core and windings, leading to low flexibility in the design. Consequently, if a higher amount of leakage inductance is required beyond what the core's limitations allow, this particular structure would not be a suitable option.

Some magnetic field-conducting sheets can be added between layers of windings to integrate the magnetic components by enhancing the leakage inductance (as a result of increasing energy stored in the window area) [131]. However, this approach suffers from lower efficiency due to the high eddy-current losses in the windings and low flexibility in design.

In the following of this section, some other techniques that can be used to increase and adjust the leakage inductance are reviewed.

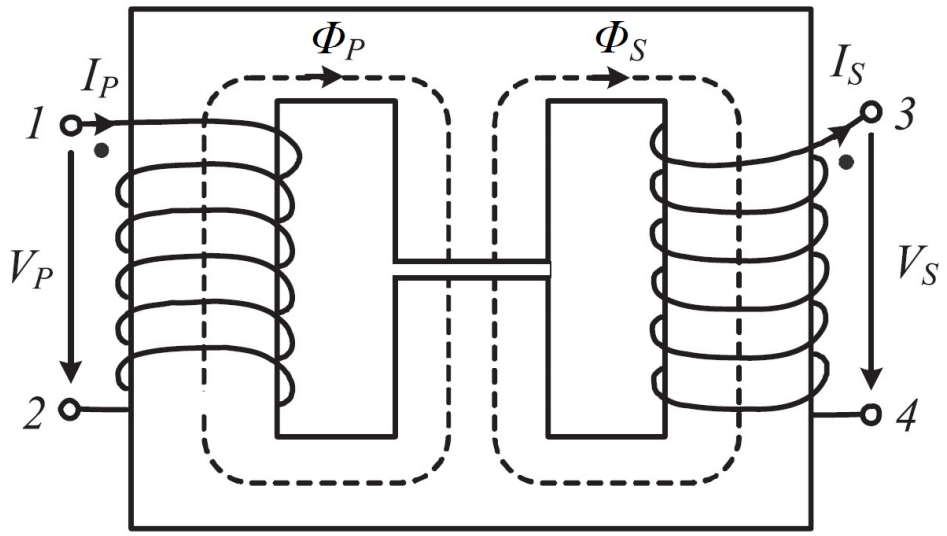

Fig. 3.10 The structure of the integrated transformer presented in [132]**.**

3.2.1.6 High leakage inductance with primary and secondary windings on the outer legs

Another structure which is suitable for the series LC and series-parallel LCC resonant converters is proposed in [132]. This structure is shown in **Fig. 3.10**. As shown, the primary and secondary windings are looped around the outer-left and outer-right legs of the transformer and an air gap is inserted into the centre leg of the E-core to achieve a controllable leakage inductance.

Although a multi-layer PCB with minimal complexity can be used as the windings, the transformer has a large footprint since the windings extend outside the transformer core. In addition, the AC resistance is high in this design, and leakage and magnetising inductances are not decoupled and cannot be designed separately. Moreover, the magnetising inductance cannot be adjusted easily in this structure since there is no air gap to regulate the mutual flux of primary and secondary windings. Hence, this structure may not be suitable for the LLC topology in which an adjustable shunt inductance is needed.

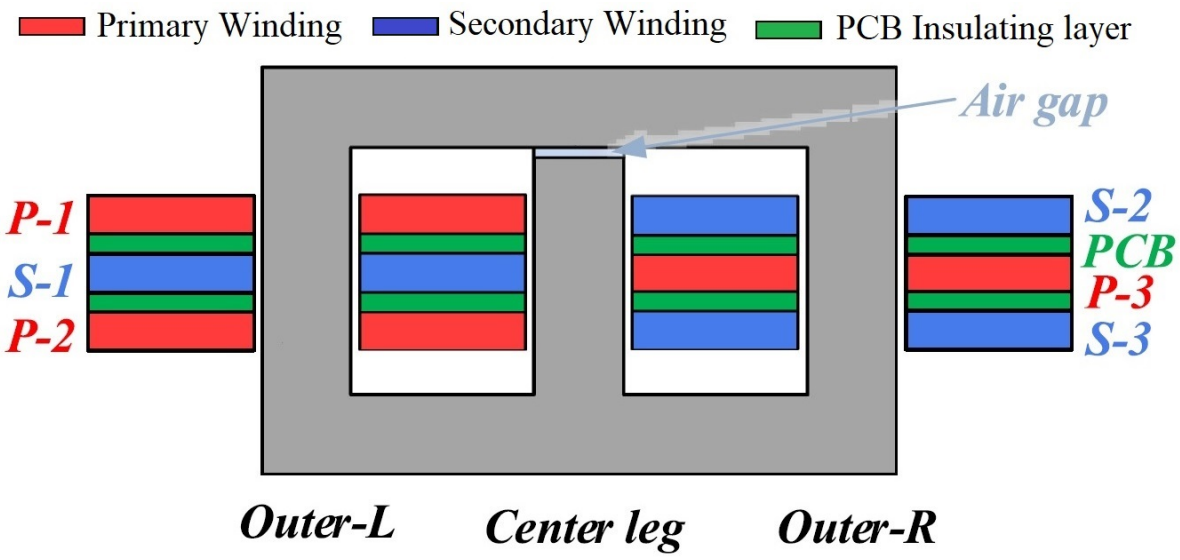

Fig. 3.11 The structure of the integrated transformer presented in [10].

3.2.1.7 High leakage inductance with interleaved primary and secondary windings

A lower AC resistance and controllable leakage inductance can be achieved with an interleaved or semi-interleaved windings structure of the transformer [10, 133]. For example, in the topology proposed in [10], shown in **Fig. 3.11**, the primary- and secondary-side windings are looped around the outer legs of the transformer core asymmetrically (i.e., placing a different number of primary- and secondary-side turns).

By asymmetrically distributing the windings, controllable leakage inductance can be generated by tuning the core reluctances, and winding interleaving, which leads to lower AC resistance, is achieved. However, in these approaches, the winding structure is complicated and the leakage and magnetising inductances are not decoupled and cannot be regulated separately, making the design process more complicated. Moreover, the primary and secondary windings are looped around the outer legs, leading to a larger footprint for the transformer, lower power density and potentially higher electromagnetic interference (EMI) for the converter.

Furthermore, in the interleaved winding structure, there is a high overlap area between the primary and secondary windings, which could increase the inter-winding capacitance to an undesirable value. Furthermore, these approaches may not be suitable for LLC topology since

the magnetising inductance cannot be adjusted easily (there is no air gap to regulate the mutual flux of the primary and secondary windings).

3.2.1.8 Inserted-shunt integrated planar transformer

The structure of an integrated planar transformer with an inserted-shunt is shown in **Fig. 3.12**. Inserting a low-permeability magnetic shunt in the centre of a planar transformer while its primary and secondary windings are separated (by being located above and below the magnetic shunt) can provide a high leakage inductance and provides greater and more precise control of its value [12, 130, 134-136].

In the inserted-shunt integrated planar transformer shown in **Fig. 3.12**, the primary winding generates a flux in the upper core, and this is responsible for producing the primary side self-inductance, L_{PP}, of which the magnetising inductance, L_{m}, is the largest contributor. A small but significant proportion of the primary flux flows through the shunt and is responsible for the primary side leakage inductance, $L_{\mathrm{Lk\_P}}$. Similar arguments lead to the provision of the secondary side leakage inductance, $L_{\mathrm{Lk\_S}}$. The remaining primary flux crosses the air gap and couples to the secondary winding and so is responsible for the ideal transformer turns ratio, $N_{\mathrm{P}}: N_{\mathrm{S}}$. In the analysis of the inserted-shunt integrated planar transformers, it is assumed that flux linkage is exactly the same for both primary and secondary windings and therefore the primary and secondary leakage inductances can be considered identical.

The relationship between the leakage and magnetising inductances and the shunt's characteristics and length of the air gaps for this method is discussed in [12, 130, 134, 135]. According to [12], the energy stored in the windings and insulation layers is far lower than that stored in the magnetic shunt and therefore the inserted-shunt is the main cause of the high leakage inductance. In addition, the leakage and magnetising inductances can be controlled for a limited range of the leakage inductance and the shunt's relative permeability by regulating the permeability of the shunt and the length of the air gaps, respectively.

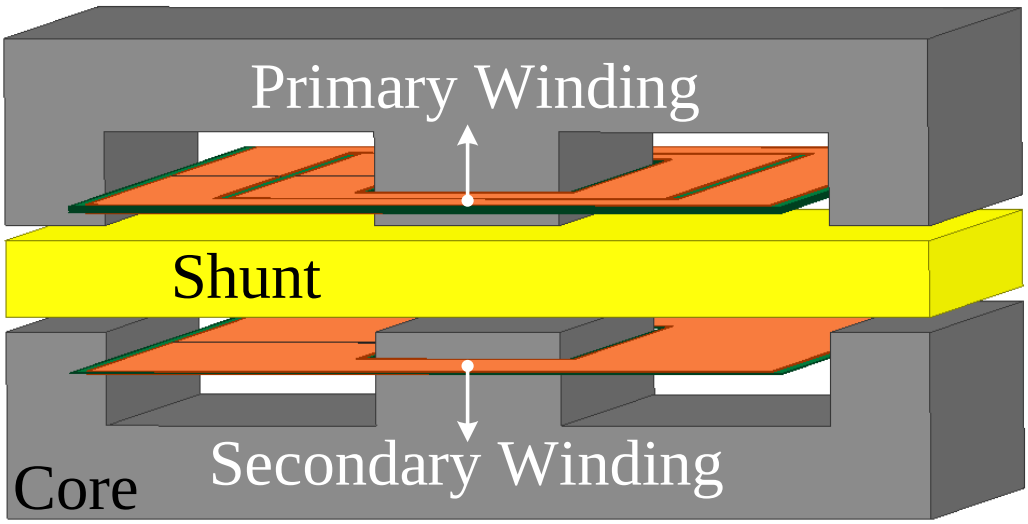

(a)

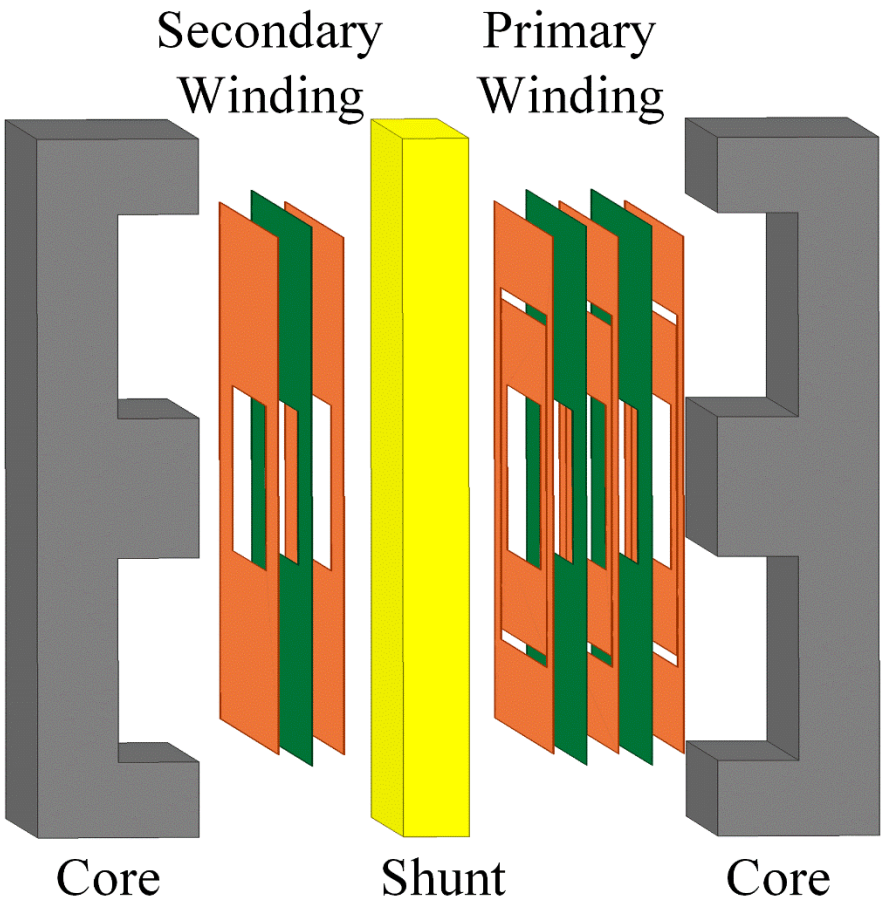

(b)

Fig. 3.12 The inserted-shunt integrated transformer. a) Structure. b) Exploded view [12].

Inserted-shunt integrated transformers can integrate all three magnetic components of an LLC resonant converter in only a transformer without any auxiliary windings, and the readily available planar cores in the market can be used without any manipulation. Therefore, this topology also benefits from the advantages of planar transformers, *viz* high power density, improved cooling capability, modularity and manufacturing simplicity [12]. In addition, the leakage and magnetising inductance are decoupled from each other and can be adjusted separately. In summary, the inserted-shunt integrated transformers could be an attractive technique to be used for magnetic integration in an LLC resonant converter; hence the focus of this thesis is further investigation of this technique and addressing its issues.

3.2.2 Research focuses for the inserted-shunt integrated planar transformer

In this section, the main issues of the inserted-shunt integrated planar transformers are discussed and then research studies to address these issues are proposed.

3.2.2.1 Second research focus of the thesis: Using a segmental high-permeability shunt instead of a low-permeability single-segment shunt

Inserting a single-segment low-permeability magnetic shunt in a planar transformer enhances the leakage inductance and makes the estimation of its value more accurate, but this idea suffers some disadvantages. The magnetic shunt must have a specific and unusually low-permeability (relative permeability <100). Suitable magnetic materials are not often readily available, and when they are, they are frequently expensive. In addition, these low-permeability materials are often found only in limited sizes while different thicknesses, widths and lengths are needed for each specific design of this integrated transformer [135, 137, 138]. Therefore, a new bespoke magnetic material with a specific size is required for each design in this approach, which makes the design expensive and less flexible.

To address these issues, a case study should be defined to propose a new structure for the inserted-shunt integrated transformer in which high-permeability materials can be used for the shunt.

In Chapter 5, two new structures (termed IT1 and IT2) are proposed that use high-permeability material for the shunt. In the proposed structures, the inserted shunt is formed by interleaving highly permeable ferrite with thin plastic spacers to form segmental magnetic shunts. This

design approximates the low-permeability material; its permeability is modulated by the ratio of ferrite-to-spacer length. The design is more economical because ferrite is widely available in the market in different sizes and for lower prices.

Both of the proposed structures are analysed and their modelling and design guidelines are provided in detail. The theoretical analysis is verified by finite-element analysis (FEA) simulation and experimental results. The AC resistance for the proposed structures is also discussed. Furthermore, an LLC converter is implemented to investigate the performance of the designed fully-integrated magnetic transformers. It is shown that this LLC converter operates properly while all of its magnetic components are integrated into the proposed structures.

3.2.2.2 Third research focus of the thesis: Using a solid high-permeability shunt instead of a segmental high-permeability shunt

The structures proposed in Chapter 5 (IT1 and IT2) do not need a shunt with specific permeabilities and dimensions. However, the inserted shunt has multiple segments and has to be located between two E-cores which makes the implementation difficult. Therefore, to address this issue, a new topology (termed IT3) for achieving high leakage inductance in inserted-shunt integrated planar transformers is proposed in Chapter 6.

In the proposed topology, two solid shunts are placed across the planar E-core air gap and between the primary and secondary windings. The proposed topology benefits using solid inexpensive ferrite shunts, making manufacturing easier. A detailed mathematical model is derived from which a design methodology is developed, providing accurate estimation for the leakage and magnetising inductances. The theoretical analysis has been verified using finite-element analysis and experimental implementation. AC resistance analysis and efficiency comparison are also presented for the proposed topology and the topology with inserted-segmental-shunt, which shows the proposed topology provides higher efficiency because of lower AC resistance. In addition, an isolated LLC resonant converter is designed and built to investigate the performance of the proposed topology in practice. The three magnetic components needed for the designed LLC resonant converter are integrated into a single planar transformer using the proposed topology and the converter operates properly.

3.2.2.3 Fourth research focus of the thesis: Inserted-shunt integrated planar transformer with low secondary leakage inductance

In integrated planar transformers with inserted-shunt, including the transformers proposed in Chapters 5 and 6 (IT1-IT3), the leakage inductance increases on both primary and secondary sides. The effects of secondary leakage inductance on LLC resonant converters are investigated in [139]. FHA has been usually used to analyse the LLC topology while the secondary leakage inductance is ignored. However, the voltage gain of an LLC converter is very sensitive to resonant components and ignoring the secondary leakage inductance causes inaccurate analysis [122, 140]. Alternatively, the primary and secondary leakage inductances are considered identical in many studies, such as the inserted-shunt integrated planar transformers, and the secondary leakage inductance is referred to the primary side of the simplified equivalent circuit according to the transformer turns ratio and the total leakage inductance is calculated by (2-61). However, this method is also not precise, especially when the magnetising inductance is purposefully reduced by inserting air gaps in transformer cores, again such as inserted-shunt integrated planar transformers [141].

The effect of secondary leakage inductance on the operation of the LLC topology is briefly investigated below.

When the leakage inductance increases on both the primary and secondary sides of an integrated transformer, the equivalent circuits presented in **Fig. 2.11(a)** and **Fig. 2.13** should be modified as equivalent circuits presented in **Fig. 3.13(a) and (b)**, respectively. Therefore, not considering the secondary leakage inductances, L_{Lk_S}, may result in incorrect analysis.

From **Fig. 3.13(b)**, the gain of the new AC circuit with a complete transformer model (CTM) may be derived from the circuit analysis as (3-1).

$$M_{AC}=\frac{2nV_o}{V_{In}}=\frac{1+\frac{L_{Lk\_S(P)}}{L_m}}{1+\frac{jf_{N\_CTM}Q_{CTM}}{\lambda_2}\left(\frac{1-f_{N\_CTM}^2}{1-\frac{f_{N\_CTM}^2}{\lambda_1}}\right)}\left(1+\frac{f_{N\_CTM}^2-1}{1-\frac{f_{N\_CTM}^2}{\lambda_1}}\right) \tag{3-1}$$

where

$$L_{\mathrm{r\_CTM}} = L_{\mathrm{Lk\_P}} + \frac{L_{\mathrm{m}} L_{\mathrm{Lk\_S(P)}}}{L_{\mathrm{m}} + L_{\mathrm{Lk\_S(P)}}} \tag{3-2}$$

$$f_{\mathrm{r\_CTM}} = \frac{1}{2\pi\sqrt{C_{\mathrm{r}} L_{\mathrm{r\_CTM}}}} \tag{3-3}$$

$$Q_{\mathrm{CTM}} = \frac{\sqrt{\frac{L_{\mathrm{r\_CTM}}}{C_{\mathrm{r}}}}}{R_{\mathrm{L\_AC(P)}}} \tag{3-4}$$

$$\lambda_1 = \frac{L_{\mathrm{r\_CTM}}}{L_{\mathrm{m}} + L_{\mathrm{Lk\_P}}} \tag{3-5}$$

$$\lambda_2 = \frac{L_{\mathrm{r\_CTM}}}{L_{\mathrm{m}} + L_{\mathrm{Lk\_S(P)}}} \tag{3-6}$$

$$f_{\mathrm{N\_CTM}} = \frac{f_{\mathrm{s}}}{f_{\mathrm{r\_CTM}}} \tag{3-7}$$

At the resonance frequency, i.e. for $f_{\mathrm{N\_CTM}}$=1, the voltage gain becomes:

$$M_{\mathrm{AC}} = 1 + \frac{L_{\mathrm{Lk\_S(P)}}}{L_{\mathrm{m}}} \tag{3-8}$$

From (3-8), after ignoring the secondary leakage inductance ($L_{\mathrm{Lk\_S}}$), the voltage gain of the simplified transformer model, which has only a leakage inductance on the primary side, becomes (3-9) which is same as (2-22) at the resonance frequency (see **Fig. 2.14**).

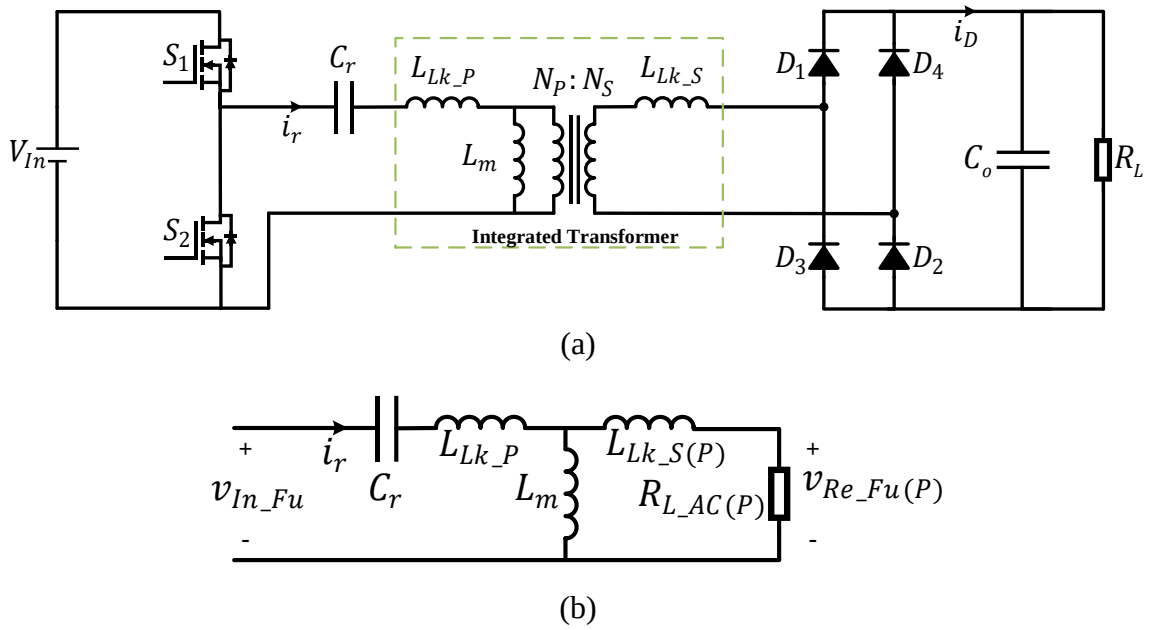

Fig. 3.13 LLC resonant converter with secondary leakage inductance. (a) Schematic. (b) AC equivalent circuit. $L_{\mathrm{Lk\_S(P)}}$ is $L_{\mathrm{Lk\_S}}$ transferred to the primary side.

Table 3.1 An exemplar transformer parameter.

N_{P}	N_{S}	$L_{\mathrm{LK\_P}}$(μH)	$L_{\mathrm{LK\_S(P)}}$(μH)	L_m(μH)
42	18	51.6	60.4	243.9

$$M_{\mathrm{AC}} = 1 \tag{3-9}$$

In order to better highlight the differences between the two cases, an exemplar transformer with characteristics, presented in **Table 3.1,** should be considered**.** A fair comparison with the simplified transformer model case must preserve the same resonance frequency as well as the same total primary inductance, measured with an open and shorted secondary winding [43]. In fact, these conditions guarantee the same ZVS behaviour at no-load. Thus, the simplified transformer model (STM) must have the following parameters:

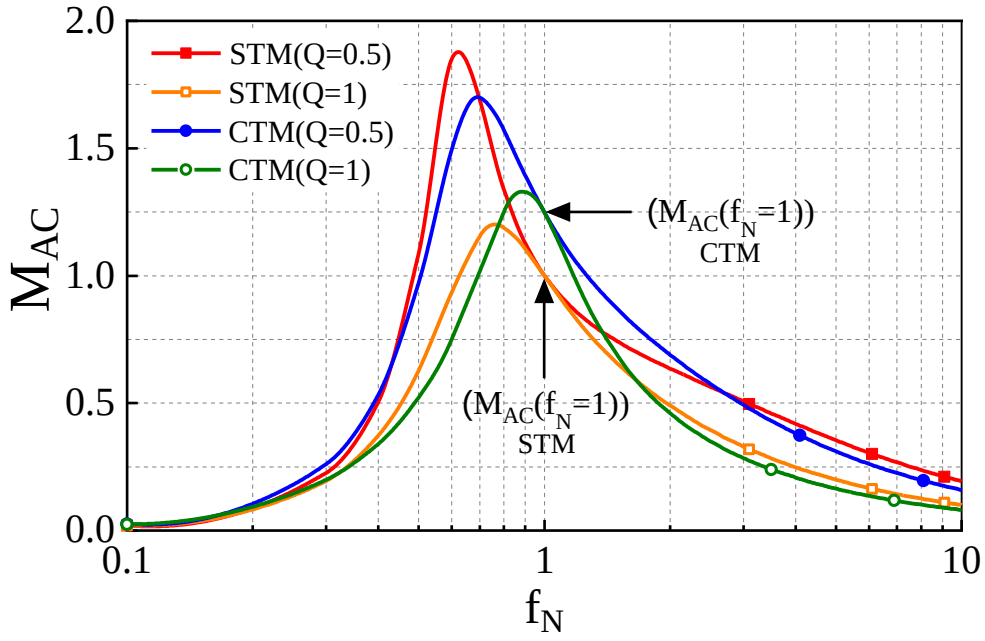

Fig. 3.14 Voltage conversion ratio magnitude comparison for STM and CTM.

$$\begin{cases} L_{\text{Lk\_S\_STM}} = 0 \\ L_{\text{Lk\_P\_STM}} = L_{\text{Lk\_P}} + \dfrac{L_{\text{m}} L_{\text{Lk\_S(P)}}}{L_{\text{m}} + L_{\text{Lk\_S(P)}}} \\ L_{\text{m\_STM}} = L_{\text{Lk\_P}} + L_{\text{m}} - L_{\text{Lk\_P\_STM}} \end{cases} \tag{3-10}$$

The comparison of the voltage conversion ratio amplitude calculated using the simplified transformer model and complete transformer model is shown in **Fig. 3.14**. As shown, the difference, at the resonance frequency, is in the order of 25%, independently of load, as forecasted by (3-8) and (3-9).

Some research has been done to model the LLC converter while the secondary leakage inductance is considered [43, 140]. Even though these models estimate the gain of the converter more precisely, the design of the converter and its control system is more complicated when there is a high secondary leakage inductance [11] and thus it is still preferred to have a negligible leakage inductance on the secondary side. Zhang, *et al*, [142] point out that, in LLC resonant converters for voltage regulator modules (VRM), the synchronous rectifier switches employ a self-driven method. In this situation, when the leakage inductance exists on the secondary side, there is an overlapping period of commutation between the secondary switches

and their currents, leading to higher losses. In addition, Noah, *et al*, [141] found that the secondary leakage inductance causes some other major problems. Firstly, the secondary leakage inductance adds a virtual gain to the gain curve of the LLC converter and the converter encounters a non-unity gain at the nominal frequency. This non-unity gain behaviour can make it difficult for the control system to achieve stable and precise regulation, as it needs to compensate for the gain variations. Secondly, it limits the current delivered to the load by increasing the converter output impedance.

It should be pointed out that the inserted-shunt integrated planar transformers can also be used in other similar topologies like phase-shifted full-bridge converters. Therefore, it is preferred that the leakage inductance only increases on one side and the topology of the converter remains the same as the original topology (for example, for LLC topology see **Fig. 2.11**) to avoid unnecessary new analysis and modification for each type of converter.

Finally, as the fourth case study of this thesis, a new structure (termed IT4) for the inserted-shunt integrated planar transformers is needed to address the key issue of high secondary leakage inductance.
In Chapter 7, a novel topology for the inserted-shunt integrated planar transformer is proposed which has low secondary leakage inductance. The inserted shunt of the proposed topology is not segmental and can be located conveniently within the transformer. In addition, the inserted shunt does not require low permeability core material, simplifying its manufacture. The design and modelling of the proposed transformer topology are presented and verified by finite-element analysis and experimental implementation. The proposed topology is also compared with the inserted-segmental-shunt integrated transformer. It is shown that the proposed transformer provides higher efficiency and lower AC resistance. Finally, to examine the performance of the proposed integrated transformer in practice, it is used in an LLC resonant converter.

3.2.2.4 Fifth research focus of the thesis: Inserted-shunt integrated transformer with asymmetric primary and secondary leakage inductances for bidirectional LLC converters

Rapid growth of residential energy storage systems (ESSs) is outpacing expectations, and these household systems are becoming important assets. For example, electric vehicles (EVs) with

vehicle-to-grid (V2G) capability can be used as distributed energy assets to provide power to the utility loads, to reduce grid frequency fluctuations and to absorb excess energy produced by renewable energy sources [143-145]. Therefore, the attention to energy storage systems (ESSs) has increased in recent years.

A bidirectional DC-DC converter and a bidirectional DC-AC converter are usually used in ESSs to transfer power in both directions between the grid and the batteries. Bidirectional DC-DC converters likewise manage the power flow between the DC bus and the batteries. The main focus of these DC-DC converters is on achieving low cost, high efficiency and power density, and wide input and output voltage ranges [146, 147].

Resonant converters can provide high efficiency and power density at a low cost since they benefit from soft-switching capability and magnetic integration. Therefore, resonant converters are becoming desirable for DC-DC applications like ESSs [20, 132, 148].

The LLC resonant converter is one of the most popular resonant topologies since it can provide high efficiency at high switching frequencies and can be designed to obtain high voltage gain at a narrow range of operating frequencies. However, the LLC topology is not suitable for bidirectional power transfer since the shunt (magnetising) inductance is effectively connected in parallel with the chopped battery voltage in regeneration (reverse-direction) mode (RM) meaning that it does not play a role in the resonant tank. The result is that, in RM, an LLC converter is equivalent to a series resonant converter.

The series LC resonant converter has a different inductive region compared to the LLC topology and to achieve ZVS it needs to operate at normalised frequencies higher than 1 (i.e., $1<f_N<f_{N\_max}$), while the LLC topology can also be switched at ZVS condition at normalised frequencies higher than the normalised boundary frequency (i.e., $f_{N\_Bo}<f_N<f_{N\_max}$, $f_{N\_Bo}<1$). Therefore, the efficiency of the series LC resonant converter drops considerably as the operating switching frequency drifts away from the resonance frequency, making it unsuitable for very wide input and output voltage range applications [149-151]. In addition, as discussed at the beginning of this section, the series LC resonant converter has difficulty to regulate the output voltage at light loads. In conclusion, the LLC resonant converter, which is a series LC

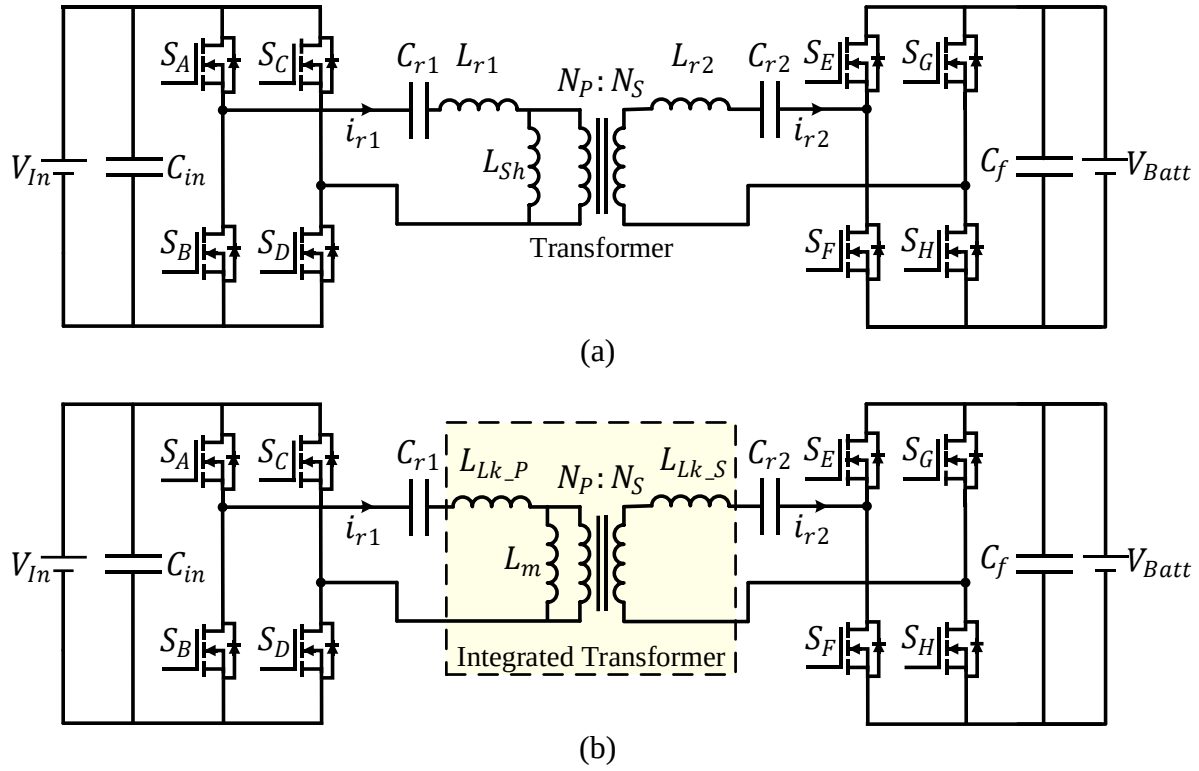

Fig. 3.15 Topology of bidirectional CLLLC resonant converter, (a) without magnetic integration, (b) with magnetic integration.

resonant converter in RM, is not suitable for bidirectional power transfer, especially in ESSs where the voltage variation is significant.

To adopt the LLC converter for bidirectional power transfer, a bidirectional CLLLC converter, which has an extra capacitor and an extra inductor on the secondary side, is proposed in [152]. The bidirectional CLLLC resonant converter is shown in **Fig. 3.15(a)**. In [152], the resonant components on the primary and secondary sides of the transformer must be symmetric ($L_{\mathrm{r1}} = n^2 L_{\mathrm{r2}}$, $C_{\mathrm{r2}} = n^2 C_{\mathrm{r1}}$, $n = N_{\mathrm{P}}/N_{\mathrm{S}}$) and the converter has unity gain. Unfortunately, the unity gain means the topology is not suitable for applications in which the input and output voltages vary during power transfer. This is particularly challenging with battery-charging type applications where the specified output voltage often has a wider range (for example, from 250 V to 450 V in vehicle-to-grid (V2G) applications) [153, 154].

In [153, 154], a design methodology for a CLLLC resonant converter is presented so that the converter can operate with wide battery voltage regulation. The converter proposed in [153, 154] is, like [152], based on the LLC topology with an extra inductor and extra capacitor on the secondary side but this time the component values can be asymmetric ($L_{\mathrm{r1}} \neq n^2 L_{\mathrm{r2}}$ and $C_{\mathrm{r2}} \neq n^2 C_{\mathrm{r1}}$). In [154], the benefits of asymmetric parameters are discussed in detail and they are again summarised in **Fig. 3.16**. **Fig. 3.16** shows the gain plots, in charging and discharging mode, of the CLLLC converter in [154], where charging and discharging gains can be defined as $V_{\mathrm{Batt}}/V_{\mathrm{In}}$ and $V_{\mathrm{In}}/V_{\mathrm{Batt}}$, resepctively. For a given operating frequency range, the range of available gains with symmetric and asymmetric primary and secondary inductances and capacitances are shown. The operating frequency range needed for a desired range of gains is significantly smaller for the asymmetric design, allowing optimisation to achieve high efficiency, reduced current stress and reduced electromagnetic interference.

The CLLLC resonant converter with asymmetric resonant components not only provides the advantages of the LLC converter but also can provide bidirectional power transfer. The CLLLC converter presented in [153, 154] is therefore a good candidate for battery charging applications and this topology is used in this thesis.

The topology of the CLLLC converter is shown in **Fig. 3.15(a)**. The operation of this converter is very similar to the LLC converter and therefore it is not presented in this thesis, and for a detailed discussion the reader can be referred to [153]. The CLLLC resonant converter benefits from soft switching capability and can be switched at high frequencies, but it needs four magnetic components including two series inductors (L_{r1} and L_{r2}), a shunt inductor (L_{Sh}) and a transformer, leading to large size and high cost. To increase the efficiency and power density, and to decrease the cost of this converter, these magnetic components should be integrated into a single transformer, as shown in **Fig. 3.15(b)**.

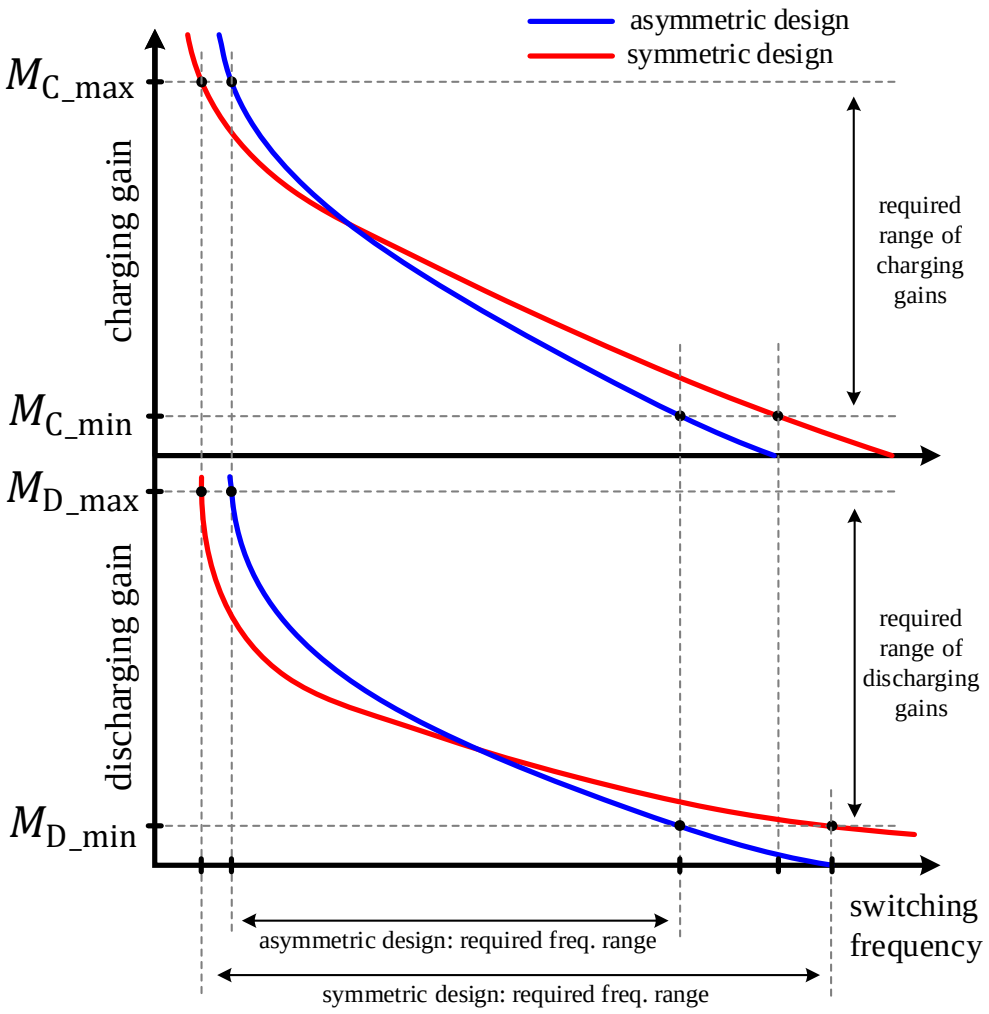

Fig. 3.16 Comparison of gain for symmetric and asymmetric designs, using data from [154]. 'C' for charging mode and 'D' for discharging mode.

The inserted-shunt integrated planar transformer is well known because of its many advantages, *viz* precise estimation of leakage inductance during design, capability for achieving high leakage inductance, the ability to use cores readily available in the market and simple manufacturing. The inserted-shunt integrated transformers discussed in the literature review and the proposed topologies in Chapters 5 and 6 (IT1-IT3) have symmetric primary and secondary leakage inductances and these inductances cannot be designed separately in these transformers. The CLLLC converter presented in [153, 154], and other similar topologies that need asymmetric primary and secondary resonant inductances could address more application challenges (especially the ones that require higher power density) if an integrated magnetic transformer were developed that can provide non-identical (asymmetric) primary and

secondary leakage inductances. Therefore, as the fifth research focus of this thesis, a new design methodology for the inserted-shunt integrated planar transformers is needed that takes into account the non-identical primary and secondary leakage inductances.

In Chapter 8, a new topology (termed IT5) for the inserted-shunt integrated magnetic planar transformer is proposed that can provide non-identical primary and secondary leakage inductances. In the proposed topology, two magnetic shunts are inserted between two E-cores and the primary and secondary windings are separated by being placed at different sides of the magnetic shunts. Commercially available planar cores can be used for the E-cores and magnetic (ferrite) sheets, which are again commercially available, can be used for the shunts, leading to cheaper and easier manufacturing.

The proposed integrated transformer is analysed in detail and its modelling and design guidelines are provided. It is shown that the magnetising inductance and the primary and secondary leakage inductances are decoupled, and they can be determined separately in the proposed topology. This theoretical analysis is verified by simulation and experimental results. To investigate performance, an exemplar CLLLC converter is designed using the proposed integrated transformer to provide experimental validation of the design process. It is shown that the implemented bidirectional CLLLC resonant converter operates properly while all its magnetic components are integrated into the proposed transformer.

3.3 Conclusion

This Chapter introduced the main issue of PWM converters, which is high switching losses at high frequencies, and the techniques that can be used to address this issue were also discussed. After investigating different methods, we could not find the answer to two questions in the literature. First question: do auxiliary soft-switching circuits always improve the performance of conventional PWM converters in terms of cost, power density and efficiency? Second question: in general, are silicon-based soft-switched DC-DC converters more efficient and/or more convenient than WBG-based hard-switched DC-DC converters, or is the reverse true? These questions will be the research focus of Chapter 4.

PWM converters, like the boost converter, suffer from a lack of soft-switching capability and thus have high switching losses under high-frequency operation. Losses are limited by

constraining the operating frequency, leading to lower power density. Even though soft-switching capability can be achieved by adding an auxiliary circuit to the conventional topology of the PWM converters, the auxiliary circuit adds complexity and cost (will be shown in Chapter 4). On the other hand, the resonant converters benefit from soft-switching capability inherently and therefore they could be a more suitable choice for high frequency and high power density converters.

It was pointed out that the LLC resonant converter needs three magnetic components which make the converter's volume large. However, the LLC resonant converter can provide a higher power density when its magnetic components are integrated into the transformer. Therefore, different techniques for magnetic integration were discussed. Amongst different techniques, the inserted-shunt integrated planar transformer seemed to be an attractive technique for magnetic integration in the LLC topology and therefore it was more investigated.

The current issues of the inserted-shunt integrated planar transformers were discussed. In general, the important issues of the inserted-shunt integrated planar transformers are requiring a bespoke material for the shunt, high leakage inductance on the secondary side, and they are not usually suitable to be used in bidirectional converters such as CLLLC converters. Therefore, four research studies to address these issues were suggested that will be the focus of Chapters 5 to 8.

Chapter 4

Evaluation of Si MOSFETs and GaN HEMTs in Soft-Switched and Hard-Switched DC-DC Boost Converters

This Chapter compares soft-switching techniques and WBG-based switches in DC-DC boost converters in the application range of hundred watts. The performance of four prototypes including the soft-switched and hard-switched DC-DC boost converters with both state-of-the-art Si and GaN switches are evaluated in terms of cost, power density, and efficiency using theoretical analysis, simulation and experimental results. It is shown that the GaN-based hard-switched converter provides higher efficiency and power density but is more expensive than its Si-based counterpart yet is cheaper than Si-based soft-switched converter. This is despite GaN-based switches being significantly more expensive than their Si counterparts. Therefore, adding an auxiliary circuit to obtain soft switching leads to a more expensive and complicated circuit and does not always guarantee a higher efficiency.

4.1 Introduction

It is well-known that the volume of passive components is inversely proportional to the switching frequency. At higher switching frequencies, in addition to reduced passive component volume, a low-capacitance and low-inductance filter can be used which also enhances the dynamic response of the system. However, increases to switching frequency are limited due to switching device availability (and cost), and also because high frequency operation increases switching losses considerably [47].

Hard-switched PWM DC-DC converters such as the boost converter play an important role in renewable energy systems. Research to increase their efficiency at high operating frequencies is important and can be achieved using soft-switching techniques; however, that approach requires an auxiliary circuit [7, 29-34]. The auxiliary circuit decreases power density and reliability while increasing the cost. Moreover, soft-switching topologies usually cannot

improve the efficiency for all power and voltage ranges. Wide bandgap (WBG) devices, such as gallium nitride (GaN), result in lower switching losses than silicon (Si), can be used to enhance the efficiency while retaining the simple structure of a hard-switched topology [13]. However, the high cost of these devices is problematic for what are frequently cost-sensitive applications and they cannot eliminate switching losses completely.

Given these isolated studies, we aim to answer the important question they raise: in general, are Si-based soft switching DC-DC converters more efficient and more convenient than WBG-based hard switched DC-DC converters, or is the reverse true? For completeness and to set benchmarks, we also investigate WBG-based soft-switched converters and Si-based hard-switched converters. For a comparison to be meaningful, all four options must use modern, high-performance devices. The super junction (SJ) Si MOSFET has good performance in terms of conduction and switching losses and we therefore compare it to WBG-based switches.

In this Chapter, the performance of four prototypes including two soft-switched and two hard-switched converters, each with either state-of-the-art Si MOSFETs or GaN HEMTs are investigated in terms of efficiency, power density, and cost. The topologies are based on the boost converter, which is one of the most ubiquitous step-up DC-DC converters available. It is chosen because of its simple structure and very low ripple input current which is necessary in renewable energy applications.

The results of this comparison are accurate for power levels of a few hundred watts and voltage levels of a few hundred volts. An exemplary application for this power and voltage range could be AC-photovoltaic modules [155, 156].

As two exemplary candidates of wide-bandgap devices, SiC MOSFETs and GaN HEMTs are regarded as the successors of Si devices in the medium-to-high-voltage (>1200 V) and low-

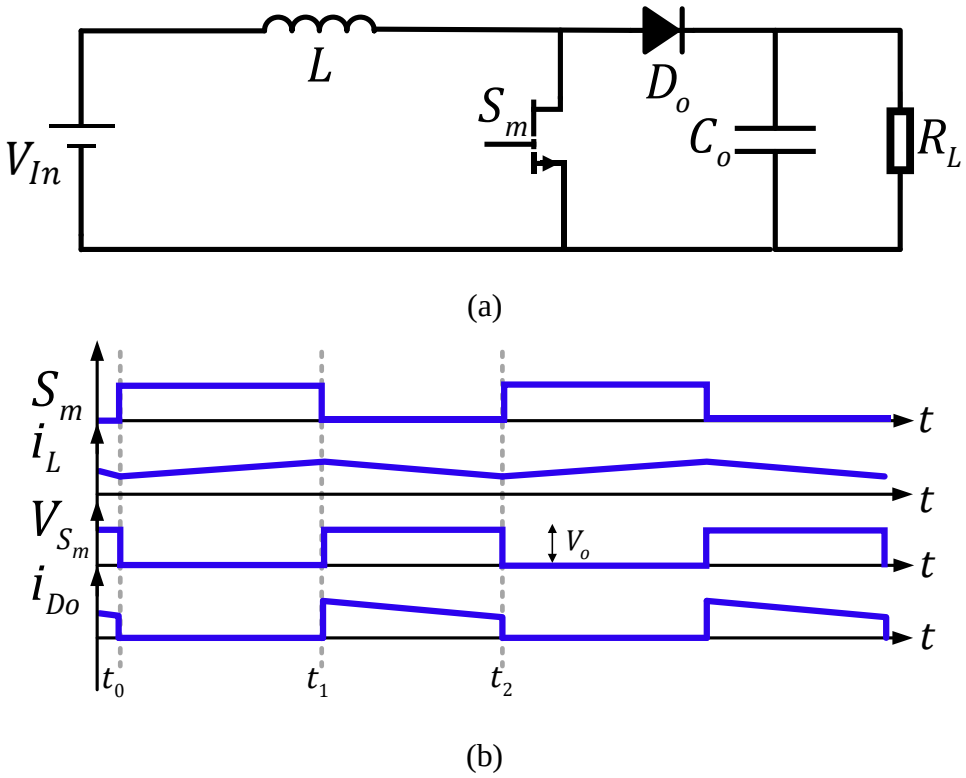

Fig. 4.1 Boost converter. (a) Schematic. (b) Key waveforms.

voltage (<650 V) domains, respectively [83]. Hence, since the voltage ranges of power switches for the designed converters is low in this work, GaN HEMT is used as WBG switch.

4.2 DC-DC converters

4.2.1 Conventional boost converter

The conventional boost converter, shown in **Fig. 4.1(a)**, is used as the benchmark of the study. It should be noted that the underlying principles which will be applied are ultimately generic and can be applied to a wide variety of DC-DC converter topologies.

The operation of the boost converter in continuous conduction mode (CCM) is investigated in [157] and the key waveforms over two switching periods are presented in **Fig. 4.1(b)**. The boost converter has two operating intervals in each switching period. In the first interval, the main switch S_{m} is turned on and the output diode D_{o} is off; thus, the boost inductor, L, is charged by the input source. The second interval starts when S_{m} is turned off and the output diode D_{o} turns on: the energy stored in the boost inductor is discharged to the output through diode D_{o}.

According to [157], the voltage gain and minimum inductance value of the boost converter in CCM operation can be calculated as (4-1) and (4-2), respectively.

$$M = \frac{V_{\mathrm{o}}}{V_{\mathrm{In}}} = \frac{1}{1-D} \tag{4-1}$$

$$L_{\min} = \frac{D(1-D)^2 V_{\mathrm{o}}^2}{2 f_{\mathrm{s}} P_{\mathrm{o}}} \tag{4-2}$$

where V_{In} and V_{o} are input and output voltages, respectively; D is the duty ratio; f_{s} is the switching frequency; and P_{o} is the output power. The inductor peak-to-peak ripple current Δi_{L} can be obtained as

$$\Delta i_{\mathrm{L}} = \frac{D V_{\mathrm{In}}}{f_{\mathrm{s}} L} \tag{4-3}$$

Similarly, peak-to-peak ripple of the output voltage can be obtained by (4-4). In (4-4), C_{o} is the output capacitance.

$$\Delta V_{\mathrm{o}} = \frac{D P_{\mathrm{o}}}{V_{\mathrm{o}} C_{\mathrm{o}} f_{\mathrm{s}}} \tag{4-4}$$

The voltage stress (i.e., peak drain-source voltage) of the main switch is equal to the output voltage. The currents through the main switch at the start of the turn-on ($t = t_0$) and turn-off ($t = t_0 + \mathrm{DT_s}$) events are given by (4-5) and (4-6), respectively. I_{In} is the average of the input current.

$$I_{\mathrm{S_m(t=t_0)}} = I_{\mathrm{In}} - \frac{\Delta i_{\mathrm{L}}}{2} \tag{4-5}$$

$$I_{\mathrm{S_m(t=t_0+DT_s)}} = I_{\mathrm{In}} + \frac{\Delta i_{\mathrm{L}}}{2} \tag{4-6}$$

Assuming $I_{\mathrm{In}} \gg \Delta i_{\mathrm{L}}$, the root-mean-square (RMS) current of the main switch can be calculated as follows:-

$$I_{\mathrm{S_{m.b(rms)}}} = I_{\mathrm{In}}\sqrt{D} \tag{4-7}$$

The average and RMS current of the output diode can be expressed as (4-8) and (4-9), respectively.

$$I_{\mathrm{D_o(avg)}} = I_{\mathrm{In}}(1-D) \tag{4-8}$$

$$I_{\mathrm{D_o(rms)}} = I_{\mathrm{In}}\sqrt{(1-D)} \tag{4-9}$$

4.2.2 Soft-Switched boost converter

Table 4.1 presents some well-known soft-switched boost converters against which a comparison could be made. In this Chapter, the soft-switched boost converter proposed in [30] is selected for analysis because, in the authors' opinion, it is well-presented and has a number of useful features. Both turn-on and turn-off are soft for both switches. In addition, the conduction losses from the auxiliary circuit are lower than its rivals. Furthermore, it requires the fewest components, reducing complexity and cost. Its topology and key waveforms are presented in **Fig. 4.2(a)** and **(b)**, respectively.

It is worth noting that there are many other soft-switched converters based on the boost converter. However, in order for the comparison made to be fair, it is important that their circuit topology does not differ significantly from the traditional boost converter. For example, there are many high-gain (and-high order) boost converters, with and without soft-switching capability, which have plentiful applications and frequently higher efficiency as a result of lower conduction loss because, for a given power rating, their switch currents are lower. However, such a converter is not comparable to the traditional boost converter. In this study, the comparison is made with the converter in [30], so that the only advantage achieved relates to reduced switching loss as a result of the soft switching.

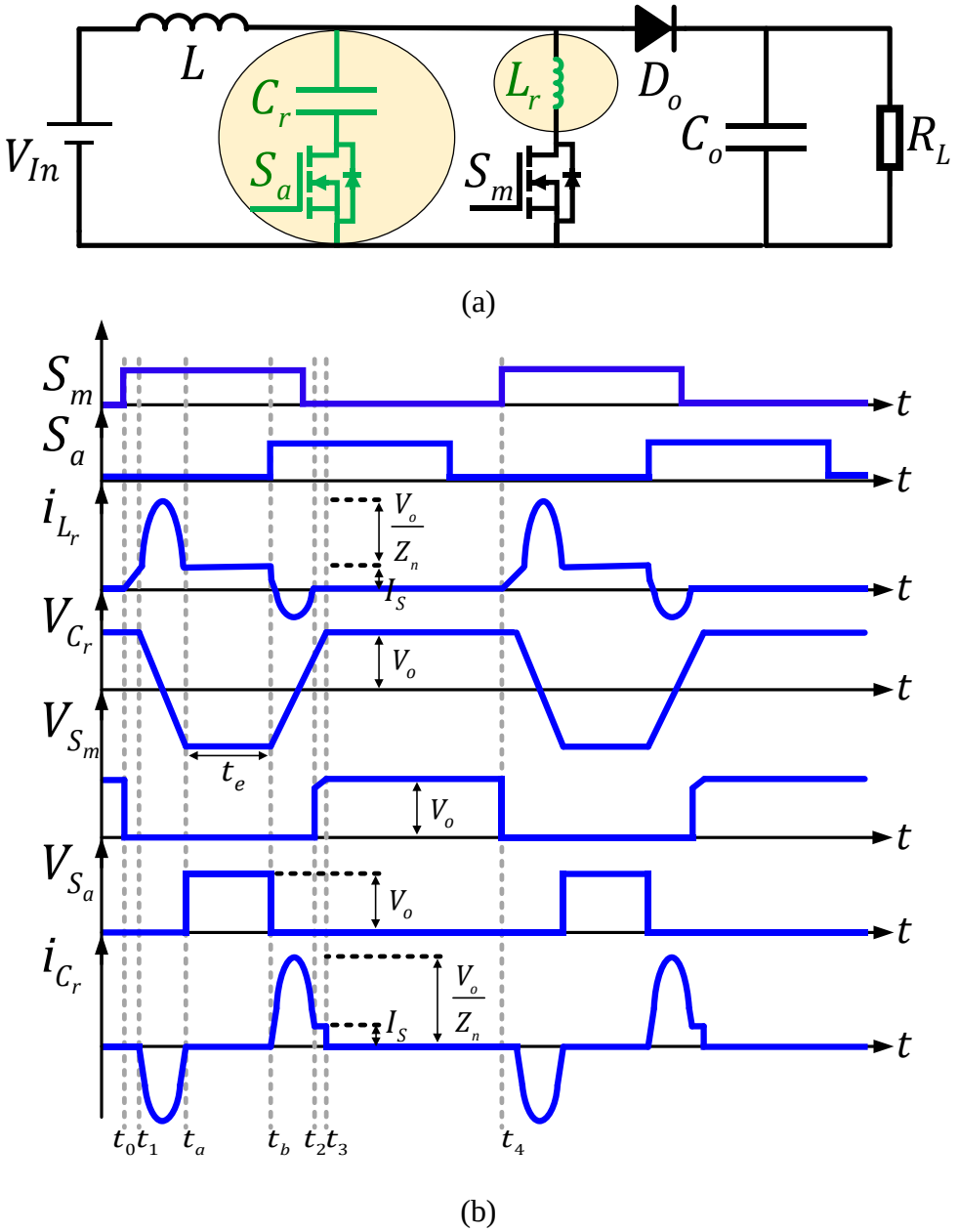

Fig. 4.2 Soft-switched boost converter introduced in [30]. (a) Schematic with differences from boost converter highlighted. (b) Key waveforms adapted from [30].

The detailed operation of the chosen converter is described comprehensively in [30]; only an overview is provided in this Chapter. As shown in **Fig. 4.2(a)**, auxiliary components consisting of a resonant inductor L_r, a resonant capacitor C_r, and an auxiliary switch S_a are added to the conventional structure of a boost converter.

Table 4.1 Comparison of well-known soft-switched boost converters.

Ref.	Main switch		Auxiliary switch		
	Turn on	Turn off	Turn on	Turn off	Conduction losses
[30]	Soft	Soft	Soft	Soft	Low
[31]	Hard	Soft	-	-	High
[32]	Soft	Hard	Soft	Hard	High
[33]	Soft	Hard	Hard	Soft	High
Ref.	Number of auxiliary diodes	Number of auxiliary inductors	Number of auxiliary capacitors	Number of auxiliary switches	Common ground for switches
[30]	0	1	1	1	Yes
[31]	5	2	2	0	-
[32]	0	1	1	2	No
[33]	3	1	1	1	Yes

The converter has six operation intervals. The main switch, S_{m}, is turned on at the zero crossing of the switch current (i.e. zero-current switched, ZCS) because it is in series with the resonant inductor L_{r} and it is turned off at zero crossing of the drain-source voltage (i.e. zero-voltage switched, ZVS) while the switch current flows through the antiparallel diode. The auxiliary switch, S_{a}, is turned on at the ZCS condition because of the presence of the resonant inductor L_{r} and boost inductor L and it is turned off at the ZVS condition after the voltage of the resonant capacitor C_{r} reaches the output voltage.

The relationships between the voltage gain, minimum inductance value, inductor current ripple, output voltage ripple, and the average and RMS current of the output diode in this converter are similar to the relationships of the conventional boost converter. However, the RMS current of the main switch is given by (4-10). The RMS current of the auxiliary switch and its body diode can be calculated by (4-11); the average current of the auxiliary switch body diode alone

is given by (4-12). It is worth mentioning that the average current of the body diode of the main switch is negligible since its current amplitude and turn-on time duration are very low.

$$I_{\mathrm{S_{m.sb}(rms)}} \simeq \sqrt{DI_{\mathrm{In}}^2 + \left(\frac{V_o}{2Z_{\mathrm{n}}\sqrt{f_{\mathrm{r}}/f_{\mathrm{s}}}}\right)^2} \tag{4-10}$$

$$I_{\mathrm{S_{a.sb}(rms)}} \simeq I_{\mathrm{D_{a.sb}(rms)}} = \frac{V_o}{2Z_{\mathrm{n}}\sqrt{f_r/f_{\mathrm{s}}}} \tag{4-11}$$

$$I_{\mathrm{D_{a.sb}(avg)}} = \frac{V_{\mathrm{o}}}{\pi Z_{\mathrm{n}} f_r/f_s} \tag{4-12}$$

In (4-10)-(4-12), subscript m is for main, a is for auxiliary, S is for switch, D is for diode and sb is for soft-switched boost converter, and Z_{n} is defined as $\sqrt{L_{\mathrm{r}}/C_{\mathrm{r}}}$ and f_{r} is the resonance frequency, $1/(2\pi\sqrt{L_{\mathrm{r}}C_{\mathrm{r}}})$. According to (4-11) and (4-12), the average and RMS currents of the auxiliary components are independent the output power. In addition, the resonant period, T_{r}, $(= 2\pi\sqrt{L_{\mathrm{r}}C_{\mathrm{r}}})$ is independent the switching frequency.

4.2.3 Design characteristics of the prototypes

The conventional and soft-switched boost converters can be designed according to the methods proposed in [30, 157], and, for brevity, the design considerations of these converters are not presented in this Chapter. Using the relationships provided in [30, 157], four prototypes including two hard-switched and two soft-switched boost topologies were designed and their specifications are presented in **Table 4.2**.

Prototypes 1 and 2 are two conventional hard-switched boost converters while prototypes 3 and 4 are soft-switched boost converters. Meanwhile, prototypes 1 and 3 use Si SJ MOSFETs while prototypes 2 and 4 use GaN HEMTs. All prototypes use a state-of-the-art low-loss SiC Schottky diode for D_{o}. To the extent possible, the rated voltage and current of all devices are similar, and each device is state-of-the-art in its category, to provide a realistic comparison.

Table 4.2 Parameters of prototypes 1-4.

Proto-type	Output power	Input voltage	Output voltage	Switching frequency	Boost Inductor	Resonant Inductor
1	500 W	100 V	400 V	200 kHz	375 µH	-
2	500 W	100 V	400 V	200 kHz	375 µH	-
3	500 W	100 V	400 V	200 kHz	375 µH	2 µH
4	500 W	100 V	400 V	200 kHz	375 µH	2 µH

Proto-type	Output Capacitor	Resonant capacitor	Switch	Diode
1	4.7 µF	-	IPW65R150CFDA	SCS220AG
2	4.7 µF	-	GS66506T	SCS220AG
3	4.7 µF	9.1 nF	IPW65R150CFDA	SCS220AG
4	4.7 µF	9.1 nF	GS66506T	SCS220AG

This research was conducted in January 2020, and it is possible that new semiconductor devices with similar or better characteristics and performance might become available in the future.

4.3 Comparison

In this section, the prototypes are compared and evaluated in terms of efficiency, power density and cost using simulation results and theoretical analysis.

4.3.1 Power loss analysis

The relationship in (4-13) is used for efficiency calculation. The losses of the components are obtained based on the losses calculation procedure presented in [3, 158].

$$\eta = \frac{P_{\mathrm{o}}}{P_{\mathrm{o}} + P_{\mathrm{Loss}}} \tag{4-13}$$

In considering the power losses of each converter, the switch losses ($\sum P_{\text{Loss}}^{\text{S}}$), diode losses ($\sum P_{\text{Loss}}^{\text{D}}$), capacitor losses ($\sum P_{\text{Loss}}^{\text{C}}$), and inductor losses ($\sum P_{\text{Loss}}^{\text{L}}$) are considered. The power losses of a converter can be obtained by (4-14).

$$P_{\text{Loss}} = \sum P_{\text{Loss}}^{\text{S}} + \sum P_{\text{Loss}}^{\text{D}} + \sum P_{\text{Loss}}^{\text{C}} + \sum P_{\text{Loss}}^{\text{L}} \tag{4-14}$$

The losses from the diodes can be obtained from (4-15), where V_{f} and R_{D} are the forward voltage drop and series resistances of the diodes, respectively and $I_{\text{D(avg)}}$ and $I_{\text{D(rms)}}$ are average and RMS currents of the diodes, respectively. To simplify the analysis, reverse recovery losses associated with D_{o} are neglected since they have negligible influence on the power losses when a SiC Schottky diode is used [159].

$$P_{\text{Loss}}^{\text{D}} = R_{\text{D}} I_{\text{D(rms)}}^2 + V_{\text{f}} I_{\text{D(avg)}} \tag{4-15}$$

The power losses of the switches ($P_{\text{Loss}}^{\text{S}}$) can be calculated by (4-16).

$$P_{\text{Loss}}^{\text{S}} = P_{\text{Loss}}^{\text{S,switching}} + P_{\text{Loss}}^{\text{S,conduction}} + P_{\text{Loss}}^{\text{S,gate}} \tag{4-16}$$

The power losses of the switches include three terms. The first term is switching losses which can be calculated from (4-17). In this equation, ΔV_{ds} is the change in drain-source voltage, $t_{\text{on.s}}$ is the current rise time plus voltage fall time, and $t_{\text{off.s}}$ is the current fall time plus voltage rise time.

$$P_{\text{Loss}}^{\text{S,switching}} = \frac{1}{2} \Delta V_{\text{ds}} (I_{\text{S}_{\text{m}}(\text{t}=t_0)} t_{\text{on.s}} + I_{\text{S}_{\text{m}}(\text{t}=t_0+\text{DT}_{\text{s}})} t_{\text{off.s}}) f_{\text{s}} \tag{4-17}$$

The second term is the conduction losses. These losses occur in the switch channel when the current is positive, and in the body diode when the current is negative. The conduction losses of switches can be calculated as (4-18).

$$P_{\text{Loss}}^{\text{S,conduction}} = R_{\text{ds(on)}} I_{\text{ds(rms,}i_{\text{ds}}>0)}^2 + P_{\text{Loss}(i_{\text{ds}}<0)}^{D} \quad (4\text{-}18)$$

where $R_{\text{ds(on)}}$ is the on-state resistance of the power switches, $I_{\text{ds(rms,}i_{\text{ds}}>0)}$ is the RMS current of the power switch when the drain current is positive, and $P_{\text{Loss}(i_{\text{ds}}<0)}^{\text{D}}$ is losses of its antiparallel diode when drain current is negative.

The third term is the gate drive losses which depends on total input gate charge of the switch Q_{g}, switching frequency f_{s}, and the voltage applied to the gate driver V_{gg} and can be calculated according to (4-19).

$$P_{\text{Loss}}^{\text{S,gate}} = f_{\text{s}} V_{\text{gg}} Q_{\text{g}} \quad (4\text{-}19)$$

The losses of the capacitors due to their equivalent series resistances (r_{C}) can be calculated by the following relationship where $I_{\text{C(rms)}}$ is the RMS current through the capacitor.

$$P_{\text{Loss}}^{\text{C}} = r_{\text{C}} I_{\text{C(rms)}}^2 \quad (4\text{-}20)$$

Losses in the inductors result from ohmic ($P_{\text{Loss}}^{\text{L,ohmic}}$) and core losses. The ohmic losses of the inductors can be calculated as (4-21).

$$P_{\text{Loss}}^{\text{L,ohmic}} = r_{\text{L}} I_{\text{L(rms)}}^2 \quad (4\text{-}21)$$

where, $I_{\text{L(rms)}}$ is the RMS current of the inductor and r_{L} is the equivalent series resistance of the inductor. Inductors also suffer eddy-current and hysteresis loss, which depend on the type of core and ripple of flux density and can be calculated from datasheet.

The simulated efficiency curves for each of the considered topologies is shown versus output power and switching frequency in **Fig. 4.3 (a)** and **(b)**, respectively. To obtain the losses accurately, all designed converters have been simulated in similar operating conditions indicated in **Table 4.2**. Since inductor design has a large influence on cost, volume and efficiency, the inductor was optimised for each switching frequency. Each design uses a

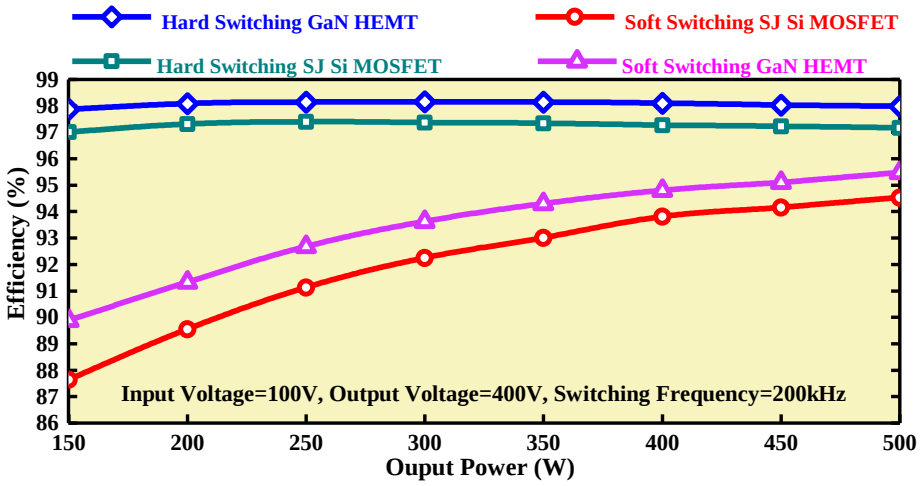

(a)

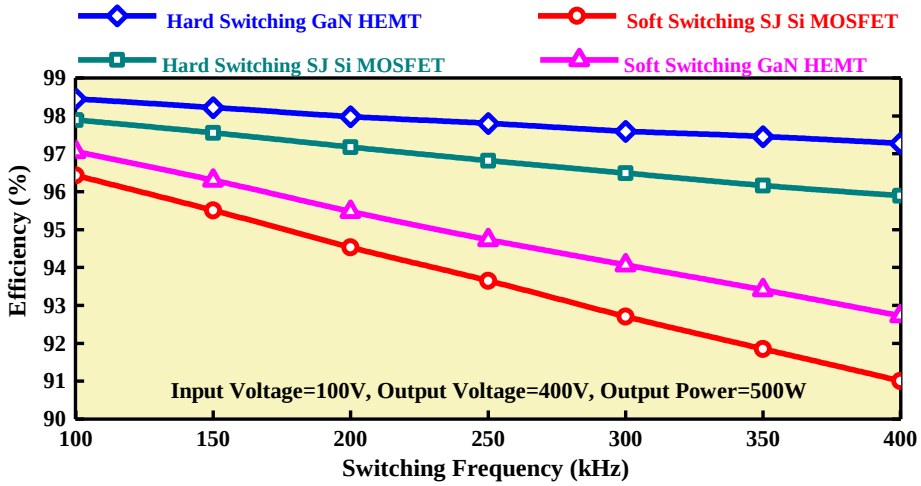

(b)

Fig. 4.3 Efficiency comparison. (a) For different output powers. (b) For different switching frequencies at nominal specifications. Case Temperature T_c =25°C, r_{C_o}=15 mΩ, r_{C_r}=15 mΩ, Powder Core (T157-8), r_L=60 mΩ, Δi_L=1 A, r_{L_r} =10 mΩ.

powder core and the design process and core selection was performed using the procedure laid out in [160], and the closest commercially available option was chosen.

In addition, the simulation is conducted in MATLAB/Simulink to obtain the voltage and currents required for the loss modelling presented in equations (4-15) to (4-21). Then, using the parasitic resistance, capacitance, and inductance values of components, which can be obtained from their datasheet (presented in **Fig. 4.3**'s caption), the power loss in each

component is calculated. Finally, the efficiency of each converter can be determined using equations (4-13) to (4-15).

The power losses and efficiencies are calculated for each data point using data provided in the components' datasheets. The DC losses of the inductors are calculated using (4-21), while their core losses are determined based on the method outlined in their datasheet [160]. Moreover, the AC losses are neglected in this analysis. The use of litz wire for winding the inductors provides reasonable accuracy for this assumption. Since only the current and voltage of the components were required, a SPICE-type model was unnecessary.

As shown in **Fig. 4.3(a)**, prototype 2, the hard-switched boost converter in which the GaN HEMT switch was used, provides the highest efficiency while prototype 1, the SJ Si-based hard-switched boost converter is ranked second. However, the soft-switched boost converters (prototypes 4 and 3), which are based on GaN HEMT and SJ Si MOSFET, are surprisingly ranked third and fourth, respectively.

Since prototype 4 uses GaN switches with lower on-resistance, it has a better efficiency compared to prototype 3. To explain why, perhaps counterintuitively, the efficiency of the hard-switched boost converter is higher than its soft-switched equivalent even though both use similar semiconductors, we consider the following:-

1) In high-gain and high-power DC-DC converters, conduction losses are usually the dominant losses. Therefore, in this case, since the power and input current of the converters are large, the influence of the switching losses is lower than the conduction losses.
2) The higher the input current, the more conduction losses there are in the auxiliary components because the resonant current should be able to reduce the main switch current to zero. Hence, even though this soft-switched converter has low conduction losses at low power and low gain applications, its conduction losses at high gain and high power applications are higher than a comparable hard-switched converter.
3) There is a resonant inductor in the auxiliary circuit which suffers significant core loss at high frequency and high current ripple.

It is worth noting that the parasitic capacitances of the high-voltage-rated (>400V) switches and diodes are about ten times higher under very low drain-source voltage (<10V) that at rated voltage. Therefore, in soft-switched converters in which switches and diodes are switched under ZVS conditions, the parasitic capacitances are high, in the nanofarad range [161]. The parasitic capacitances of the semiconductors, PCB tracks and passive components usually cause high frequency voltage oscillation across the semiconductor devices of the converter. In very low voltage converters (<50V), the amplitude of this oscillation is also low; however, it becomes significant at high voltage, which increases the losses of the converter, especially core losses.

To show the effect of high parasitic capacitance on the operation of the converter, the simulation results for the voltage and current of the switches in the soft-switched converter with Si SJ MOSFETs (prototype 3, presented in **Table 4.2**) when the components are ideal and non-ideal are shown in **Fig. 4.4** and **Fig. 4.5**, respectively. As shown in these figures, the parasitic elements have a noticeable influence on the circuit operation and hence efficiency in the high power and voltage ranges.

According to (4-11) and (4-12), since the resonant current is relatively load-independent and its losses are near-constant from low power to high power, the efficiency of the soft-switched converter decreases at light power. Hence, the soft-switched topology can only provide high efficiency at nominal load condition. Accordingly, in PV systems and other applications where input or load variation is considerable and hence operation is far away from the nominal design, boost converters featuring auxiliary circuits have reduced suitability due to the detrimental effects of currents circulating in their auxiliary branch.

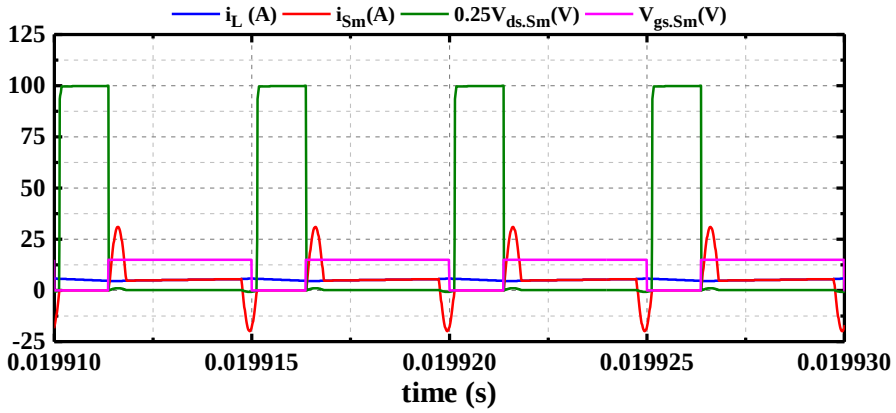

(a)

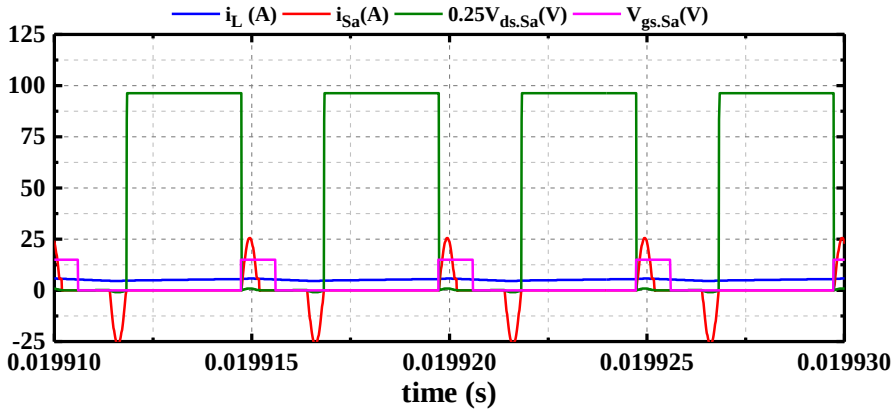

(b)

Fig. 4.4 Simulation results of the ideal soft-switched boost converter. (a) i_{L}, $i_{\mathrm{S_m}}$, $V_{\mathrm{ds.S_m}}$, $V_{\mathrm{gs.S_m}}$. (b) i_{L}, $i_{\mathrm{S_a}}$, $V_{\mathrm{ds.S_a}}$, $V_{\mathrm{gs.S_a}}$.

The efficiency of the GaN-based hard-switched converter (prototype 2) is higher than SJ Si-based hard-switched converter (prototype 1), not only because the GaN switch has lower switching losses, but also because the switch benefits from lower conduction losses due to lower on-state resistance. Since the GaN-based hard-switched converter does not have any auxiliary circuits its efficiency does not decrease at low powers, but actually increases due to lower conduction losses. Hence, this converter is suitable for renewable energy applications such as AC-PV module systems.

In **Fig. 4.3(b)**, the simulated efficiency of the each considered topology operated at different switching frequencies at nominal specifications are presented. The efficiency of the hard-switched topologies decreases with higher switching frequency as expected. In addition,

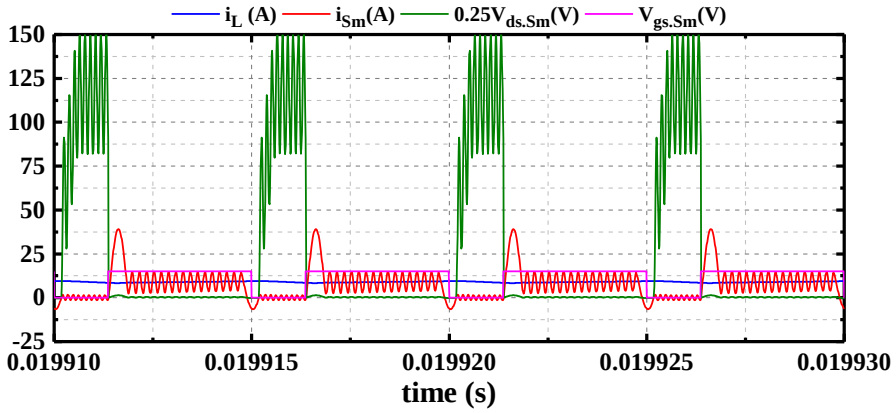

(a)

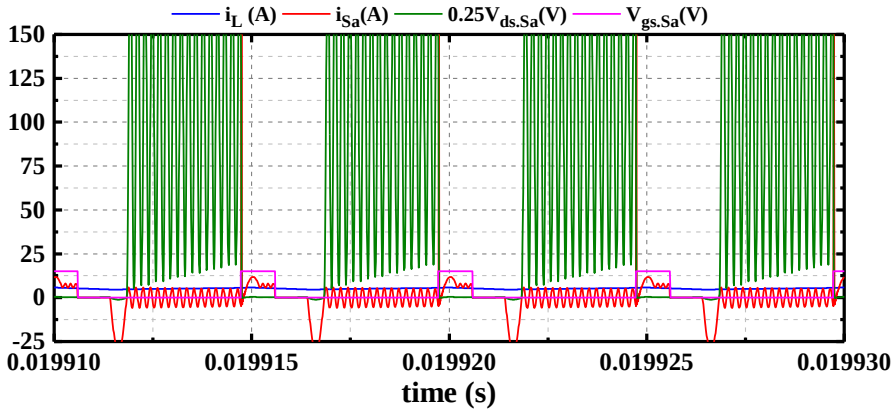

(b)

Fig. 4.5 Simulation results of the non-ideal soft-switched boost converter. (a) i_{L}, $i_{\mathrm{S_m}}$, $V_{\mathrm{ds.S_m}}$, $V_{\mathrm{gs.S_m}}$. (b) i_{L}, $i_{\mathrm{S_a}}$, $V_{\mathrm{ds.S_a}}$, $V_{\mathrm{gs.S_a}}$.

because the GaN-based switches have a reduced switching loss compared to Si-based switches, the difference in efficiency between GaN-based and Si-based hard-switched converters increases as the switching frequency increases. For example, at 100 kHz, the difference is 0.5% while it is 1% at 400 kHz.

One might predict that the influence of switching frequency is lower for soft-switched converters. However, for the aforementioned reasons, the dominant losses in microinverter applications are conduction losses, and, since the resonant period is switching frequency-independent and does not decrease with switching period, the conduction losses in the auxiliary components increase at higher switching frequency. In addition, the core loss of the resonant inductor increases noticeably as the switching frequency increases.

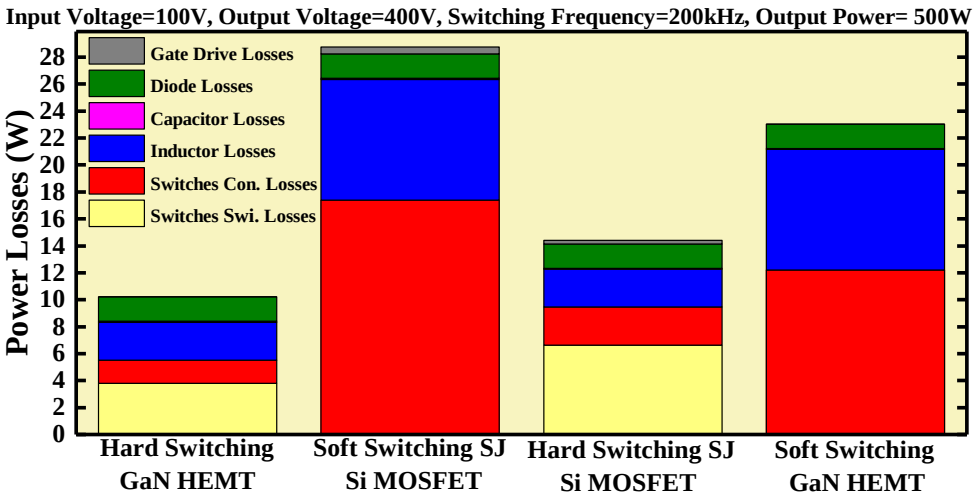

Fig. 4.6 Loss distribution of the converters. T_c =25°C, r_{C_o}=15 mΩ, r_{C_r}=15 mΩ, Powder Core (T157-8), r_L=60 mΩ, Δi_L=1 A, r_{L_r} =10 mΩ.

The loss distributions of all the prototypes at nominal specifications are illustrated in **Fig. 4.6**. It can be observed that the Si-based hard-switched converters have the highest switching losses; the switching losses of the soft-switched converters are negligible. However, the soft-switched converters suffer from higher conduction and core losses since they have auxiliary switch, capacitor, and inductor. In spite of low value of the resonant inductor, it has high core losses because it is in series with the main switch which experiences a high current ripple.

Although the soft-switched converter has lower switching losses than a hard-switched converter which uses a state-of-the-art power switch, it has lower efficiency and it cannot provide high efficiency for light load ranges. Therefore, on efficiency alone, the GaN-based hard-switched converter is a better choice for applications in which the power is not constant and varies.

4.3.2 Power density analysis

In this section, the volume of the components used in implementation of the converters, including capacitors, inductors, switches, diodes, gate drivers and heatsinks are compared. In order to simplify the analysis, the volume of control system and PCB layout are not considered.

In order to provide a fair comparison, the design power of each of the converters is 500 W. The volumes, which will be presented in **Fig. 4.7(a)**, are therefore inversely proportional to the power density and are themselves an indication of performance.

The following relationship is used to calculate the minimum thermal resistance of the required heatsink, R_{sa}, for each device.

$$R_{\mathrm{sa}} = \left[\frac{T_{\mathrm{j}} - T_{\mathrm{a}}}{P_{\mathrm{d}}} - R_{\mathrm{jc}} - R_{\mathrm{cs}}\right] \tag{4-22}$$

where, P_{d} represents the losses of the device, T_{a} is ambient temperature (assumed in this work to be 25°C), T_{j} is junction temperature, R_{jc} is junction-to-case thermal resistance, and R_{cs} is the case-to-heatsink thermal resistance. In cases where no heatsink is required, the junction temperature of the device can be calculated from (4-23).

$$T_{\mathrm{j}} = P_{\mathrm{d}} R_{\mathrm{ja}} + T_{\mathrm{a}} \tag{4-23}$$

In this equation, R_{ja} is junction to ambient thermal resistance. Assuming the use of SIL PAD TSP 1800ST insulating pad [162], the case-to-heatsink thermal resistance R_{cs} for the output diode, GaN HEMT and SJ Si MOSFET are 1.6, 8.6, and 0.57 W/°C, respectively. Note that, since the GaN HEMT switch has the smallest contact area, its case-to-heatsink thermal resistance is the largest. The losses of the output diode in all prototypes at nominal specifications are around 1.8 W therefore, according to (4-23) the output diode does not require a heatsink since its junction temperature does not exceed the maximum tolerable value. However, it might need a heatsink in higher power ranges ($P_{\mathrm{o}} > 500W$). The values of R_{jc} and T_{j} for all semiconductors are given in their datasheets. The power losses of the main switch in the Si MOSFET-based and GaN HEMT-based hard-switched boost converters at nominal

specifications are 9.4 W and 5.5 W, respectively. According to (4-22), the main switches of GaN-based and Si-based hard-switched topologies each need a heatsink with R_{sa} lower than 13.4 W/°C and 11 W/°C, respectively. Therefore, the Fischer Electronic SK 55275AL and SK 55250AL heatsinks are selected for the main switches of the prototypes 1 and 2, respectively. In prototype 3, the losses of the main and auxiliary switches at nominal conditions are about 10.6 and 6.8 W, respectively. Hence, since the main and auxiliary switches need a heatsink with R_{sa} lower than 9.5 and 16.4 W/°C, respectively, the Fischer Electronic SK 55275AL and SK 55225AL heatsinks are selected for the main and auxiliary switches, respectively. Finally, the losses of the main and auxiliary switches in prototype 4 are 6.9 and 5.3 W, respectively. Thus, since the main and auxiliary switches need heatsink with R_{sa} lower than 8.8 and 14.3 W/°C, respectively, the Fischer Electronic SK 552100AL and SK 55237.5AL heatsinks are selected for the main and auxiliary switches, respectively.

The volume and power density of all the converters are compared in **Fig. 4.7(a)** and **(b)**, respectively. Soft-switched boost converters have the larger volume. The volume of their control system and PCB layout are larger, however, even without considering them, the hard-switched converters still have lower volume than the soft-switched topologies. As shown in **Fig. 4.7(a)**, the GaN-based hard-switched converter (prototype 2) is the smallest converter. Despite the higher case-to-heatsink thermal resistance of the GaN HEMT compared to the SJ Si MOSFET, it requires a smaller heatsink since it has far lower losses. However, in the soft-switched prototypes, the GaN-based topology (prototype 4) needs a larger heatsink than the Si-based topology (prototype 3) because the difference between the switch losses are small.

The GaN HEMT-based hard-switched boost converter thus has a better power density than the SJ Si MOSFET-based soft switching boost converter. It is therefore a better choice for AC-PV module applications in which a DC-DC converter is needed for each PV module.

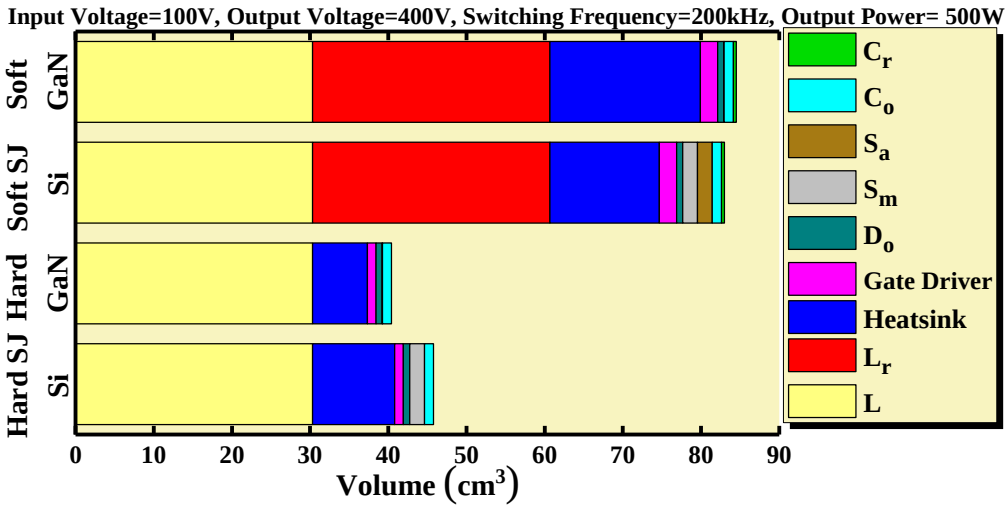

(a)

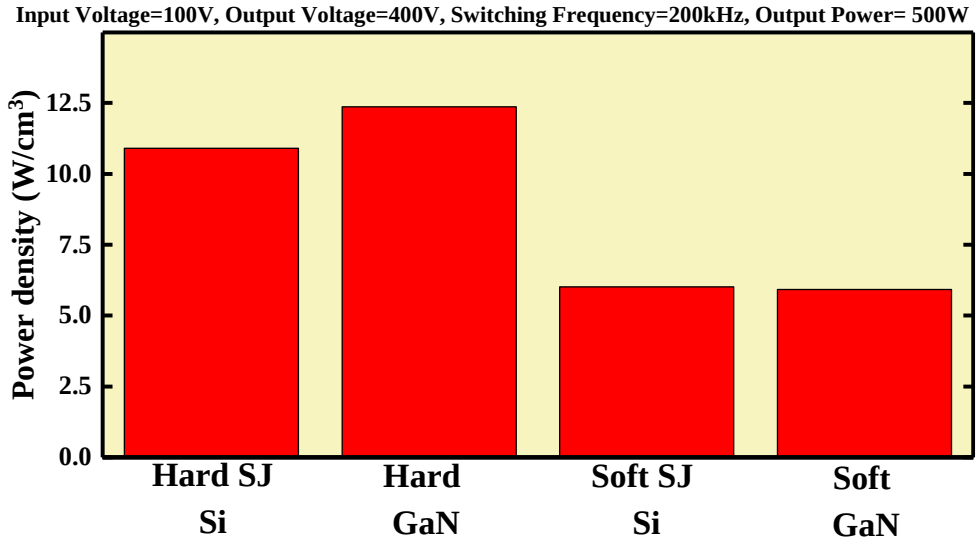

(b)

Fig. 4.7 Comparison between all prototypes. (a) Volume. (b) Power density. L=L_r=T157-8, C_o= KEMET ESH475M450AH2AA, C_r= WIMA FKP2J014701I00HSSD.

4.3.3 Cost analysis

In this section, the costs of the all prototypes are evaluated based on the average price of their components in the main international distributors of electronic components [163-165].

According to the components used in power density subsection, the cost of all components and converters are presented in **Table 4.3** and **Fig. 4.8**, respectively. It has to be mentioned that this analysis is provided in January 2020, and these prices may have changed since. Power

switches, capacitors, inductors, gate drivers, heatsinks, and diodes are considered, and to simplify the analysis, the cost of PCB, inductor winding and control system are neglected. As shown in the **Fig. 4.8**, the GaN HEMT-based hard-switched converter (prototype 2) is £10.57 more expensive than SJ Si MOSFET-based hard-switched converter (prototype 1). However, even though GaN switches are far more expensive than SJ Si switches, the GaN HEMT-based hard-switched converter is still cheaper than the soft-switched converters (£3 cheaper than prototype 3 and £24 cheaper than prototype 4). It is worth noting that the technology of Si and GaN switches are not equally mature and this cost gap may close in the future. The cost of the control system and PCB layout for the soft-switched converter is likely higher than for the hard-switched converter, but even neglecting this, the cost of the GaN-based hard-switched converter is lower than the soft-switched topologies. The GaN-based hard-switched topology is therefore a better choice for renewable energy applications like AC-PV module systems in which cost is critically important. However, considering cost alone, the hard-switched topology which uses SJ Si switches is the best choice since it has the lowest cost presently.

Table 4.3 Component costs.

Component	Cost (£)	Supplier
IPW65R150CFDA	4.25	Mouser Electronics [163]
GS66506T	14.85	Mouser Electronics [163]
SCS220AG	7.86	Mouser Electronics [163]
WIMA FKP2J014701I00HSSD	0.47	Mouser Electronics [163]
SI8261BAC-C-IP	2.10	Mouser Electronics [163]
KEMET ESH475M450AH2AA	0.43	Mouser Electronics [163]
SK 55225AL	0.26	Anglialive [164]
SK 55250AL	0.42	Anglialive [164]
SK 55275AL	0.45	Anglialive [164]
SK 552100AL	0.49	Anglialive [164]
SK 55237.5AL	0.28	Anglialive [164]
T-157-8	6.5	Pace Components [165]

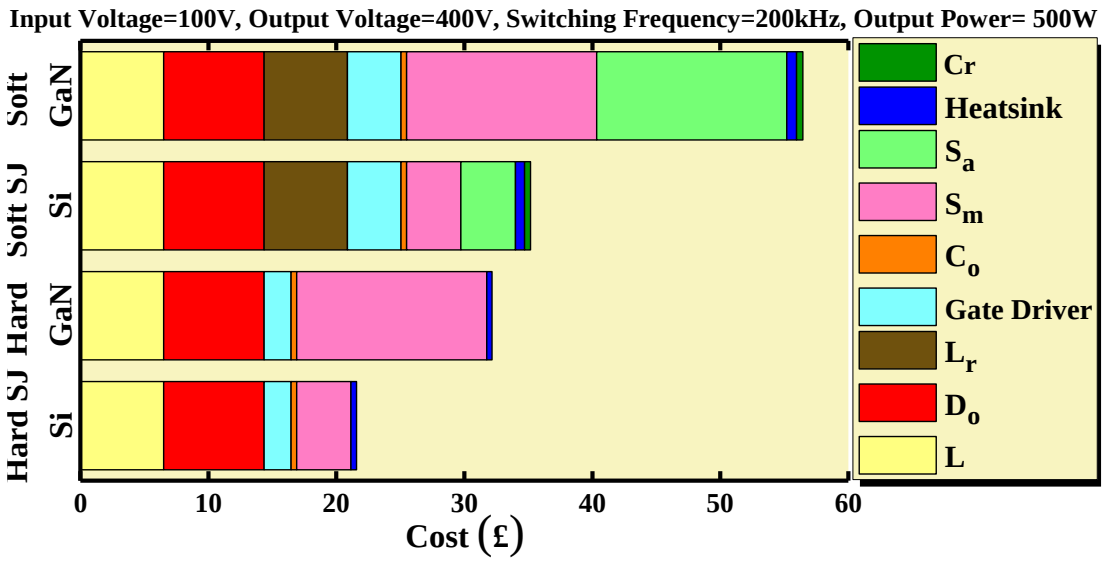

Fig. 4.8 Cost comparison for all prototypes.

4.3.4 Final remarks

According to the aforementioned results, it is clear that the GaN HEMT-based hard-switched converter has a better performance in terms of efficiency and power density compared to Si SJ MOSFET-based hard-switched topology and soft switching topologies. However, this converter is more expensive than Si SJ MOSFET-based hard-switching topology, but is less costly than either soft-switched topologies.

Finally, the results of this comparison are accurate for boost DC-DC converters with power levels of a few hundred watts and voltage levels of a few hundred volts. Therefore, changing the topology and specifications of the converter may lead to different results.

4.4 Experimental results

In order to confirm the theoretical analysis and simulation results, all four prototypes were implemented and compared using experimental results. The laboratory set-up is shown in **Fig. 4.9**. The DC link voltage is kept constant at 100 V by a DC power supply and a power analyser (Yokogawa PX8000) is used to measure the efficiency of the converters. An ARM-based microcontroller STM32F407VGTx discovery board is used to generate the gating pulses with

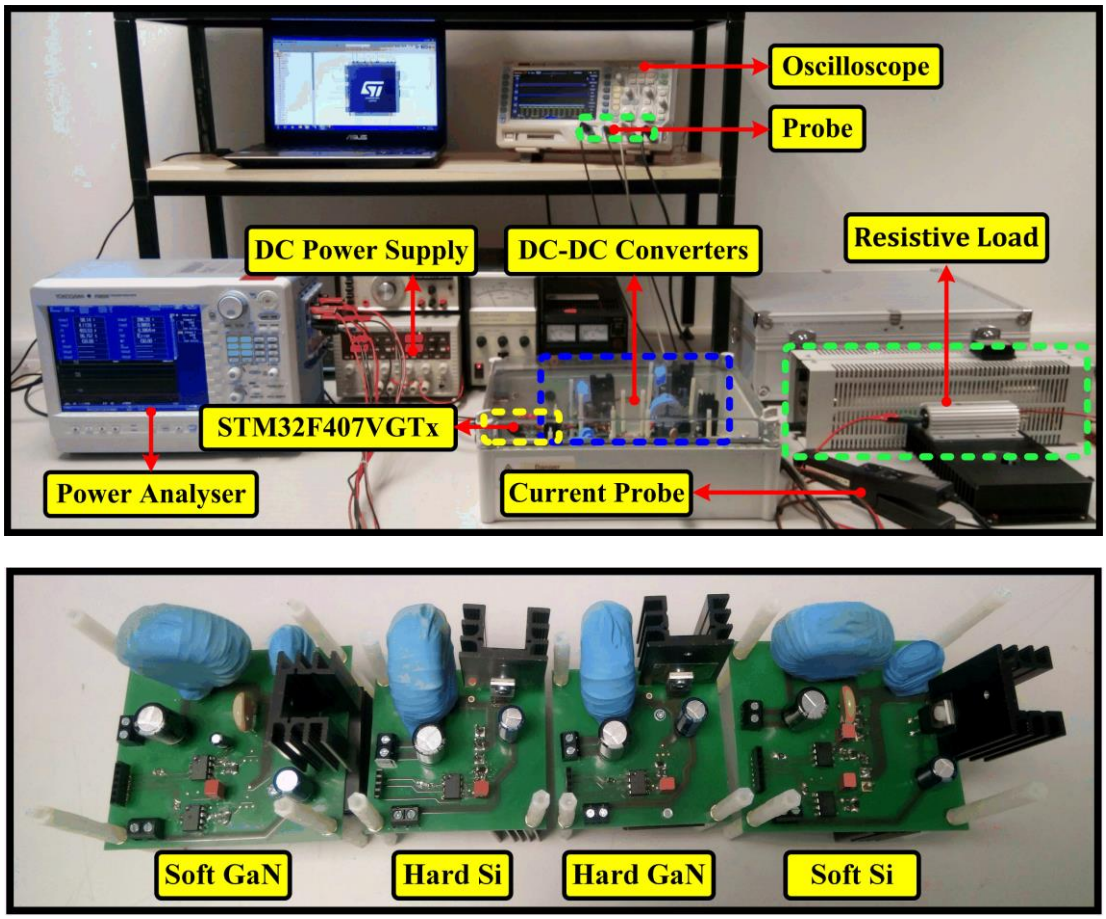

Fig. 4.9 Experimental set-up.

appropriate duty ratio for the switches of the converters. The load includes a constant resistance (150 Ω) in series with a rheostat which can be changed from 10 Ω to 1000 Ω to adjust the output power of the converters.

To maximise the performance of the converters, some of the design techniques implemented in this set-up are presented as follows. First of all, the earth tracks are placed immediately below the supply tracks on the PCB to decrease the stray magnetic flux and reduce EMI due to leakage inductance. Secondly, small film capacitors (1 μF) are placed near to the switches to create a low impedance path for the switching signals, and the gate drivers are placed as close as possible to their switches. Thirdly, the effects due to stray electric and magnetic fields are reduced by minimising the length of tracks. In addition, the heatsink is connected to the

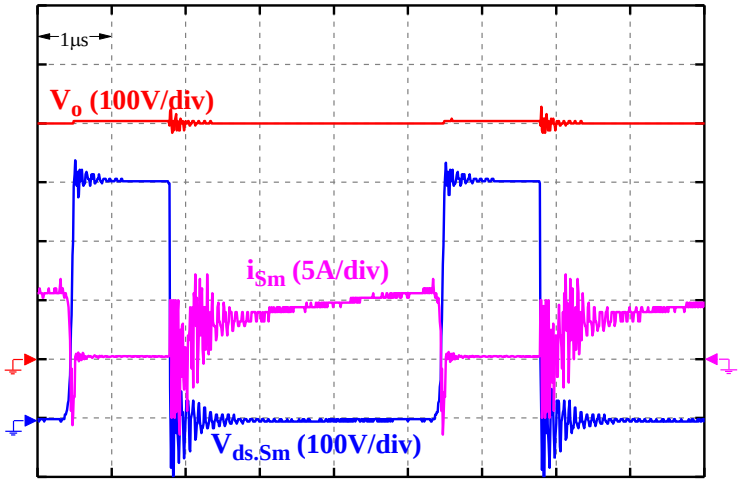

(a)

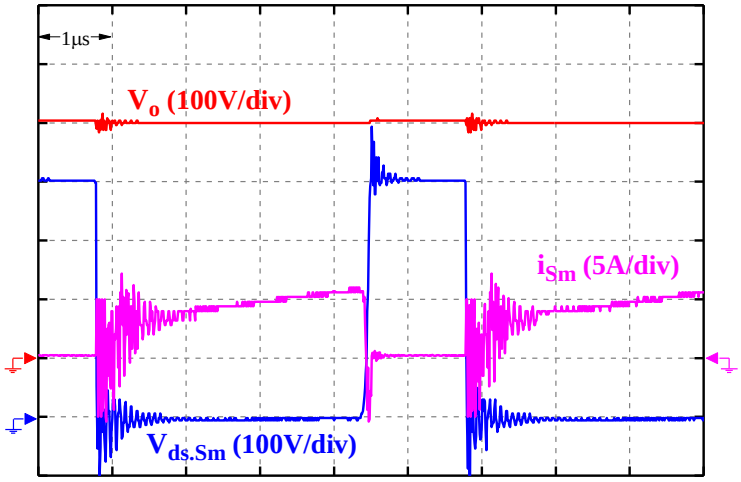

(b)

Fig. 4.10 Experimental results. V_{o}, $V_{\mathrm{ds.S_m}}$, $V_{\mathrm{gs.S_m}}$, and $i_{\mathrm{S_m}}$ in (a) prototype 1, (b) prototype 2.

underside of PCB such that it does not act as a voltage-driven antenna. Finally, the initial temperature of the heatsink was 25°C.

The output voltage, V_{o}, the drain-source voltage, $V_{\mathrm{ds.S_m}}$, drain current, $i_{\mathrm{S_m}}$ and gate-source voltage of the main switch, $V_{\mathrm{gs.S_m}}$ in Si-based and GaN-based hard-switched boost converters are shown in **Fig. 4.10(a)** and **(b)**, respectively. The switching frequency is 200 kHz, output power is 500 W, and output and input voltages are 400 V and 100 V, respectively. The main switches of the both converters are turned on and off at the hard switching condition which causes switching losses.

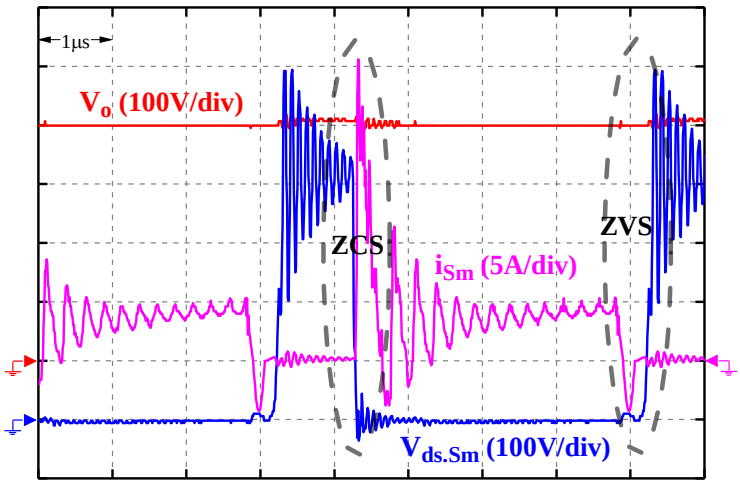

(a)

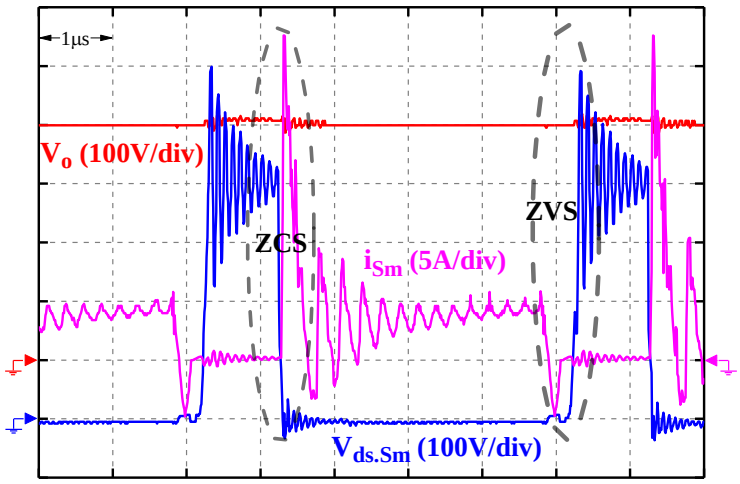

(b)

Fig. 4.11 Experimental results. V_{o}, $V_{\mathrm{ds.S_m}}$, $V_{\mathrm{gs.S_m}}$, and $i_{\mathrm{S_m}}$ in (a) prototype 3, (b) prototype 4.

The output voltage, V_{o}, the drain-source voltage, $V_{\mathrm{ds.S_m}}$, drain current, $i_{\mathrm{S_m}}$, and gate-source voltage of the main switch, $V_{\mathrm{gs.S_m}}$ in Si-based and GaN based soft-switched boost converters are illustrated in **Fig. 4.11(a)** and **(b)**, respectively. As shown in **Fig. 4.11(a)** and **(b)**, the operation of the soft-switched and hard-switched boost converters are the same in general, since the boost inductor is charged by the input source and then discharges to the output. In addition, it can be seen that, in prototypes 3 and 4, the switches are switched at soft switching conditions (they are turned on at ZCS condition and turned off at ZVS condition), which makes their switching losses negligible. In addition, as predicted in section 4.3, the parasitic components causes a high frequency oscillation in the circuits, especially for ZVS topologies.

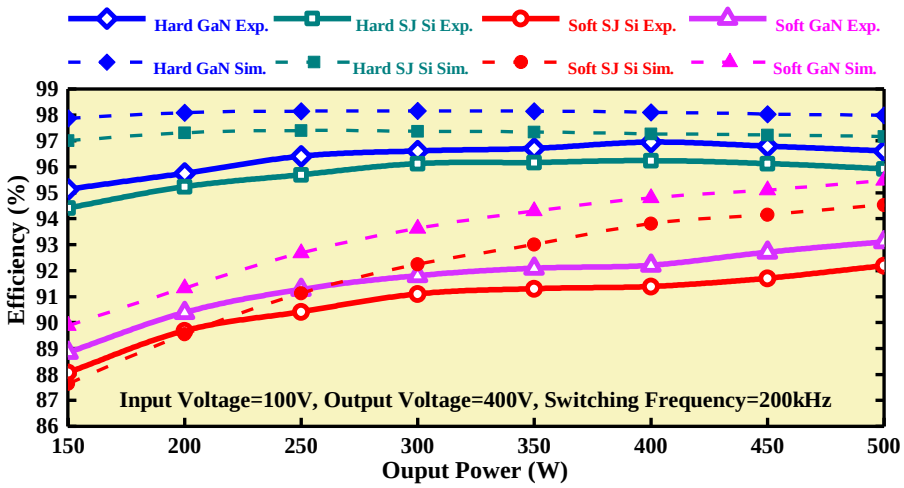

(a)

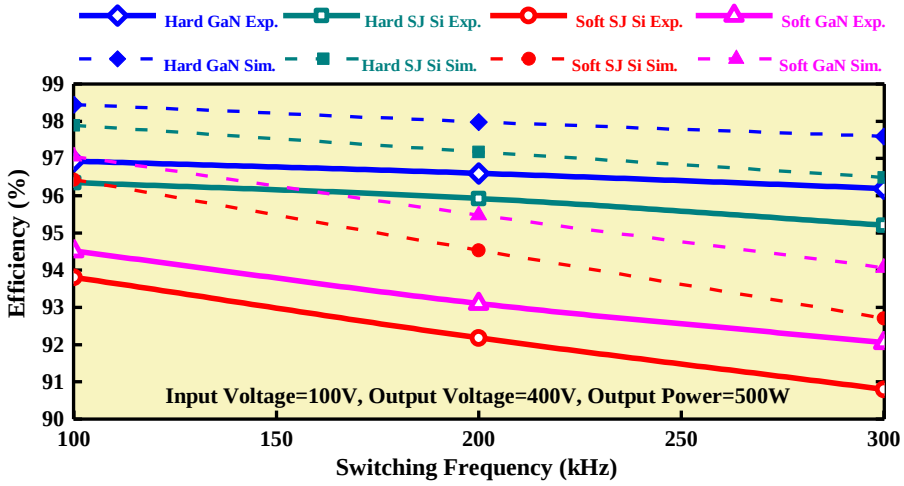

(b)

Fig. 4.12 Experimental efficiency comparison. (a) For different output powers. (b) For different switching frequencies at nominal specifications.

The efficiency of all prototypes versus output power and switching frequency are measured and compared in **Fig. 4.12(a)** and **(b)**, respectively. In addition, the predicted efficiency of the prototypes calculated by the simulation results are shown with dotted line in **Fig. 4.12(a)** and **(b)**. The experimental results confirm the efficiency comparison provided in **Fig. 4.3**. The difference between the measured efficiency and the theoretical prediction ranges from 1% in the hard-switched topologies to about 3% in the soft-switched topologies.

There are a number of factors which explain these discrepancies. Firstly, the parasitic resistances, capacitances, and inductances of the paths in the PCB layout were not considered in the theoretical analysis due to simplification and their negligible effect. Second, the variable nature of the switching frequency, whose experimental value is sensitive to unmodelled parasitic elements, does not result precisely in the expected theoretical value. The component characteristics, sourced from the datasheets and used for theoretical analysis, are subject to tolerance and voltage- and temperature-dependency, especially for their parasitic elements. Moreover, even though the switching losses are neglected in the soft-switched topologies, they are not eliminated completely. Furthermore, as mentioned in section 4.3, the parasitic capacitors have an important influence on the operation of the soft-switched converter, especially conduction and core losses.

By using the exact SPICE models of components and conducting SPICE simulations, it is possible to reduce discrepancies in the results. However, even considering these discrepancies, the experimental results still confirm the predicted efficiencies provided in section 4.3. As predicted in the theoretical analysis, the GaN-based hard-switched boost converters is the most efficient while the Si-based soft-switched boost converter has the lowest efficiency. In addition, the Si-based hard-switched converter and GaN-based soft-switched converter are ranked second and third, respectively. All the aforementioned explanations for **Fig. 4.3** provided in section 4.3.1 remain valid for **Fig. 4.12** and so are not repeated here.

The power density and cost comparison provided in section 4.3 are based on the experimental results and are not subject to experimental validation, as datasheet dimensions and price-list values are not prone to experimental variation.

4.5 Discussion and conclusion

In this Chapter, to investigate various methods used to decrease the switching losses of the DC-DC converters, four prototypes are implemented and evaluated. These were: 1) a hard-switched DC-DC boost converter which uses a state-of-the-art SJ Si MOSFET; 2) a version of prototype 1 using a GaN HEMT power switch; 3) a fully soft-switched DC-DC boost converter based on SJ Si MOSFET; and 4) a GaN HEMT version of prototype 3. All the prototypes were simulated and tested experimentally under the same operating conditions to compare their efficiency,

power density and cost when they are designed to be used in renewable energy applications such as AC-PV module systems.

The GaN-based hard-switched converter can provide the highest efficiency from light power (100 W) to nominal power (500 W) range, and Si-based hard-switched converter is ranked second (see **Fig. 4.12**). However, the GaN-based and Si-based soft-switched converters hold the third and fourth rank, respectively. In addition, the efficiency of the soft-switched converters decreases noticeably at light power range; thus, they are not a good choice for PV systems in which power range varies across hours and seasons. Furthermore, it is shown that the GaN-based hard-switched converter occupies the smallest volume.

The Si-based hard switching is the cheapest converter, and the GaN-based hard switching converter is ranked second. However, the GaN-based hard-switched converter remains cheaper than Si-based soft-switched converter, even though GaN switches are far more expensive than Si switches. This cost gap between Si and GaN switches may close in the future. Overall, since using GaN in DC-DC converters does not alter the simple traditional, simple structure of the converter and has better performance in terms of power density, cost, and efficiency than the soft-switched converter, it is a better choice for renewable energy applications.

Last and most importantly, it is clear from the results that adding an auxiliary circuit to obtain soft switching for PWM converters leads to a more expensive and complicated circuit and does not always guarantee a higher efficiency. In addition, WBG devices cannot eliminate switching losses and therefore at the operating frequencies in MHz range, PWM converters will suffer from high switching losses even when they use WBG semiconductor devices. Therefore, the remainder of this thesis focuses on resonant converters which benefits from soft switching capability inherently and are a better choice for high power density and efficiency applications.

Chapter 5

Fully-Integrated Planar Transformer with a Segmental Shunt for LLC Resonant Converters

This Chapter presents two topologies (termed IT1 and IT2), which provide high leakage inductance for shunt-inserted integrated magnetic transformers. These differ from conventional designs by replacing the low-permeability magnetic shunt of a planar transformer with high-permeability magnetic shunt segments, separated by many small air gaps. This approach results in a shunt with the same bulk permeability as the conventional design, while using lower cost and readily available magnetic materials such as ferrite. A modelling and design approach, which can estimate the leakage and magnetising inductances precisely is provided for each topology. Theoretical analysis is presented and verified using finite-element analysis and experimental implementation. AC resistance analysis for both transformer topologies is also presented. In addition, an LLC resonant converter is built to verify the performance of the proposed fully-integrated magnetic transformers in practice. It is shown that the proposed topologies can integrate all three magnetic components of an isolated LLC resonant converter in a single planar transformer, which reduces the converter's volume and cost.

5.1 Introduction

PWM converters, like the boost converter, suffer from the lack of soft switching capability and thus have high switching losses under high frequency operation. Losses are limited by constraining the operating frequency, leading to lower power density [3, 166]. As shown in Chapter 4, even though soft switching capability can be achieved by adding an auxiliary circuit to the conventional topology of the PWM converters, the auxiliary circuit adds complexity and cost [6, 7]. On the other hand, resonant converters provide soft-switching capability inherently. Hence, resonant converters can achieve high efficiency at high switching frequency and are a good choice for the applications in which high power density alongside high efficiency is needed.

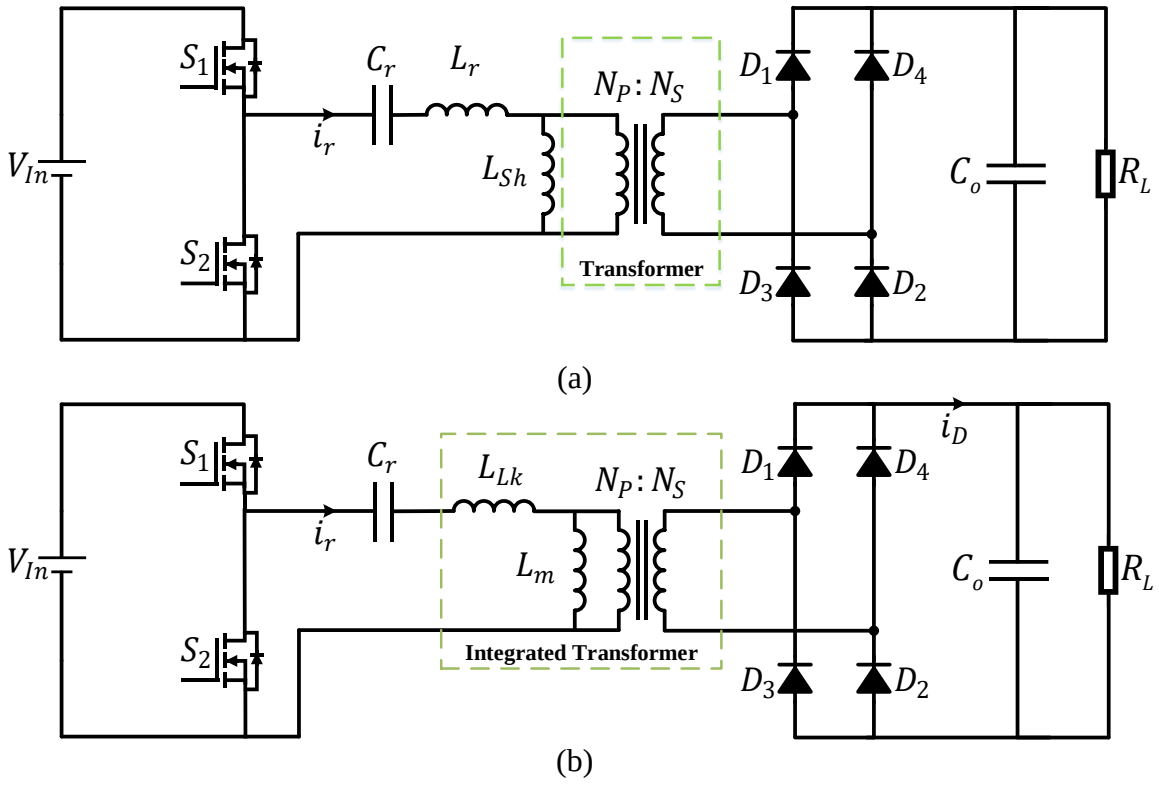

Fig. 5.1 Topology of the half-bridge LLC resonant converter, (a) without magnetic integration, (b) with magnetic integration.

The LLC topology is one of the most popular amongst resonant converters and has been used in many applications [150, 151, 167]. An isolated LLC resonant converter, which is again shown in **Fig. 5.1(a)**, uses three magnetic components: a shunt (or parallel) inductor, a series (or resonant) inductor and a transformer. In order to decrease the volume and cost, and increase the efficiency of the LLC resonant converter, all three magnetic elements are usually integrated into a single magnetic transformer as presented in **Fig. 5.1(b)**.

There are many methods, which can be used to integrate the magnetic components of the LLC resonant converter. Amongst them, the inserted-shunt integrated transformer has gained popularity recently [12, 130, 134, 135] and is chosen to be further investigated in this thesis.

Inserting a single piece low-permeability magnetic shunt in a planar transformer enhances the leakage inductance and makes the estimation of its value more accurate, but this idea suffers from some disadvantages. The magnetic shunt must have a specific and unusually low permeability. Suitable magnetic materials are not often readily available, and when they are,

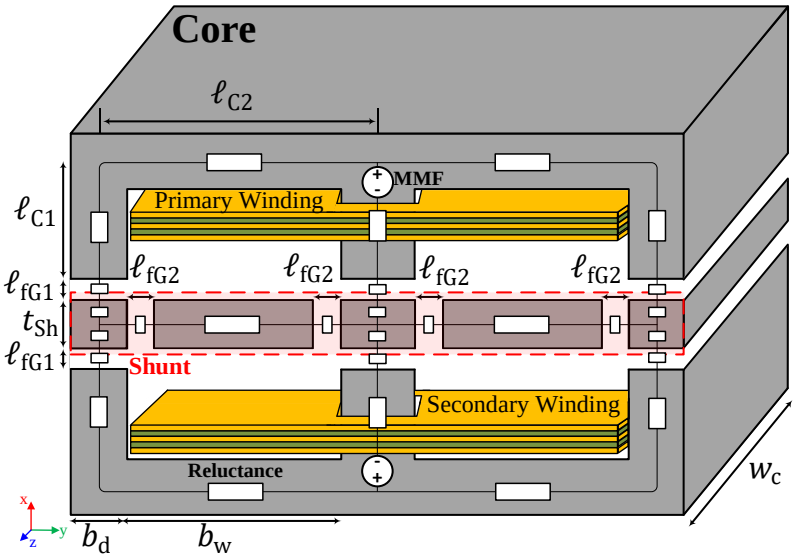

Fig. 5.2 The proposed five-segment shunt-inserted integrated magnetic transformer (IT1).

they are frequently expensive. In addition, these low-permeability materials are often found only in limited sizes [135, 137, 138]. Furthermore, the low-permeability magnetic shunt has temperature-dependent permeability, leading to non-stable leakage inductance.

To address these issues, two new structures (termed IT1 and IT2) shown in **Fig. 5.2** and **Fig. 5.3** are proposed in this Chapter. These structures are formed by interleaving highly permeable ferrite with thin plastic spacers to form segmental magnetic shunts. This design approximates the low-permeability material in [12, 130, 134]; its permeability is modulated by the ratio of ferrite-to-spacer length. The design is more economical because ferrite is widely available in the market with different sizes and for lower price.

Both of the proposed structures are analysed and their modelling and design guidelines are provided in detail. The theoretical analysis is verified by finite-element analysis (FEA) simulation and experimental results. The AC resistance for the proposed structures is also discussed. Furthermore, an LLC converter is implemented to investigate the performance of the designed fully-integrated magnetic transformers. It is shown that this LLC converter works properly while all of its magnetic components are integrated in the proposed structures.

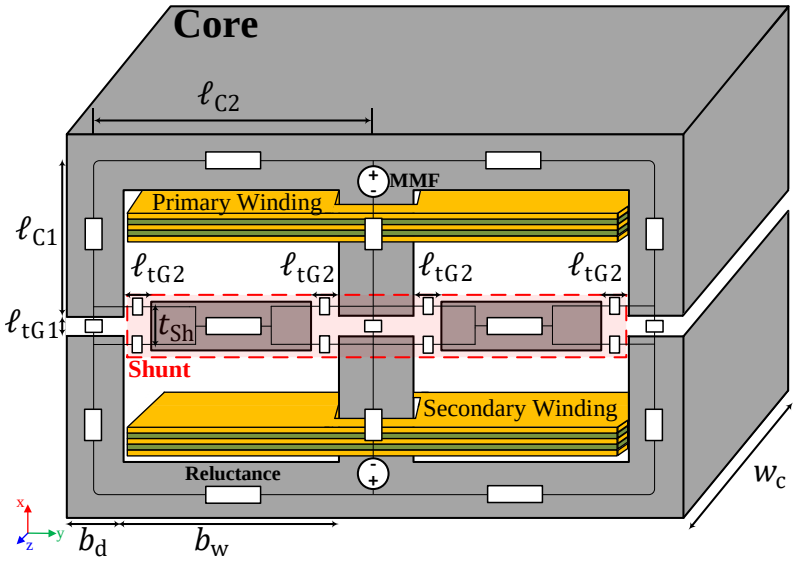

Fig. 5.3 The proposed two-segment shunt-inserted integrated magnetic transformer (IT2).

5.2 Proposed integrated magnetic transformers

The structures of the first and second proposed integrated transformers are shown in **Fig. 5.2** and **Fig. 5.3**, respectively. Subscripts *f* and *t* mean five-segment and two-segment, respectively. As shown in in **Fig. 5.2** and **Fig. 5.3**, a segmental magnetic shunt is inserted between the magnetic cores of a planar transformer in both topologies. The magnetic shunt of the first (termed IT1) and second (termed IT2) topologies have five and two segments, respectively. For both topologies the primary and secondary windings are separated by being placed at opposite sides of the shunt. A lumped parameter magnetic equivalent circuit is superimposed on the transformer geometry to show the locations of the core, shunt and air gap reluctances, and the winding magnetomotive force (MMFs). The modelling of the proposed topologies is discussed in the following sections.

5.2.1 Relationship between magnetising and leakage inductances

From (2-59) and (2-61), the total leakage inductance of a transformer referred to the primary side may be obtained as (5-1).

$$L_{Lk} = 2L_{PP} - 2L_m \tag{5-1}$$

5.2.2 Five-segment magnetic shunt

The topology of the integrated transformer based on a five-segment magnetic shunt (IT1) is shown in **Fig. 5.2**. The shunt incorporates four equal vertical air gaps with length ℓ_{fG2} (nb. 'f' refers to five segments) to achieve same bulk permeability as the conventional design with the low-permeability shunt. In addition, the horizontal air gaps between the cores and shunt are assumed equal with the length ℓ_{fG1}. The reluctance model of this topology is presented in **Fig. 5.4(a)**, where $\mathcal{R}_{\mathrm{fG1}}$, $\mathcal{R}_{\mathrm{fGG}}$ and $\mathcal{R}_{\mathrm{fG2}}$ are air-gap reluctances, $\mathcal{R}_{\mathrm{fC1}}$, $\mathcal{R}_{\mathrm{fC2}}$ and $\mathcal{R}_{\mathrm{fCC}}$ are core reluctances and $\mathcal{R}_{\mathrm{fSh1}}$, $\mathcal{R}_{\mathrm{fSh2}}$ and $\mathcal{R}_{\mathrm{fSh}}$ are shunt reluctances. These are obtained as follows:—

$$\mathcal{R}_{\mathrm{fC1}} = \frac{\ell_{\mathrm{C1}}}{\mu_0 \mu_{\mathrm{r}} b_{\mathrm{d}} w_{\mathrm{c}}} \tag{5-2}$$

$$\mathcal{R}_{\mathrm{fC2}} = \frac{\ell_{\mathrm{C2}}}{\mu_0 \mu_{\mathrm{r}} b_{\mathrm{d}} w_{\mathrm{c}}} \tag{5-3}$$

$$\mathcal{R}_{\mathrm{fCC}} = \frac{\ell_{\mathrm{C1}}}{\mu_0 \mu_{\mathrm{r}} A_{\mathrm{c}}} \tag{5-4}$$

$$\mathcal{R}_{\mathrm{fSh1}} = \frac{t_{\mathrm{Sh}}}{2\mu_0 \mu_{\mathrm{Sh}} b_{\mathrm{d}} w_{\mathrm{c}}} \tag{5-5}$$

$$\mathcal{R}_{\mathrm{fSh2}} = \frac{b_{\mathrm{w}} - 2\ell_{\mathrm{fG2}}}{\mu_0 \mu_{\mathrm{Sh}} t_{\mathrm{Sh}} w_{\mathrm{c}}} \tag{5-6}$$

$$\mathcal{R}_{\mathrm{fSh}} = \frac{t_{\mathrm{Sh}}}{2\mu_0 \mu_{\mathrm{Sh}} A_{\mathrm{c}}} \tag{5-7}$$

$$\mathcal{R}_{\mathrm{fG1}} = \frac{\ell_{\mathrm{fG1}}}{\mu_0 (b_{\mathrm{d}} + \ell_{\mathrm{fG1}})(w_{\mathrm{c}} + \ell_{\mathrm{fG1}})} \tag{5-8}$$

$$\mathcal{R}_{\mathrm{fG2}} = \frac{\ell_{\mathrm{fG2}}}{\mu_0 (t_{\mathrm{Sh}} + \ell_{\mathrm{fG2}})(w_{\mathrm{c}} + \ell_{\mathrm{fG2}})} \tag{5-9}$$

$$\mathcal{R}_{\mathrm{fGG}} = \frac{\ell_{\mathrm{fG1}}}{\mu_0(2b_{\mathrm{d}}+\ell_{\mathrm{fG1}})(w_{\mathrm{c}} + \ell_{\mathrm{fG1}})} \tag{5-10}$$

where μ_0 is the permeability of the air and μ_{r} and μ_{Sh} are the relative permeabilities of the core and shunt, respectively. A_{c} is the core effective cross-sectional area and the definition of other quantities can be found in **Fig. 5.2**. Hurley, *et al*, [168] showed that an effective cross-sectional area of the air gap with dimension *a* by *b* are equal to (*a*+*g*) by (*b*+*g*) when the fringing effect is considered and *g* is the length of the studied air gap.

The reluctance model of the topology with a five-segment shunt is shown in **Fig. 5.4(a)**. Circuit analogue analysis allows mutual flux of the five-segment topology, ϕ_{fPS}, to be calculated as

$$\phi_{\mathrm{fPS}} = \frac{2N_{\mathrm{P}}i_{\mathrm{P}}(\mathcal{R}_{\mathrm{fSh2}} + 2\mathcal{R}_{\mathrm{fG2}})}{\mathcal{R}_{\mathrm{fE}}(\mathcal{R}_{\mathrm{fE}} + 2(\mathcal{R}_{\mathrm{fSh2}} + 2\mathcal{R}_{\mathrm{fG2}}))} \tag{5-11}$$

where $\mathcal{R}_{\mathrm{fE}}$ is an equivalent reluctance defined as

$$\mathcal{R}_{\mathrm{fE}} = \mathcal{R}_{\mathrm{fC1}} + \mathcal{R}_{\mathrm{fC2}} + 2\mathcal{R}_{\mathrm{fCC}} + \mathcal{R}_{\mathrm{fSh1}} + \mathcal{R}_{\mathrm{fG1}} + 2\mathcal{R}_{\mathrm{fSh}} + 2\mathcal{R}_{\mathrm{fGG}} \tag{5-12}$$

By substituting (5-11) into (2-56), the magnetising inductance of the five-segment topology, L_{fm}, may be calculated using (5-13).

$$L_{\mathrm{fm}} = \frac{2N_{\mathrm{P}}^2(\mathcal{R}_{\mathrm{fSh2}} + 2\mathcal{R}_{\mathrm{fG2}})}{\mathcal{R}_{\mathrm{fE}}(\mathcal{R}_{\mathrm{fE}} + 2(\mathcal{R}_{\mathrm{fSh2}} + 2\mathcal{R}_{\mathrm{fG2}}))} \tag{5-13}$$

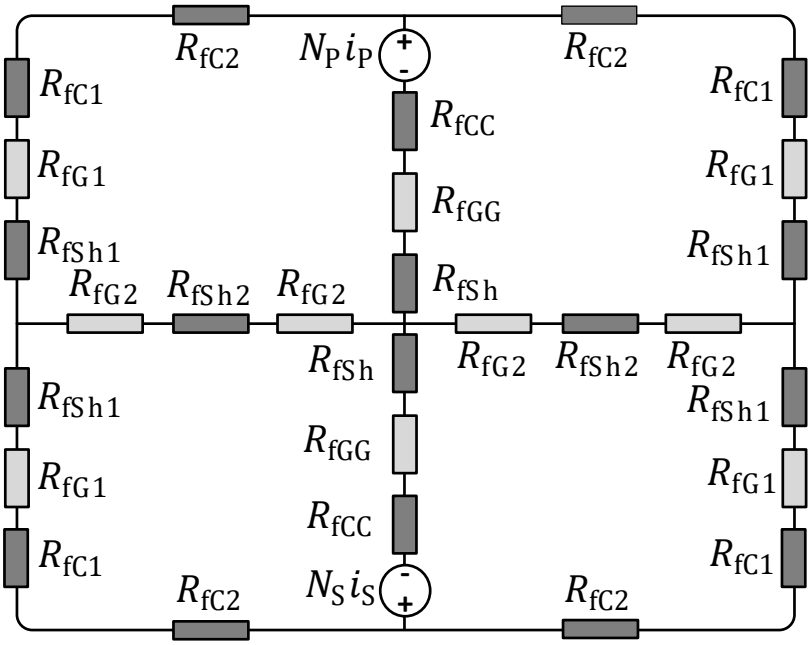

(a)

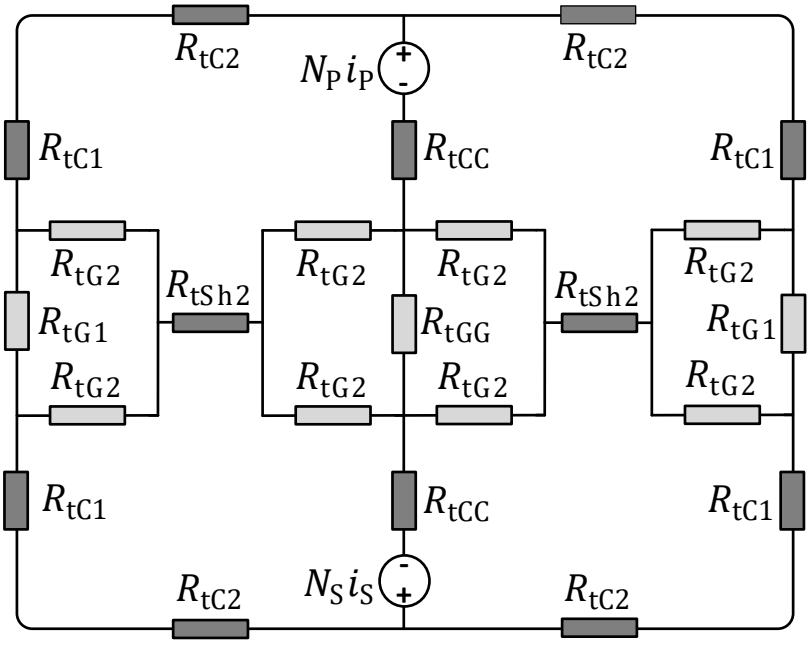

(b)

Fig. 5.4 The reluctance model of the proposed segmental shunt-inserted integrated magnetic transformers. (a) Five-segment topology (IT1). (b) Two-segment topology (IT2).

From (2-57) and the reluctance model presented in **Fig. 5.4(a)**, the self-inductance of the primary winding of the five-segment topology, L_{fPP}, may be calculated using (5-14).

$$L_{\mathrm{fPP}} = \frac{2N_{\mathrm{P}}^2(\mathcal{R}_{\mathrm{fSh2}} + 2\mathcal{R}_{\mathrm{fG2}} + \mathcal{R}_{\mathrm{fE}})}{\mathcal{R}_{\mathrm{fE}}(\mathcal{R}_{\mathrm{fE}} + 2(\mathcal{R}_{\mathrm{fSh2}} + 2\mathcal{R}_{\mathrm{fG2}}))} \tag{5-14}$$

Applying (5-1), (5-13) and (5-14), the total leakage inductance caused by the shunt and referred to the primary side of the five-segment topology, $L_{\mathrm{flk-Sh}}$, may be calculated using (5-15).

$$L_{\mathrm{fLk\_Sh}} = \frac{4N_{\mathrm{P}}^2}{\mathcal{R}_{\mathrm{fE}} + 2(\mathcal{R}_{\mathrm{fSh2}} + 2\mathcal{R}_{\mathrm{fG2}})} \tag{5-15}$$

Therefore, from (5-13) and (5-15), the magnetising and leakage inductances can be calculated for the design of the transformer.

5.2.3 Two-segment magnetic shunt

An alternative approach uses a two-segment shunt (IT2) and the topology of its integrated transformer is shown in **Fig. 5.3**. This topology benefits from fewer segments which makes the implementation easier. However, in this topology, the entirety of the window area cannot be used for windings and the distance between windings and shunt is reduced, which leads to higher eddy-current losses in the windings as a result of the fringing effect. The magnetic shunt includes two identical segments and there are air gaps between each segment and the cores with length ℓ_{tG2} (nb. 't' refers to two segments). In addition, there are horizontal air gaps between the top and bottom cores with length ℓ_{tG1}. The reluctance model of this topology is presented in **Fig. 5.4(b)**, where $\mathcal{R}_{\mathrm{tG1}}$, $\mathcal{R}_{\mathrm{tGG}}$ and $\mathcal{R}_{\mathrm{tG2}}$ are air gap reluctances, $\mathcal{R}_{\mathrm{tC1}}$, $\mathcal{R}_{\mathrm{tC2}}$ and $\mathcal{R}_{\mathrm{tCC}}$ are core reluctances and $\mathcal{R}_{\mathrm{tSh2}}$ is shunt reluctance and they may be obtained as follows:-

$$\mathcal{R}_{\mathrm{tC1}} = \frac{\ell_{\mathrm{C1}}}{\mu_0\mu_{\mathrm{r}}b_{\mathrm{d}}w_{\mathrm{c}}} \tag{5-16}$$

$$\mathcal{R}_{\mathrm{tC2}} = \frac{\ell_{\mathrm{C2}}}{\mu_0\mu_{\mathrm{r}}b_{\mathrm{d}}w_{\mathrm{c}}} \tag{5-17}$$

$$\mathcal{R}_{\mathrm{tCC}} = \frac{\ell_{\mathrm{C1}}}{\mu_0 \mu_{\mathrm{r}} A_{\mathrm{c}}} \tag{5-18}$$

$$\mathcal{R}_{\mathrm{tSh2}} = \frac{b_{\mathrm{w}} - 2\ell_{\mathrm{tG2}}}{\mu_0 \mu_{\mathrm{Sh}} t_{\mathrm{Sh}} w_{\mathrm{c}}} \tag{5-19}$$

$$\mathcal{R}_{\mathrm{tG1}} = \frac{\ell_{\mathrm{tG1}}}{\mu_0 (b_{\mathrm{d}} + \ell_{\mathrm{tG1}})(w_{\mathrm{c}} + \ell_{\mathrm{tG1}})} \tag{5-20}$$

$$\mathcal{R}_{\mathrm{tG2}} = \frac{2\ell_{\mathrm{tG2}}}{\mu_0 (t_{\mathrm{Sh}} + \ell_{\mathrm{tG2}})(w_{\mathrm{c}} + \ell_{\mathrm{tG2}})} \tag{5-21}$$

$$\mathcal{R}_{\mathrm{tGG}} = \frac{\ell_{\mathrm{tG1}}}{\mu_0 (2b_{\mathrm{d}} + \ell_{\mathrm{tG1}})(w_{\mathrm{c}} + \ell_{\mathrm{tG1}})} \tag{5-22}$$

According to the reluctance model of the topology with a two-segment shunt presented in **Fig. 5.4(b)**, the mutual flux of the two-segment topology, ϕ_{tPS}, may be calculated using (5-23).

$$\phi_{\mathrm{tPS}} = \frac{2N_{\mathrm{P}} I_{\mathrm{P}} (\mathcal{R}_{\mathrm{tSh2}} + \mathcal{R}_{\mathrm{A}} + \mathcal{R}_{\mathrm{B}})}{\mathcal{R}_{\mathrm{tE}} (\mathcal{R}_{\mathrm{tE}} + 2(\mathcal{R}_{\mathrm{tSh2}} + \mathcal{R}_{\mathrm{A}} + \mathcal{R}_{\mathrm{B}}))} \tag{5-23}$$

where $\mathcal{R}_{\mathrm{tE}}$ can be defined as

$$\mathcal{R}_{\mathrm{tE}} = \mathcal{R}_{\mathrm{tC1}} + \mathcal{R}_{\mathrm{tC2}} + 2\mathcal{R}_{\mathrm{tCC}} + \mathcal{R}_{\mathrm{C}} + \mathcal{R}_{\mathrm{D}} \tag{5-24}$$

and $\mathcal{R}_{\mathrm{A}}$, $\mathcal{R}_{\mathrm{B}}$, $\mathcal{R}_{\mathrm{C}}$ and $\mathcal{R}_{\mathrm{D}}$ are defined as

$$\mathcal{R}_{\mathrm{A}} = \frac{\mathcal{R}_{\mathrm{tG2}}^2}{\mathcal{R}_{\mathrm{tG1}} + 2\mathcal{R}_{\mathrm{tG2}}} \tag{5-25}$$

$$\mathcal{R}_{\mathrm{B}} = \frac{\mathcal{R}_{\mathrm{tG2}}^2}{2\mathcal{R}_{\mathrm{tGG}} + 2\mathcal{R}_{\mathrm{tG2}}} \tag{5-26}$$

$$\mathcal{R}_{\mathrm{C}} = \frac{\mathcal{R}_{\mathrm{tG1}}\mathcal{R}_{\mathrm{tG2}}}{\mathcal{R}_{\mathrm{tG1}} + 2\mathcal{R}_{\mathrm{tG2}}} \tag{5-27}$$

$$\mathcal{R}_{\mathrm{D}} = \frac{2\mathcal{R}_{\mathrm{tGG}}\mathcal{R}_{\mathrm{tG2}}}{2\mathcal{R}_{\mathrm{tGG}} + 2\mathcal{R}_{\mathrm{tG2}}} \tag{5-28}$$

By substituting (5-23) into (2-56), the magnetising inductance of the two-segment topology, L_{tm}, is

$$L_{\mathrm{tm}} = \frac{2N_{\mathrm{P}}^2(\mathcal{R}_{\mathrm{tSh2}} + \mathcal{R}_{\mathrm{A}} + \mathcal{R}_{\mathrm{B}})}{\mathcal{R}_{\mathrm{tE}}(\mathcal{R}_{\mathrm{tE}} + 2(\mathcal{R}_{\mathrm{tSh2}} + \mathcal{R}_{\mathrm{A}} + \mathcal{R}_{\mathrm{B}}))} \tag{5-29}$$

From (2-57) and the reluctance model presented in **Fig. 5.4(b)**, the self-inductance of the primary winding of the two-segment topology, L_{tPP}, is

$$L_{\mathrm{tPP}} = \frac{2N_{\mathrm{P}}^2(\mathcal{R}_{\mathrm{tSh2}} + \mathcal{R}_{\mathrm{A}} + \mathcal{R}_{\mathrm{B}} + \mathcal{R}_{\mathrm{tE}})}{\mathcal{R}_{\mathrm{tE}}(\mathcal{R}_{\mathrm{tE}} + 2(\mathcal{R}_{\mathrm{tSh2}} + \mathcal{R}_{\mathrm{A}} + \mathcal{R}_{\mathrm{B}}))} \tag{5-30}$$

From (5-1), (5-29) and (5-30), the leakage inductance caused by the shunt and referred to the primary of the two-segment topology is

$$L_{\mathrm{tLk\_Sh}} = \frac{4N_{\mathrm{P}}^2}{\mathcal{R}_{\mathrm{tE}} + 2(\mathcal{R}_{\mathrm{tSh2}} + \mathcal{R}_{\mathrm{A}} + \mathcal{R}_{\mathrm{B}})} \tag{5-31}$$

Therefore, from (5-29) and (5-31), the magnetising and leakage inductances can be calculated.

5.3 Leakage inductance caused by window area and windings

The total energy stored in the leakage inductance of the proposed topologies consists of the energy stored in the windows area of the cores and the primary and secondary windings and

flux conducting through the inserted-shunt (including its air gaps). Careful calculation of the total leakage inductance is needed for accurate modelling of the proposed topologies.

Fig. 5.5 shows a cross-section of the right-hand side of the transformers divided into several regions contributing the stored energy by the leakage inductance. The primary winding consists of N_P turns and is constructed from n_P layers each with k_P turns ($N_\mathrm{P} = k_\mathrm{P} n_\mathrm{P}$). Each primary winding layer has a height h_P and an associated insulating layer with a height $h_{\Delta\mathrm{P}}$. Similar notation is used for the secondary winding, $N_\mathrm{S} = k_\mathrm{S} n_\mathrm{S}$, with each layer having a height h_S and insulating layer height $h_{\Delta\mathrm{S}}$. Regions E_P and E_S refer to the energy stored in the primary and secondary winding. E_air is the energy stored in the proportion of the winding window not occupied by the windings and shunt.

Assuming the permeability of the core is very high then any energy that is stored in the transformer must be located outside of the core. The total leakage inductance, L_Lk, may be obtained by (5-32).

$$E = \frac{1}{2}\iiint_V BH \,\mathrm{d}V = \frac{1}{2} L_\mathrm{Lk} i_\mathrm{P}^2 \tag{5-32}$$

where V is the total volume with a cross-section consisting of the window area and the shunt, i_P is the primary current, B is the flux density and H is the magnetic field intensity. The MMF of each layer of the primary winding, $\mathfrak{F}_\mathrm{P}$, may be obtained from (5-33), where k_P is the number of turns in each layer of the primary winding.

$$\mathfrak{F}_\mathrm{P} = k_\mathrm{P} i_\mathrm{P} \tag{5-33}$$

If n_P and n_S are defined as the number of layers of the primary and secondary windings, respectively, the MMF within the window area, $\mathfrak{F}_\mathrm{air}$, is $n_\mathrm{P}\mathfrak{F}_\mathrm{P}$ and the magnetic field intensity within the air area, H_air, may be obtained by the following equation.

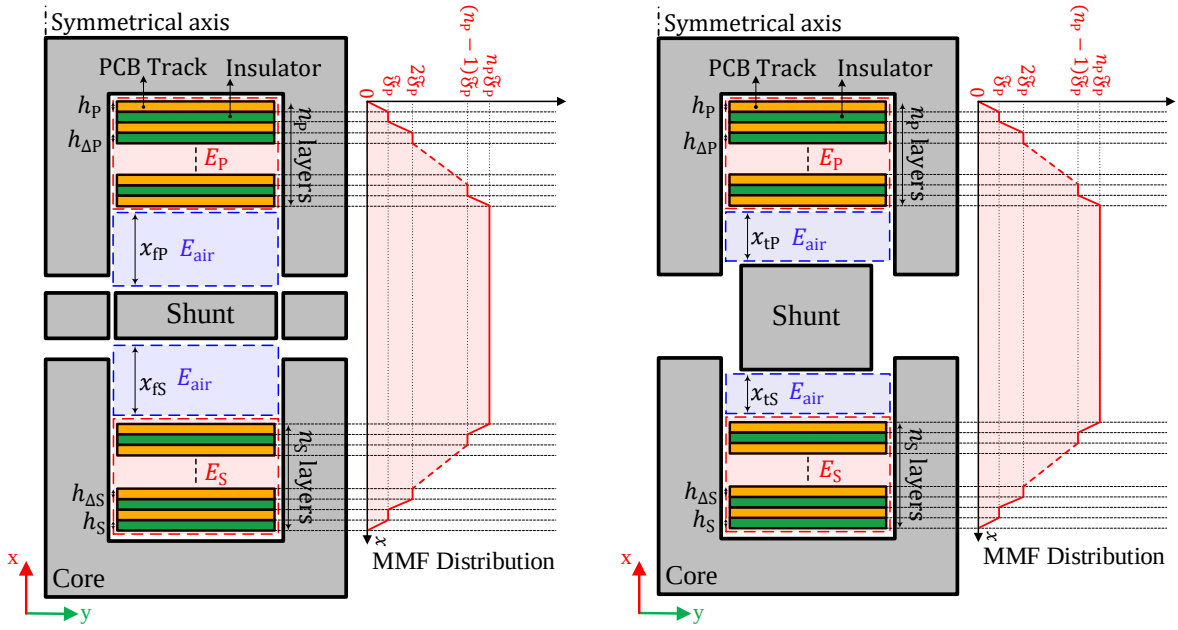

(a) (b)

Fig. 5.5 MMF distribution of the proposed integrated transformers. (a) Five-segment topology (IT1). (b) Two-segment topology (IT2).

$$H_{\text{air}} = \frac{n_{\text{P}}\mathfrak{F}_{\text{P}}}{b_{\text{w}}} \tag{5-34}$$

In addition, from (5-32), the energy stored in the air, E_{air}, (the area of E_{air} is shown in **Fig. 5.5**) may be obtained as follows:-

$$E_{\text{air}} = \frac{1}{2}\mu_0 w_{\text{c}} b_{\text{w}} \int_{-x_{\text{fS}}(\text{or } x_{\text{tS}})}^{x_{\text{fP}}(\text{or } x_{\text{tP}})} H_{\text{air}}^2 \text{d}x \tag{5-35}$$

where w_{c} is the core depth and x_{fP} and x_{fS} are the distances between the primary and secondary windings and the shunt for the five-segment topology shown in **Fig. 5.5(a)**, respectively. x_{tP} and x_{tS} are the distances between the primary and secondary windings and the shunt for the two-segment topology shown in **Fig. 5.5(b)**, respectively.

From (5-34) and (5-35), the energy stored in in both windows (left and right windows of an E-core) of the five-segment (E_{fair}) and two-segment topologies (E_{tair}) may be obtained by (5-36) and (5-37), respectively.

$$E_{\mathrm{fair}} = \mu_0 w_{\mathrm{c}} \frac{n_{\mathrm{P}}^2 k_{\mathrm{P}}^2 i_{\mathrm{P}}^2}{b_{\mathrm{w}}} (x_{\mathrm{fP}} + x_{\mathrm{fS}}) \tag{5-36}$$

$$E_{\mathrm{tair}} = \mu_0 w_{\mathrm{c}} \frac{n_{\mathrm{P}}^2 k_{\mathrm{P}}^2 i_{\mathrm{P}}^2}{b_{\mathrm{w}}} (x_{\mathrm{tP}} + x_{\mathrm{tS}}) \tag{5-37}$$

The energy stored in the primary and secondary windings, which is the energy stored in the PCB layers of the planar transformer, can be obtained according to the MMF distribution presented in **Fig. 5.5** [129, 130, 134]. Ouyang , *et al*, [129] showed that it may be calculated as follows for primary and secondary:-

$$E_{\mathrm{P}} = \frac{1}{6} \mu_0 \frac{w_{\mathrm{c}}}{b_{\mathrm{w}}} k_{\mathrm{P}}^2 [h_{\Delta \mathrm{P}} (2n_{\mathrm{P}}^3 - 3n_{\mathrm{P}}^2 + n_{\mathrm{P}}) + 2h_{\mathrm{P}} n_{\mathrm{P}}^3] i_{\mathrm{P}}^2 \tag{5-38}$$

$$E_{\mathrm{S}} = \frac{1}{6} \mu_0 \frac{w_{\mathrm{c}}}{b_{\mathrm{w}}} k_{\mathrm{S}}^2 [h_{\Delta \mathrm{S}} (2n_{\mathrm{S}}^3 - 3n_{\mathrm{S}}^2 + n_{\mathrm{S}}) + 2h_{\mathrm{S}} n_{\mathrm{S}}^3] i_{\mathrm{S}}^2 \tag{5-39}$$

In (5-38) and (5-39), the thickness of the PCB layers of the primary and secondary windings are shown by h_{P} and h_{S}, respectively, and the thickness of insulation layers of the primary and secondary windings are shown by $h_{\Delta \mathrm{P}}$ and $h_{\Delta \mathrm{S}}$, respectively.

From (5-15), (5-31), (5-32) and (5-36)-(5-39), the total leakage inductance of the five-segment and two-segment topologies may be obtained by (5-40) and (5-41), respectively.

$$L_{\mathrm{fLk}} = 2\mu_0 w_{\mathrm{c}} \frac{N_{\mathrm{P}}^2}{b_{\mathrm{w}}} (x_{\mathrm{fP}} + x_{\mathrm{fS}}) + \frac{4N_{\mathrm{P}}^2}{\mathcal{R}_{\mathrm{fE}} + 2(\mathcal{R}_{\mathrm{fSh2}} + 2\mathcal{R}_{\mathrm{fG2}})} + \frac{1}{3} \mu_0 \frac{w_{\mathrm{c}}}{b_{\mathrm{w}}} k_{\mathrm{P}}^2 n_{\mathrm{P}}^2 \sum_{i=\mathrm{P,S}} \left[h_{\Delta i} \left(2n_i - 3 + \frac{1}{n_i} \right) + 2h_i n_i \right] \tag{5-40}$$

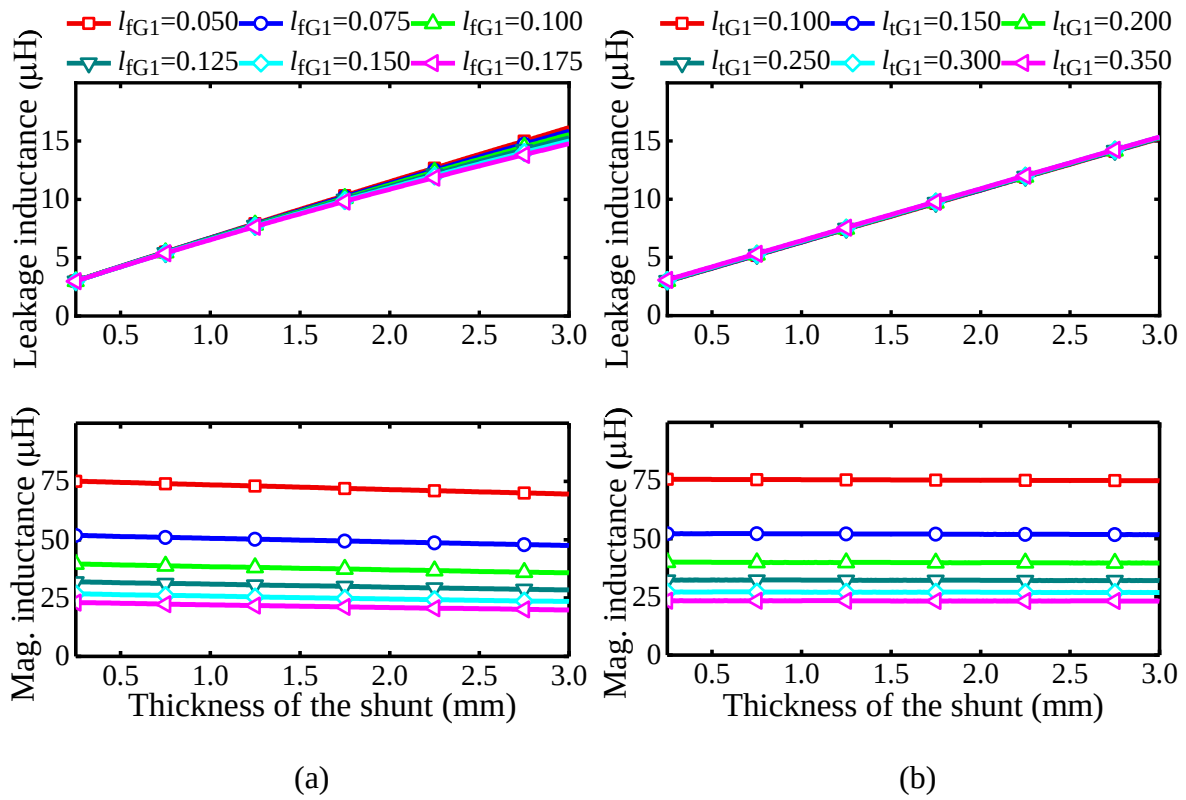

Fig. 5.6 The calculated leakage and magnetising inductance values. (a) Five-segment topology (IT1). (b) Two-segment topology (IT2). Core: E32/6/20/R-3F4, ℓ_{fG2}=ℓ_{tG2}=0.5mm, ℓ_{fG1} and ℓ_{tG1} in mm, N_P=10, N_S=2, n_P=5, n_S=2, k_P=2, k_S=1, x_{fP}= x_{fS}=1.5mm, x_{tP}= x_{tS}=0.76mm.

$$L_{tLk} = 2\mu_0 w_c \frac{N_P^2}{b_w}(x_{tP} + x_{tS}) + \frac{4N_P^2}{\mathcal{R}_{tE} + 2(\mathcal{R}_{tSh2} + \mathcal{R}_A + \mathcal{R}_B)} + \frac{1}{3}\mu_0 \frac{w_c}{b_w} k_P^2 n_P^2 \sum_{i=P,S} \left[h_{\Delta i}\left(2n_i - 3 + \frac{1}{n_i}\right) + 2h_i n_i \right] \quad (5\text{-}41)$$

The calculated leakage and magnetising inductances for the five-segment and two-segment topologies are shown in **Fig. 5.6(a)** and **(b)**, respectively. It is clear that the magnetising and leakage inductances are mainly influenced by the horizontal air gaps (ℓ_{fG1} or ℓ_{tG1}) and the thickness of the shunt, respectively. Hence, the leakage and magnetising inductances are sufficiently decoupled from each other in the proposed topologies and can be regulated separately by the thickness of the shunt and the length of the horizontal air gap, respectively.

5.4 FEA simulation and experimental verification

Simulation and experimental verification for both topologies with specification presented in **Table 5.1** (designed according to the sections 5.2 and 5.3) are provided in this section in order to confirm the modelling of the proposed topologies. Rather than design a converter to fit the transformer, the transformer is designed for a typical LLC converter with specification shown later in **Table 5.4**.

5.4.2 FEA simulation

The FEA simulations were conducted using ANSYS Maxwell, a commercial software package that specializes in electromagnetic simulations. The transformer geometry was modelled using solid modelling techniques, with each part of the transformer accurately represented as a separate object. The material properties of the transformer were defined using manufacturer datasheets, and the simulation was set up to consider the transformer's operating conditions. The simulation mesh was refined to ensure accurate results, with a minimum element length of 0.1 mm for small parts and maximum length of 2 mm for big parts. Suitable region was applied to the simulation to reduce computational cost and ensure the accuracy of the simulation. The simulation was performed using a transient solution type, which allowed for the analysis of the transformer's performance over time. External circuits were used to provide excitation to the transformer windings during the FEA simulations. These circuits were carefully designed to accurately represent the operating conditions of the transformer when it is used in an LLC resonant converter with specification shown later in **Table 5.4** and ensure that the simulation results were as realistic as possible. By using these external circuits, the simulation was able to capture the behaviour of the transformer under the operating conditions.

Simulation allowed for a thorough analysis of the transformer's performance characteristics and helped to identify any potential issues that could arise under different operating conditions. Overall, the FEA simulations were performed with great rigour and attention to detail and provide a comprehensive understanding of the transformer's performance characteristics.

TABLE 5.1 Proposed structures' specification.

Symbol	Parameter	Value
N_{P}	Primary turns	10
N_{S}	Secondary turns	2
k_{P}	Turns per layer in primary	2
k_{S}	Turns per layer in secondary	1
n_{P}	Number of primary layers	5
n_{S}	Number of secondary layers	2
h_{P}, h_{S}	Primary and secondary conduction thickness	35 μm
$h_{\Delta\mathrm{P}}$, $h_{\Delta\mathrm{S}}$	Primary and secondary insulation thickness	30 μm
w_{PT}	Primary PCB trace wideness	3.1 mm
w_{ST}	Secondary PCB trace wideness	5.7 mm
t_{Sh}	Shunt thickness	1.5 mm
ℓ_{fG1}	Five-segment topology horizontal air gap	0.13 mm
ℓ_{tG1}	Two-segment topology horizontal air gap	0.28 mm
ℓ_{fG2}	Five-segment topology vertical air gap	0.5 mm
ℓ_{tG2}	Two-segment topology vertical air gap	0.5 mm
x_{fP}, x_{fS}	Distance between primary and secondary windings and shunt for five-segment topology	1.5 mm 1.5 mm
x_{tP}, x_{tS}	Distance between primary and secondary windings and shunt for two-segment topology	0.76 mm 0.76 mm

The magnetic field intensity and flux density vectors for the five-segment and two-segment topologies are presented in **Fig. 5.7(a)** and **(b)**, respectively. From **Fig. 5.7**, it is clear that the leakage inductance is mainly caused by the shunt since the magnetic field intensity and flux density vectors are higher in the shunt air gaps than window area and windings. The leakage and magnetising inductances versus thickness of the shunt and horizontal air gaps (ℓ_{fG1} and ℓ_{tG1}) calculated from (5-13), (5-29), (5-40) and (5-41) and obtained by FEA simulation for the five-segment and two-segment topologies are presented in **Fig. 5.8(a)** and **(b)**, respectively. As shown, there is only a small discrepancy between the theoretical and simulation results, which verifies the modelling of the proposed topologies.

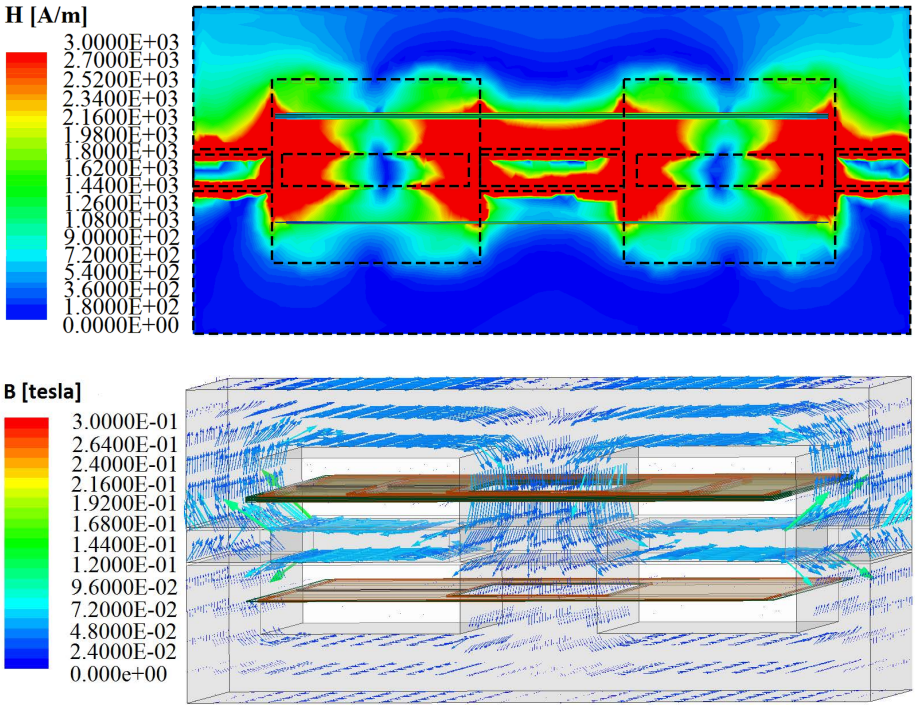

(a)

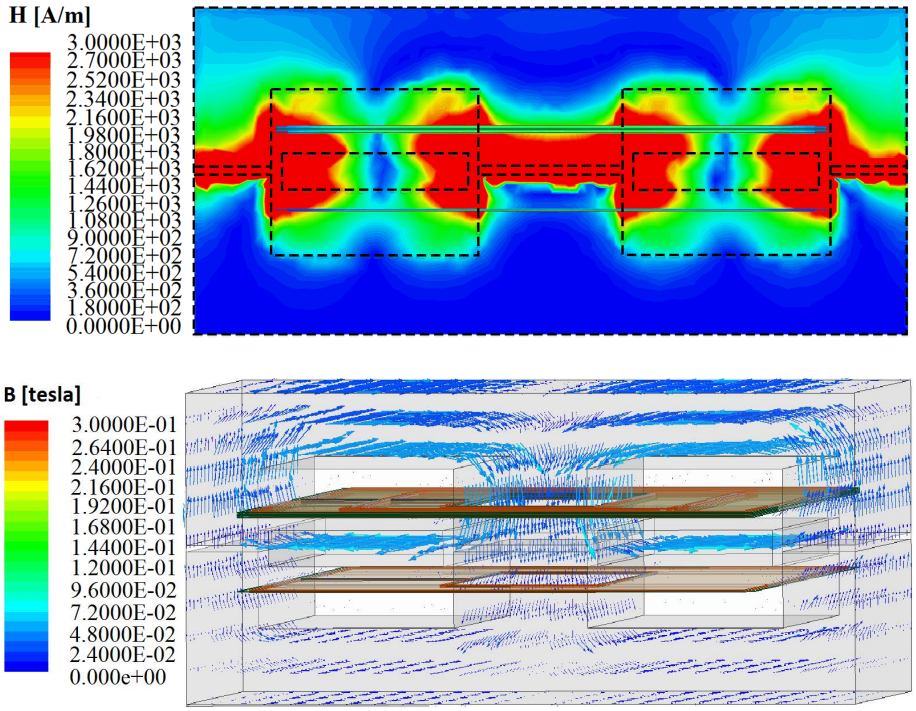

(b)

Fig. 5.7 Magnetic field intensity and magnetic flux density vectors. (a) Five-segment topology (IT1). (b) Two-segment topology (IT2). E32/6/20/R-3F4.

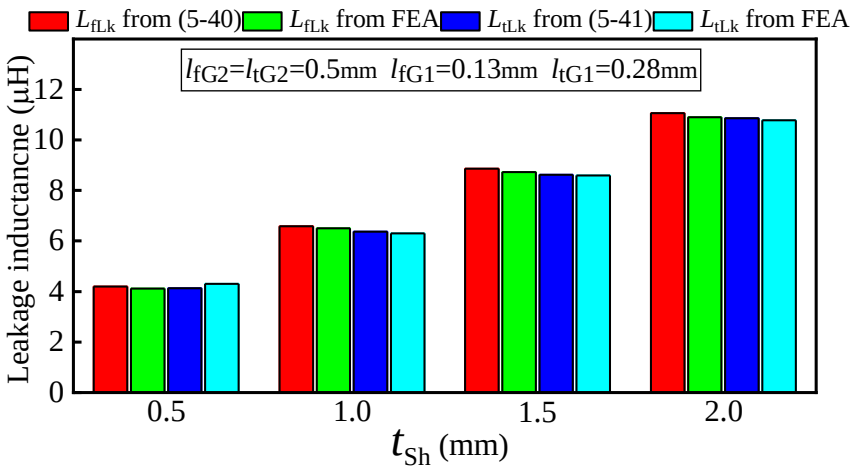

(a)

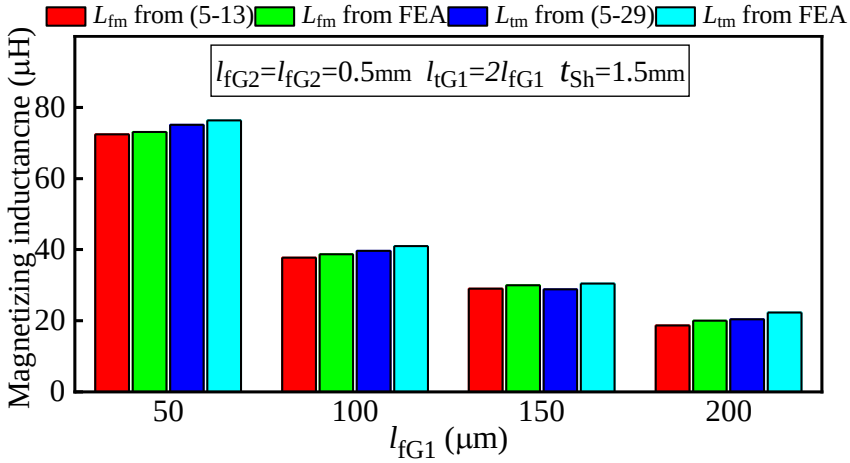

(b)

Fig. 5.8 Modelling verification by simulation results. (a) Leakage inductance. (b) Magnetising inductance.

The loss distribution of the proposed topologies and the conventional low-permeability one-segment shunt topology obtained by FEA is shown in **Fig. 5.9**. It can be seen that the two-segment topology has higher conduction losses compared to the five-segment topology and the reason is explained later. Therefore, even though the two-segment shunt topology benefits from easier manufacturing and smaller volume, it suffers from higher losses. As shown in **Fig. 5.9**, both proposed topologies have slightly higher conduction losses compared to the conventional single low-permeability shunt topology. This is because a high-permeability shunt with air gaps suffers from higher fringing than a solid low-permeability shunt, leading to higher AC resistance. It should be noted that Sullivan *,et al,* [137] have suggested a quasi-distributed gap technique which addresses the issue and could be incorporated into the proposal.

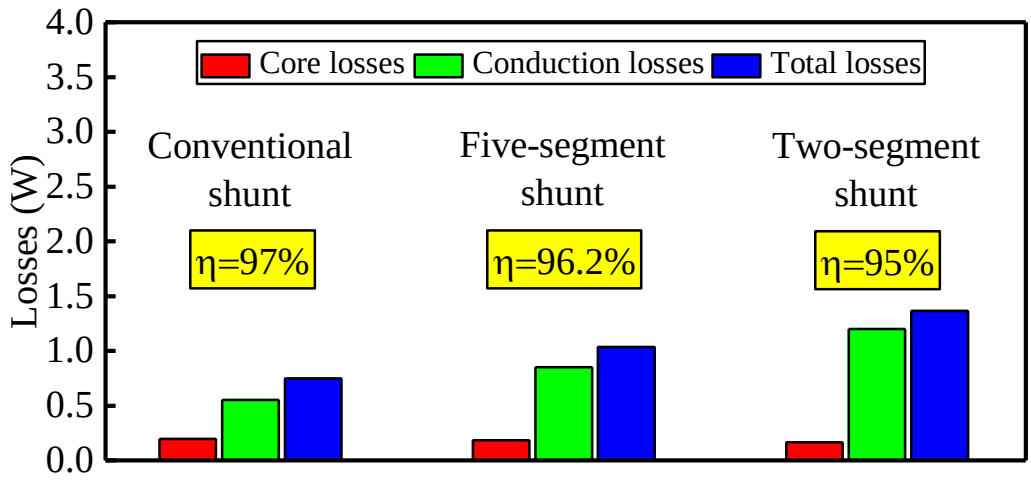

Fig. 5.9 Loss distribution of different topologies for output power of 25W.

TABLE 5.2 Volume comparison between different topologies.

Topology	t_{Sh} (mm)	μ_{Sh}	ℓ_{fG1}, ℓ_{tG1} (mm)	ℓ_{fG2}, ℓ_{tG2} (mm)	Volume (mm^3)
[12]	1.5	9.5	0.052	-	9228
[12]	1.4	10	0.06	-	9174
Five-segment	1.5	800	0.13	0.48	9328
Five -segment	1.4	800	0.13	0.45	9264
Two-segment	1.5	800	0.28	0.48	8374
Two-segment	1.4	800	0.28	0.45	8374

In **Table 5.2**, the volumes of the proposed topologies and the conventional topology with a low-permeability shunt for the same specifications are provided. As shown, the two-segment topology provides the lowest volume even though it suffers from lowest efficiency. In addition, the proposed topologies can provide the same specification with a range of designs for the shunt (which can be optimised as needed). However, the shunt in the conventional topology cannot be changed for a particular specification unless the permeability of the shunt itself changes. Therefore, based on **Table 5.2**, not only can the proposed topologies provide a higher power density but they also benefit from increased flexibility in design.

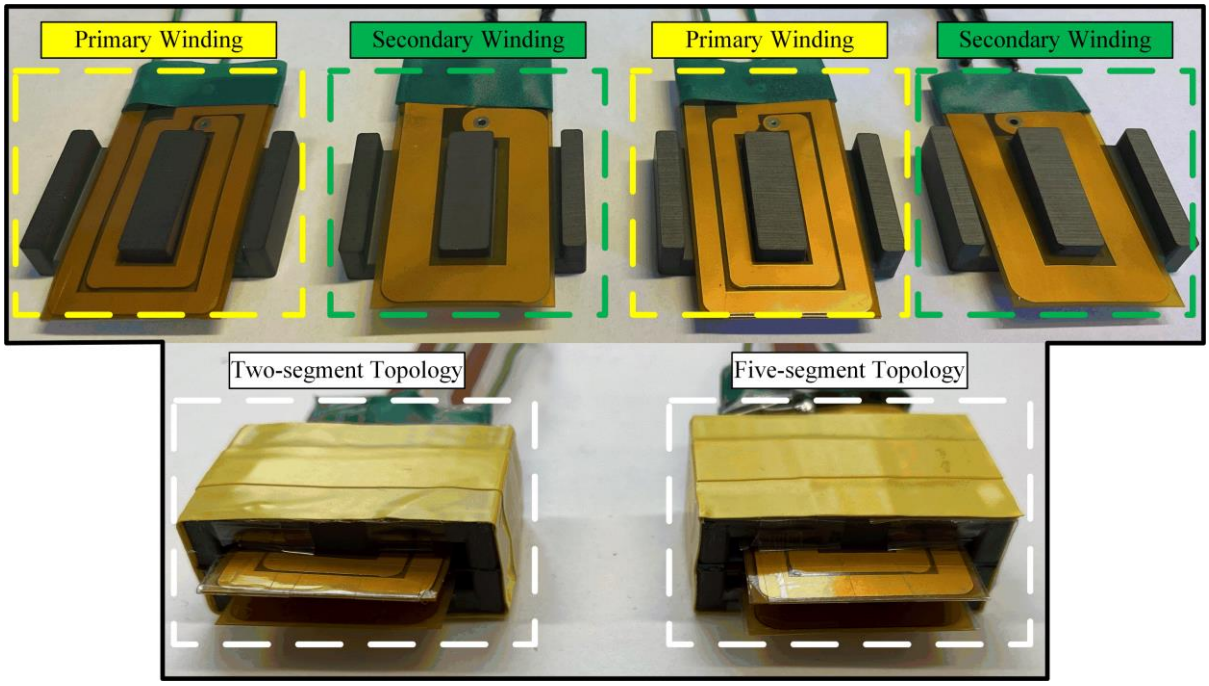

Fig. 5.10 Prototypes of the proposed topologies. Core: E32/6/20/R-3F4.

5.4.3 Experimental verification

To confirm the theoretical analysis and simulation results, the two- and five-segment topologies are built for the specification presented in **Table 5.1** and their prototypes are shown in **Fig. 5.10**. The measured leakage and magnetising inductances of both topologies at 200 kHz, measured by frequency analyser Omicron Bode 100, are presented in **Table 5.3**. The measured values are very close to the values obtained by modelling and simulation results. In addition, the primary self- and leakage inductance, and the AC resistance versus frequency for the five-segment and two-segment topologies are shown in **Fig. 5.11(a)** and **(b)**, respectively. As shown, the AC resistance of the two-segment topology is higher than the five-segment topology and therefore it has a lower efficiency. Proximity of the gap to the windings in the two-segment topology leads to higher fringing which explains the reason of this discrepancy.

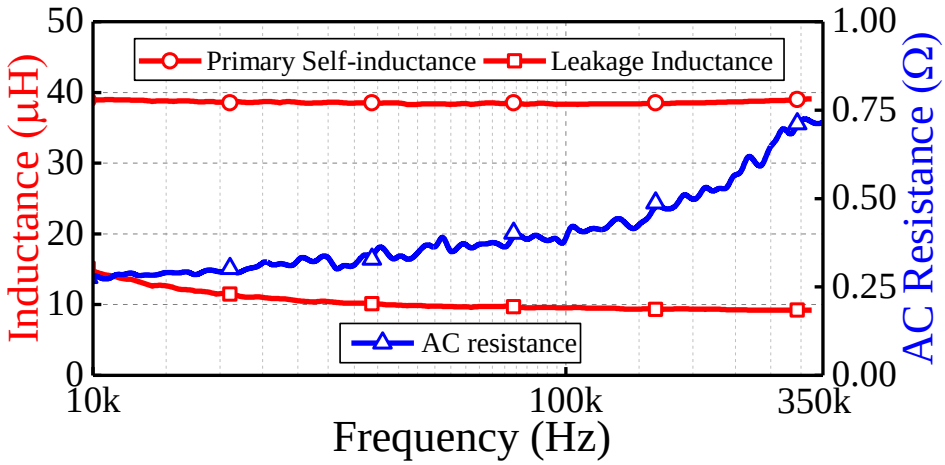

(a)

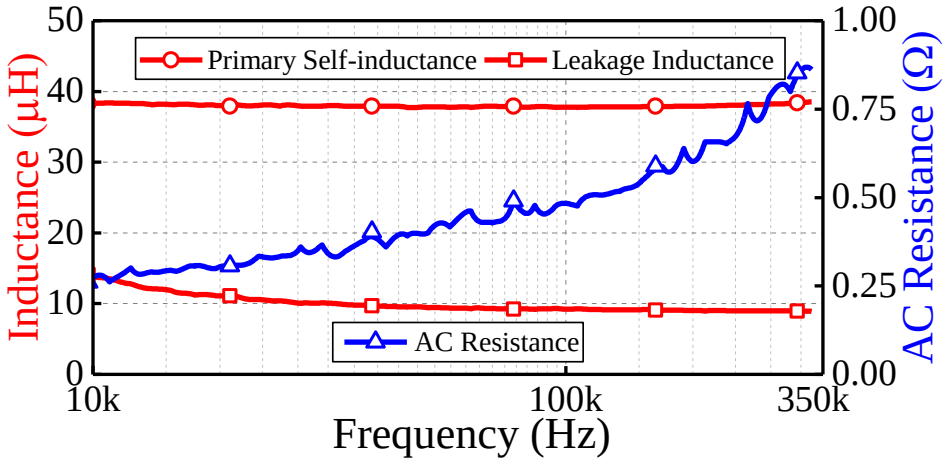

(b)

Fig. 5.11 Primary self-inductance and leakage inductance and AC resistance versus frequency. (a) Five-segment topology (IT1). (b) Two-segment topology (IT2).

TABLE 5.3 Parameters of the implemented transformers.

Topology	SYMBOL	Modeling	Simulation	Measurement
Five-segment	L_{fm}	29.08 µH	30.1 µH	29.6 µH
	L_{fLk}	8.86 µH	8.72 µH	9.23 µH
Two-segment	L_{tm}	28.81 µH	30.4 µH	28.95 µH
	L_{tLk}	8.61 µH	8.59 µH	8.95 µH

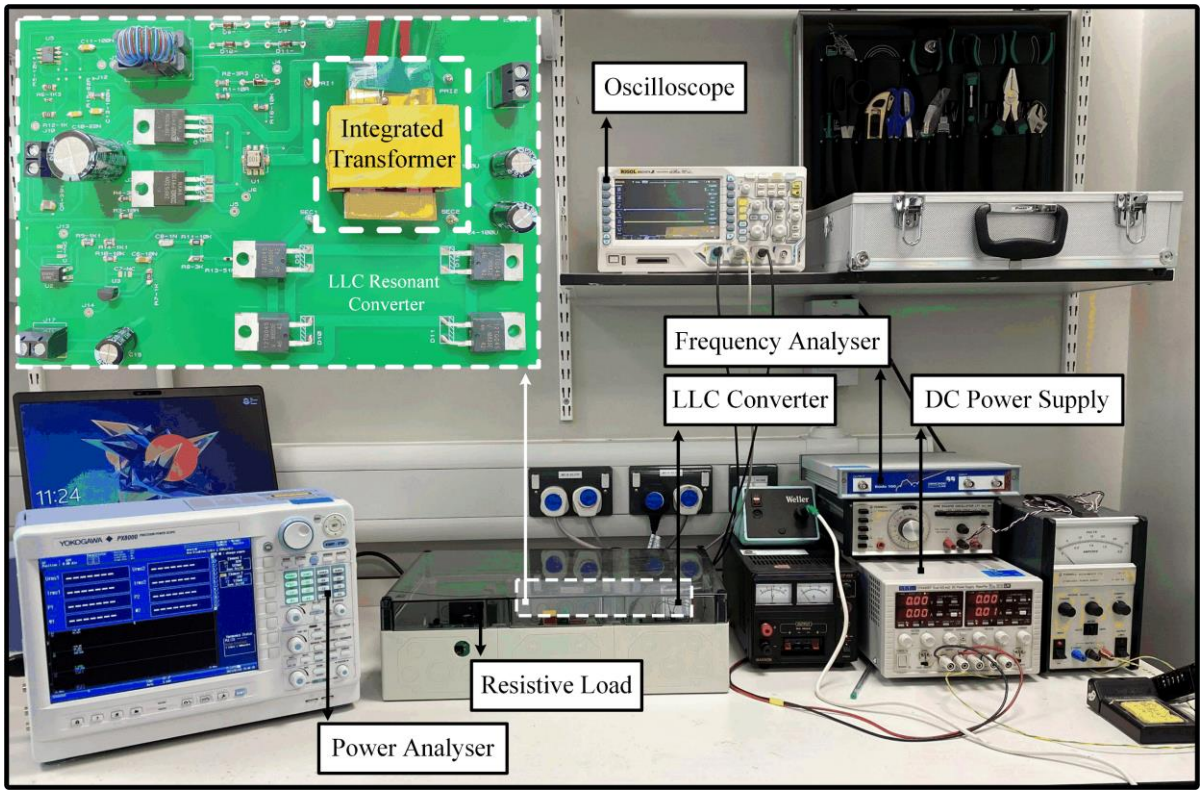

Fig. 5.12 Prototypes of the implemented LLC resonant converter.

To verify the performance of the proposed integrated transformers in practice, an LLC converter is implemented and shown in **Fig. 5.12**. The LLC converter has been designed according to the procedure outlined in Chapter 2 and [46] and its specification is shown in **Table 5.4**. In this design, the series and parallel inductors are integrated into the transformer.

TABLE 5.4 The implemented LLC converter's specification.

Symbol	Parameter	Value
$N_P: N_S$	Turns ratio	10:2
L_m	Magnetising inductance	29 μH
L_r	Resonant (series) inductance	9 μH
C_r	Resonant capacitance	39 nF
V_{In}	Input voltage	45-55 V
V_o	Output voltage	5 V
P_o	Output power	25 W
f_s	Switching frequency	200-350 kHz
S	Switches	IRF530N
D	Rectifier diodes	12CTQ045

The waveforms of the converter operating at a 210 kHz switching frequency using five-segment and two-segment topologies are shown in **Fig. 5.13(a)** and **(b)**, respectively. It can be seen that the switches are turned on at zero voltage (ZVS) because the drain-source voltage drops to zero and then the gate turns on immediately.

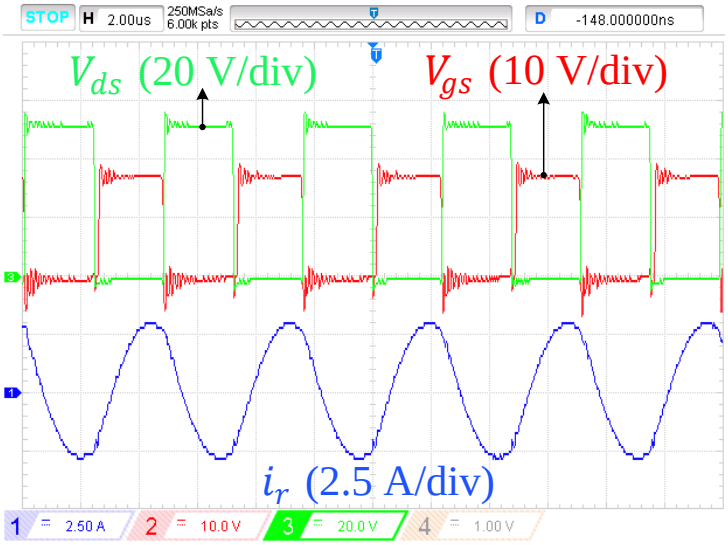

(a)

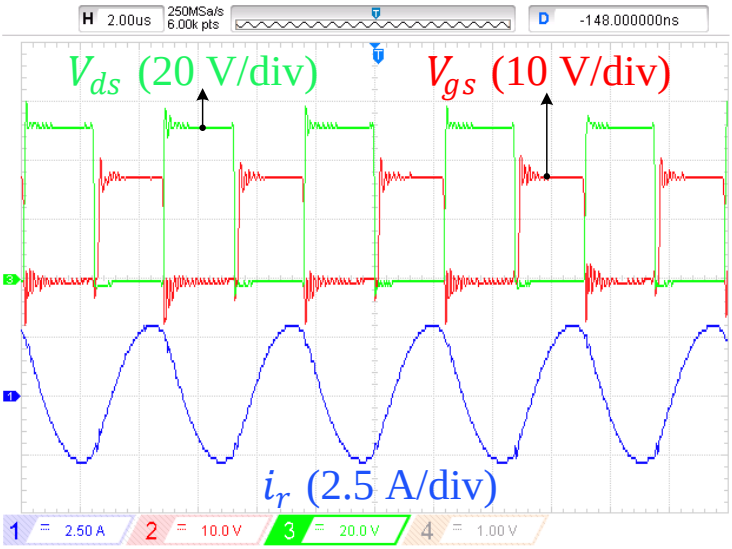

(b)

Fig. 5.13 Experimental results of the implemented LLC converter. (a) Five-segment topology (IT1). (b) Two-segment topology (IT2). V_{ds} is drain to source voltage, V_{gs} is gate to source voltage and i_r is the resonant current (primary current of the transformer).

The efficiency of the converter for both topologies (IT1 and IT2) is shown in **Fig. 5.14**. For this figure, the effect of the asynchronous rectifier is excluded because it is the dominant loss mechanism. It can be seen that, since the two-segment topology has higher AC resistance, it

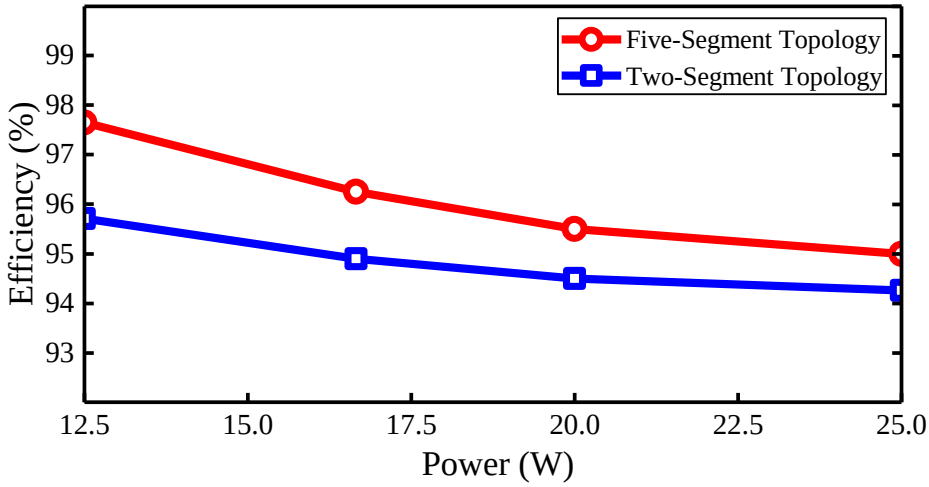

Fig. 5.14 Efficiency of the LLC converter (excluding the rectifier) at different load conditions.

suffers from lower efficiency compared to the five-segment topology. However, it benefits from easier manufacture since it needs only two segments and has smaller volume.

Thermal images of the proposed five- and two-segment topologies at nominal operating conditions are shown in **Fig. 5.15(a)** and **(b)**, respectively. It can be seen that the proposed transformer with five-segment shunt has a lower temperature (about 0.5°C) compared to the two-segment topology since it benefits from lower losses. In addition, the windings have a higher temperature compared to the cores since they have higher losses, which confirms the loss distribution presented in **Fig. 5.9**. Moreover, **Fig. 5.15** shows that the designed integrated transformer operates within an acceptable temperature range, ensuring that neither the core nor the windings are damaged.

It is worth noting that conducting an experimental comparison between the proposed topologies with high-permeability shunt and the conventional topology with low-permeability shunt would have provided even stronger support for the analysis. Unfortunately, during the time of the experiment, it was not feasible to find and order low-permeability materials suitable for the shunt. This situation further highlights the challenges posed by the unavailability of low-permeability materials in the market.

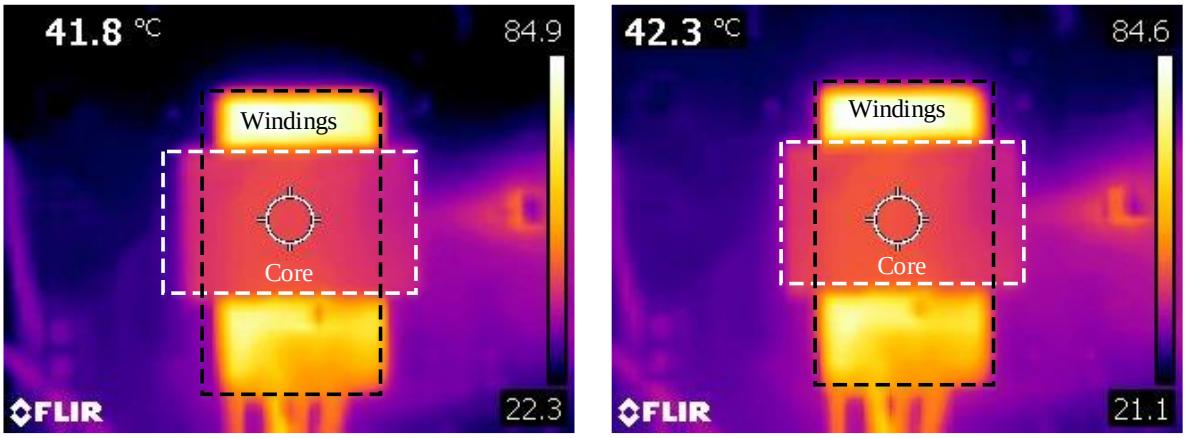

(a) (b)

Fig. 5.15 Thermal image of the transformer. (a) Five-segment topology (IT1). (b) Two-segment topology (IT2).

The higher number of segments leads the manufacturing to difficulty and higher cost, but it improves the efficiency of the transformer because of lower fringing. For odd-numbered segments, a five-segment shunt is considered in this work since the reluctance modelling of the topology is very similar to the conventional topology with low-permeability shunt presented in [12]. The even-numbered shunts (for example two) provide a higher power density since the window area is occupied for the shunt. However, even-numbered shunts suffer from higher losses because of fringing effect. Higher odd- and even-numbered segments could have been considered for the proposed topologies to improve the efficiency, but it would come with the penalty of more complicated manufacturing and higher cost.

It should also be noted that the application of the proposed topologies is not limited only to the LLC converter and can also be extended to other converters *viz* phase-shifted full-bridge converters and dual-active bridge converters.

5.5 Discussion

The proposed topologies and the conventional topology share similar structures, with the only difference lying in their shunt configurations. As a result, the proposed topologies still retain the benefits of planar transformers, including high power density, enhanced cooling capability, modularity, and manufacturing simplicity. However, a high-permeability segmental magnetic

shunt technique slightly decreases the efficiency of the transformer; thus, a fair question is whether using the proposed high-permeability segmental shunts is a suitable alternative to using the conventional low-permeability single shunt approach. Hence, the advantages of the proposed topologies are discussed below.

The low-permeability magnetic shunt has temperature-dependent permeability which results in non-stable leakage inductance.

The natural permeability of soft ferrites is a high value. For a particular chemical composition, there is only one permeability and it is therefore easily made available in a range of geometries and sizes. This differs from low-permeability materials whose permeability must be artificially reduced to meet the particular requirement of an application. For these reasons, high-permeability shunts are generally both cheaper and more widely available than low-permeability shunts.

Low-permeability materials offer limited options in terms of permeability, which restricts the flexibility of the integrated transformer's design. However, the proposed topologies use vertical air gaps to approximate the same bulk permeability as a conventional low-permeability one-segment shunt. This allows the transformer to be designed with greater flexibility. In other words, adjusting the air gaps in a segmental shunt is much easier compared to modifying the permeability of a non-segmental shunt.

In the proposed topologies, the magnetising and leakage inductances are decoupled in the design process, leading to higher flexibility in design. This is in contrast to the low-permeability single shunt topology where the leakage and magnetizing inductances are only decoupled for a limited range.

The efficiency difference between the five-segment topology and conventional topology is 0.8 percentage points, which is negligible. In addition, even though the two-segment topology has lower efficiency compared to the conventional one (2 percentage points – see **Fig. 5.9**), it provides higher power density (10% more as presented in **Table 5.2**).

In addition, it has been already shown in the literature [137, 138] that using distributed air gaps in a core is better than using low-permeability materials due to the limitations of the low-permeability materials. This distribution air gap method could be extended to be used in the proposed topologies to address the issue of lower efficiency.

The reduced costs from using standard high-permeability materials are likely to be reduced (although not eliminated) for very large production runs. However, there are many small-scale manufacturers with production runs of hundreds to thousands of items for whom a specific magnetic shunt is prohibitively expensive. These manufacturers can still benefit from planar transformers with shunts to achieve high efficiency, but using materials they can access quickly and at commercially viable costs. While less important, availability for prototyping is also a consideration, especially since the proposal allows for rapid reconfiguration using off-the-shelf materials.

5.6 Conclusion

Two new structures (IT1 and IT2) for the shunt-inserted integrated planar transformers have been presented in this Chapter. These structures benefit from a segmental magnetic shunt based on widely-available high-permeability materials which can be found in different sizes and at lower price. The analysis and modelling of both structures, considering the leakage flux going through the shunt, window area and windings, are presented. The leakage and magnetising inductances are decoupled from each other in the proposed topologies and can be designed separately by the thickness of the shunt and the length of the horizontal air gap, respectively.

FEA simulation and experimental verification are provided, and they show a good agreement with theoretical predictions. It is shown that while the efficiency of the proposed topologies is slightly less than the conventional topology with low-permeability materials, the power density is enhanced about 10%.

An LLC resonant converter is implemented to prove the performance of the proposed integrated transformers in practice. The prototype shows that both topologies can integrate all three magnetic components of an LLC converter in a single planar transformer as the converter operates properly and its switches are switched at ZVS. The efficiency of the LLC converter (excluding the rectifier) with proposed transformers are measured. According to the measured

values, the efficiency of the five-segment topology is 1 percentage points more than two-segment topology even though its power density is about 11% less than two-segment topology. Finally, the advantages of the proposed topologies compared to the conventional topology with low -permeability shunt are discussed to show they can be a suitable alternative for the conventional topology.

The structures (IT1 and IT2) proposed in Chapter 5 do not need a shunt with specific permeability and dimensions. However, the inserted shunt has multiple segments and has to be located between two E-cores which makes the implementation difficult and leads to high assembly cost. Therefore, to address this issue, a new topology (termed IT3) for achieving high leakage inductance in inserted-shunt integrated planar transformers is proposed in Chapter 6.

Chapter 6

Fully-Integrated Solid Shunt Planar Transformer for LLC Resonant Converters

In this Chapter, a new topology (termed IT3) for achieving high leakage inductance in inserted-shunt integrated magnetic planar transformers is proposed. In the proposed topology, two one-segment shunts are placed across the planar E-core air gap and between the primary and secondary windings. The proposed topology benefits using solid inexpensive ferrite shunts, making manufacturing easier. A detailed mathematical model is derived from which a design methodology is developed, providing accurate estimation for the leakage and magnetising inductances. The theoretical analysis has been verified using finite-element analysis and experimental implementation. AC resistance analysis and efficiency comparison are also presented for the proposed topology and one of the inserted-segmental-shunt topologies presented in Chapter 5, which shows the proposed topology provides higher efficiency because of lower AC resistance. In addition, an isolated LLC resonant converter is designed and built to investigate the performance of the proposed topology in practice. The three magnetic components needed for the designed LLC resonant converter is integrated in a single planar transformer using the proposed topology and the converter operates properly.

6.1 Introduction

Inserting a low-permeability magnetic shunt in the centre of a planar transformer while its primary and secondary windings are separated (by being located above and below the magnetic shunt) can provide a high leakage inductance and provides greater and more precise control of its value [12, 130, 134]. Even though this structure enhances the leakage inductance and allows for its value to be estimated precisely, the inserted shunt must have a specific and unusually low permeability, leading the design and manufacturing to difficulty and higher cost [135, 137, 138].

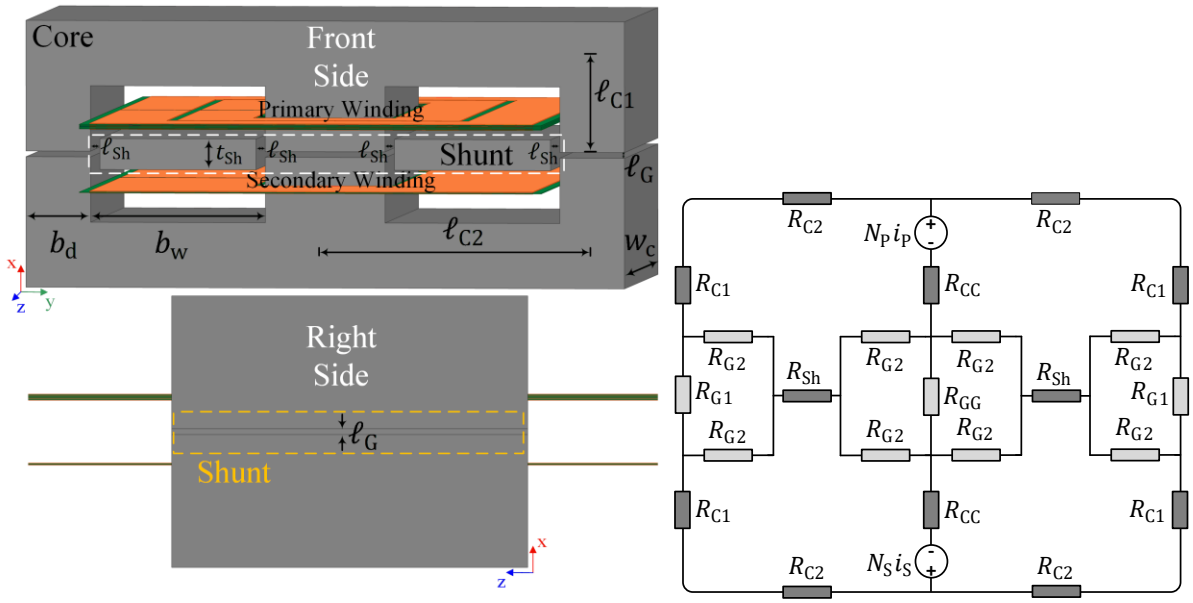

(a) (b)

Fig. 6.1 The inserted-shunt integrated planar transformer with segmental shunt (IT2). (a) Schematic. (b) Reluctance model.

Two new structures (IT1 and IT2) were suggested in Chapter 5 to overcome this problem. These structures are formed by interleaving highly permeable ferrite with thin plastic spacers to form segmental magnetic shunts. In these structures, a shunt with the same bulk permeability as the conventional design (which uses a low-permeability shunt) is approximated by regulating the length of the air gaps between segments across the high-permeability shunt (ℓ_{Sh}).

The topology of an inserted-segmental-shunt integrated planar transformer (IT2) and its reluctance model are shown in **Fig. 6.1(a)** and **(b)**, respectively. **Fig. 6.1(a)** shows this topology when a two-segment shunt (IT2) is used and this topology with five-segment (IT1) shunt can also be found in Chapter 5. As shown in **Fig. 6.1**, a segmental shunt is inserted between the E-cores in line with air gap, and the primary and secondary windings are separated by being placed above and below the segmental shunt.

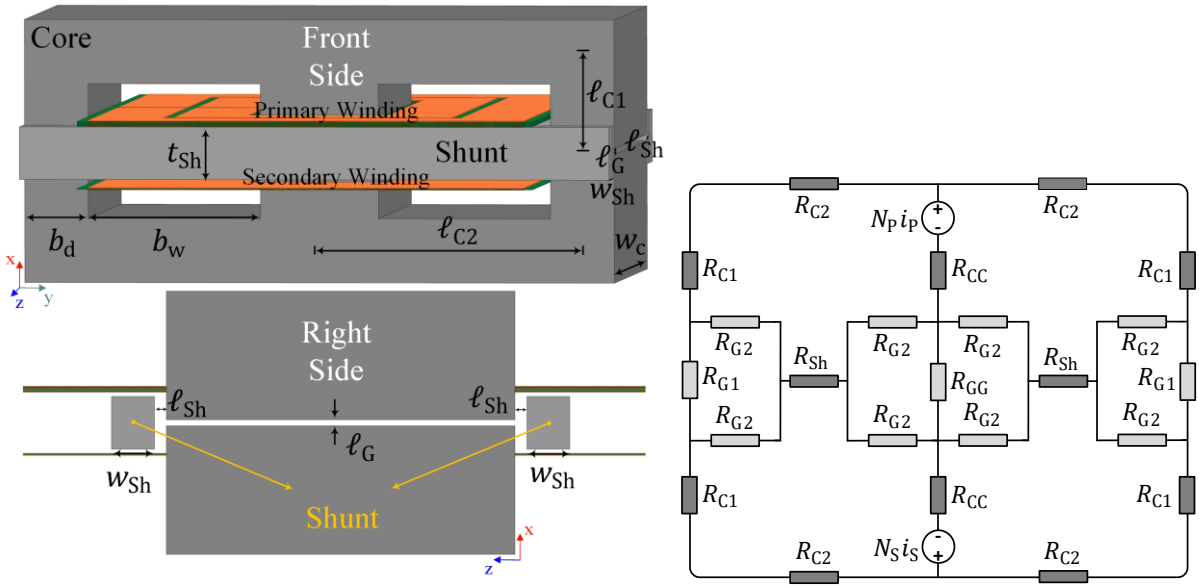

(a) (b)

Fig. 6.2 The inserted-shunt integrated planar transformer with solid shunt (IT3). (a) Schematic. (b) Reluctance model.

In this topology, the leakage inductance can be regulated by changing the thickness of the shunt, t_{Sh}, and the shunt air gap length, ℓ_{Sh}, and the magnetising inductance can be regulated by air gap length, ℓ_G, separation between the E-cores. This topology guarantees a high leakage inductance and accurate estimation of its value. However, the difficulty with this topology is locating the segmental shunt in between the E-cores and requiring a segmental shunt (minimum two segments), which results in manufacturing difficulty. To address this issue, a new topology (termed IT3) for the integrated transformer is proposed, which benefits from overlaying the solid shunt across the E-core air gap and thereby simplifying manufacture.

The new structure (IT3) shown in **Fig. 6.2(a)** is proposed in this Chapter. In the proposed topology, two solid shunts are placed on the front and back (x-y plane) of a planar transformer while primary and secondary windings are separated by being located above and below the shunts such that some of the primary winding generated flux is shunted away from the secondary winding in order to realise the leakage inductance.

In this topology (**Fig. 6.2**), the bulk permeability of the shunts is regulated by changing their distance from the core (ℓ_{Sh}). Therefore, not only does the proposed structure benefit from using

high-permeability materials for the shunts but its inserted shunts also do not need to be segmental and can be located easier.

The proposed structure is analysed and modelled and a design guideline is also provided. The theoretical analysis is verified by comparison with finite-element analysis (FEA) simulation and experimental measurements. The AC resistance analysis and efficiency comparison for the proposed structure and one of the inserted-segmental-shunt presented in Chapter 5 (IT2) are provided. In addition, in order to examine the performance of the proposed structure in practice, an isolated LLC resonant converter using the proposed integrated transformer is implemented and investigated. The prototype proves that the proposed structure can integrate all three magnetic components of an LLC converter in a single planar transformer.

6.2 Proposed integrated magnetic transformers

The schematic of the proposed topology and its reluctance model are shown in **Fig. 6.2(a)** and **(b)**, respectively. The air gap ℓ_{G} is inserted in between the E-cores to regulate magnetising inductance and the air gap ℓ_{Sh} is added in between the shunts and E-cores to regulate the leakage inductance. As shown in **Fig. 6.1** and **Fig. 6.2**, the proposed topology provides the same reluctance model as the inserted-segmental-shunt topology (IT2) but its inserted shunts are not segmental and can be located more easily.

One might think that inserting one solid low-permeability shunt between two E-cores (presented in [12]) would be easier than overlaying two identical solid shunts on the front and back of the transformer. However, manufacturing a solid shunt from low-permeability materials (e.g. a powder core) is harder and more expensive than manufacturing a solid shunt based on high-permeability materials like ferrite. In addition, low-permeability magnetic materials have temperature-dependent permeability, leading to unstable leakage inductance [133, 135, 137, 138, 169].

In the following, the modelling of the proposed structure is discussed for estimation of the leakage and magnetising inductances.

Equation (6-1) can be used to calculate the total leakage inductance, L_{Lk}.

$$E = \frac{1}{2}\iiint_V BH \,\mathrm{d}V = \frac{1}{2}L_{\mathrm{Lk}} i_{\mathrm{P}}^2 \tag{6-1}$$

where V is the cuboid that incorporates the magnetic shunt, window area and the windings, i_{P} is the primary current, B is the flux density and H is the magnetic field intensity.

From (6-1), to calculate the leakage inductance, the energy stored in the windows area, and the primary and secondary windings, alongside the inserted shunts (including their air gaps) need to be calculated. Therefore, the energy stored in each part is calculated separately in the following and then the total leakage inductance can be obtained by summation of energies and from (6-1).

6.2.1 Energy stored in window area

The magnetomotive force (MMF) of each layer of the primary winding, $\mathfrak{F}_{\mathrm{P}}$, may be obtained from (6-2), where k_{P} is the number of turns in each layer of the primary winding.

$$\mathfrak{F}_{\mathrm{P}} = k_{\mathrm{P}} i_{\mathrm{P}} \tag{6-2}$$

If n_{P} and n_{S} are the number of layers of the primary and secondary windings, respectively, then the MMF within the window area, $\mathfrak{F}_{\mathrm{air}}$, is equal to $n_{\mathrm{P}}\mathfrak{F}_{\mathrm{P}}$ and the magnetic field intensity within the air area, H_{air}, may be obtained by (6-3).

$$H_{\mathrm{air}} = \frac{n_{\mathrm{P}}\mathfrak{F}_{\mathrm{P}}}{b_{\mathrm{w}}} \tag{6-3}$$

where b_{w} is the width of the winding area (defined in **Fig. 6.2(a)**). From (6-1), the stored energy of leakage inductance in air area, E_{air}, (defined in **Fig. 6.3**) can be calculated as (6-4).

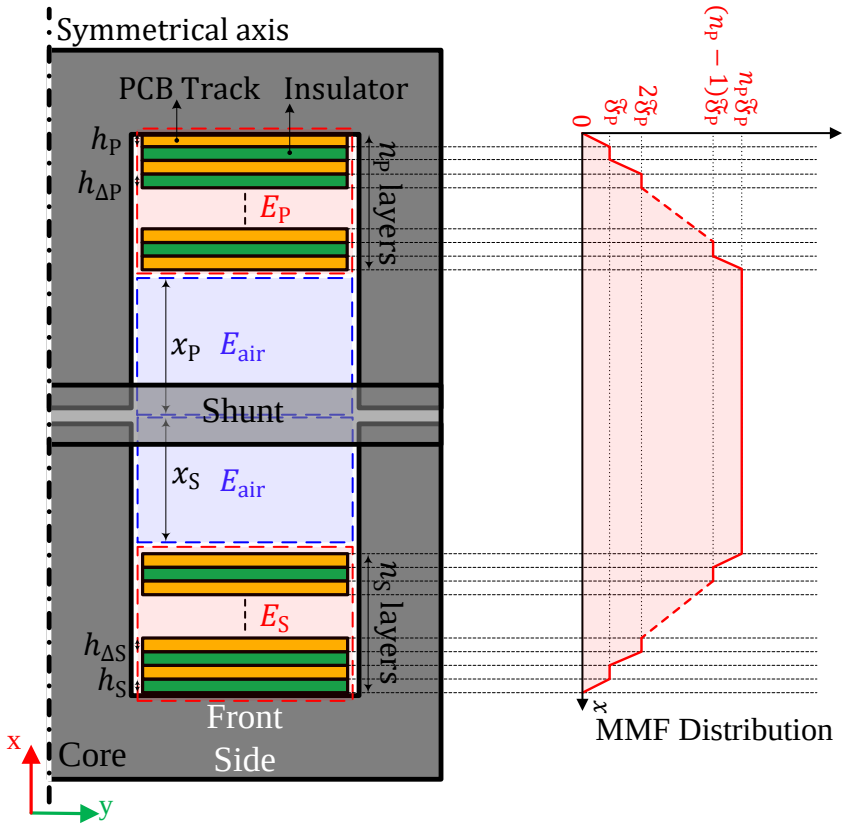

Fig. 6.3 MMF distribution for the proposed structure (IT3).

$$E_{air} = \frac{1}{2}\mu_0 w_c b_w \int_{-x_S}^{x_P} H_{air}^2 dx \tag{6-4}$$

where w_c is the core depth and x_P and x_S are the distances from the primary and secondary windings to centre of the transformer, respectively, shown in **Fig. 6.3**. By substituting (6-2) and (6-3) into (6-4), E_{air} in both right and left windows of E-cores can be calculated as (6-5).

$$E_{air} = \mu_0 w_c \frac{n_P^2 k_P^2 i_P^2}{b_w}(x_P + x_S) \tag{6-5}$$

6.2.2 Energy stored in primary and secondary windings

According to the MMF distribution presented in **Fig. 6.3** (obtained based on method outlined in [129, 130, 134]), the stored energy in PCB layers of primary and secondary windings can be

calculated. Ouyang, *et al*, [129] proved that energy stored in the primary and secondary windings may be obtained as (6-6) and (6-7), respectively.

$$E_{\mathrm{P}} = \frac{1}{6}\mu_0 \frac{w_{\mathrm{c}}}{b_{\mathrm{w}}} k_{\mathrm{P}}^2 [h_{\Delta\mathrm{P}}(2n_{\mathrm{P}}^3 - 3n_{\mathrm{P}}^2 + n_{\mathrm{P}}) + 2h_{\mathrm{P}} n_{\mathrm{P}}^3] i_{\mathrm{P}}^2 \tag{6-6}$$

$$E_{\mathrm{S}} = \frac{1}{6}\mu_0 \frac{w_{\mathrm{c}}}{b_{\mathrm{w}}} k_{\mathrm{S}}^2 [h_{\Delta\mathrm{S}}(2n_{\mathrm{S}}^3 - 3n_{\mathrm{S}}^2 + n_{\mathrm{S}}) + 2h_{\mathrm{S}} n_{\mathrm{S}}^3] i_{\mathrm{S}}^2 \tag{6-7}$$

In (6-6) and (6-7), h_{P} and h_{S} are defined as the thickness of the PCB tracks of the primary and secondary windings, respectively, and $h_{\Delta\mathrm{P}}$ and $h_{\Delta\mathrm{S}}$ are defined as the thickness of PCB insulation layers of the primary and secondary windings, respectively.

6.2.3 Energy stored in magnetic shunts

The energy stored in the shunts can be calculated by the method outlined in Chapter 5. The reluctance model of the proposed topology is presented in **Fig. 6.2(b)**, where $\mathcal{R}_{\mathrm{G1}}$, $\mathcal{R}_{\mathrm{GG}}$ and $\mathcal{R}_{\mathrm{G2}}$ are air gap reluctances, $\mathcal{R}_{\mathrm{C1}}$, $\mathcal{R}_{\mathrm{C2}}$ and $\mathcal{R}_{\mathrm{CC}}$ are core reluctances and $\mathcal{R}_{\mathrm{Sh}}$ is shunt reluctance and they can be calculated by (6-8)-(6-14). In the reluctance modelling presented in **Fig. 6.2(b)**, it is assumed both shunts are located at the same distance from the cores (ℓ_{Sh}), and therefore they can be considered only one shunt but with double thickness ($2t_{\mathrm{Sh}}$).

$$\mathcal{R}_{\mathrm{C1}} = \frac{\ell_{\mathrm{C1}}}{\mu_0 \mu_{\mathrm{r}} b_{\mathrm{d}} w_{\mathrm{c}}} \tag{6-8}$$

$$\mathcal{R}_{\mathrm{C2}} = \frac{\ell_{\mathrm{C2}}}{\mu_0 \mu_{\mathrm{r}} b_{\mathrm{d}} w_{\mathrm{c}}} \tag{6-9}$$

$$\mathcal{R}_{\mathrm{CC}} = \frac{\ell_{\mathrm{C1}}}{\mu_0 \mu_{\mathrm{r}} A_{\mathrm{c}}} \tag{6-10}$$

$$\mathcal{R}_{\mathrm{Sh}} = \frac{b_{\mathrm{w}}}{2\mu_0 \mu_{\mathrm{Sh}} t_{\mathrm{Sh}} w_{\mathrm{Sh}}} \tag{6-11}$$

$$\mathcal{R}_{G1} = \frac{\ell_G}{\mu_0(b_d + \ell_G)(w_c + \ell_G)} \tag{6-12}$$

$$\mathcal{R}_{G2} = \frac{\ell_{Sh}}{\mu_0(b_d + \ell_{Sh})(t_{Sh} + \ell_{Sh})} \tag{6-13}$$

$$\mathcal{R}_{GG} = \frac{\ell_G}{\mu_0(2b_d + \ell_G)(w_c + \ell_G)} \tag{6-14}$$

where μ_0 is μ_r and μ_{Sh} are the permeability of the air, and the relative permeability of the core and shunt, respectively. A_c is the core effective cross-sectional area and the definition of other quantities can be found in **Fig. 6.2(a)**. Hurley, *et al*, [168] showed that an effective cross-sectional area of the air gap with dimension *a* by *b* are equal to (*a*+*g*) by (*b*+*g*) when the fringing effect is considered and *g* is the length of the studied air gap.

According to the reluctance model presented in **Fig. 6.2(b)** and the method outlined in Chapter 5, the leakage inductance caused by the inserted magnetic shunts referred to the primary side and magnetising inductance for the proposed topology can be calculated by (6-15) and (16), respectively.

$$L_{Lk\_Sh} = \frac{4N_P^2}{\mathcal{R}_E + 2(\mathcal{R}_{Sh} + \mathcal{R}_A + \mathcal{R}_B)} \tag{6-15}$$

$$L_m = \frac{2N_P^2(\mathcal{R}_{Sh} + \mathcal{R}_A + \mathcal{R}_B)}{\mathcal{R}_E(\mathcal{R}_E + 2(\mathcal{R}_{Sh} + \mathcal{R}_A + \mathcal{R}_B))} \tag{6-16}$$

where N_P is primary turns number ($n_P k_P$) and R_E can be defined as

$$\mathcal{R}_E = \mathcal{R}_{C1} + \mathcal{R}_{C2} + 2\mathcal{R}_{CC} + \mathcal{R}_C + \mathcal{R}_D \tag{6-17}$$

and $\mathcal{R}_A$, $\mathcal{R}_B$, $\mathcal{R}_C$ and $\mathcal{R}_D$ are defined as follows:-

$$\mathcal{R}_{\mathrm{A}} = \frac{\mathcal{R}_{\mathrm{G2}}^2}{\mathcal{R}_{\mathrm{G1}} + 2\mathcal{R}_{\mathrm{G2}}} \tag{6-18}$$

$$\mathcal{R}_{\mathrm{B}} = \frac{\mathcal{R}_{\mathrm{G2}}^2}{2\mathcal{R}_{\mathrm{GG}} + 2\mathcal{R}_{\mathrm{G2}}} \tag{6-19}$$

$$\mathcal{R}_{\mathrm{C}} = \frac{\mathcal{R}_{\mathrm{G1}}\mathcal{R}_{\mathrm{G2}}}{\mathcal{R}_{\mathrm{G1}} + 2\mathcal{R}_{\mathrm{G2}}} \tag{6-20}$$

$$\mathcal{R}_{\mathrm{D}} = \frac{2\mathcal{R}_{\mathrm{GG}}\mathcal{R}_{\mathrm{G2}}}{2\mathcal{R}_{\mathrm{GG}} + 2\mathcal{R}_{\mathrm{G2}}} \tag{6-21}$$

From (6-1), (6-5)-(6-7) and (6-15), the total leakage inductance of the proposed topology may be obtained by (6-22).

$$L_{\mathrm{Lk}} = 2\mu_0 w_{\mathrm{c}} \frac{N_{\mathrm{P}}^2}{b_{\mathrm{w}}}(x_{\mathrm{P}} + x_{\mathrm{S}}) + \frac{4N_{\mathrm{P}}^2}{\mathcal{R}_{\mathrm{E}} + 2(\mathcal{R}_{\mathrm{Sh}} + \mathcal{R}_{\mathrm{A}} + \mathcal{R}_{\mathrm{B}})} + \frac{1}{3}\mu_0 \frac{w_{\mathrm{c}}}{b_{\mathrm{w}}} k_{\mathrm{P}}^2 n_{\mathrm{P}}^2 \sum_{i=\mathrm{P,S}} \left[h_{\Delta i}\left(2n_i - 3 + \frac{1}{n_i}\right) + 2h_i n_i \right] \tag{6-22}$$

Therefore, (6-16) and (6-22) can be used to design an integrated transformer according to the required magnetising and leakage inductances.

To demonstrate the fidelity of control achievable with the proposed topology, the calculated leakage and magnetising inductances for the proposed topology for different thickness of the shunt, t_{Sh}, and air-gap lengths, ℓ_{G} and ℓ_{Sh}, are presented in **Fig. 6.4(a)** and **(b)**, respectively. It can be seen that the magnetising inductance is only influenced by air-gap length between cores (ℓ_{G}) and is not significantly affected by changing the thickness of the shunt and ℓ_{Sh}. On the other hand, the leakage inductance is mainly affected by the distance between shunts and cores (ℓ_{Sh}) and also the thickness of the shunt (t_{Sh}). Hence, in the proposed structure, the leakage and magnetising inductances are decoupled from each other and can be regulated separately, leading the design process to higher flexibility.

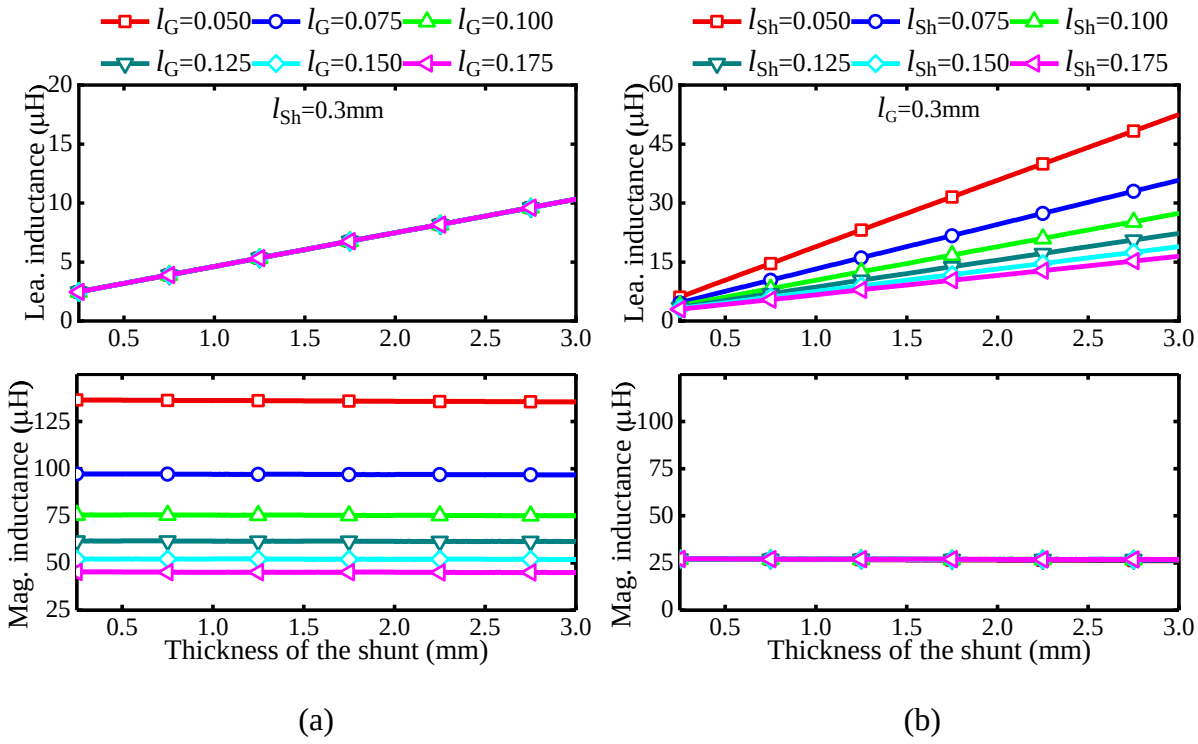

(a) (b)

Fig. 6.4 The calculated leakage and magnetising inductance versus thickness of the shunt. (a) For different E-core air gaps (ℓ_G). (b) For different distances from shunts to cores (ℓ_{Sh}). Core: E32/6/20/R-3F4, ℓ_G and ℓ_{Sh} in mm, w_{Sh}=2.5mm, N_P=10, N_S=2, n_P=5, n_S=2, k_P=2, k_S=1, x_P= x_S=1.5mm.

The leakage inductance distribution (between shunt, air and winding) of the proposed integrated transformer for different thicknesses of the shunt (t_{Sh}) and distances from shunts to cores (ℓ_{Sh}) are shown in **Fig. 6.5(a)** and **(b)**, respectively. As shown, the leakage inductance (L_{Lk}) is mainly affected by the shunt's dimensions and ℓ_{Sh}. The leakage inductance, caused by the window area (L_{Lk_air}) and windings (L_{Lk_Wi}), is only affected by the geometries of the core and PCB windings.

The characteristics of the proposed integrated transformer are now fully investigated and it is shown that the transformer can be designed for most reasonable specifications of leakage and magnetising inductances. It does not need any low-permeability materials or segmental shunts. Therefore, the proposed transformer is a great candidate for use in an LLC resonant converter where it can integrate the magnetic components into only a single transformer. In the following, the operation of the proposed transformer when it is designed to be used in a typical LLC resonant converter is investigated and its modelling is verified by simulation and experimental results.

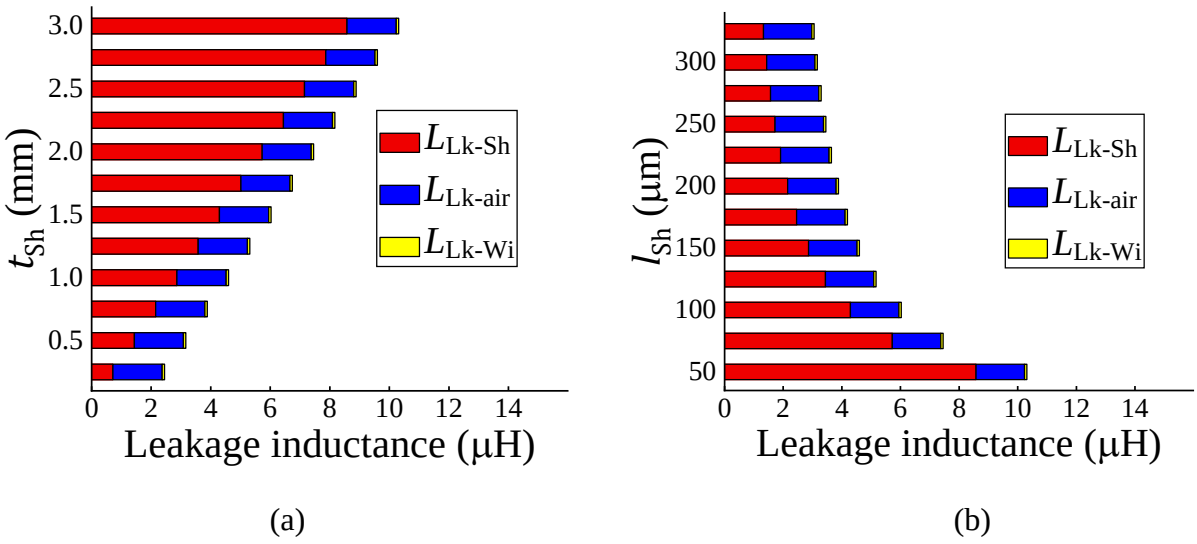

Fig. 6.5 Leakage inductance distribution. (a) For different thicknesses of the shunt (t_{Sh}), ℓ_{Sh}=0.3mm. (b) For different distances from shunts to cores (ℓ_{Sh}), t_{Sh}=0.5mm. Core: E32/6/20/R-3F4, w_{Sh}=2.5mm, N_P=10, N_S=2, n_P=5, n_S=2, k_P=2, k_S=1, x_P= x_S=1.5mm.

6.3 Simulation results

To verify the theoretical analysis presented in Section 6.2, FEA simulation of the proposed integrated transformer is provided. Therefore, an integrated transformer is designed and its specification is presented in **Table 6.1**. The leakage and magnetising inductances and the turns ratio of the designed transformer are selected according to the specification of an exemplar isolated LLC resonant converter presented in **Table 6.3**. The transformer core (E32/6/20/R-3F4) is selected based on the design guidelines outlined by core manufacturer in its catalogue [170], which provides charts indicating the appropriate core according to the stored energy and operating frequency. The thickness of the shunt and air gap lengths (ℓ_G and ℓ_{Sh}) are estimated in order to provide the required leakage and magnetising inductances using (6-16) and (6-22) and considering the dimensions of the selected core. In addition, the windings are designed considering the dimensions, skin effect, their root-mean-square (RMS) currents and the difficulty of manufacturing.

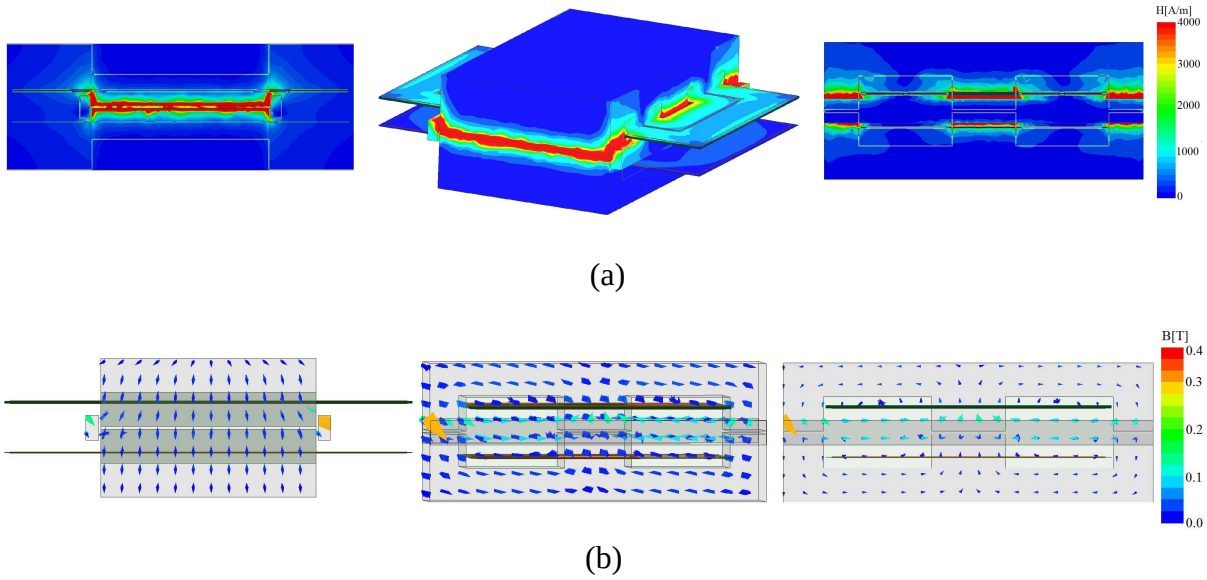

Fig. 6.6 FEA simulation results of the proposed topology. (a) Magnetic field intensity. (b) Magnetic flux density vectors. Core: E32/6/20/R-3F4.

The magnetic field intensity and flux density vectors for the proposed integrated transformer, while it is used in an LLC converter with specification presented in **Table 6.3**, are shown in **Fig. 6.6(a)** and **(b)**, respectively. According to **Fig. 6.6**, the magnetic field intensity and flux density vectors are dominant in the shunts and their air gaps (ℓ_{Sh}) rather than window area and PCB windings. The leakage flux and, therefore, inductance is mainly caused by the shunts. In addition, since the magnetic field intensity is highest in the core air gap (ℓ_{G}), the magnetising inductance is mainly affected by ℓ_{G}.

TABLE 6.1 Proposed structure's specification.

Symbol	Parameter	Value
N_{P}	Primary turns	10
N_{S}	Secondary turns	2
k_{P}	Turns per layer in primary	2
k_{S}	Turns per layer in secondary	1
n_{P}	Number of primary layers	5
n_{S}	Number of secondary layers	2
h_{P}, h_{S}	Primary and secondary conduction thickness	35 μm
$h_{\Delta\mathrm{P}}$, $h_{\Delta\mathrm{S}}$	Primary and secondary insulation thickness	30 μm
t_{Sh}	Shunt thickness	2.3 mm
w_{Sh}	Shunt wideness	1.5 mm
ℓ_{G}	Transformer air gap	0.28 mm
ℓ_{Sh}	Distance between shunt and cores	0.23 mm
x_{P}, x_{S}	Distance between primary and secondary windings and centre of cores	1.5 mm 1.5 mm

The leakage and magnetising inductances versus thickness of the shunt (t_{Sh}) and transformer air gap (ℓ_{G}) obtained from (6-16) and (6-22) and measured by FEA simulation are presented for the proposed topology in **Fig. 6.7(a)** and **(b)**, respectively. **Fig. 6.7** shows a good agreement between the theoretical and simulation results, verifying the analysis of the proposed structure.

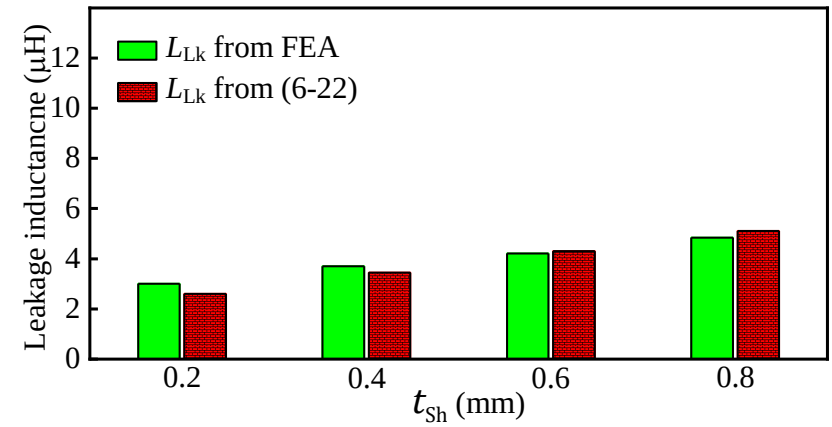

(a)

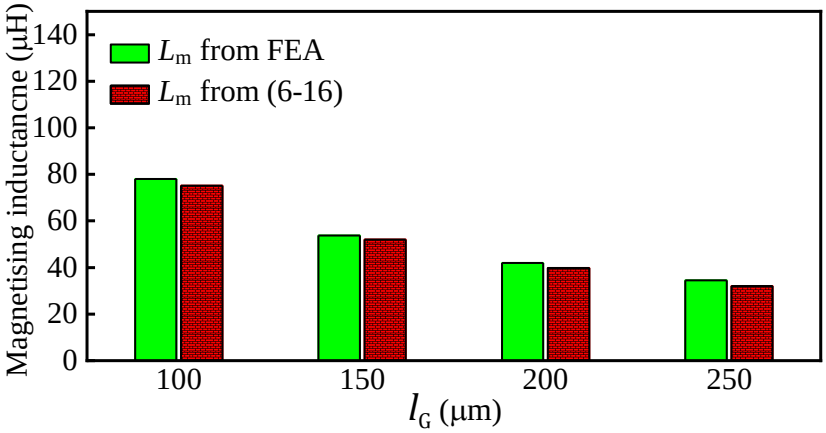

(b)

Fig. 6.7 Modelling validation by simulation study. (a) Leakage inductance ($\ell_G = 0.05$mm). (b) Magnetising inductance ($t_{Sh} = 1$mm). E32/6/20/R-3F4, $\ell_{Sh} = 0.2$mm.

The loss distribution and efficiency of the proposed topology (IT3) and that of the segmental-shunt topology (IT2), while they are used in the LLC converter at nominal operation, were calculated using FEA and are presented in **Fig. 6.8(a)** and **(b)**, respectively. As shown, the proposed topology benefits from lower conduction losses and therefore provides higher efficiency.

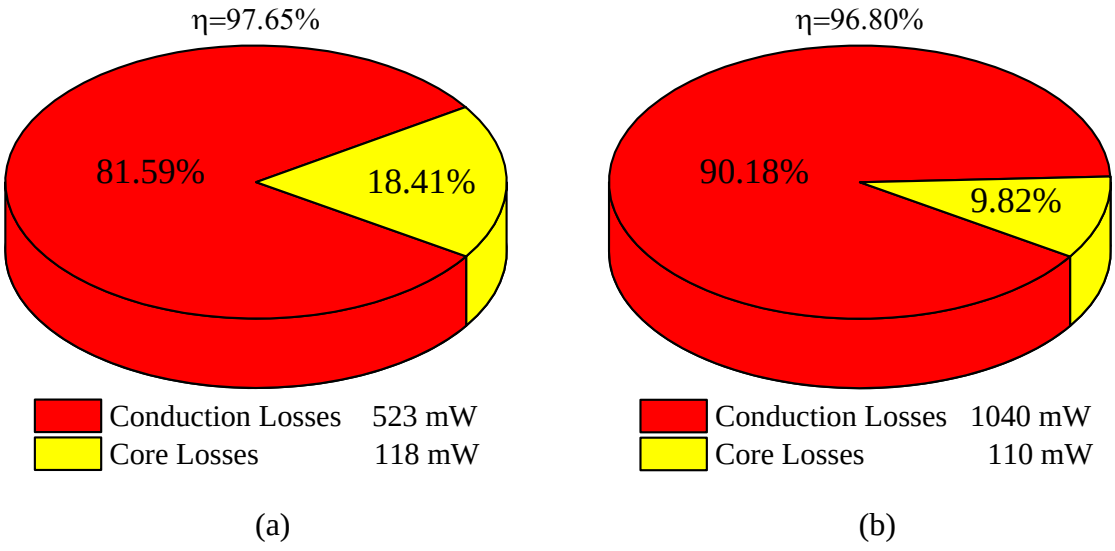

Fig. 6.8 Loss distribution. (a) Proposed topology (IT3). (b) Inserted-segmental-shunt topology (IT2). Core: E32/6/20/R-3F4.

TABLE 6.2 Parameters of the implemented integrated transformer.

Parameter	Symbol	Modelling	Simulation	Measurement
Magnetising inductance	L_{m}	28.7 μH	29.15 μH	29.4 μH
Leakage inductance	L_{Lk}	10.3 μH	9.3 μH	9.4 μH

6.4 Experimental verification

To verify theoretical analysis and simulation results, an integrated transformer based on the proposed structure with specification presented in **Table 6.1** is built and its prototype is shown in **Fig. 6.9**. In addition, the proposed topology (IT3) is compared with the inserted-segmental-shunt topology (IT2, called conventional) which is built with the same specification, also shown in **Fig. 6.9**.

Fig. 6.9 Prototypes of the proposed (IT3) and inserted-segmental-shunt (IT2, conventional) topologies. Core: E32/6/20/R-3F4.

The measured leakage and magnetising inductances of the proposed topology at 200 kHz measured by an Omicron Bode 100 analyser are shown in **Table 6.2**. The measured values are close to the values obtained by modelling and simulation results. In addition, the AC resistance, primary self-inductance and leakage inductance versus frequency for the proposed topology and the segmental shunt topology are shown in **Fig. 6.10(a)** and **(b)**, respectively. The measurement was carried out by the precision impedance analyser Omicron Bode 100 while the windings and shunt were located inside the planar cores. As shown in **Fig. 6.10**, both transformers have similar magnetising and leakage inductances. However, the AC resistance of the topology with inserted segmental shunt is higher than the proposed topology because of its high fringing losses (as mentioned in Chapter 5). As seen in **Fig. 6.2**, in the proposed topology, the air gaps of the shunt (labelled ℓ_{Sh}) are located further from the windings, reducing their coupling with the fringing field and hence reducing losses. In the segmental topology, the air gaps are between the lower and upper parts of the winding and therefore have greater coupling and therefore greater losses.

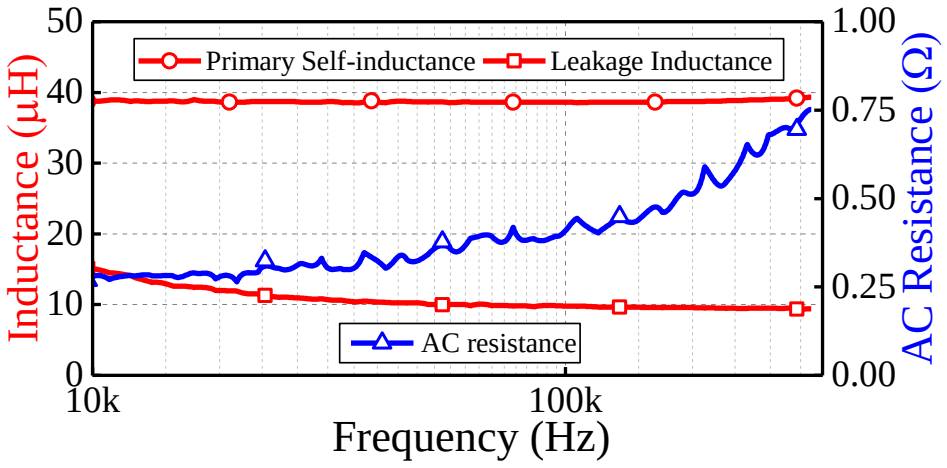

(a)

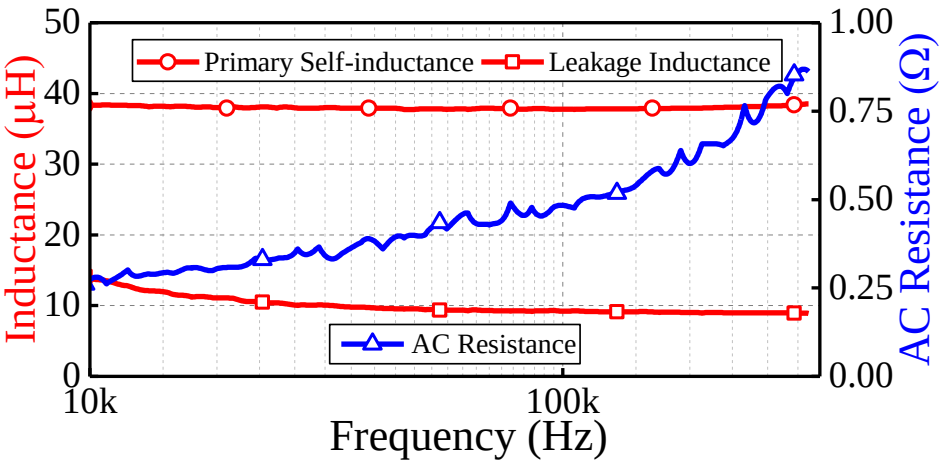

(b)

Fig. 6.10 AC resistance, primary self-inductance and leakage inductance versus frequency. (a) Proposed topology (IT3). (b) Inserted-segmental-shunt topology (IT2).

To verify the performance of the proposed integrated transformer in practice, an LLC resonant converter is implemented with the specification presented in **Table 6.3** calculated according to the design procedure outlined in Chapter 2 and [46], as shown in **Fig. 6.11**. In this design, the series and parallel inductances are integrated into the transformer. The waveforms of the converter operating at 210 kHz using (a) the proposed topology and (b) the topology with inserted-segmental-shunt are shown in **Fig. 6.12**. It can be seen that the switches are turned on at zero voltage (ZVS) because the switch gate turns on after its drain-source voltage drops to zero.

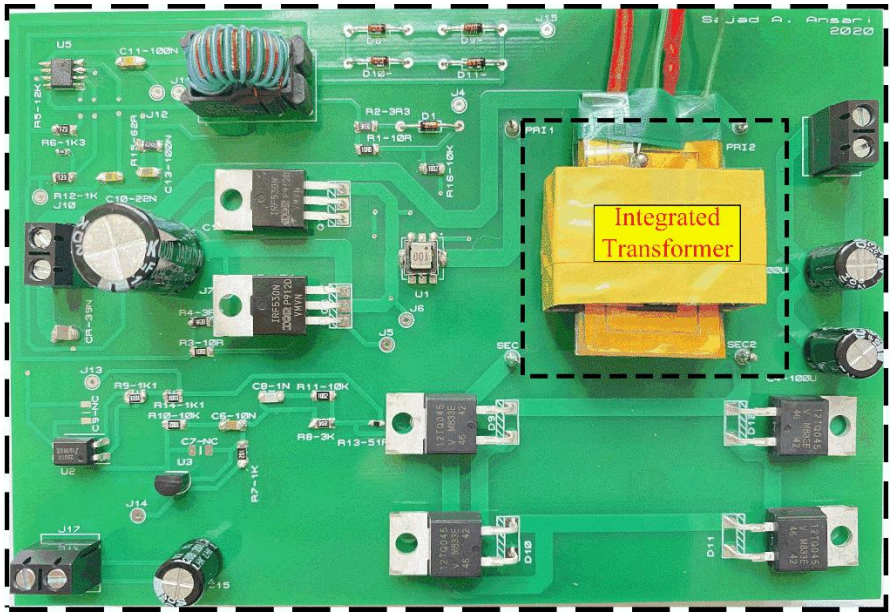

Fig. 6.11 Prototype of the designed LLC converter.

TABLE 6.3 The implemented LLC converter's specification.

Symbol	Parameter	Value
$N_P : N_S$	Turns ratio	10:2
L_m	Magnetising inductance	29 µH
L_r	Resonant (series) inductance	9 µH
C_r	Resonant capacitance	39 nF
V_{In}	Input voltage	45-55 V
V_o	Output voltage	5 V
P_o	Output power	25 W
f_s	Switching frequency	200-350 kHz
S	Switches	IRF530N
D	Rectifier diodes	12CTQ045

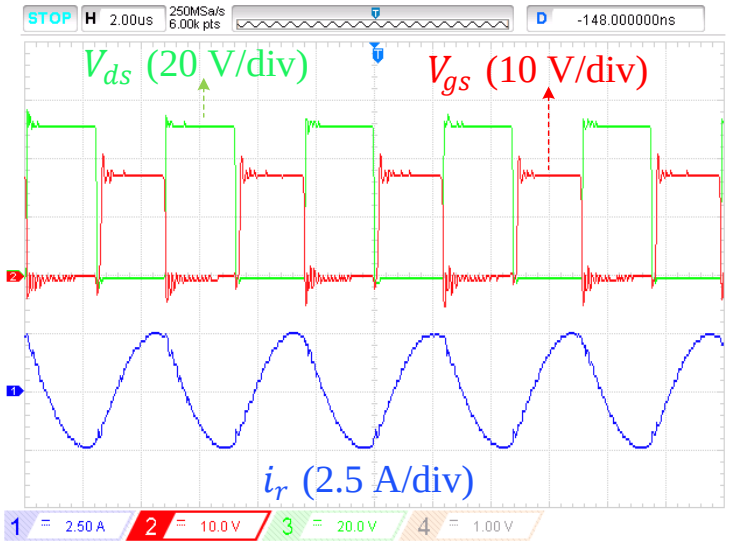

(a)

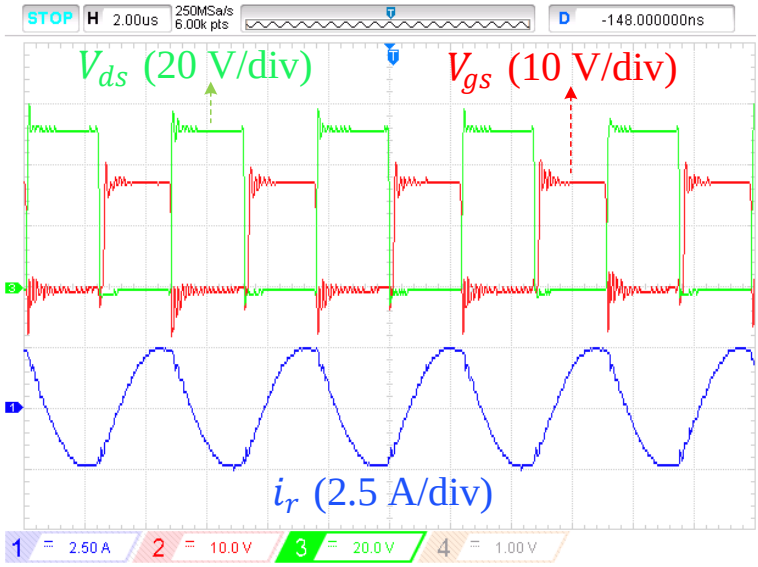

(b)

Fig. 6.12 Experimental waveforms of the designed LLC converter. (a) Using proposed topology (IT3). (b) Using the inserted-segmental-shunt topology (IT2). V_{ds} is drain to source voltage, V_{gs} is gate to source voltage and i_r is the resonant current (defined in **Fig. 5.1**).

The efficiency of the implemented LLC converter using the proposed integrated transformer and inserted-segmental-shunt integrated transformer are shown in **Fig. 6.13** for different output powers. It can be seen that, since the topology with inserted-segmental-shunt suffers from higher AC resistance, it has a lower efficiency compared to the proposed topology. The efficiency of the converter is evaluated after removing the rectifier stage from the circuit since the losses from an asynchronous rectifier are higher than losses in the magnetics. Rectifier design is not the focus of this work and thus the rectifier is not optimised.

Thermal images of the proposed topology and inserted-segmental-shunt transformer at nominal operating conditions are shown in **Fig. 6.14(a)** and **(b)**, respectively. It can be seen that the proposed transformer has a lower temperature (about 2°C) compared to the inserted-segmental-shunt transformer since it benefits from lower losses. In addition, the windings have a higher temperature compared to the cores since they have higher losses, which confirms the loss distribution presented in **Fig. 6.8**.

It should be noted that the application of the proposed integrated transformer can be extended to other converters such as the phase-shifted full-bridge converters and dual-active-bridge converters and is not only restricted to the LLC resonant converter.

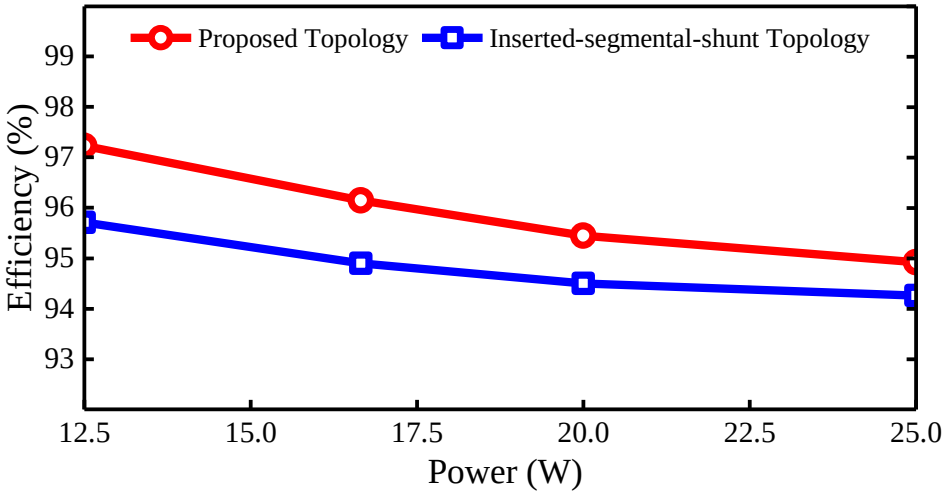

Fig. 6.13 Efficiency of the designed LLC converter without the rectifier stage using the proposed inserted-solid-shunt (IT3) and inserted-segmental-shunt integrated transformers (IT2).

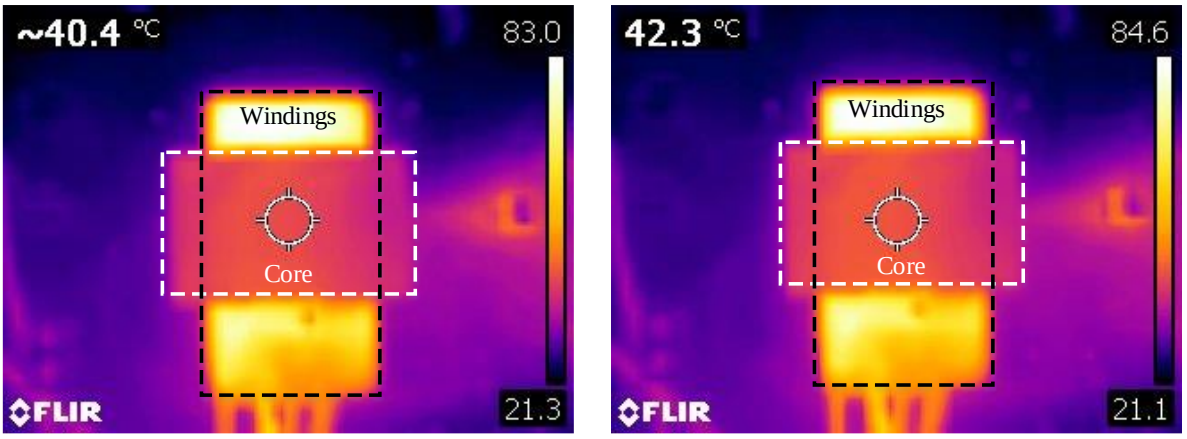

(a) (b)

Fig. 6.14 Thermal image of the transformer. (a) Proposed topology (IT3). (b) Inserted-segmental-shunt topology (IT2).

To sum up, not only does the proposed shunt-inserted integrated transformer address the main issues of the segmental shunt topology, but it also provides a higher efficiency without fundamentally redesigning the planar transformer or its associated converter.

6.5 Conclusion

A new topology for the inserted-shunt integrated planar transformers is proposed in this Chapter. The inserted shunts are solid in the proposed topology, leading to easier manufacturing compared to segmental shunt topology (presented in Chapter 5). In addition, the shunts are based on high-permeability materials like ferrite, which is widely available in the market with different sizes and lower price. Therefore, the proposed structure benefits from both advantages of the high-permeability segmental shunt and low-permeability one-segment shunt topologies.

The analysis and modelling of the proposed structure are presented. The leakage and magnetising inductances are decoupled from each other in the proposed structure and can be regulated separately, leading to a flexible design process. FEA simulation and experimental implementation are provided to verify the theoretical analysis. In addition, according to the presented results, the proposed topology can provide a higher efficiency compared to the inserted-segmental-shunt topology. An LLC resonant converter is also implemented to examine the performance of the proposed integrated transformer in practice. The prototype shows that the proposed topology can integrate all the three magnetic components of the LLC converter into a single planar transformer.

There is still one important issue with the topologies (IT1-IT3) proposed in Chapter 5 and 6: they all increase the leakage inductance on both primary and secondary sides. As discussed in Chapter 3, a high leakage inductance on the secondary side is not preferred and therefore a new topology (termed IT4) is presented in Chapter 7 which does not increase the secondary leakage inductance.

Chapter 7

Inserted-shunt Integrated Planar Transformer with Low Secondary Leakage Inductance for LLC Resonant Converters

In this Chapter, a novel topology (termed IT4) for inserted-shunt integrated transformers is proposed which has low secondary leakage inductance. The inserted shunt of the proposed topology is not segmental and can be located conveniently within the transformer. In addition, the inserted shunt does not require low permeability core material, simplifying its manufacture. The design and modelling of the proposed transformer topology are presented and verified by finite-element analysis and experimental implementation. The proposed topology is also compared with one of the inserted-segmental-shunt integrated transformers presented in Chapter 5. It is shown that the proposed transformer provides higher efficiency and lower AC resistance. Finally, an LLC resonant converter is implemented to examine the performance of the proposed integrated transformer in practice.

7.1 Introduction

A low-permeability magnetic shunt, such as a powder core, can be inserted into a planar transformer to achieve a high leakage inductance [12, 130, 134]. In this inserted-shunt integrated transformer topology, there is no need for either an auxiliary winding or an unusual magnetic core and all three magnetic components of the isolated LLC converter can be integrated into only a single planar transformer. However, the inserted shunt must have a specific and unusually low permeability in this topology, leading the design and manufacturing to difficulty and higher cost. Therefore, in Chapter 5, integrated planar transformers (IT1 and IT2) with a segmental shunt were suggested to address this problem. The magnetic shunt in this topology is formed by interleaving high permeability ferrite with thin plastic spacers to form a distributed air gap ferrite shunt with the same bulk permeability as the conventional low-permeability shunt. The design becomes more economical in this structure because high-permeability materials like ferrite, which is widely available in different sizes and for lower

price, can be used for the shunt. However, in this topology, the inserted shunt has several segments and must be placed in between two E-cores which makes the implementation difficult and lead to high assembly cost. Therefore, in Chapter 6, a new structure (IT3) was presented in which the inserted shunts are solid, leading to easier manufacturing compared to segmental shunt topology.

In all reported inserted-shunt integrated transformers [12, 130, 134], and the topologies (IT1-IT3) presented in Chapter 5 and 6, the main issue is that the leakage inductance does not only increase in the primary side but also it increases in the secondary side. The negative effects of the secondary leakage inductance on the LLC resonant converters are investigated in Chapter 3 and in [122, 139-142]. It was pointed out that a new topology for the inserted-shunt integrated transformer is needed to avoid the increase of secondary leakage inductance.

In this Chapter, a new structure (termed IT4) for the inserted-shunt integrated transformers is proposed to address the key issue of reducing high secondary leakage inductance. **Fig. 7.1** shows the structure and reluctance model of the proposed integrated magnetic transformer. **Fig. 7.1(a)** shows the transformer in the x-y plane and is divided into a primary section (consisting of an E-core half and winding) and a secondary section separated by an air gap. Two shunts are placed across x-y faces of the primary E-core. **Fig. 7.1(b)** shows the location of the shunts in the x-z plane. Since the shunts only provide a low-reluctance route for leakage flux of the primary winding, the primary leakage inductance only increases. In the proposed structure, the bulk permeability of the shunts can be regulated by changing their distances from the core rather than changing the air gaps length across them, which is in contrast with the segmental-shunt topology presented in Chapters 5. Hence, the proposed structure not only has the advantage of using high-permeability materials for the shunts but also requires solid, rather than segmental shunts.

The proposed structure is analysed and modelled in detail. The theoretical analysis is verified by finite-element analysis (FEA) simulation and experimental results. An efficiency comparison and AC resistance analysis for the proposed structure and the inserted-segmental-shunt topology (IT2) presented in Chapter 5 are provided. In addition, the performance of the proposed integrated transformer is investigated in practice by implementing an isolated LLC

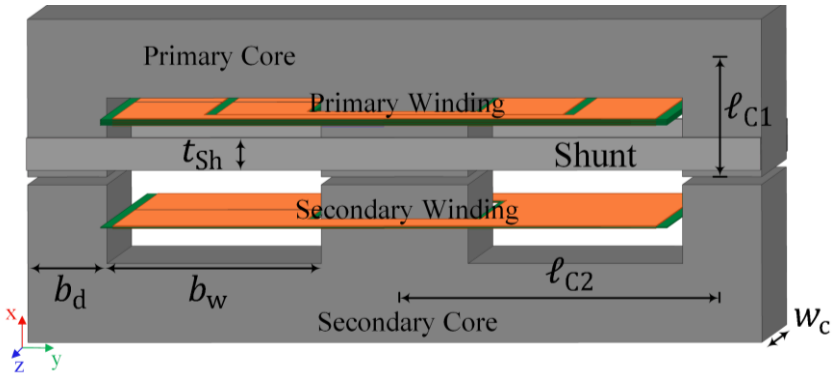

(a)

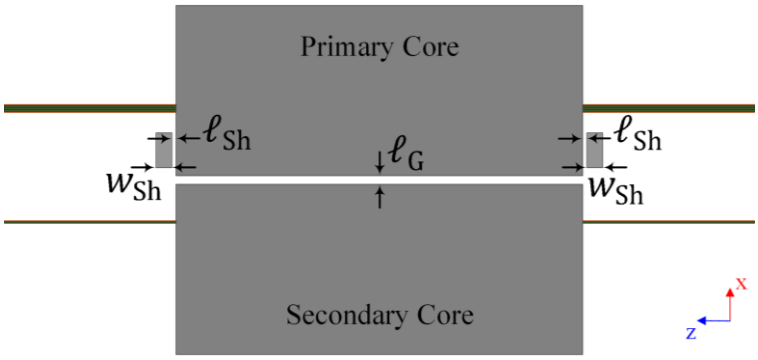

(b)

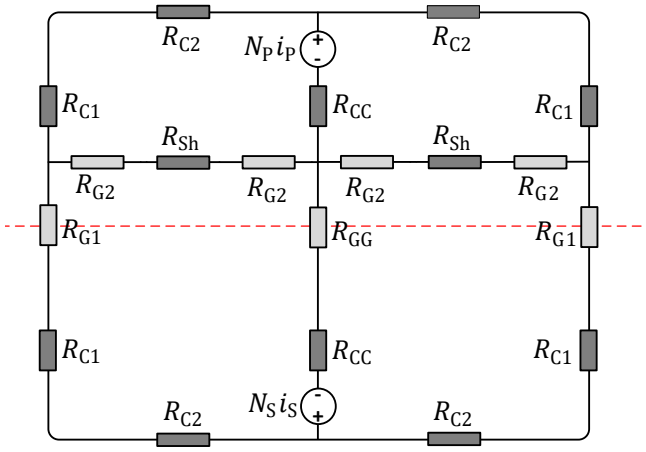

(c)

Fig. 7.1 The proposed integrated transformer (IT4). (a) Schematic in x-y plane. (b) Schematic in x-z plane. (c) Reluctance model.

resonant converter. The experimental results show that the proposed structure can integrate all three magnetic components of an LLC converter into a single planar transformer.

7.2 Proposed integrated magnetic transformers

The schematic of the proposed structure, geometry/dimensions and reluctance model are shown in **Fig. 7.1(a)**, **(b)** and **(c)**, respectively. An air gap ℓ_{G} is inserted between the E-cores to regulate magnetising inductance and an air gap ℓ_{Sh} is located in between shunts and primary E-core to adjust the leakage inductance. The dashed line shown in the reluctance model, **Fig. 7.1(c)**, divides the contribution into primary section (above the line) and secondary section (below the line) with the dividing line crossing the air gap reluctances $\mathcal{R}_{\mathrm{G1}}$ and $\mathcal{R}_{\mathrm{GG}}$. The flux produced by the magnetic field of the current in the primary winding that links with the secondary winding is diverted away from the secondary winding by the reluctance route provided by the inserted shunts. However, this route does not affect the flux produced by the magnetic field of the current in the secondary winding that links with the primary winding since core reluctances, $\mathcal{R}_{\mathrm{C1}}$, $\mathcal{R}_{\mathrm{C2}}$ and $\mathcal{R}_{\mathrm{CC}}$ are negligible compared to air gap reluctance of the shunt, $\mathcal{R}_{\mathrm{G2}}$.

In the following this section, the modelling of the proposed structure is discussed for estimation of the leakage and magnetising inductances.

Assuming the permeability of the core is very high then any energy that is stored in the transformer must be located outside of the core. Equation (7-1) shows the energy stored in the volume of the winding, the window area and the shunt is equal the energy stored in the leakage inductance, L_{Lk}.

$$E = \frac{1}{2}\iiint_V BH \,\mathrm{d}V = \frac{1}{2}L_{\mathrm{Lk}} i_{\mathrm{P}}^2 \tag{7-1}$$

where V is the total volume of window area, windings and inserted-shunts, i_{P} is the primary current, B is the flux density and H is the magnetic field intensity.

The energy stored in the winding window area of cores and primary and secondary windings alongside the inserted shunts form the total energy stored by the leakage inductance. **Fig. 7.2** shows a cross-section of the right-hand side of the transformer divided into several regions contributing the stored energy by the leakage inductance. The primary winding consists of N_{P}

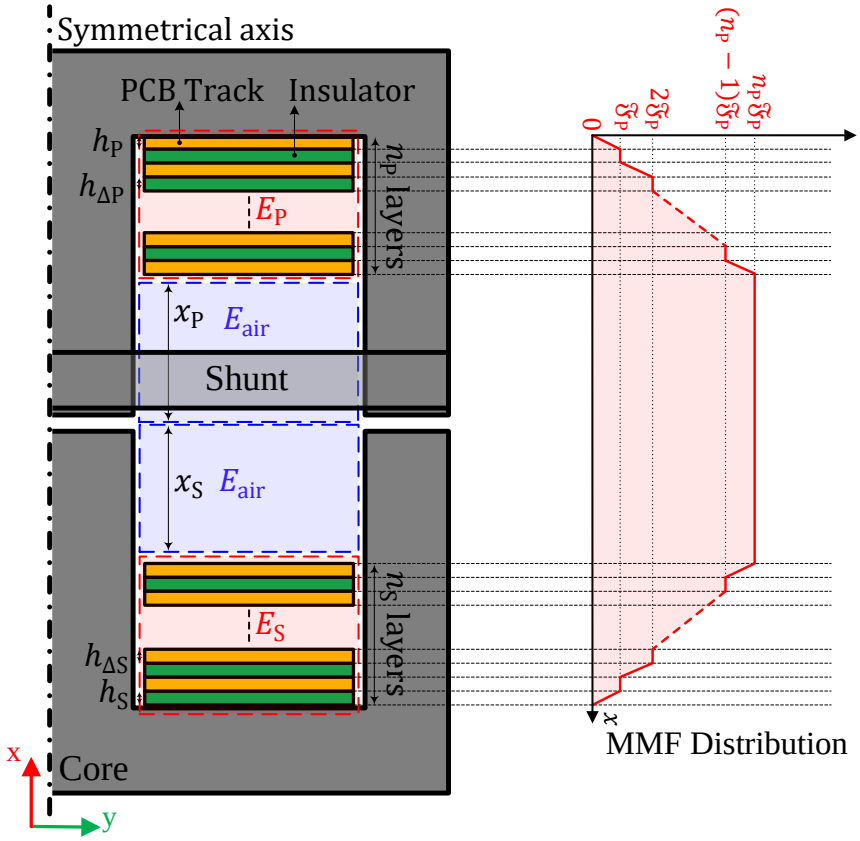

Fig. 7.2 Core half representation of the MMF distribution for the proposed integrated transformer (IT4).

turns and is constructed from n_P layers each with k_P turns ($N_P = k_P n_P$). Each primary winding layer has a height h_P and an associated insulating layer with a height $h_{\Delta P}$. Similar notation is used for the secondary winding, $N_S = k_S n_S$, with each layer having a height h_S and insulating layer height $h_{\Delta S}$. Regions E_P and E_S refer to the energy stored in the primary and secondary winding. E_{air} is the energy stored in the proportion of the winding window not occupied by the windings and this is divided into a primary region of height x_P and a secondary region of height x_S. Therefore, the energy stored in each part needs to be obtained first and the total leakage inductance can be then calculated by their summation and (7-1).

7.2.1 Energy stored in window area – E_{air}

The magnetomotive force (MMF) of each layer of the primary winding, $\mathfrak{F}_P$, may be obtained from (7-2), where k_P is the number of turns in each layer of the primary winding.

$$\mathfrak{F}_{\mathrm{P}} = k_{\mathrm{P}} I_{\mathrm{P}} \tag{7-2}$$

If n_{P} and n_{S} are defined as the number of layers of the primary and secondary windings, respectively, the MMF within the window area, $\mathfrak{F}_{\mathrm{air}}$, is equal to $n_{\mathrm{P}}\mathfrak{F}_{\mathrm{P}}$ and the magnetic field intensity within the air area, H_{air}, may be obtained by (7-3).

$$H_{\mathrm{air}} = \frac{n_{\mathrm{P}}\mathfrak{F}_{\mathrm{P}}}{b_{\mathrm{w}}} \tag{7-3}$$

From (7-1), the stored energy in window area not occupied by the winding, E_{air}, (defined in **Fig. 7.2**) can be obtained as (7-4).

$$E_{\mathrm{air}} = \frac{1}{2}\mu_0 w_{\mathrm{c}} b_{\mathrm{w}} \int_{-x_{\mathrm{S}}}^{x_{\mathrm{P}}} H_{\mathrm{air}}^2 \mathrm{d}x \tag{7-4}$$

where w_{c} is the core depth and x_{P} and x_{S} are the distances from the primary and secondary windings to the centre of the transformer, respectively, defined in **Fig. 7.2**. From (7-2)-(7-4), E_{air} in both windows (left and right windows of an E-core) can be obtained as follows:-

$$E_{\mathrm{air}} = \mu_0 w_{\mathrm{c}} \frac{n_{\mathrm{P}}^2 k_{\mathrm{P}}^2 i_{\mathrm{P}}^2}{b_{\mathrm{w}}} (x_{\mathrm{P}} + x_{\mathrm{S}}) \tag{7-5}$$

7.2.2 Energy stored in primary and secondary PCB windings

From the MMF distribution presented in **Fig. 7.2** which has been obtained based on method outlined in [129, 130, 134], the stored energy in PCB layers of primary and secondary windings can be obtained. Ouyang, *et al*, [129] proved that energy stored in the primary and secondary windings may be calculated as (7-6) and (7-7), respectively.

$$E_{\mathrm{P}} = \frac{1}{6}\mu_0 \frac{w_{\mathrm{c}}}{b_{\mathrm{w}}} k_{\mathrm{P}}^2 [h_{\Delta\mathrm{P}}(2n_{\mathrm{P}}^3 - 3n_{\mathrm{P}}^2 + n_{\mathrm{P}}) + 2h_{\mathrm{P}} n_{\mathrm{P}}^3] i_{\mathrm{P}}^2 \tag{7-6}$$

$$E_{\mathrm{S}} = \frac{1}{6}\mu_0 \frac{w_{\mathrm{c}}}{b_{\mathrm{w}}} k_{\mathrm{S}}^2 [h_{\Delta\mathrm{S}}(2n_{\mathrm{S}}^3 - 3n_{\mathrm{S}}^2 + n_{\mathrm{S}}) + 2h_{\mathrm{S}} n_{\mathrm{S}}^3] i_{\mathrm{S}}^2 \tag{7-7}$$

In (7-6) and (7-7), h_{P} and h_{S} are defined as the thickness of the PCB tracks of the primary and secondary windings, respectively, and $h_{\Delta\mathrm{P}}$ and $h_{\Delta\mathrm{S}}$ are defined as the thickness of the PCB insulation layers of the primary and secondary windings, respectively.

7.2.3 Energy stored in inserted shunts

The stored energy in the inserted shunts can be obtained from the reluctance model using the method outlined in Chapter 5. Referring to **Fig. 7.1(c)**, $\mathcal{R}_{\mathrm{G1}}$, $\mathcal{R}_{\mathrm{GG}}$ and $\mathcal{R}_{\mathrm{G2}}$ are air gap reluctances, $\mathcal{R}_{\mathrm{C1}}$, $\mathcal{R}_{\mathrm{C2}}$ and $\mathcal{R}_{\mathrm{CC}}$ are core reluctances and $\mathcal{R}_{\mathrm{Sh}}$ is shunt reluctance and they can be calculated by (7-8)-(7-14). In the provided reluctance modelling, it is assumed that both shunts are located at the same distance from the cores (ℓ_{Sh}), and therefore only a single shunt of double thickness ($2t_{\mathrm{Sh}}$) needs to be considered.

$$\mathcal{R}_{\mathrm{C1}} = \frac{\ell_{\mathrm{C1}}}{\mu_0 \mu_{\mathrm{r}} b_{\mathrm{d}} w_{\mathrm{c}}} \tag{7-8}$$

$$\mathcal{R}_{\mathrm{C2}} = \frac{\ell_{\mathrm{C2}}}{\mu_0 \mu_{\mathrm{r}} b_{\mathrm{d}} w_{\mathrm{c}}} \tag{7-9}$$

$$\mathcal{R}_{\mathrm{CC}} = \frac{\ell_{\mathrm{C1}}}{\mu_0 \mu_{\mathrm{r}} A_{\mathrm{c}}} \tag{7-10}$$

$$\mathcal{R}_{\mathrm{Sh}} = \frac{b_{\mathrm{w}}}{2\mu_0 \mu_{\mathrm{Sh}} t_{\mathrm{Sh}} w_{\mathrm{Sh}}} \tag{7-11}$$

$$\mathcal{R}_{\mathrm{G1}} = \frac{\ell_{\mathrm{G}}}{\mu_0 (b_{\mathrm{d}} + \ell_{\mathrm{G}})(w_{\mathrm{c}} + \ell_{\mathrm{G}})} \tag{7-12}$$

$$\mathcal{R}_{\mathrm{G2}} = \frac{\ell_{\mathrm{Sh}}}{2\mu_0 (b_{\mathrm{d}} + \ell_{\mathrm{Sh}})(t_{\mathrm{Sh}} + \ell_{\mathrm{Sh}})} \tag{7-13}$$

$$\mathcal{R}_{\mathrm{GG}} = \frac{\ell_{\mathrm{G}}}{\mu_0(2b_{\mathrm{d}}+\ell_{\mathrm{G}})(w_{\mathrm{c}} + \ell_{\mathrm{G}})} \tag{7-14}$$

where μ_0, μ_{r} and μ_{Sh} are the permeability of the air, and the relative permeability of the core and shunt, respectively. A_{c} is the core effective cross-sectional area and other variables are defined in **Fig. 7.1(a)**. Hurley, *et al*, [168] showed that an effective cross-sectional area of the air gap with dimension *a* by *b* are equal to (*a*+*g*) by (*b*+*g*) when the fringing effect is considered and *g* is the length of the studied air gap.

From the reluctance model presented in **Fig. 7.1(c)** and the method outlined in Chapter 5, the magnetising inductance of the proposed integrated transformer (evaluated at the primary side) can be obtained as follows:-

$$L_{\mathrm{m\_P}} = \frac{2N_{\mathrm{P}}^2}{\mathcal{R}_{\mathrm{A}}\mathcal{R}_{\mathrm{B}} - (2\mathcal{R}_{\mathrm{G2}}+\mathcal{R}_{\mathrm{Sh}})} \tag{7-15}$$

where $\mathcal{R}_{\mathrm{A}}$ and $\mathcal{R}_{\mathrm{B}}$ can be defined as (7-16) and (7-17), respectively.

$$\mathcal{R}_{\mathrm{A}} = \frac{\mathcal{R}_{\mathrm{G1}} + 2\mathcal{R}_{\mathrm{GG}} + \mathcal{R}_{\mathrm{B}}}{2\mathcal{R}_{\mathrm{G2}}+\mathcal{R}_{\mathrm{Sh}}} \tag{7-16}$$

$$\mathcal{R}_{\mathrm{B}} = \mathcal{R}_{\mathrm{C1}} + \mathcal{R}_{\mathrm{C2}} + 2\mathcal{R}_{\mathrm{CC}} + 2\mathcal{R}_{\mathrm{G2}}+\mathcal{R}_{\mathrm{Sh}} \tag{7-17}$$

And the primary self-inductance can be obtained by

$$L_{\mathrm{PP}} = \frac{N_{\mathrm{P}}^2}{\mathcal{R}_{\mathrm{T\_P}}} \tag{7-18}$$

where $\mathcal{R}_{\mathrm{T\_P}}$ is the core reluctance (evaluated from the primary side) and can be obtained as (7-19).

$$\mathcal{R}_{\mathcal{R}_{\mathrm{T\_P}}} = \mathcal{R}_{\mathrm{CC}} + \frac{\mathcal{R}_{\mathrm{C1}} + \mathcal{R}_{\mathrm{C2}}}{2} + \frac{(2\mathcal{R}_{\mathrm{GG}} + 2\mathcal{R}_{\mathrm{CC}} + \mathcal{R}_{\mathrm{G1}} + \mathcal{R}_{\mathrm{C1}} + \mathcal{R}_{\mathrm{C2}})(2\mathcal{R}_{\mathrm{G2}} + \mathcal{R}_{\mathrm{Sh}})}{2(\mathcal{R}_{\mathrm{G1}} + 2\mathcal{R}_{\mathrm{GG}} + \mathcal{R}_{\mathrm{B}})} \quad (7\text{-}19)$$

Finally, the primary leakage inductance due to the inserted shunts, $L_{\mathrm{Lk\_P\_Sh}}$, can be calculated by (7-20).

$$L_{\mathrm{Lk\_P\_Sh}} = L_{\mathrm{PP}} - L_{\mathrm{m\_P}} \quad (7\text{-}20)$$

The secondary magnetising inductance (using a similar approach) can be obtained as (7-21).

$$L_{\mathrm{m\_S}} = \frac{2N_{\mathrm{S}}^2}{\mathcal{R}_{\mathrm{C}}\mathcal{R}_{\mathrm{D}} - (2\mathcal{R}_{\mathrm{G2}} + \mathcal{R}_{\mathrm{Sh}})} \quad (7\text{-}21)$$

where $\mathcal{R}_{\mathrm{C}}$ and $\mathcal{R}_{\mathrm{D}}$ can be defined as (7-22) and (7-23), respectively.

$$\mathcal{R}_{\mathrm{C}} = \frac{\mathcal{R}_{\mathrm{B}}}{2\mathcal{R}_{\mathrm{G2}} + \mathcal{R}_{\mathrm{Sh}}} \quad (7\text{-}22)$$

$$\mathcal{R}_{\mathrm{D}} = \mathcal{R}_{\mathrm{G1}} + 2\mathcal{R}_{\mathrm{GG}} + \mathcal{R}_{\mathrm{B}} \quad (7\text{-}23)$$

And the secondary self-inductance can be obtained by

$$L_{\mathrm{SS}} = \frac{N_{\mathrm{S}}^2}{\mathcal{R}_{\mathrm{T\_S}}} \quad (7\text{-}24)$$

where $\mathcal{R}_{\mathrm{T\_S}}$ is the core reluctance (evaluated from the secondary side) and can be obtained as (7-25).

$$\mathcal{R}_{\mathrm{T\_S}} = \mathcal{R}_{\mathrm{GG}} + \mathcal{R}_{\mathrm{CC}} + \frac{\mathcal{R}_{\mathrm{G1}} + \mathcal{R}_{\mathrm{C1}} + \mathcal{R}_{\mathrm{C2}}}{2} + \frac{(2\mathcal{R}_{\mathrm{CC}} + \mathcal{R}_{\mathrm{C1}} + \mathcal{R}_{\mathrm{C2}})(2\mathcal{R}_{\mathrm{G2}} + \mathcal{R}_{\mathrm{Sh}})}{2\mathcal{R}_{\mathrm{B}}} \quad (7\text{-}25)$$

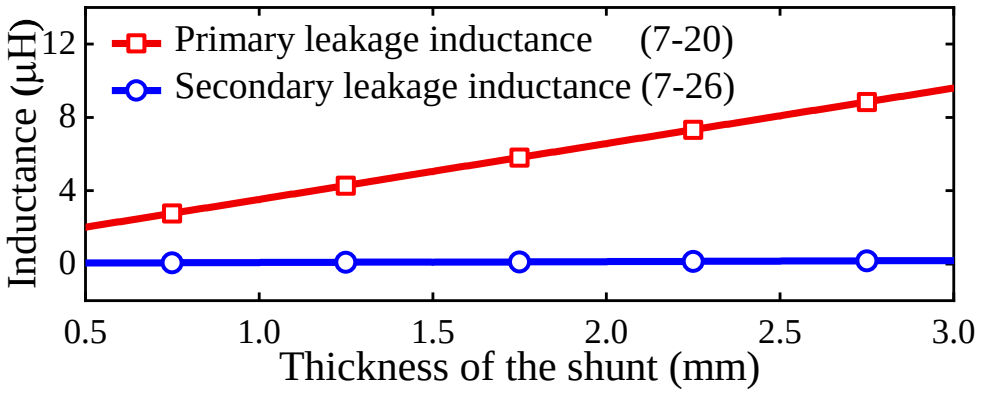

Fig. 7.3 Primary and secondary leakage inductances caused by the shunts. Core: E32/6/20/R-3F4, shunt material: Fair-Rite M6, ℓ_{G}=ℓ_{Sh}=0.3mm, w_{Sh}=0.8mm, N_{P}=N_{S}=10.

Finally, the secondary leakage inductance due to the inserted shunts, $L_{\mathrm{Lk\_S\_Sh}}$, can be calculated by (7-26).

$$L_{\mathrm{Lk\_S\_Sh}} = L_{\mathrm{SS}} - L_{\mathrm{m\_S}} \tag{7-26}$$

In **Fig. 7.3**, from (7-20) and (7-26), the primary and secondary leakage inductances caused by shunts of different thickness are presented. As shown, the shunts do not have a noticeable influence on the secondary leakage inductance, but the primary leakage inductance can be increased by the shunts. This is because the mutual inductance from primary to secondary is reduced by the reluctance route through the inserted shunts. However, this route does not affect the flux produced by the secondary winding that links with the primary winding since core reluctances, $\mathcal{R}_{\mathrm{C1}}$, $\mathcal{R}_{\mathrm{C2}}$ and $\mathcal{R}_{\mathrm{CC}}$ are negligible compared to air gap reluctance of the shunt, $\mathcal{R}_{\mathrm{G2}}$.

As presented in **Fig. 7.3**, the secondary leakage inductance caused by the shunts can be neglected and, therefore, from (7-1), (7-5)-(7-7) and (7-20), the total leakage inductance of the proposed integrated transformer can be calculated as follows:-

$$L_{\mathrm{Lk}} = L_{\mathrm{Lk\_P\_Sh}} + 2\mu_0 w_{\mathrm{C}} \frac{N_{\mathrm{P}}^2}{b_w}(x_{\mathrm{P}} + x_{\mathrm{S}}) + \frac{1}{3}\mu_0 \frac{w_{\mathrm{c}}}{b_{\mathrm{w}}} k_{\mathrm{P}}^2 n_{\mathrm{P}}^2 \sum_{i=\mathrm{P,S}} \left[h_{\Delta i}\left(2n_i - 3 + \frac{1}{n_i}\right) + 2h_i n_i \right] \quad (7\text{-}27)$$

where N_{P} is the primary turns number. Therefore, from (7-15) and (7-27), an integrated transformer for the required magnetising and leakage inductances can be designed. For the remainder of the Chapter, the magnetising inductance of the transformer, L_{m}, is defined equal to $L_{\mathrm{m\_P}}$.

The calculated leakage and magnetising inductances of the proposed integrated transformer for different thicknesses of the shunt, t_{Sh}, air gap length, ℓ_{G}, and distance between shunts and cores, ℓ_{Sh}, are presented in **Fig. 7.4(a)** and **(b)**, using a E32/6/20/R-3F4 core as reference to determine the main factors of influence in a design (details of the geometry provided in the figure caption). It is clear that the magnetising inductance is mainly influenced by air gap length between cores, ℓ_{G}, and cannot be changed appreciably by varying t_{Sh} and ℓ_{Sh}. However, the leakage inductance can be regulated by changing ℓ_{Sh} and t_{Sh} and is not affected by ℓ_{G}. Therefore, in the proposed integrated transformer, the leakage and magnetising inductances are sufficiently decoupled from each other and can be separately realised, leading the design process to higher flexibility.

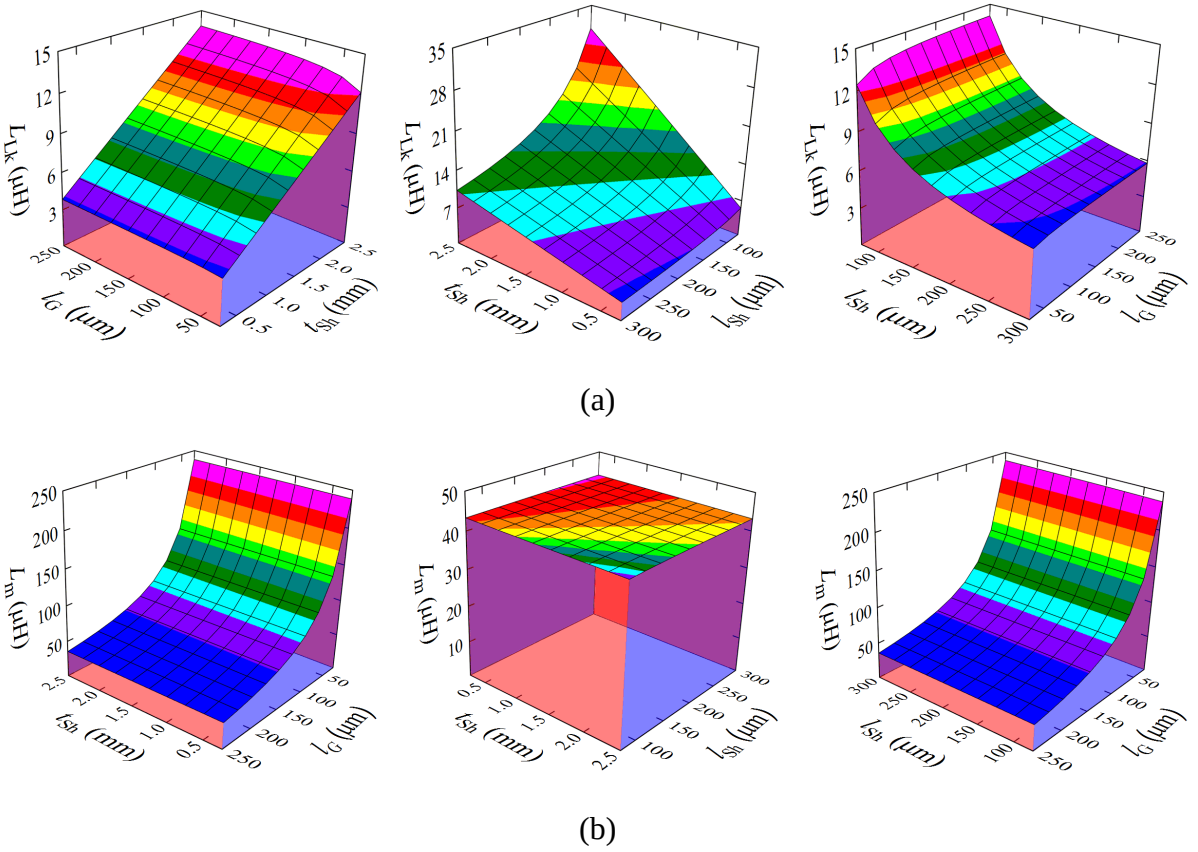

Fig. 7.4 The calculated leakage and magnetising inductances versus thickness of the shunt (t_{Sh}), transformer air gaps (ℓ_{G}) and distance between shunts and cores (ℓ_{Sh}). (a) Leakage inductance. (b) Magnetising inductance. Core: E32/6/20/R-3F4, shunt material: Fair-Rite M6, t_{Sh}=1mm, ℓ_{G}=ℓ_{Sh}=0.2mm, w_{Sh}=0.8mm, N_{P}=10, N_{S}=2, n_{P}=5, n_{S}=2, k_{P}=2, k_{S}=1, x_{P}=2.5mm, x_{S}=1.5mm.

The modelling of the proposed integrated transformer is now fully investigated and it is shown that the transformer can be designed for most reasonable specifications in terms of leakage and magnetising inductances. These designs do not require low-permeability materials or segmental shunts and with the advantage of not increasing the leakage inductance on the secondary side. Therefore, the proposed transformer is an attractive candidate for use in an LLC resonant converter to integrate its magnetic components into a single transformer. In the following, the operation of the proposed transformer when it is designed to be used in an exemplar LLC resonant converter is investigated and its modelling is verified by FEA simulation and experimental implementation.

TABLE 7.1 Proposed structure's specification.

Symbol	Parameter	Value
N_{P}	Primary turns	10
N_{S}	Secondary turns	2
k_{P}	Turns per layer in primary	2
k_{S}	Turns per layer in secondary	1
n_{P}	Number of primary layers	5
n_{S}	Number of secondary layers	2
h_{P}, h_{S}	Primary and secondary conduction thickness	35 μm
$h_{\Delta\mathrm{P}}$, $h_{\Delta\mathrm{S}}$	Primary and secondary insulation thickness	30 μm
t_{Sh}	Shunt thickness	1.3 mm
w_{Sh}	Shunt wideness	0.8 mm
ℓ_{G}	Transformer air gap	0.32 mm
ℓ_{Sh}	Distance between shunt and cores	0.20 mm
x_{P}, x_{S}	Distance between primary and secondary windings and centre of E-cores, respectively	2.5 mm 1.5 mm

7.3 Simulation results

An integrated transformer with minimum secondary leakage inductance is designed based on the equations provided in Section 7.2 and its specifications are presented in **Table 7.1**. The magnetising and leakage inductances and turns ratio of the designed transformer are chosen according to the specification of an exemplar isolated LLC resonant converter presented in **Table 7.3**. The transformer core (E32/6/20/R-3F4) is selected based on the design guidelines outlined by the catalogue of the core provided by its manufacturer [170], which presents guidelines for appropriate core selection based on the operating frequency and power. The thickness of the shunt and air-gap lengths (ℓ_{G} and ℓ_{Sh}) are estimated in order to provide the required leakage and magnetising inductances, using (7-15) and (7-27), and considering the dimensions of the selected core. Moreover, the windings are designed considering the dimensions, skin effect, their root-mean-square (RMS) currents and the difficulty of manufacturing.

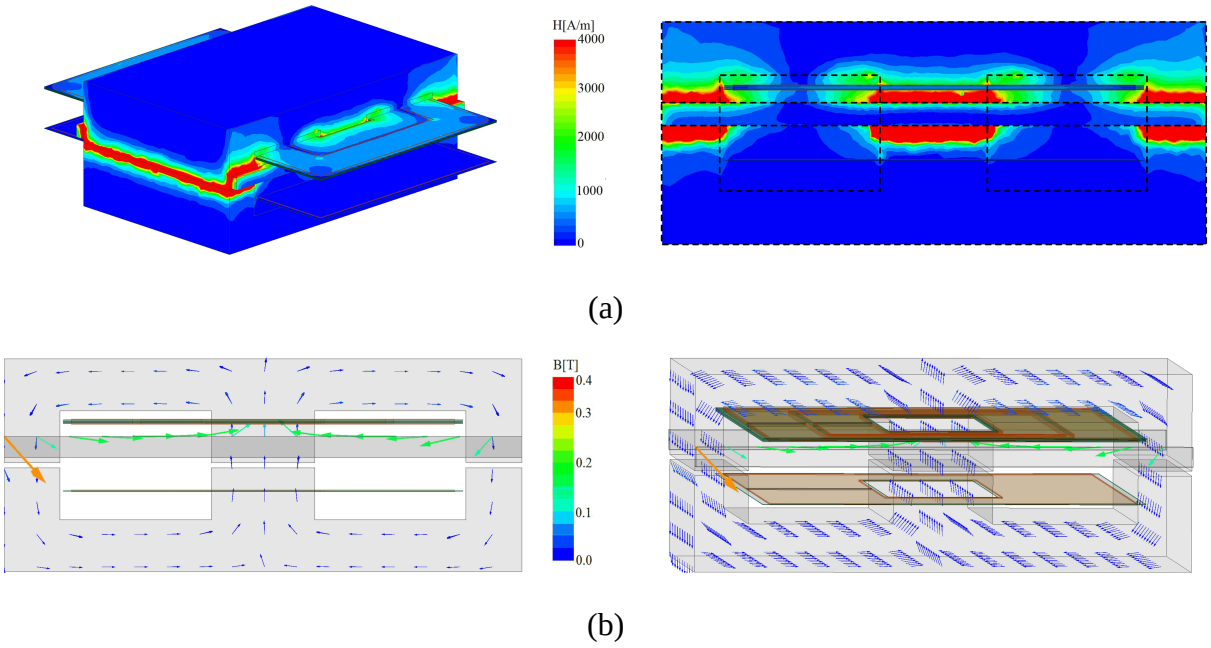

Fig. 7.5 FEA simulation results. (a) Magnetic field intensity. (b) Magnetic flux density vectors. E32/6/20/R-3F4 and shunt material: Fair-Rite M6, and frequency=200 kHz.

To verify the theoretical analysis, the FEA simulation results of the designed transformer are presented below.

The magnetic field intensity and flux density vectors for the proposed topology, while it is used in an LLC converter with specification presented in **Table 7.3**, are shown in **Fig. 7.5(a)** and **(b)**, respectively. According to **Fig. 7.5**, the magnetic field intensity and flux density vectors are dominant in the shunts and their air gaps (ℓ_{Sh}) rather than windows area and PCB windings. The leakage inductance is therefore mainly caused by the inserted shunts. In addition, since the magnetic field intensity is highest in the cores air gap (ℓ_{G}), the magnetising inductance is mainly affected by ℓ_{G}.

From **Fig. 7.5**, it can be observed that the magnetic flux density for the shunts is around 0.2 T, which is below saturation. A design can avoid saturation for the shunts whether a low-permeability material or high-permeability material is used for the shunts.

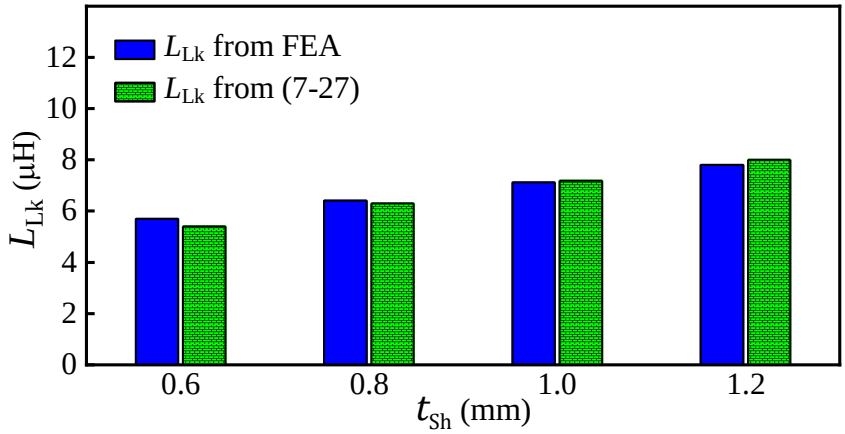

(a)

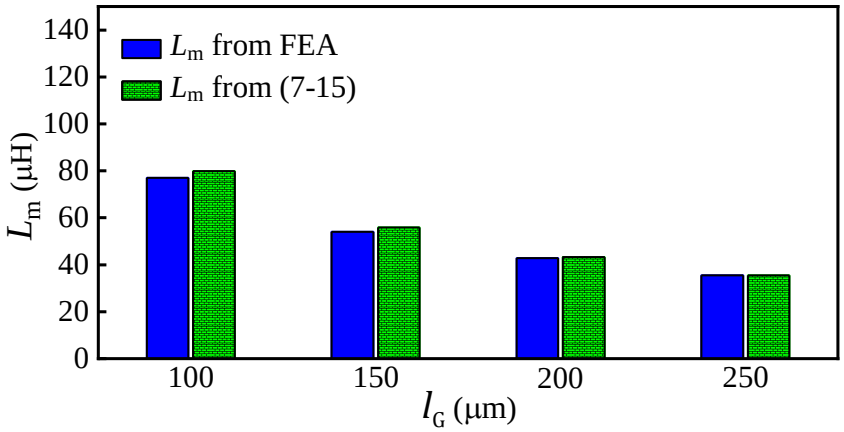

(b)

Fig. 7.6 Modelling validation by simulation study. (a) Leakage inductance ($\ell_G = 0.05$mm). (b) Magnetising inductance ($t_{Sh} = 1$mm). E32/6/20/R-3F4, shunt material: Fair-Rite M6, $\ell_{Sh} = 0.2$mm, and frequency=200 kHz.

The leakage and magnetising inductances versus thickness of the shunt (t_{Sh}) and transformer air gap (ℓ_G) obtained from (7-15) and (7-27) and measured by FEA simulation are presented for the proposed topology in **Fig. 7.6(a)** and **(b)**, respectively. According to **Fig. 7.6**, there is a good agreement between the theoretical and simulation results, verifying the model developed in this Chapter.

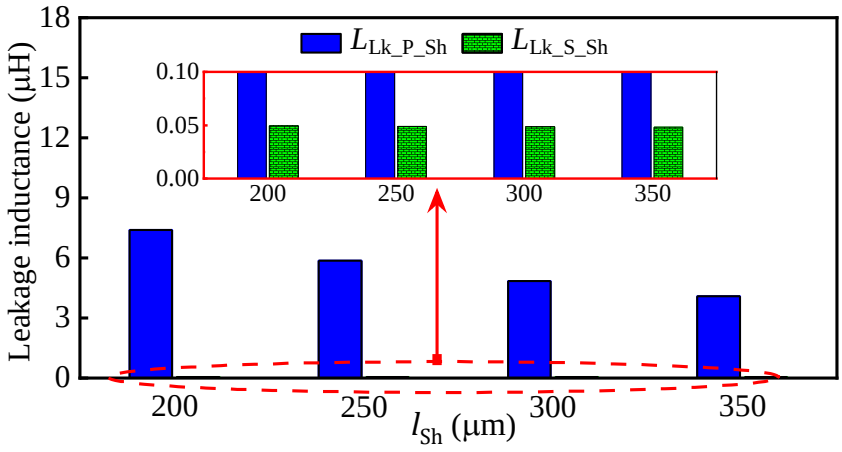

Fig. 7.7 Primary and secondary leakage inductances caused by the shunts. E32/6/20/R-3F4, shunt material: Fair-Rite M6, and frequency=200 kHz.

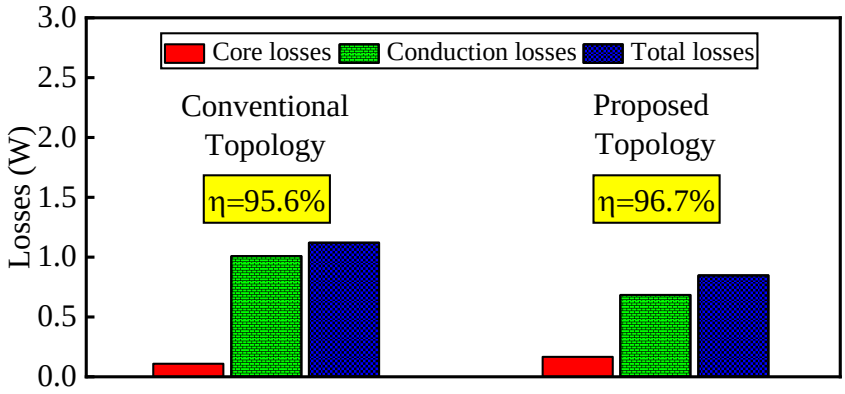

Fig. 7.8 Loss distribution of the proposed (IT4) and conventional (IT2) topologies for output power of 25W. E32/6/20/R-3F4, shunt material: Fair-Rite M6, and frequency=200 kHz.

Primary and secondary leakage inductances caused by the shunts for the proposed integrated transformer are presented in **Fig. 7.7**. As shown, the secondary leakage inductance is not affected by the shunts' characteristics and has a negligible value, verifying **Fig. 7.3**.

Loss distribution of the proposed topology, while it is used in an LLC converter with specification presented in **Table 7.3**, is presented in **Fig. 7.8**. For comparison, an integrated

TABLE 7.2 Parameters of the implemented integrated transformer.

Parameter	FEA modelling	Simulation	Measurement
Magnetising inductance, L_{m}	28.5 μH	28.85 μH	29.5 μH
Primary leakage inductance, $L_{\mathrm{Lk\_P}}$	8 μH	8.2 μH	8.3 μH
Secondary leakage inductance, $L_{\mathrm{Lk\_S}}$	0.03 μH	0.04 μH	0.03 μH

transformer with inserted-segmental shunt (IT2), presented in Chapter 5, is also designed to the same specification and simulated, shown in **Fig. 7.8**. As shown, the proposed transformer has lower conduction losses and therefore provides higher efficiency compared to the inserted-segmental-shunt (conventional) topology.

7.4 Experimental verification

To verify theoretical analysis and simulation results, an integrated transformer based on the proposed structure with specifications presented in **Table 7.1** is built and its prototype is shown in **Fig. 7.9(a)**. For comparison, an integrated transformer with inserted-segmental-shunt (IT2) presented in Chapter 5 is also built to the same specification, shown in **Fig. 7.9(b)**. The shunts for this work were made by cutting ferrite sheets and gluing them in parallel.

The measured leakage and magnetising inductances of the proposed topology at 200 kHz obtained using an Omicron Bode 100 frequency analyser are shown in **Table 7.2**. According to **Table 7.2**, the leakage and magnetising inductances obtained by FEA simulation and modelling are close to the experimental results. The proposed topology does not increase the secondary leakage inductance despite the inserted magnetic shunt. The secondary leakage inductance, while low, is non-zero because there is leakage flux in the window area of the E-core.

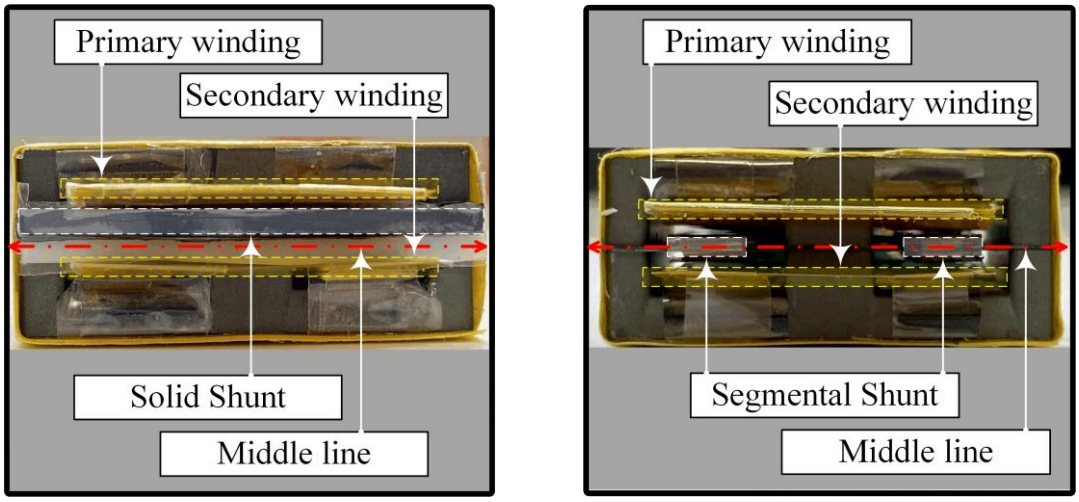

(a) (b)

Fig. 7.9 Prototypes of the implemented transformers. (a) The proposed transformer (IT4). (b) The inserted-segmental-shunt transformer (IT2). Core: E32/6/20/R-3F4 and shunt material: Fair-Rite M6.

AC resistance, primary self-inductance and leakage inductance versus frequency for the proposed topology and integrated transformer with inserted-segmental-shunt (IT2, conventional) are presented in **Fig. 7.10**. As shown, the magnetising and leakage inductances of both implemented topologies are very similar. However, the integrated transformer with inserted-segmental-shunt suffers from higher AC resistance compared to the proposed topology and this is because of higher fringing fields due to the inserted-segmental-shunt topology (as already pointed in Chapter 5). Therefore, the proposed topology benefits from lower conduction losses, which verifies **Fig. 7.8**. As shown in **Fig. 7.1**, in the proposed topology, the right and left air-gaps of the shunt (labelled ℓ_{Sh}) are further from the windings, reducing their coupling with the fringing field. However, in the segmental topology (IT2), all of the air-gaps are between the lower and upper windings and therefore they have greater coupling with the fringing field, leading to higher AC losses.

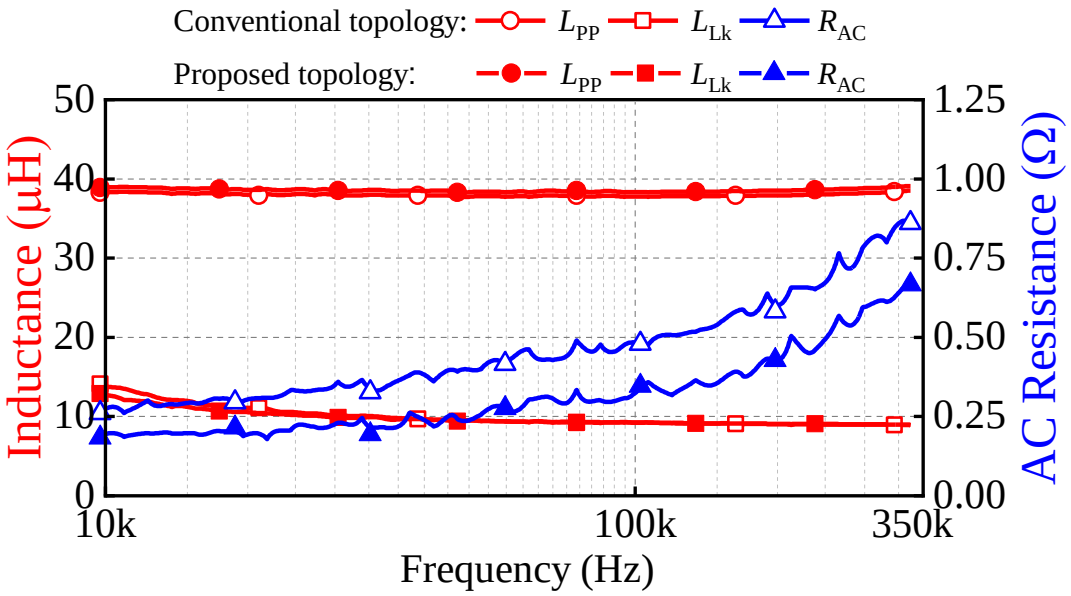

Fig. 7.10 AC resistance, R_{AC}, primary self-inductance, L_{PP}, and leakage inductance, L_{Lk}, versus frequency for the proposed (IT4) and conventional (IT2, inserted-segmental-shunt) topologies.

TABLE 7.3 The implemented LLC converter's specification.

Symbol	Parameter	Value
N_P: N_S	Turns ratio	10:2
L_m	Magnetising inductance	29 µH
L_r	Resonant (series) inductance	9 µH
C_r	Resonant capacitance	39 nF
V_{In}	Input voltage	45-55 V
V_o	Output voltage	5 V
P_o	Output power	25 W
f_s	Switching frequency	200-350 kHz
S	Switches	IRF530N
D	Rectifier diodes	12CTQ045

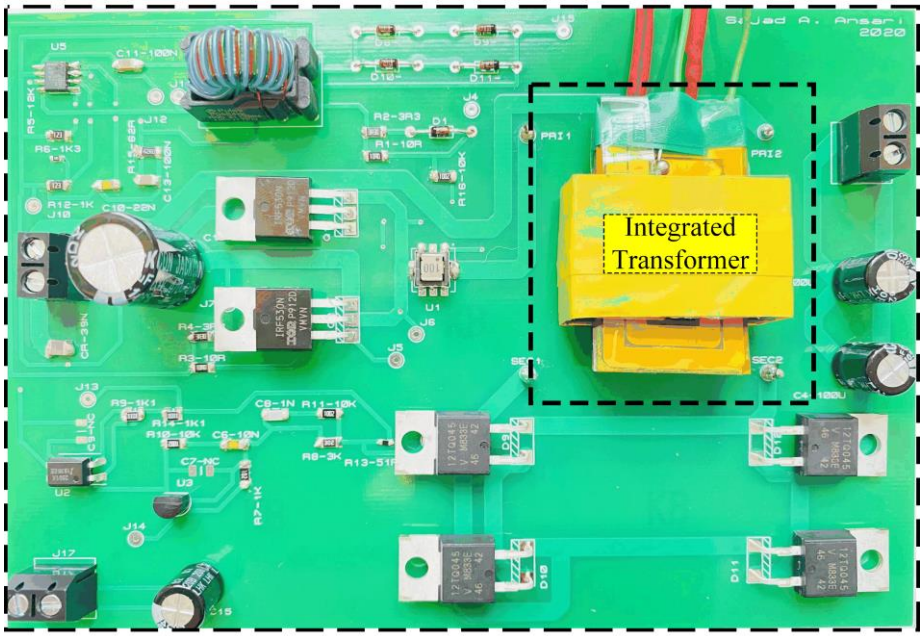

Fig. 7.11 Prototype of the designed LLC converter.

To verify the performance of the proposed integrated transformer, it was incorporated within an LLC converter designed according to the procedure outlined in Chapter 2 (Section 2.3.2) and [46], shown in **Fig. 7.11** (this is the same LLC converter presented in Chapters V and VI but with the new transformer). The specification of the designed LLC converter is presented in **Table 7.3** in which the series and parallel inductances are integrated into the transformer.

The waveforms of the LLC converter operating at 210 kHz and 280 kHz switching frequency using the proposed topology (IT4) and the topology with inserted-segmental shunt (IT2) are measured and presented in **Fig. 7.12(a)-(d)**. It can be seen that the converter operates correctly and the MOSFETs are turned on at zero voltage switching (ZVS) because the switch gate turns on after its drain-source voltage drops to zero. The converter's switching frequency ranges from 200 kHz to 350 kHz. To show the converter’s capability to provide ZVS for the switches at different frequencies and its proper operation, the waveforms for two different switching frequencies (one low and one high) are presented.

As discussed in Section 2.3.2, the choice of frequency range for designing the resonant components of the LLC topology should be based on the availability of your hardware and

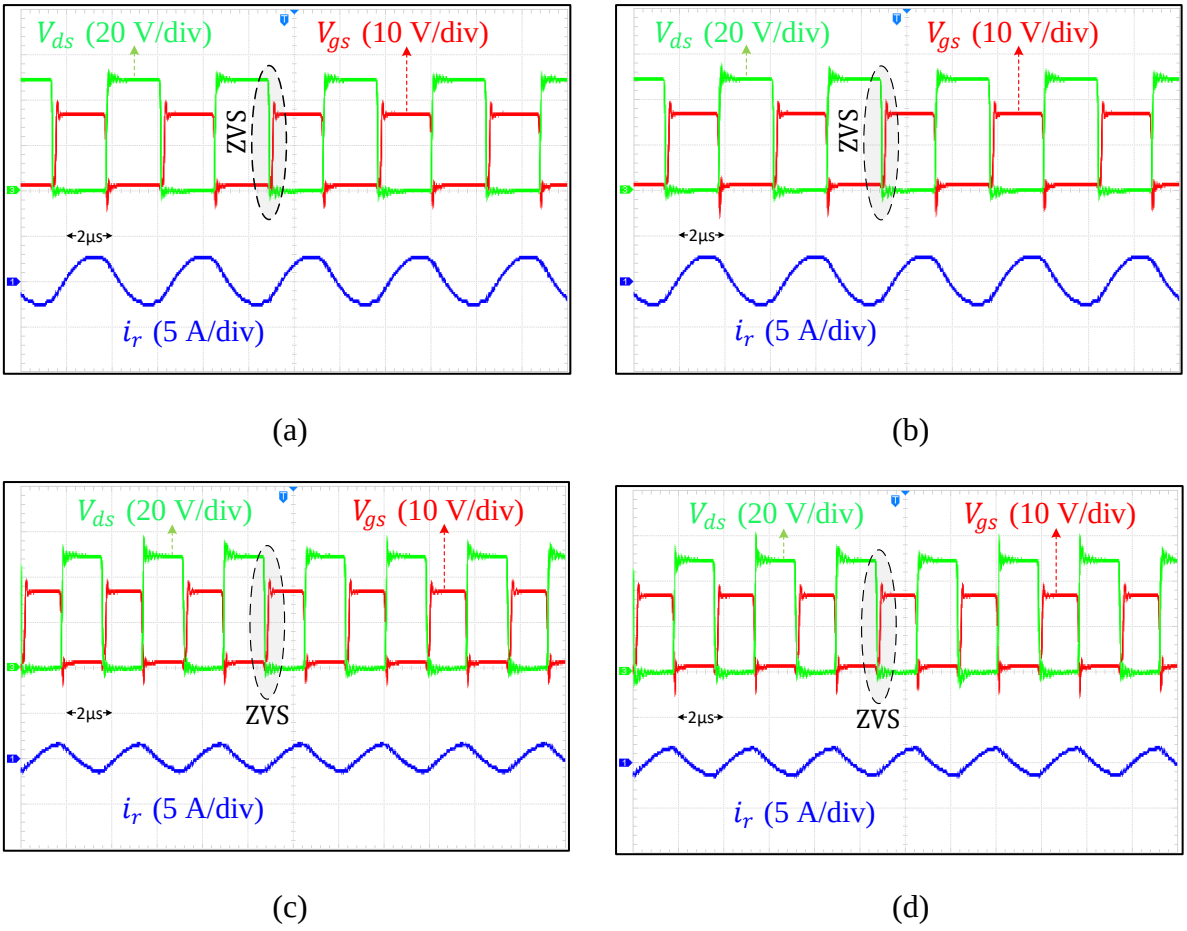

Fig. 7.12 Experimental waveforms of the designed LLC converter utilising (a) the proposed integrated transformer, IT4, (f_s=210 kHz), (b) the inserted-segmental-shunt integrated transformer, IT2, (f_s=210 kHz), (c) the proposed integrated transformer, IT4, (f_s=280 kHz), (d) the inserted-segmental-shunt integrated transformer, IT2, (f_s=280 kHz). V_{ds} is drain to source voltage, V_{gs} is gate to source voltage and i_r is the resonant current (defined in **Fig. 5.1**).

efficiency optimization considerations. The frequency range for LLC converters with power less than 50 W typically falls within the range of a few tens of kilohertz to a few hundred kilohertz. The actual frequency will depend on the specific design and application requirements of the converter.

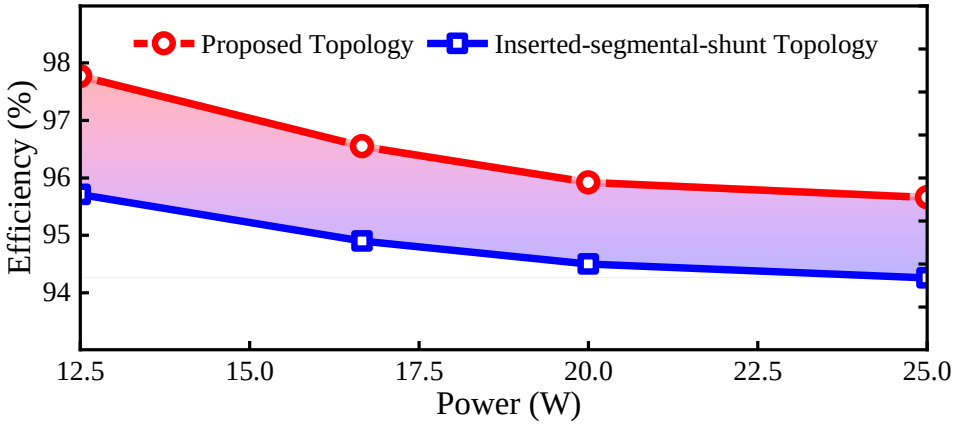

Fig. 7.13 Efficiency of the converter for the proposed topology (IT4) and inserted-segmental-shunt integrated transformer (IT2).

The efficiency of the LLC converter versus different loads for the proposed integrated transformer (IT4) and inserted-segmental-shunt integrated (IT2, conventional) transformer is presented in **Fig. 7.13**. According to **Fig. 7.10** and **Fig. 7.13**, the proposed topology benefits from higher efficiency compared to the topology with inserted-segmental-shunt and the lower AC resistance of the proposed topology explains the reason of this discrepancy. It needs to be pointed that the rectifier diodes cause the dominant losses in the implemented converter and it is hard to show the efficiency difference between the proposed topology and inserted-segmental-shunt integrated transformer when they are operating in the circuit. Hence, the rectifier diodes are removed from the converter to measure the efficiency.

The thermal images of the proposed integrated transformer (IT4) and inserted-segmental-shunt integrated transformer (IT2) while they are used in the implemented LLC resonant converter at nominal operating condition are shown in **Fig. 7.14(a)** and **(b)**, respectively. As shown, the proposed topology operates at a lower temperature since it has lower losses, verifying **Fig. 7.13**. In addition, the temperature of windings is higher than the cores since conduction losses are the dominant losses in the inserted-shunt integrated transformers, verifying the loss distribution presented in **Fig. 7.8**.

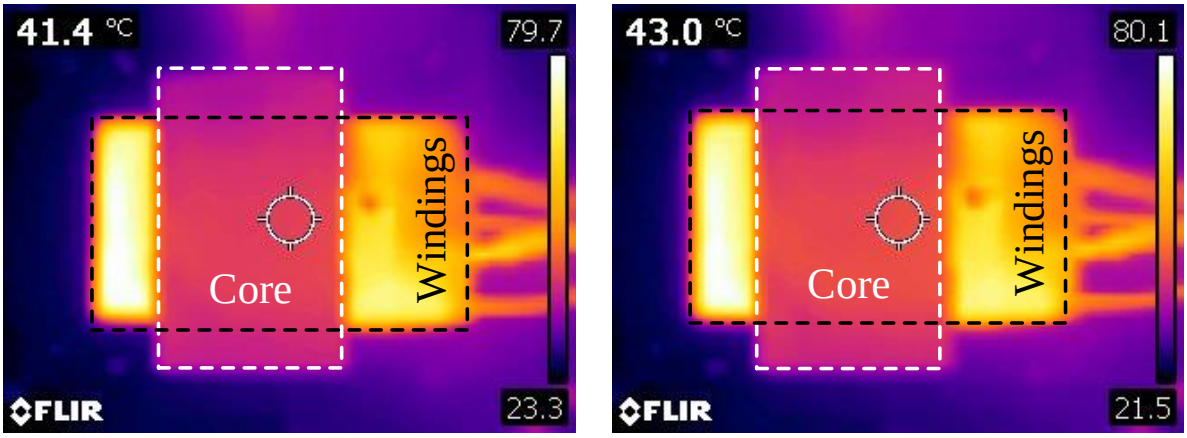

(a) (b)

Fig. 7.14 Thermal images of the transformers. (a) Proposed topology (IT4). (b) Inserted-segmental-shunt topology (IT2).

It should be noted that the application of the proposed integrated transformer can be also extended to other similar converters like phase-shifted full-bridge converters and is not only restricted to the LLC resonant converter.

7.5 Conclusion

A new topology (IT4) for the inserted-shunt integrated planar transformers was proposed which has low secondary leakage inductance. The proposed topology overcomes the main issue of inserted-shunt integrated transformers which is high leakage inductance in the secondary side. In addition, the proposed topology benefits from both advantages of high-permeability segmental shunt and low-permeability one-segment shunt topologies.

The proposed topology is analysed and modelled in detail. It is shown that the design of leakage and magnetising inductances are decoupled from each other completely. Therefore, they can be determined separately, leading the design process to higher flexibility. FEA simulation and experimental results are presented to verify the theoretical analysis. The inserted-segmental-shunt integrated transformer (IT2) presented in Chapter 5 was compared experimentally with the proposed transformer in terms of efficiency and AC resistance and the new design is found to provide higher efficiency. In addition, an LLC resonant converter was built to investigate the performance of the proposed topology in practice. Results show that the proposed topology

can integrate all three magnetic components of the LLC converter into only a single planar transformer while the converter operates properly.

The reported inserted-shunt integrated transformers and the topologies presented in Chapters 5 to 7 are not suitable for use in bidirectional LLC-type resonant converters when different primary and secondary leakage inductances are needed, such as where variable gain is required. Therefore, in Chapter 8, a new topology (termed IT5) for inserted-shunt integrated transformers is proposed that can be used in bidirectional LLC-type converters while it still benefits from simple manufacturing and using commercially available materials.

Chapter 8

Fully-integrated Transformer with Asymmetric Primary and Secondary Leakage Inductances for a Bidirectional Resonant Converters

In this Chapter, a new topology (termed IT5) for an inserted-shunt integrated transformer which can provide tuneable, asymmetric leakage (series) inductances on the primary and secondary sides is presented. Two magnetic shunts, with appropriate air gaps, are inserted between two E-cores and the primary and secondary windings are separated by being placed at opposite sides of the shunts. The proposed transformer is analysed in detail and modelling and design guidelines are provided. It is shown that the magnetising inductance and the primary and secondary leakage inductances are decoupled from each other, and they can be determined separately. The design has the advantage of using planar E-cores and magnetically permeable sheets that are commercially available. The theoretical analysis is verified by simulation and experimental results. In addition, to demonstrate the performance of the proposed integrated transformer in practice, an exemplar bidirectional CLLLC resonant converter is designed, constructed and tested using the new integrated transformer.

8.1 Introduction

As discussed in Chapter 3, the LLC converter is not suitable for bidirectional power transfer and an extra capacitor and inductor are needed to be added to the secondary side of the transformer for bidirectional power transfer [152-154]. The topology of CLLLC converter is again shown in **Fig. 8.1(a).** This converter needs asymmetric primary and secondary resonant inductances when a high battery voltage regulation is needed [154]. Even though this converter benefits from soft switching capability and can be switched at high frequencies, it needs four magnetic components including two series inductors (L_{r1} and L_{r2}), a shunt inductor (L_{Sh}) and a transformer, leading to large size and high cost. To increase the efficiency and power density,

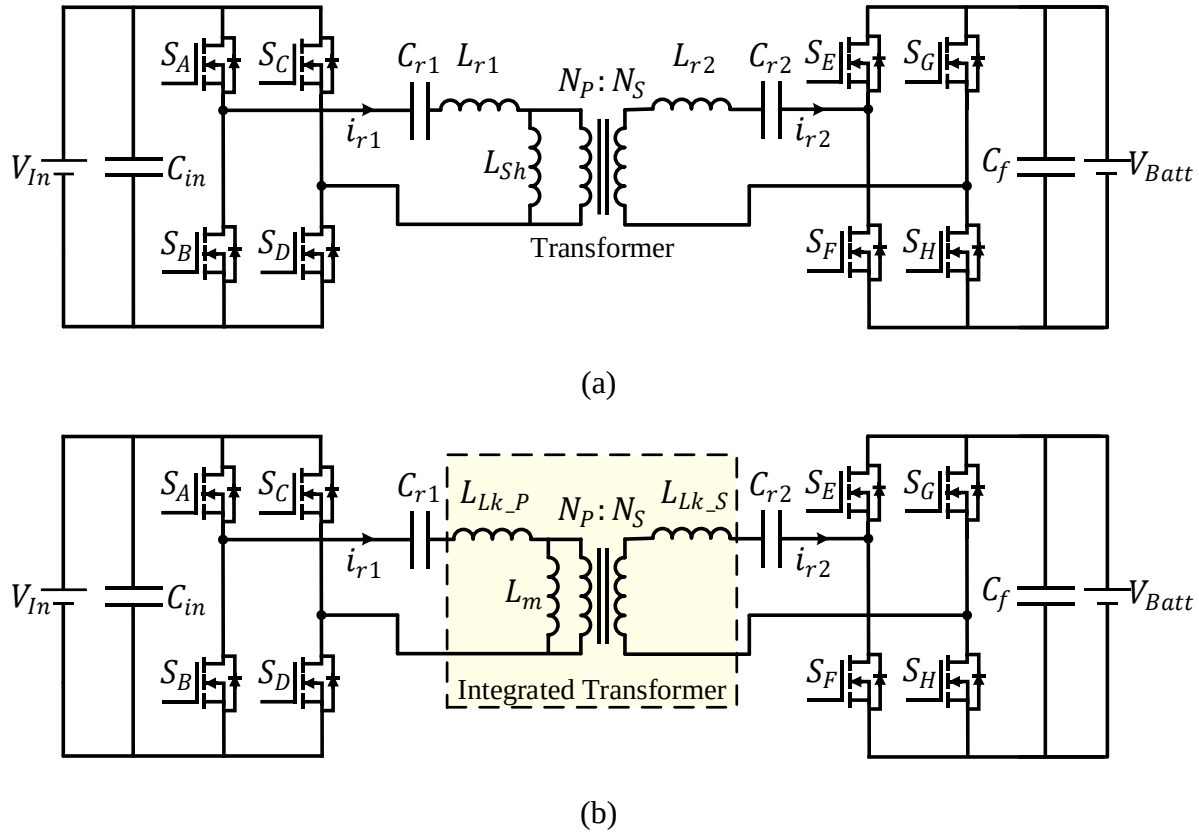

Fig. 8.1 Topology of bidirectional CLLLC resonant converter, (a) without magnetic integration, (b) with magnetic integration.

and to decrease the cost of this converter, these magnetic components can be integrated into a single transformer, as shown in **Fig. 8.1(b)**.

Amongst different methods for magnetic integration, the inserted-shunt integrated planar transformer is well-known [10, 130]. The reported inserted-shunt integrated transformers including the topologies proposed in Chapters 5 and 6 (IT1-IT3) have symmetric primary and secondary leakage inductances and these inductances cannot be designed separately in these transformers. The CLLLC converter presented in [153, 154], and other similar topologies may need asymmetric primary and secondary resonant inductances. Therefore, a new design methodology for the inserted-shunt integrated transformers is needed that takes into account the non-identical primary and secondary leakage inductances. Hence, the primary focus of this chapter is to present an integrated transformer that is well-suited for bidirectional power transfer in LLC resonant converters.

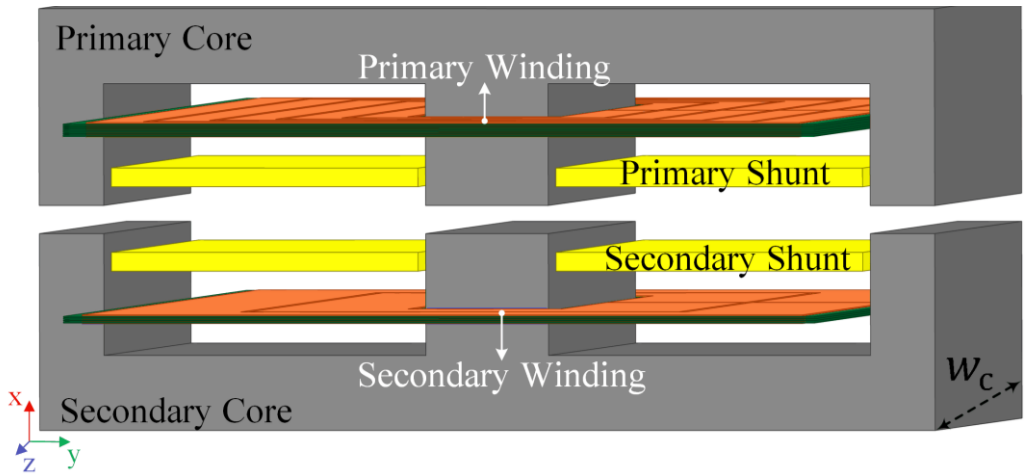

Fig. 8.2 Schematic of the proposed integrated transformer (IT5) in x-y-z plane.

In this Chapter, a new topology (termed IT5) for the inserted-shunt integrated magnetic planar transformer is proposed that can provide non-identical primary and secondary leakage inductances. The structure of the proposed integrated transformer is shown in **Fig. 8.2**. Two magnetic shunts are inserted between two E-cores and the primary and secondary windings are separated by being placed at different sides of the magnetic shunts. Commercially available planar cores can be used for the E-cores and magnetic (ferrite) sheets, which are again commercially available, can be used for the shunts, leading to cheaper and easier manufacturing.

The proposed integrated transformer is analysed in detail and its modelling and design guidelines are provided. It is shown that the magnetising inductance and the primary and secondary leakage inductances are decoupled, and they can be determined separately in the proposed topology. This theoretical analysis is verified by simulation and experimental results. To investigate performance, an exemplar CLLLC converter is designed using the proposed integrated transformer to provide experimental validation of the design process. It is shown that the implemented bidirectional CLLLC resonant converter operates properly while all its magnetic components are integrated into the proposed transformer.

8.2 Proposed inserted-shunt integrated transformer

The schematic of the proposed integrated transformer is shown in **Fig. 8.2**. The structure is divided into primary and secondary sections. The primary section contains an E-core (primary core), a magnetic shunt (primary shunt) and a winding (primary winding), and the secondary

section contains the corresponding secondary pieces (secondary core, the shunt and winding). With reference to the equivalent circuit shown in **Fig. 2.17**, the operating principle of the transformer is summarised below with more detailed descriptions being provided in the following sections.

The primary winding generates a flux in the primary core and this is responsible for producing the primary side inductance (L_{PP} in **Fig. 2.17(a)**) of which the magnetising inductance (L_{m} in **Fig. 2.17(b)**) is the largest contributor. A small but significant proportion of the primary flux flows through the primary shunts and is responsible for the primary side leakage inductance, $L_{\mathrm{Lk\_P}}$. Similar arguments lead to the provision of the secondary side leakage inductance ($L_{\mathrm{Lk\_S}}$). The remaining primary flux crosses the air gap and couples to the secondary winding and so is responsible for the ideal transformer $N_{\mathrm{P}}{:}\,N_{\mathrm{S}}$ in **Fig. 2.17(b)**.

8.2.1 Basic definition of magnetising and primary and secondary leakage inductances

In subsection 2.4, it is shown that the primary ($L_{\mathrm{Lk\_P}}$) and secondary ($L_{\mathrm{Lk\_S}}$) leakage inductances can be achieved from primary (L_{PP}) and secondary (L_{SS}) self-inductances and magnetising inductance (L_{m}) as follows:—

$$L_{\mathrm{Lk\_P}} = L_{\mathrm{PP}} - L_{\mathrm{m}} \tag{8-1}$$

$$L_{\mathrm{Lk\_S}} = L_{\mathrm{SS}} - \frac{N_S^2}{N_{\mathrm{P}}^2} L_{\mathrm{m}} \tag{8-2}$$

8.2.2 Calculation of magnetising inductance

The structure of the proposed transformer, with its geometry and dimensions, is shown in **Fig. 8.3(a)**. An air gap of length ℓ_{G} is inserted between the two E-cores to regulate the magnetising inductance. Air gap ℓ_{GP} is located between primary shunt and primary E-core to set the primary leakage inductance, and the air gap ℓ_{GS} is located between secondary shunt and secondary E-core to set the secondary leakage inductance. **Fig. 8.3(b)** shows the reluctance model of the proposed integrated transformer. In this model, the permeability of the core is assumed to be much larger than the permeability of the air and the shunts, and thus only the reluctances of the

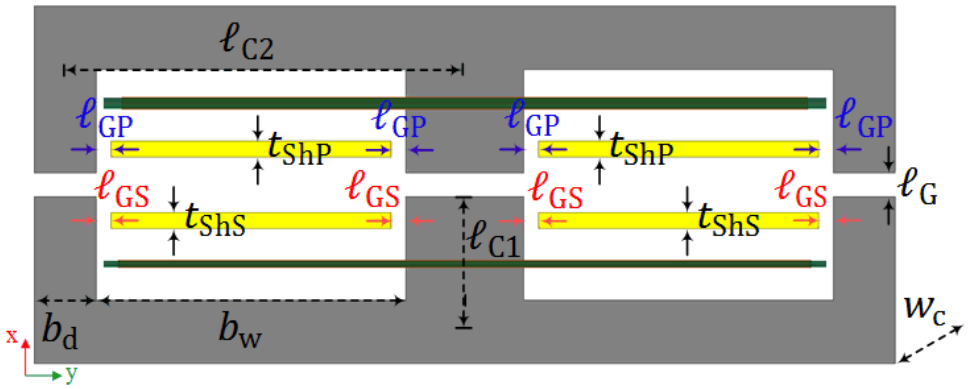

(a)

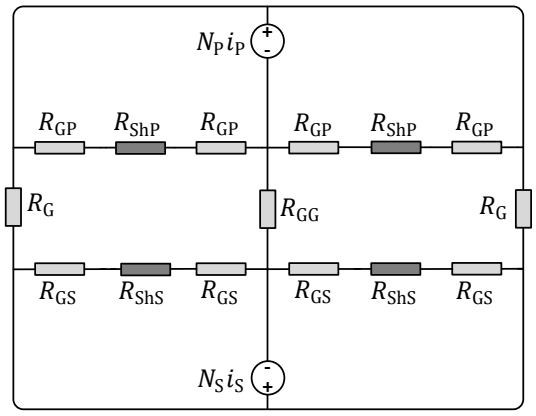

(b)

Fig. 8.3 The proposed integrated transformer (IT5). (a) Geometry in x-y plane. (b) Reluctance model.

air gaps and shunts are considered for the analysis. In **Fig. 8.3(b)**, $\mathcal{R}_{ShP}$ and $\mathcal{R}_{ShS}$ are the reluctances of the primary and secondary shunts, respectively; $\mathcal{R}_{GP}$ and $\mathcal{R}_{GS}$ are the air gap reluctances of the primary and secondary shunts; and $\mathcal{R}_G$ and $\mathcal{R}_{GG}$ are the reluctances of the air gaps between the two E-cores. These reluctances may be obtained as follows:—

$$\mathcal{R}_{ShP} = \frac{b_w - 2\ell_{GP}}{\mu_0 \mu_{ShP} t_{ShP} w_c} \tag{8-3}$$

$$\mathcal{R}_{ShS} = \frac{b_w - 2\ell_{GS}}{\mu_0 \mu_{ShS} t_{ShS} w_c} \tag{8-4}$$

$$\mathcal{R}_{\mathrm{GP}} = \frac{\ell_{\mathrm{GP}}}{\mu_0(t_{\mathrm{ShP}} + \ell_{\mathrm{GP}})(w_{\mathrm{c}} + \ell_{\mathrm{GP}})} \tag{8-5}$$

$$\mathcal{R}_{\mathrm{GS}} = \frac{\ell_{\mathrm{GS}}}{\mu_0(t_{\mathrm{ShS}} + \ell_{\mathrm{GS}})(w_{\mathrm{c}} + \ell_{\mathrm{GS}})} \tag{8-6}$$

$$\mathcal{R}_{\mathrm{G}} = \frac{\ell_{\mathrm{G}}}{\mu_0(b_d + \ell_{\mathrm{G}})(w_{\mathrm{c}} + \ell_{\mathrm{G}})} \tag{8-7}$$

$$\mathcal{R}_{\mathrm{GG}} = \frac{\ell_{\mathrm{G}}}{\mu_0(2b_d + \ell_{\mathrm{G}})(w_{\mathrm{c}} + \ell_{\mathrm{G}})} \tag{8-8}$$

where μ_0 is the air permeability and μ_{ShP} and μ_{ShS} are the relative permeabilites of the primary and secondary shunts, respectively. The meaning of other quantities, such as areas, can be found in **Fig. 8.3(a)**. Hurley, *et al*, [168] show that the effective cross-sectional area of the air gap with dimensions *a* by *b* is equal to (*a*+*g*) by (*b*+*g*) when the fringing effect is considered and *g* is the length of the studied air-gap.

According to the reluctance model presented in **Fig. 8.3(b)**, the mutual fluxes ϕ_{PS} and ϕ_{SP} may be approximated by (8-9) and (8-10), respectively.

$$\phi_{\mathrm{PS}} = \frac{2N_{\mathrm{P}}i_{\mathrm{P}}}{\mathcal{R}_{\mathrm{G}} + 2\mathcal{R}_{\mathrm{GG}}} \tag{8-9}$$

$$\phi_{\mathrm{SP}} = \frac{2N_{\mathrm{S}}i_{\mathrm{S}}}{\mathcal{R}_{\mathrm{G}} + 2\mathcal{R}_{\mathrm{GG}}} \tag{8-10}$$

Finally, from (8-9) and (2-56), the magnetising inductance may be obtained,

$$L_{\mathrm{m}} = \frac{2N_{\mathrm{P}}^2}{\mathcal{R}_{\mathrm{G}} + 2\mathcal{R}_{\mathrm{GG}}} \tag{8-11}$$

8.2.3 Energy stored by primary and secondary leakage inductances

Assuming the permeability of the core is high then any energy that is stored in the transformer must be located outside the core and, therefore, within the window area. Equation (8-12) shows the total energy stored in the volume of the windings, the window area and the shunts (including their air gaps, ℓ_{GP} and ℓ_{GS}) is equal the energy stored in the primary and secondary leakage inductances.

$$E = \frac{1}{2}\iiint_V BH \,\mathrm{d}V = \frac{1}{2}L_{\mathrm{Lk\_P}}i_{\mathrm{P}}^2 + \frac{1}{2}L_{\mathrm{Lk\_S}}i_{\mathrm{S}}^2 \tag{8-12}$$

where V is the total volume of window area, B is the flux density and H is the magnetic field intensity.

A cross section of the right-hand side of the proposed integrated transformer, divided into several regions contributing to the energy stored by the leakage inductances, is shown in **Fig. 8.4**. In **Fig. 8.4**, N_{P} and N_{S} are the number of primary and secondary turns, respectively; n_{P} and n_{S} are the number of the primary and secondary winding layers, respectively; and k_{P} and k_{S} are number of turns per layer for the primary and secondary windings ($N_{\mathrm{P}} = k_{\mathrm{P}}n_{\mathrm{P}}$ and $N_{\mathrm{S}} = k_{\mathrm{S}}n_{\mathrm{S}}$), respectively. Each primary winding layer has a thickness h_{P} and its associated insulating layer has thickness $h_{\Delta\mathrm{P}}$. Similar symbols are used for the secondary winding with each layer having a thickness h_{S} and insulating layer thickness $h_{\Delta\mathrm{S}}$. E_{P} and E_{S} refer to the energy stored in the primary and secondary windings. E_{air} is the energy stored in that part of the window which is not occupied by the windings or shunts, and this is divided into a primary region of height x_{P} and a secondary region of height x_{S}. Hence, the energy stored in each region and the energy stored in the shunts, E_{Sh}, (including their air gaps, ℓ_{GP} and ℓ_{GS}) needs to be obtained and the primary and secondary leakage inductances can be then obtained from $E = E_{\mathrm{air}} + \mathrm{E_P} + \mathrm{E_S} + E_{\mathrm{Sh}}$ and (8-12).

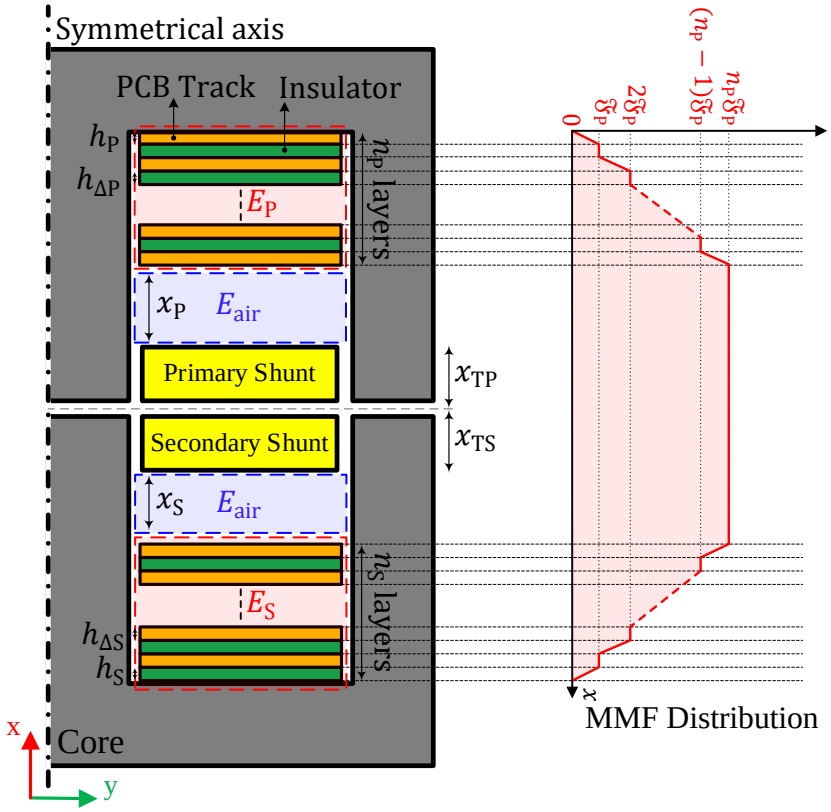

Fig. 8.4 Right hand side cross section showing the energy allocation and associated MMF distribution for the proposed topology (IT5).

8.3 Calculation of primary and secondary leakage inductances

As discussed at the end of Section 8.2, to calculate the primary and secondary leakage inductances, the energy stored in each region and the energy stored in the shunts need to be obtained.

8.3.1 Energy stored in window area – E_{air}

The magnetomotive force (MMF) of each layer of the primary winding, $\Im_P$, may be obtained from (8-13).

$$\Im_P = k_P i_P \tag{8-13}$$

The MMF within the window area, $\Im_{air}$, is equal to $n_P\Im_P$ and the magnetic field intensity within the air area, H_{air}, may be found from (8-14).

$$H_{\text{air}} = \frac{n_{\text{P}}\Im_{\text{P}}}{b_{\text{w}}} \tag{8-14}$$

From (8-12), the energy stored in the window (excluding the windings and shunts), E_{air}, (shown in **Fig. 8.4**) is given by,

$$E_{\text{air}} = \frac{1}{2}\mu_0 w_{\text{c}} b_{\text{w}} \left(\int_{x_{\text{TP}}}^{x_{\text{TP}}+x_{\text{P}}} H_{\text{air}}^2 \text{d}x + \int_{-x_{\text{TS}}-x_{\text{S}}}^{-x_{\text{TS}}} H_{\text{air}}^2 \text{d}x \right) \tag{8-15}$$

where w_{c} is the core depth and x_{P} and x_{S} are the distances from the primary and secondary windings to the primary and secondary shunts, respectively, as defined in **Fig. 8.4**.

From (8-13)-(8-15), E_{air} in both windows (left and right windows of the E-cores) may be found from (8-16).

$$E_{\text{air}} = \mu_0 w_{\text{c}} \frac{n_{\text{P}}^2 k_{\text{P}}^2 i_{\text{P}}^2}{b_{\text{w}}} (x_{\text{P}} + x_{\text{S}}) \tag{8-16}$$

8.3.2 Energy stored in primary and secondary windings

The MMF distribution of the transformer is presented in **Fig. 8.4** which is obtained based on a method outlined in [129, 130, 134]. According to **Fig. 8.4**, the stored energy in the PCB layers of primary and secondary windings can be found. Ouyang, *et al*, [129] derived a closed-form expression for the energy stored in the primary and secondary windings, shown in (8-17) and (8-18), respectively.

$$E_{\text{P}} = \frac{1}{6}\mu_0 \frac{w_{\text{c}}}{b_{\text{w}}} k_{\text{P}}^2 [h_{\Delta\text{P}}(2n_{\text{P}}^3 - 3n_{\text{P}}^2 + n_{\text{P}}) + 2h_{\text{P}} n_{\text{P}}^3] i_{\text{P}}^2 \tag{8-17}$$

$$E_{\text{S}} = \frac{1}{6}\mu_0 \frac{w_{\text{c}}}{b_{\text{w}}} k_{\text{S}}^2 [h_{\Delta\text{S}}(2n_{\text{S}}^3 - 3n_{\text{S}}^2 + n_{\text{S}}) + 2h_{\text{S}} n_{\text{S}}^3] i_{\text{S}}^2 \tag{8-18}$$

8.3.3 Energy stored in primary and secondary shunts

The energy stored in the inserted shunts and their corresponding air gaps can be obtained from the reluctance model using the method outlined in Chapter 5. According to the reluctance model presented in **Fig. 8.3(b)**, the self-inductance of the primary and secondary windings may be obtained as shown in (8-19) and (8-20), respectively.

$$L_{\mathrm{PP}} = \frac{N_{\mathrm{P}}^2(\mathcal{R}_{\mathrm{ShP}} + 2\mathcal{R}_{\mathrm{GP}} + \mathcal{R}_{\mathrm{G}} + 2\mathcal{R}_{\mathrm{GG}})}{(\mathcal{R}_{\mathrm{ShP}} + 2\mathcal{R}_{\mathrm{GP}})(\mathcal{R}_{\mathrm{G}} + 2\mathcal{R}_{\mathrm{GG}})} \tag{8-19}$$

$$L_{\mathrm{SS}} = \frac{N_{\mathrm{S}}^2(\mathcal{R}_{\mathrm{ShS}} + 2\mathcal{R}_{\mathrm{GS}} + \mathcal{R}_{\mathrm{G}} + 2\mathcal{R}_{\mathrm{GG}})}{(\mathcal{R}_{\mathrm{ShS}} + 2\mathcal{R}_{\mathrm{GS}})(\mathcal{R}_{\mathrm{G}} + 2\mathcal{R}_{\mathrm{GG}})} \tag{8-20}$$

From (8-1), (8-2), (8-11), (8-19) and (8-20), the primary and secondary leakage inductances caused by the inserted shunts and their corresponding air gaps may be calculated as shown in (8-21) and (8-22), respectively.

$$L_{\mathrm{Lk\_P\_Sh}} = \frac{2N_{\mathrm{P}}^2}{\mathcal{R}_{\mathrm{ShP}} + 2\mathcal{R}_{\mathrm{GP}}} \tag{8-21}$$

$$L_{\mathrm{Lk\_S\_Sh}} = \frac{2N_{\mathrm{S}}^2}{\mathcal{R}_{\mathrm{ShS}} + 2\mathcal{R}_{\mathrm{GS}}} \tag{8-22}$$

Finally, from (8-12), (8-16)-(8-18), (8-21) and (8-22), the primary and secondary leakage inductances of the proposed inserted-shunt integrated transformer may be obtained as shown in (8-23) and (8-24), respectively.

$$L_{\mathrm{Lk\_P}} = L_{\mathrm{Lk\_P\_Sh}} + \mu_0 w_{\mathrm{c}} \frac{N_{\mathrm{P}}^2}{b_{\mathrm{w}}}(x_{\mathrm{P}} + x_{\mathrm{S}}) + \frac{1}{3}\mu_0 \frac{w_{\mathrm{c}}}{b_{\mathrm{w}}} k_{\mathrm{P}}^2 [h_{\Delta \mathrm{P}}(2n_{\mathrm{P}}^3 - 3n_{\mathrm{P}}^2 + n_{\mathrm{P}}) + 2h_{\mathrm{P}} n_{\mathrm{P}}^3] \tag{8-23}$$

$$L_{\mathrm{Lk\_S}} = L_{\mathrm{Lk\_S\_Sh}} + \mu_0 w_{\mathrm{c}} \frac{N_{\mathrm{S}}^2}{b_w}(x_{\mathrm{P}} + x_{\mathrm{S}}) + \frac{1}{3}\mu_0 \frac{w_{\mathrm{c}}}{b_{\mathrm{w}}} k_{\mathrm{S}}^2 [h_{\Delta \mathrm{S}}(2n_{\mathrm{S}}^3 - 3n_{\mathrm{S}}^2 + n_{\mathrm{S}}) + 2h_{\mathrm{S}} n_{\mathrm{S}}^3] \tag{8-24}$$

For the design process of the proposed transformer, the required primary and secondary leakage inductances and magnetising inductance can be obtained by (8-11), (8-23) and (8-24). Particular values can be selected for a particular design by regulating the air gaps ℓ_{G}, ℓ_{GP} and ℓ_{GS}, and the shunt thicknesses t_{ShP} and t_{ShS}.

8.4 Modelling discussion

The calculated primary and secondary leakage inductances and magnetising inductance of the proposed integrated transformer for different thicknesses of the shunts (t_{ShP} and t_{ShS}), transformer air gap (ℓ_{G}) and shunt-core air gaps (ℓ_{GP} and ℓ_{GS}) are presented in **Fig. 8.5(a)-(f)**. An E58/11/38-3F36 core was used as reference to determine the main factors of influence on a design. As shown in **Fig. 8.5(a)-(d)**, the primary leakage inductance is mainly affected by the primary shunt air gap (ℓ_{GP}), primary shunt thickness (t_{ShP}) and relative permeability of the primary shunt (μ_{ShP}). The secondary shunt's characteristics and transformer air gap (ℓ_{G}) do not have noticeable influence on the primary leakage inductance. The secondary leakage inductance is mainly affected by the secondary shunt's characteristics (ℓ_{GS}, t_{ShS} and μ_{ShS}) and it is not affected by the characteristics of the primary shunt (ℓ_{GP}, t_{ShP} and μ_{ShP}) or the transformer air gap (ℓ_{G}). Therefore, in the proposed topology, the primary and secondary leakage inductances are decoupled, and they may be controlled separately by regulating their shunt's characteristics.

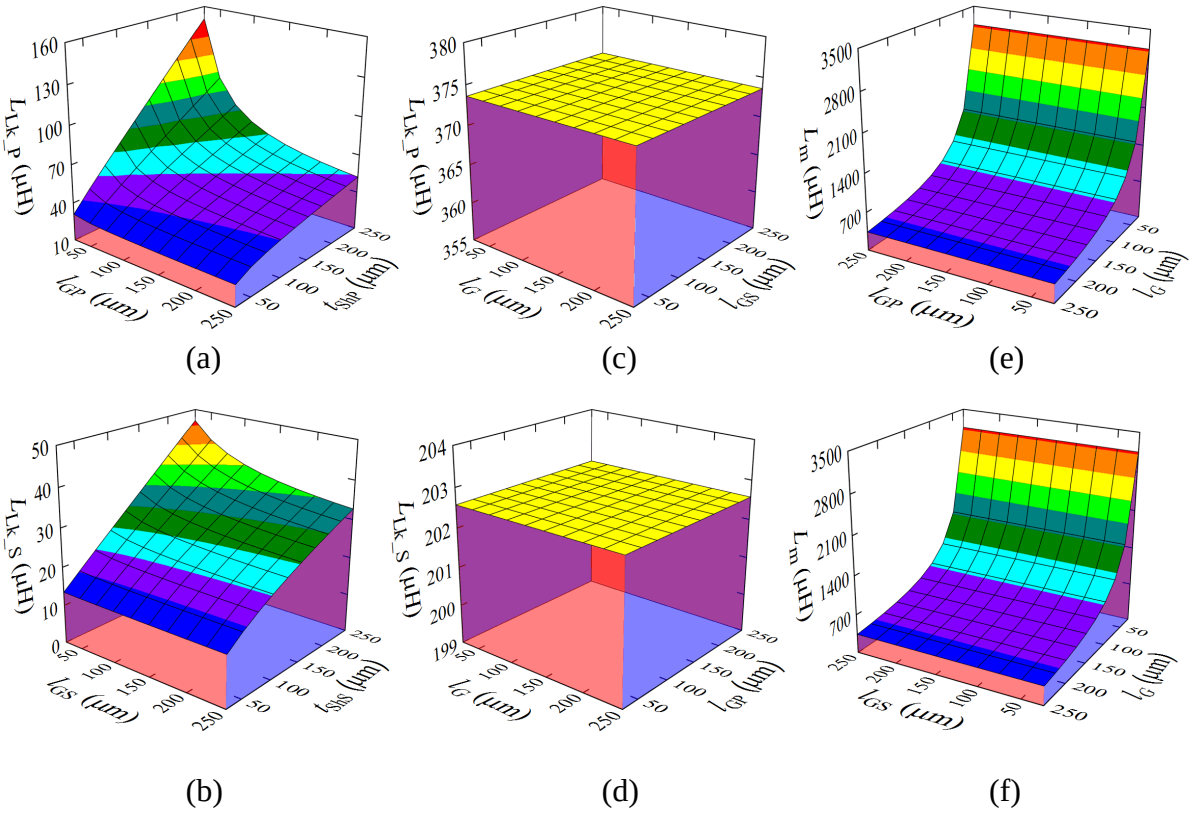

Fig. 8.5 The calculated leakage and magnetising inductances versus thickness of the shunts, transformer air gap and air gap between the shunts and E-cores. (a) Primary leakage inductance, t_{ShS}=2mm and ℓ_{GS}=0.1mm. (b) Secondary leakage inductance, t_{ShP}=2mm and ℓ_{GP}=0.1mm. (c) Primary leakage inductance, t_{ShS}=t_{ShP}=2mm and ℓ_{GP}=0.1mm. (d) Secondary leakage inductance, t_{ShS}=t_{ShP}=2mm and ℓ_{GS}=0.1mm. (e) Magnetising inductance, t_{ShS}=t_{ShP}=2mm and ℓ_{GS}=0.1mm. (f) Magnetising inductance, t_{ShS}=t_{ShP}=2mm and ℓ_{GP}=0.1mm. Core: E58/11/38-3F36, μ_{ShP}=800, μ_{ShS}=100, N_{P}=20, N_{S}=20, n_{P}=5, n_{S}=5, k_{P}=4, k_{S}=4, x_{P}=5mm, x_{S}=5mm.

Fig. 8.5(e) and **(f)** show that the magnetising inductance is mainly affected by the transformer air gap, ℓ_{G}, and does not change appreciably by varying the shunts' air gaps, thicknesses and relative permeabilities (ℓ_{GP}, ℓ_{GS}, t_{ShP}, t_{ShS}, μ_{ShP} and μ_{ShS}). Therefore, in the proposed integrated transformer, the leakage and magnetising inductances are sufficiently decoupled.

The transformer can be designed for most reasonable magnetic component values including the leakage and magnetising inductances. Careful designs can provide different primary and secondary leakage inductances. Because the leakage (series) inductances can be selected independently of each other, a CLLLC resonant converter or similar topology which uses the proposed integrated transformer can be designed with high flexibility. In addition, the transformer provides all four (asymmetric) magnetic components.

The proposed topology does not require any unusual core-piece geometries and those widely available commercially can be used. In addition, magnetic (ferrite) sheets, which are available in different sizes and can be cut easily, can be used for the inserted shunts. It should be noted that the proposed inserted-shunt integrated transformer would need an atypical former design for massive production. However, a bespoke former is already needed for any inserted-shunt integrated transformers.

In addition, where a design requires it, the proposed topology can achieve identical primary and secondary leakage inductances by regulating the primary and secondary shunts air gaps. This compares favourably to conventional inserted-shunt integrated transformers which typically have minor asymmetry due to differences between primary and secondary window areas and winding designs in these transformers.

8.5 Simulation results

To verify the inductance equations provided in sections 8.2 and 8.3, an integrated transformer was simulated using the parameters presented in **Table 8.1**. The integrated transformer is designed for embedding within a CLLLC resonant converter with specifications presented in **Table 8.2**. The electrical specifications provided in **Table 8.2** are achieved using the design methodology described in [153] and they are translated into the integrated transformer equivalent circuit components (see **Fig. 8.1(a)** and **(b)**).

TABLE 8.1 Proposed structure's parameters.

Symbol	Parameter	Value
N_{P}	Primary turns	20
N_{S}	Secondary turns	4
k_{P}	Turns per layer in primary	5
k_{S}	Turns per layer in secondary	2
n_{P}	Number of primary layers	4
n_{S}	Number of secondary layers	2
h_{P}, h_{S}	Primary and secondary conduction thickness	55, 70 μm
$h_{\Delta\mathrm{P}}$, $h_{\Delta\mathrm{S}}$	Primary and secondary insulation thickness	45, 60 μm
t_{ShP}	Primary shunt thickness	2.5 mm
t_{ShS}	Secondary shunt thickness	1.2 mm
ℓ_{G}	Transformer air gap	0.9 mm
ℓ_{GP}	Distance between primary shunt and E-core	0.2 mm
ℓ_{GS}	Distance between secondary shunt and E-core	0.32 mm
x_{P}, x_{S}	Distance between primary and secondary windings and shunts, respectively	3.5 mm 4.5 mm

The power and voltage levels of this converter are distinct from the unidirectional LLC converter presented in previous chapters. Bidirectional LLC converters are commonly used for higher power applications, such as in electric vehicles (EVs). Moreover, the design of this bidirectional converter exhibits slight differences compared to a unidirectional converter (which were discussed in previous chapters). Due to the specific hardware available in our lab and considering the given specifications, a new design approach for this converter, presented in [153], has been pursued. As a result, this converter operates at a different frequency compared to the converters discussed in previous chapters.

Following the transformer design process described in the Magnetics Inc design catalogue [170], a suitable core is chosen allowing the minimum number of turns for the primary and secondary windings to be determined. The transformer core (E58/11/38-3F36) is selected based

TABLE 8.2 The implemented CLLLC converter's specification.

Symbol	Parameter	Value
$N_{\mathrm{P}}: N_{\mathrm{S}}$	Turns ratio	20:4
L_{m}	Magnetising inductance	110 μH
L_{r1}	Primary resonant inductance	50 μH
L_{r2}	Secondary resonant inductance	1.2 μH
C_{r1}	Primary resonant capacitance	39 nF
C_{r2}	Secondary resonant capacitance	1 μF
V_{In}	Input voltage	125 V
V_{o}	Output voltage	20-26 V
P_{o}	Output power	200 W
f_{s}	Switching frequency	60-130 kHz
S_{P}	Primary switches	IPW65R110CFDA
S_{S}	Secondary switches	IRFP4137PBF

on the power, voltage and frequency suitability guidelines in [170]. The KEMET polymer magnetic shielding sheet (series EFS) is chosen for both the primary and the secondary shunts.

The magnetising inductance, primary and secondary leakage inductances and turns ratio of the designed transformer are chosen to suit the CLLLC resonant converter (**Table 8.2**). The thickness and air gap length of the primary and secondary shunts (ℓ_{GP}, ℓ_{GS}, t_{ShP} and t_{ShS}) are estimated in order to provide the required primary and secondary leakage inductances, using (8-23) and (8-24), and considering the dimensions of the selected core. Similarly, the transformer air gap length (ℓ_{G}) is estimated to provide the required magnetising inductance, using (8-11).

The designed integrated transformer is simulated in Ansys Maxwell, and the simulation results while the transformer is used in the exemplar CLLLC resonant converter are presented in this section.

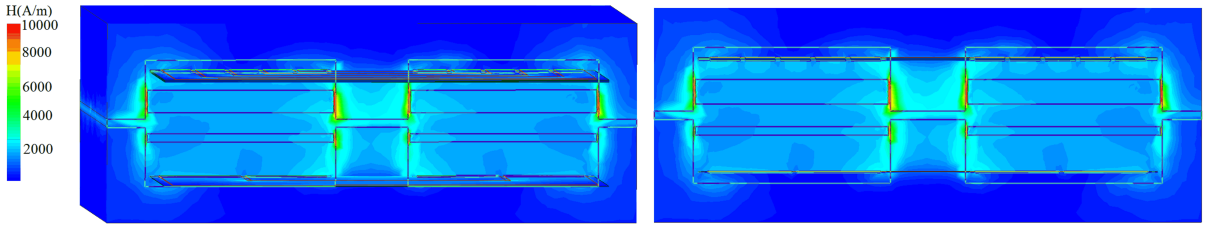

(a)

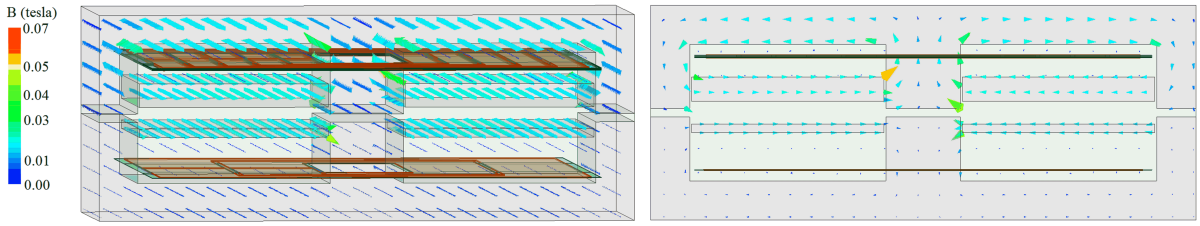

(b)

Fig. 8.6 FEA simulation results. (a) Magnetic field intensity. (b) Magnetic flux density vectors. Frequency=100 kHz.

The magnetic field intensity and flux density vectors for the proposed integrated transformer are shown in **Fig. 8.6(a)** and **(b)**, respectively. As shown, the magnetic field intensity and flux density vectors are dominant in the shunts and their air gaps (ℓ_{GP} and ℓ_{GS}) rather than window region and PCB windings. Therefore, the main part of the energy stored by the leakage inductances is caused by the inserted shunts and their air gaps. In addition, since the magnetic field intensity is highest in the transformer air gap (ℓ_{G}), the energy stored in the magnetising inductance is mainly stored in ℓ_{G}.

The primary and secondary leakage inductances and the magnetising inductance versus thickness of the shunts (t_{ShP} and t_{ShS}) and transformer air gap (ℓ_{G}) obtained from (8-11), (8-23) and (8-24) and measured by FEA simulation are presented in **Fig. 8.7(a)-(c)**, respectively. As shown, the FEA confirms the proposed model derived in sections 8.2 and 8.3 since there is good agreement between the values achieved from the modelling and simulation results.

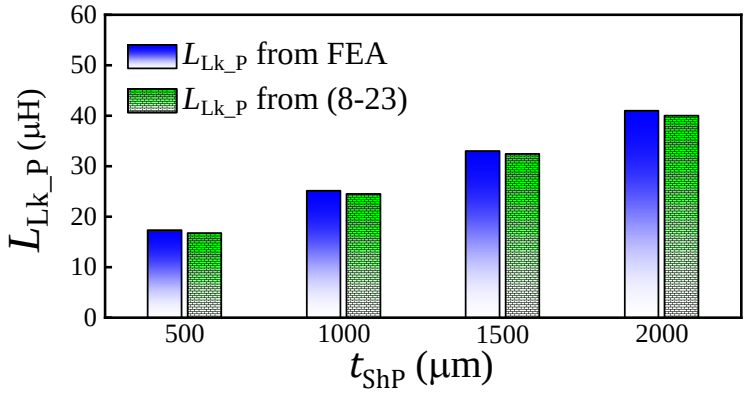

(a)

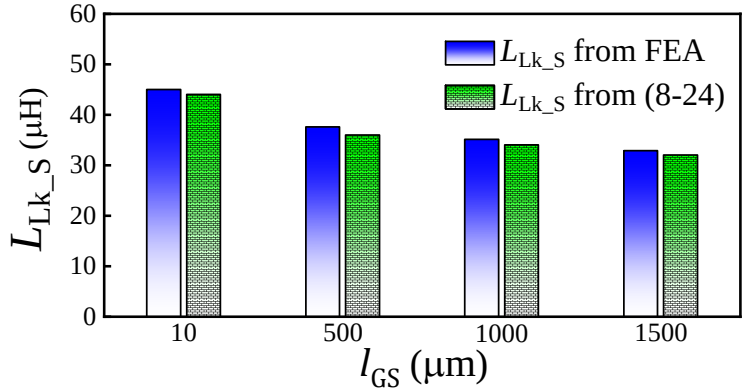

(b)

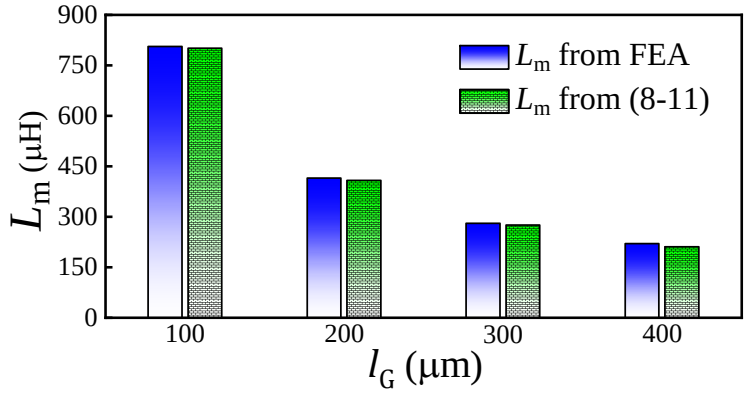

(c)

Fig. 8.7 Modelling validation by FEA. (a) Primary leakage inductance ($l_{GP} = 0.2$mm). (b) Secondary leakage inductance ($t_{ShS} = 2$mm). (c) Magnetising inductance. Core: E58/11/38-3F36, μ_{ShP}= μ_{ShS}=10, N_P=20, N_S=20, n_P=5, n_S=5, k_P=4, k_S=4, x_P=5mm, x_S=5mm.

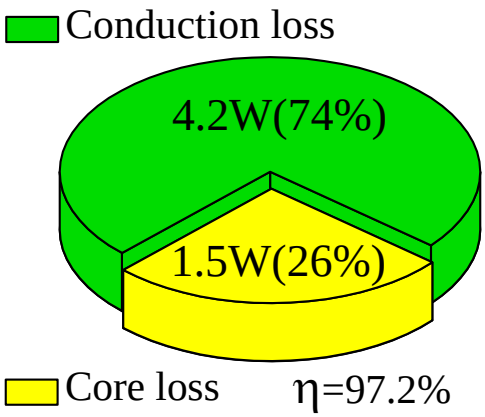

Fig. 8.8 Loss distribution of the proposed topology (IT5) for output power of 200W and frequency of 100 kHz.

Loss distribution of the proposed topology is presented in **Fig. 8.8**. As shown, the conduction losses are the dominant losses in the proposed topology which are mainly because of AC losses in the winding.

8.6 Experimental verification

An integrated transformer based on the proposed structure with parameters presented in **Table 8.1** is built, as shown in **Fig. 8.9**. E58/11/38-3F36 is used for the cores and the shunts for this prototype were made by cutting KEMET polymer magnetic shielding sheets (series EFS) and gluing them in parallel to create a stack with the desired thickness.

The measured leakage and magnetising inductances of the constructed transformer, obtained using an Omicron Bode 100 vector network analyser, are presented in **Table 8.3**. As shown, the primary and secondary leakage inductances and magnetising inductance obtained by modelling are close to the experimental and simulation results. In addition, the proposed structure provides different primary and secondary leakage inductances.

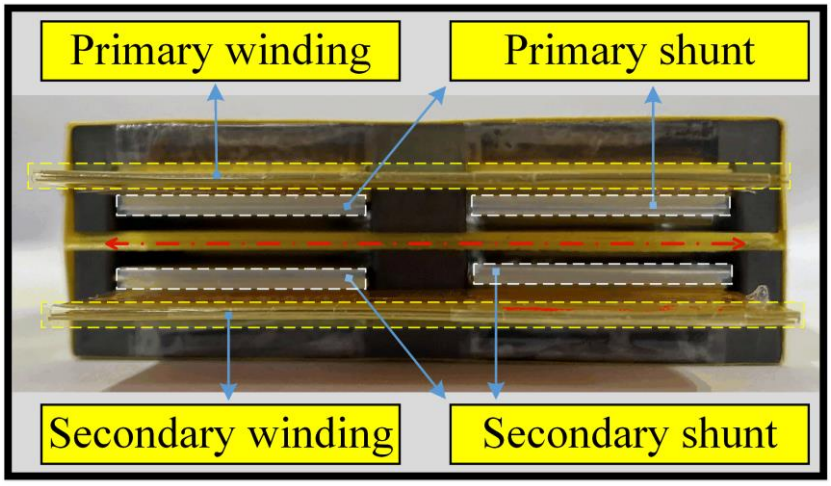

Fig. 8.9 Prototype implemented transformers.

TABLE 8.3 Parameters of the implemented integrated transformer.

Parameter	FEA modelling	Simulation	Measurement
Magnetising inductance, L_{m}	111 µH	113 µH	109 µH
Primary leakage inductance, $L_{\mathrm{Lk\_P}}$	47.9 µH	51.2 µH	49.5 µH
Secondary leakage inductance, $L_{\mathrm{Lk\_S}}$	1.15 µH	1.24 µH	1.20 µH

AC resistance, primary and secondary self-inductances, measured inductance from the primary winding while the secondary winding is short-circuited, and the measured inductance from the secondary winding while the primary winding is short-circuited versus frequency for the constructed transformer are presented in **Fig. 8.10**. As shown, the AC resistance increases with frequency, which is due to high-frequency phenomena including skin and fringing effects. The primary and secondary leakage inductances and magnetising inductance presented in **Table 8.3** are obtained from data presented in **Fig. 8.10** and the method outlined by Ansari, *et al*, [22].

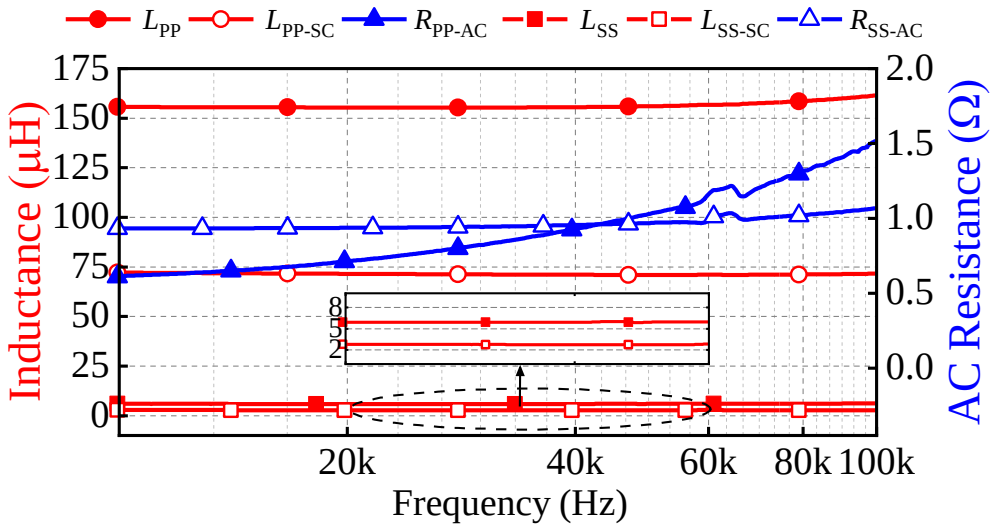

Fig. 8.10 Primary AC resistance, R_{PP-AC}, secondary AC resistance, R_{SS-AC}, primary self-inductance, L_{PP}, secondary self-inductance, L_{SS}, primary inductance with secondary shorted, L_{PP-SC}, and secondary inductance with primary shorted, L_{SS-SC} for the proposed integrated transformer (IT5).

To examine the performance of the proposed topology in practice, it was incorporated within an exemplar bidirectional CLLLC resonant converter designed according to the procedure outlined in [153]. The prototype of the converter is shown in **Fig. 8.11** and its specification is presented in **Table 8.2** in which all four series and parallel inductances are integrated into the transformer.

As presented in **Table 8.2**, in battery charging mode (BCM), the exemplar bidirectional converter should be able to provide output voltage (battery voltage, $V_{o(BCM)}$) ranging from 20 V to 26 V while the input voltage (DC bus voltage, $V_{In(BCM)}$) is constant at 125 V. In regeneration mode (RM), the converter must therefore provide a constant voltage of 125 V at its output (DC bus voltage, $V_{o(RM)}$) while the input voltage (battery voltage, $V_{In(RM)}$) varies from 20 V to 26 V.

Fig. 8.11 Prototype of the implemented CLLLC resonant converter.

The waveforms of the CLLLC converter switching at 105 kHz and 130 kHz using the proposed topology are presented for BCM in **Fig. 8.12(a)-(d)**. As shown, the converter operates correctly since the MOSFETs are turned on at zero voltage because the gate-source voltage (of switch S_D, **Fig. 8.1**) rises after the drain-source voltage drops to zero while the converter provides 20 V and 26 V at the output.

The waveforms of the CLLLC converter operating at 60 kHz and 80 kHz switching frequency using the proposed topology are presented for reverse mode (RM) in **Fig. 8.13(a)-(d)**. As shown, the converter operates correctly since the MOSFETs are turned on at zero voltage because the gate-source voltage (of switch S_H, **Fig. 8.1**) rises after its drain-source voltage drops to zero, and the converter provides 125 V at the output while the input voltage varies from 20 V to 26 V.

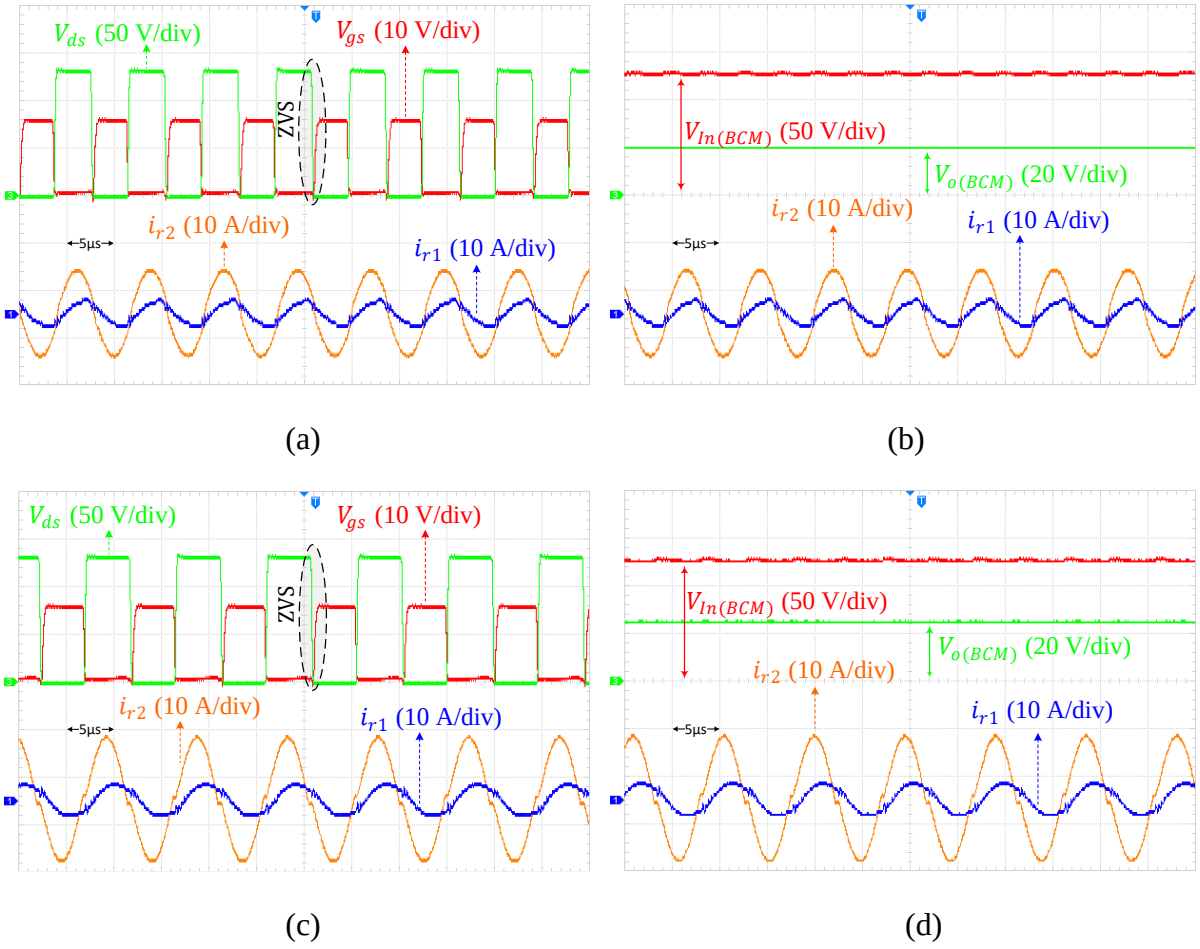

Fig. 8.12 Experimental waveforms of the CLLLC resonant converter in BCM. (a) V_{gs}, V_{ds}, i_{r1} and i_{r2} (f_s=130 kHz, $V_{o(BCM)} = 20$ V, $V_{In(BCM)} = 125$ V and $I_{o(BCM)} \cong 7$ A). (b) $V_{o(BCM)}$, $V_{In(BCM)}$, i_{r1} and i_{r2} (f_s=130 kHz and $I_{o(BCM)} \cong 7$ A). (c) V_{gs}, V_{ds}, i_{r1} and i_{r2} (f_s=105 kHz, $V_{o(BCM)} = 26$ V, $V_{In(BCM)} = 125$ V and $I_{o(BCM)} \cong 9$ A). (d) $V_{o(BCM)}$, $V_{In(BCM)}$, i_{r1} and i_{r2} (f_s=105 kHz and $I_{o(BCM)} \cong 9$ A). $I_{o(BCM)}$ is output current in BCM, V_{ds} is drain-to-source voltage, V_{gs} is gate-to-source voltage, i_{r1} and i_{r2} are the primary and secondary resonant currents, respectively (defined in **Fig. 8.1**).

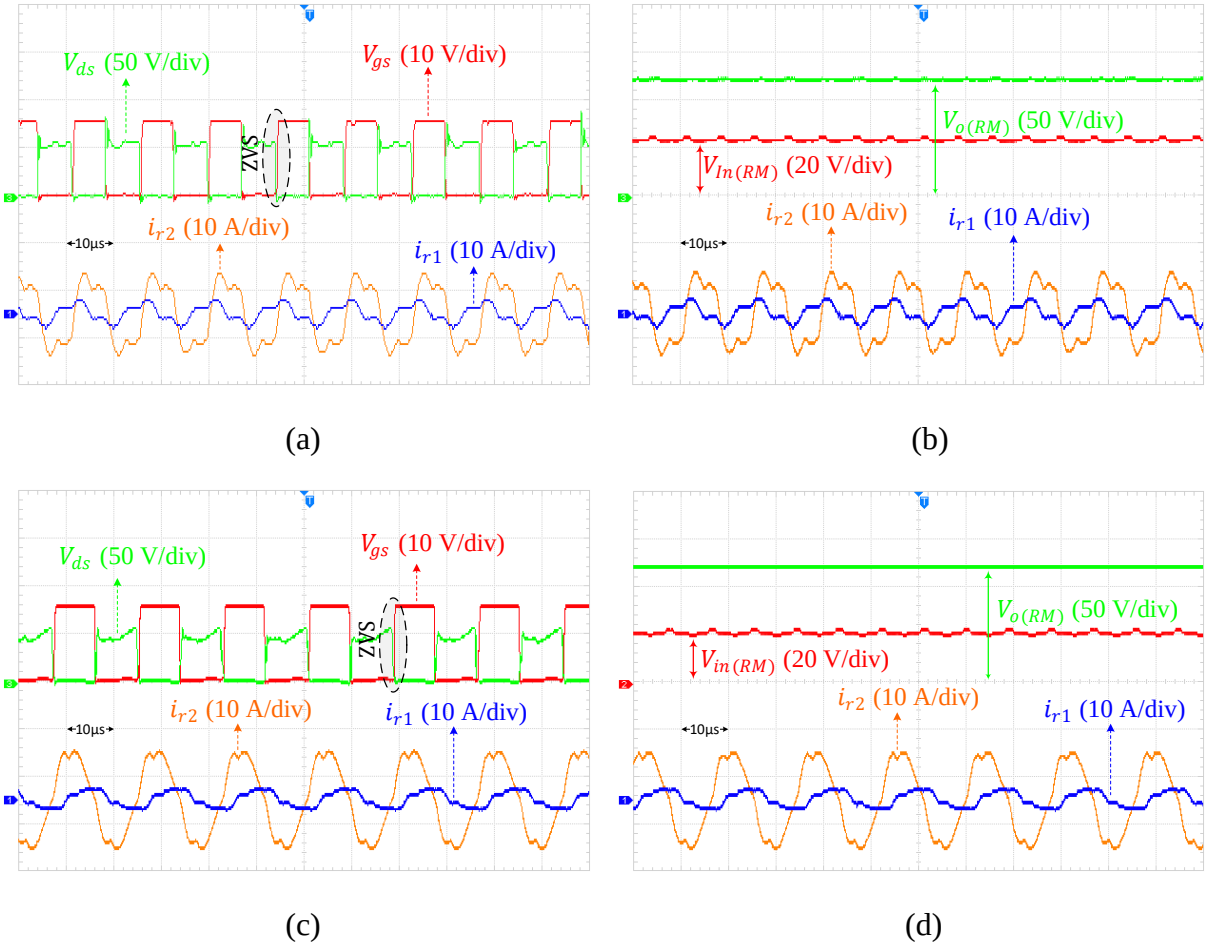

Fig. 8.13 Experimental waveforms of the CLLLC resonant converter in RM. (a) V_{gs}, V_{ds}, i_{r1} and i_{r2} (f_{s}=80 kHz, $V_{\mathrm{o(RM)}} = 125$ V, $V_{\mathrm{In(RM)}} = 26$ V and $I_{\mathrm{o(RM)}} \cong 1.6$ A). (b) $V_{\mathrm{o(RM)}}$, $V_{\mathrm{In(RM)}}$, i_{r1} and i_{r2} (f_{s}=80 kHz and $I_{\mathrm{o(RM)}} \cong 1.6$ A). (c) V_{gs}, V_{ds}, i_{r1} and i_{r2} (f_{s}=60 kHz, $V_{\mathrm{o(RM)}} = 125$ V, $V_{\mathrm{In(RM)}} = 20$ V and $I_{\mathrm{o(RM)}} \cong 1.6$ A). (d) $V_{\mathrm{o(RM)}}$, $V_{\mathrm{In(RM)}}$, i_{r1} and i_{r2} (f_{s}=60 kHz and $I_{\mathrm{o(RM)}} \cong 1.6$ A). $I_{\mathrm{o(RM)}}$ is output current in RM.

The efficiency of the CLLLC converter at different loads for BCM and RM using the proposed integrated transformer is presented in **Fig. 8.14**.

Thermal images of the proposed integrated transformer, while it is used in the implemented CLLLC resonant converter for BCM and RM, are shown in **Fig. 8.15(a)** and **(b)**, respectively. As shown, the proposed transformer operates at 37.9°C and 39.8°C for BCM and RM, respectively, and these temperatures do not damage the windings and core. In addition, the temperature of windings is higher than the cores since conduction losses are the dominant loss mode in the proposed inserted-shunt integrated transformer, verifying the loss distribution presented in **Fig. 8.8**.

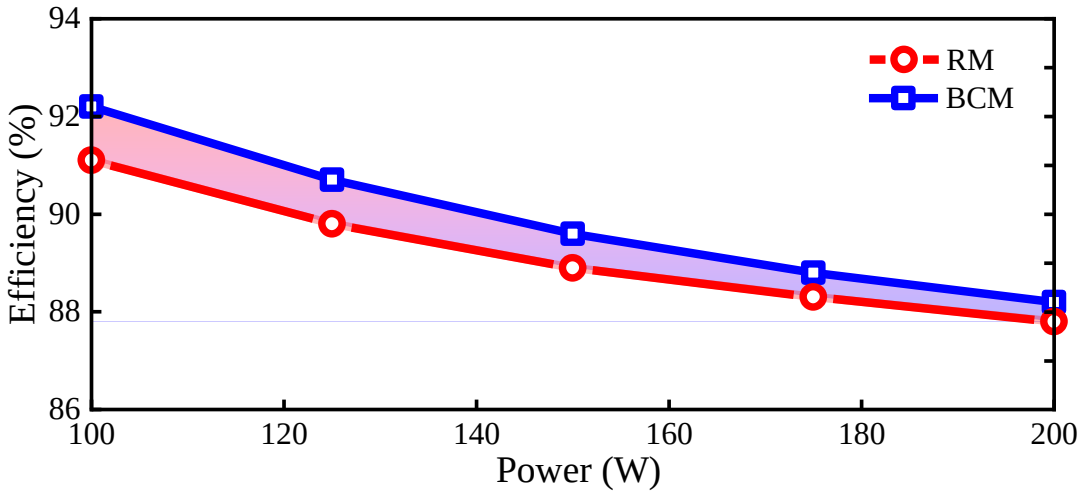

Fig. 8.14 Efficiency of the CLLLC resonant converter for BCM and RM.

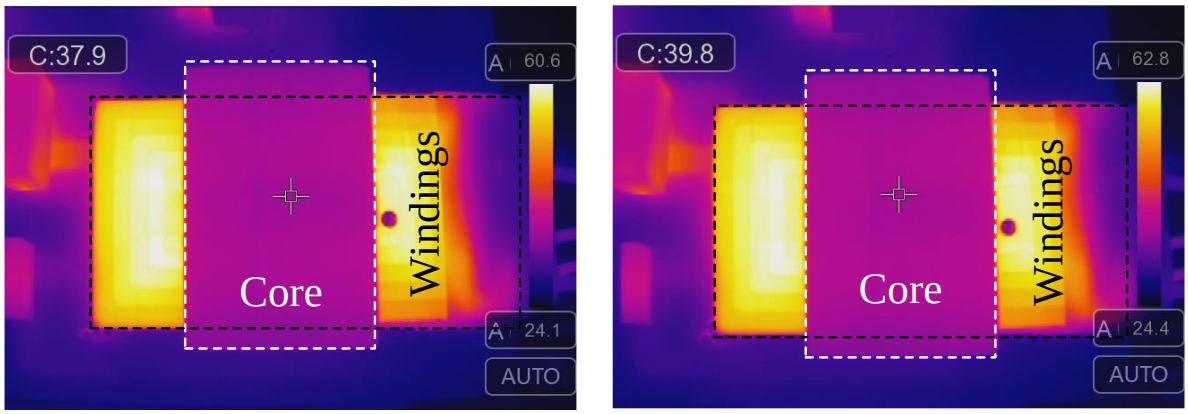

(a) (b)

Fig. 8.15 Thermal images of the proposed transformer (IT5) for (a) BCM and (b) RM.

It should be noted that the application of the proposed integrated transformer is not only restricted to the CLLLC resonant converter; it can be extended to other similar converters.

8.7 Conclusion

In this Chapter, a new topology (IT5) for an inserted-shunt integrated planar transformer was proposed which can provide different primary and secondary leakage inductances. The proposed topology is suitable for bidirectional converters like the CLLLC resonant converter

and it can integrate all required magnetic components into a single transformer. The proposed structure can be constructed using cores and magnetic (ferrite) sheets readily available on the market; it does not need bespoke magnetic components. The proposed topology is analysed in detail. It is shown that the magnetising inductance and the primary and secondary leakage inductances are decoupled and can be determined separately. FEA is used to verify the theoretical analysis. A bidirectional CLLLC resonant converter is constructed to demonstrate the transformer and investigate its practical performance. The operating waveforms of the converter in both BCM and RM for different switching frequencies are presented. In addition, thermal images and efficiency measurements for both BCM and RM are presented. Results confirm that the proposed structure can integrate all four magnetic components of an efficient CLLLC converter into a single planar transformer.

Chapter 9

Conclusions

In this Chapter, the work presented in the thesis is summarised and discussed as a whole. All the Chapters are then brought together to provide an overall conclusion. Proposals for further work which expand this thesis are also suggested.

9.1 Discussion and conclusions

This thesis has proposed a range of techniques to improve magnetic integration in inserted-shunt integrated transformers for resonant converters.

The principal motivation of this work is the impetus for smaller, more power dense power electronics systems, which has come about due to the pervasiveness of power electronics in a range of applications, such as desktop computers and electric vehicles. Magnetic integration is identified as one of the vital techniques for the enhancement of power density. This thesis, therefore, focuses on magnetic integration for resonant converters and offers a contribution to the state-of-the-art, as described below.

Chapter 2 introduces PWM DC-DC converters. It explains the switching losses of PWM converters and the soft-switching techniques that can be applied to reduce the switching losses. In addition, the advantages and disadvantages of PWM converters for high frequency operation are discussed. Resonant converters are introduced, and it is pointed out that resonant converters, such as the LLC topology, could be a better option compared to the PWM converters for achieving both high efficiency and power density. The LLC topology is presented and analysed in detail. In addition, design guidelines for an LLC-type resonant converter are provided. Finally, the benefits of magnetic integration for the LLC resonant converter are discussed.

To facilitate the research, the state of the art as reported in the existing literature is presented in Chapter 3. This chapter explains the advantages and disadvantages of soft switching techniques that can be applied to reduce switching losses of PWM DC-DC converters. In addition, it discusses the costs and benefits of state-of-the-art semiconductor devices that can be used to decrease switching losses. Finally, it introduces the first research focus of this thesis (discussed in Chapter 4) to further investigate the PWM converters which either use soft-switching techniques or new WBG semiconductor devices or both or neither of them to find the most beneficial method for achieving lower switching losses.

In general, a higher power density can be achieved by using a higher switching frequency. PWM converters such as buck and boost cannot be switched at high frequencies due to high switching losses. In addition, adding soft-switching capability to the PWM converters comes with the penalty of more complicated circuit and more expensive prototype. On the other hand, resonant converters such as the LLC converter benefit from soft switching capability inherently and therefore they can still provide a high efficiency at high frequencies. However, resonant converters need magnetic integration for a high power density since they usually have several magnetic components in their topologies.

A full review of integrated transformers suitable for LLC-type topologies is also provided in Chapter 3. Amongst different techniques for magnetic integration, inserted-shunt integrated transformer could be an attractive technique to be used for magnetic integration in an LLC resonant converter; thus the focus of this thesis was a further investigation of this technique. At the end of Chapter 3, four main issues of the inserted-shunt integrated transformers are presented which are addressed later in Chapters 5 to 8.

In Chapter 4, to investigate various methods used to decrease the switching losses of the PWM DC-DC converters, four prototypes are implemented and evaluated. These were: 1) a hard-switched DC-DC boost converter which uses a state-of-the-art SJ Si MOSFET; 2) a version of prototype 1 using a GaN HEMT power switch; 3) a fully soft-switched DC-DC boost converter based on SJ Si MOSFET; and 4) a GaN HEMT version of prototype 3. All the prototypes were simulated and tested experimentally under the same operating conditions to compare their efficiency, power density and cost when they are designed to be used in renewable energy applications such as AC-PV module systems.

The GaN-based hard-switched converter can provide the highest efficiency from light power (100 W) to nominal power (500 W) range, and Si-based hard-switched converter is ranked second. However, the GaN-based and Si-based soft-switched converters hold the third and fourth rank, respectively. In addition, the efficiency of the soft-switched converters decreases noticeably at light power range; thus, they are not a good choice for PV systems in which power range varies across hours and seasons. Furthermore, it is shown that the GaN-based hard-switched converter occupies the smallest volume.

The Si-based hard-switched converter is the cheapest converter, and the GaN-based hard-switched converter is ranked second. However, the GaN-based hard-switched converter remains cheaper than Si-based soft-switched converter, even though GaN switches are far more expensive than Si switches. In addition, this cost gap between Si and GaN switches may close in the future. Overall, since using GaN in DC-DC converter does not alter the simple traditional, simple structure of the converter and has better performance in terms of power density, cost, and efficiency than the soft-switched converter, it may be a better choice in some applications such as renewable energy systems.

Chapter 4 showed that adding soft-switching capability does not always guarantee a high efficiency at high switching frequencies and it leads to a more expensive and complicated circuit. In addition, using WBG semiconductor dose not eliminate switching losses, leading to low efficiency at high frequencies. Therefore, this thesis focused on resonant converters for achieving higher power density without decreasing the efficiency since these converters benefit from soft switching capability inherently.

According to Chapter 3, inserted-shunt integrated transformers were a suitable choice for magnetic integration in LLC-type resonant converters to enhance their power density and efficiency and decrease their cost. However, one of the main disadvantages of inserted-shunt integrated transformers was using low-permeability materials for the shunt. Suitable magnetic materials with low permeability are not often readily available, and when they are, they are frequently expensive. Chapter 5 presents two topologies (IT1 and IT2) which provide high leakage inductance in shunt-inserted integrated magnetic transformers. These differ from conventional designs by replacing the low-permeability magnetic shunt of a planar transformer with high-permeability magnetic shunt segments, separated by many small air gaps. This

approach results in a shunt with the same bulk permeability as the conventional design, while using lower cost and readily available magnetic materials such as ferrite. A modelling and design approach which can estimate the leakage and magnetising inductances precisely is provided for each topology. Theoretical analysis is presented and verified using finite-element analysis and experimental implementation. AC resistance analysis for both transformer topologies is also presented. In addition, an LLC resonant converter is built to verify the performance of the proposed fully-integrated magnetic transformers in practice. It is shown that the proposed topologies can integrate all three magnetic components of an isolated LLC resonant converter in a single planar transformer, which reduces the converter's volume and cost.

Although the structures proposed in Chapter 5 (IT1 and IT2) eliminates the need for shunts with specific permeabilities and dimensions, the inserted shunt has multiple segments and has to be placed between two E-cores which makes the implementation difficult and leads to high assembly cost. Therefore, to address this issue, a new topology (IT3) for achieving high leakage inductance in inserted-shunt integrated planar transformers is proposed in Chapter 6.

In the proposed topology (IT3), two one-segment shunts are placed across the planar E-core air gap and between the primary and secondary windings. The proposed topology benefits using solid inexpensive ferrite shunts, making manufacturing easier. A detailed mathematical model is derived from which a design methodology is developed, providing accurate estimation for the leakage and magnetising inductances. The theoretical analysis has been verified using finite-element analysis and experimental implementation. AC resistance analysis and efficiency comparison are also presented for the proposed topology and the topology with inserted-segmental-shunt, which shows the proposed topology provides higher efficiency because of lower AC resistance. In addition, an isolated LLC resonant converter is designed and built to investigate the performance of the proposed topology in practice. The three magnetic components needed for the designed LLC resonant converter is integrated in a single planar transformer using the proposed topology and the converter operates properly.

The leakage inductance of an inserted-shunt integrated transformer is usually utilised as the series inductor of an LLC topology. However, leakage inductance exists on both primary and secondary sides of an inserted-shunt integrated transformer and secondary leakage inductance

leads the control and design of the converter to difficulty. In Chapter 7, a novel topology (IT4) for inserted-shunt integrated transformers is proposed which has low secondary leakage inductance. The inserted shunt of the proposed topology is not segmental and can be located conveniently within the transformer. In addition, the inserted shunt does not require low permeability core material, simplifying its manufacture. The design and modelling of the proposed transformer topology are presented and verified by finite-element analysis and experimental implementation. The proposed topology is also compared with the inserted-segmental-shunt integrated transformer. It is shown that the proposed transformer provides higher efficiency and lower AC resistance. Finally, to examine the performance of the proposed integrated transformer in practice, it is used in an LLC resonant converter.

Typically, inserted-shunt integrated transformers have symmetric primary and secondary leakage inductances. However, bidirectional resonant converters typically operate more efficiently with different primary and secondary series inductances. In Chapter 8, a new topology (IT5) for an inserted-shunt integrated transformer which can provide tuneable, asymmetric leakage (series) inductances on the primary and secondary sides is presented. Two magnetic shunts, with appropriate air gaps, are inserted between two E-cores and the primary and secondary windings are separated by being placed at opposite sides of the shunts. The proposed transformer is analysed in detail and modelling and design guidelines are provided. It is shown that the magnetising inductance and the primary and secondary leakage inductances are decoupled from each other, and they can be determined separately. The design has the advantage of using planar E-cores and magnetic sheets that are readily available commercially. The theoretical analysis is verified by simulation and experimental results. To demonstrate the performance of the proposed integrated transformer in practice, an exemplar bidirectional CLLLC resonant converter is designed, constructed and tested using the new integrated transformer.

It should be mentioned that the bidirectional CLLLC resonant converter could be used in EV applications if designed for power levels of a few kilowatts. The scope of this work was proposing an integrated transformer suitable for the bidirectional CLLLC resonant converter and investigating its modelling, design, and operation in practice. However, due to hardware limitations and safety reasons, the converter was designed as a laboratory setup in the range of a few hundred watts to only investigate its operation and modelling in practice. The proposed

integrated transformers (IT1-IT5) should be able to work at higher power levels as well, but investigating it is out of the scope of this work and could be the future work of this thesis.

The research encompassed in this thesis has been published in five journal papers and six conference proceedings papers, demonstrating the relevance of the findings to the power electronics community.

9.2 Future work

Although this thesis presents a coherent body of work which offers an improvement over the-state of-the-art, it is recognised that further improvements could be made to increase the impact of the work. The following subsections summarise several areas for further development which lead on from this thesis.

9.2.1 Winded shunt

In an inserted-shunt integrated planar transformer, a winding could be looped around the shunt to adjust the leakage inductance by controlling the current flowing through the shunt's winding. This, in turn, controls the flux passing through the shunt. This approach can add more flexibility to the design of the integrated transformer since the leakage inductance is no longer restricted only to the characteristics of the shunt. In addition, this topology provides the opportunity of changing the inductance ratio ($L_{\mathrm{Lk}}/L_{\mathrm{m}}$) of the LLC resonant converter under different operating conditions, leading to overall performance improvements for the LLC converter. In other words, by having the ability to dynamically change the inductance ratio, it becomes possible to adjust the maximum/minimum gain, resonance frequency, and ZVS region at different load/input voltage conditions, resulting in better LLC converter operation.

9.2.2 Optimisation

The aim of this thesis was to address current issues related to inserted-shunt integrated transformers, such as requiring bespoke materials for the shunt, unwanted high leakage inductance on the secondary side, and unsuitability for use in bidirectional resonant converters, such as CLLLC converters. Therefore, optimising the proposed integrated transformers in terms of cost, efficiency, or power density was not within the scope of this thesis. However, it

is believed that these optimisations could further enhance the proposed transformers and increase the impact of this work.

To achieve the highest efficiency for a chosen core, optimisation should consider the thickness of the windings for AC losses and the operating flux density for core losses. This optimisation process can be carried out through 3D modelling of the transformer using FEA software such as Ansys Maxwell.

9.2.3 Effect of parasitic capacitance of the integrated transformer

In the design of the LLC resonant converter, it is commonly assumed that the parasitic capacitance is negligible. However, an integrated planar transformer can have a significant parasitic capacitance that may negatively impact the soft-switching operation of the converter, especially when dealing with integrated planar transformers where the parasitic capacitance is high. Therefore, as a case study, it is necessary to investigate the effect of the transformer's parasitic capacitance on the soft-switching capability of the LLC topology utilizing integrated planar transformers. Additionally, a new design procedure should be developed to ensure the proper operation of the converter, even when dealing with high parasitic capacitances.

9.2.4 Integrating the primary and secondary resonant capacitors into the integrated transformer

The inserted-shunt integrated planar transformers suffer from a high parasitic capacitance. However, this capacitance can be employed as the resonant (series) capacitors of the bidirectional CLLLC resonant converter, particularly at high frequencies where a lower resonant capacitance is required. Therefore, as a case study, it is proposed to first investigate the effect of different winding configurations on the value of the parasitic capacitances of the inserted-shunt integrated planar transformers. Then, it should be investigated whether the parasitic capacitances could be adjusted, estimated, and used as the series resonant capacitors of the CLLLC topology. By doing so, all five passive elements of a bidirectional CLLLC resonant converter can be integrated into a single magnetic element, which will likely increase power density and efficiency and reduce costs even further.

References

[1] Torob [Online] Available: https://www.torob.com/

[2] J. Davidson, "Advanced thermal modelling and management techniques to improve power density in next generation power electronics," University of Sheffield, 2015.

[3] S. A. Ansari and J. S. Moghani, "A novel high voltage gain noncoupled inductor SEPIC converter," *IEEE Transactions on Industrial Electronics*, vol. 66, no. 9, pp. 7099-7108, 2018.

[4] Y. Li, X. Ruan, J. Dai, and Y. Wang, "Design considerations for the wide input-voltage range Class E dc-dc converter with ON-OFF control in multi-megahertz applications," in *IECON 2018-44th Annual Conference of the IEEE Industrial Electronics Society*, 2018: IEEE, pp. 1146-1151.

[5] S. De Simone, C. Adragna, and C. Spini, "Design guideline for magnetic integration in LLC resonant converters," in *2008 International Symposium on Power Electronics, Electrical Drives, Automation and Motion*, 2008: IEEE, pp. 950-957.

[6] S. A. Ansari and J. S. Moghani, "Soft switching flyback inverter for photovoltaic AC module applications," *IET Renewable Power Generation*, vol. 13, no. 13, pp. 2347-2355, 2019.

[7] S. Arab Ansari, J. S. Moghani, and M. Mohammadi, "Analysis and implementation of a new zero current switching flyback inverter," *International Journal of Circuit Theory and Applications*, vol. 47, no. 1, pp. 103-132, 2019.

[8] R.-L. Lin and W.-C. Ju, "LLC DC/DC resonant converter with PLL control scheme," in *APEC 07-Twenty-Second Annual IEEE Applied Power Electronics Conference and Exposition*, 2007: IEEE, pp. 1537-1543.

[9] R.-L. Lin and C.-W. Lin, "Design criteria for resonant tank of LLC DC-DC resonant converter," in *IECON 2010-36th Annual Conference on IEEE Industrial Electronics Society*, 2010: IEEE, pp. 427-432.

[10] B. Li, Q. Li, and F. C. Lee, "High-frequency PCB winding transformer with integrated inductors for a bi-directional resonant converter," *IEEE Transactions on Power Electronics*, vol. 34, no. 7, pp. 6123-6135, 2018.

[11] H.-P. Park and J.-H. Jung, "Power stage and feedback loop design for LLC resonant converter in high-switching-frequency operation," *IEEE Transactions on Power Electronics*, vol. 32, no. 10, pp. 7770-7782, 2016.

[12] M. Li, Z. Ouyang, and M. A. Andersen, "High-frequency LLC resonant converter with magnetic shunt integrated planar transformer," *IEEE Transactions on Power Electronics*, vol. 34, no. 3, pp. 2405-2415, 2018.

[13] E. A. Jones, F. F. Wang, and D. Costinett, "Review of commercial GaN power devices and GaN-based converter design challenges," *IEEE Journal of Emerging and Selected Topics in Power Electronics*, vol. 4, no. 3, pp. 707-719, 2016.

[14] S. A. Ansari, J. N. Davidson, and M. P. Foster, "Evaluation of silicon MOSFETs and GaN HEMTs in soft-switched and hard-switched DC-DC boost converters for domestic PV applications," *IET Power Electronics*, vol. 14, no. 5, pp. 1032-1043, 2021.

[15] S. A. Ansari, J. N. Davidson, and M. P. Foster, "Fully-integrated planar transformer with a segmental shunt for LLC resonant converters," *IEEE Transactions on Industrial Electronics*, vol. 69, no. 9, pp. 9145-9154, 2021.

[16] S. A. Ansari, J. N. Davidson, and M. P. Foster, "Fully-Integrated Solid Shunt Planar Transformer for LLC Resonant Converters," *IEEE Open Journal of Power Electronics*, vol. 3, pp. 26-35, 2021.

[17] S. A. Ansari, J. Davidson, and M. Foster, "Inserted-shunt Integrated Planar Transformer with Low Secondary Leakage Inductance for LLC Resonant Converters," *IEEE Transactions on Industrial Electronics*, vol. 70, no. 3, pp. 2652 - 2661, 2022.

[18] S. A. Ansari, J. Davidson, and M. Foster, "Fully-integrated Transformer with Asymmetric Primary and Secondary Leakage Inductances for a Bidirectional Resonant Converters " *IEEE Transactions on Industry Applications*, 2023.

[19] S. A. Ansari, J. N. Davidson, and M. P. Foster, "COMPARATIVE EVALUATION OF Si MOSFET-BASED SOFT-SWITCHED DC-DC CONVERTERS AND GaN HEMT-BASED HARD-SWITCHED DC-DC CONVERTERS," 2021.

[20] S. A. Ansari, J. N. Davidson, and M. P. Foster, "Analysis, Design and Modelling of Two Fully-Integrated Transformers with Segmental Magnetic Shunt for LLC Resonant Converters," in *IECON 2020 The 46th Annual Conference of the IEEE Industrial Electronics Society*, 2020: IEEE, pp. 1273-1278.

[21] S. A. Ansari, J. N. Davidson, M. P. Foster, and D. A. Stone, "Design and analysis of a Fully-integrated planar transformer for LCLC resonant converters," in *2021 23rd European Conference on Power Electronics and Applications (EPE'21 ECCE Europe)*, 2021: IEEE, pp. P. 1-P. 8.

[22] S. A. Ansari, J. N. Davidson, M. P. Foster, and D. A. Stone, "Analysis of Test Methods for Measurement of Leakage and Magnetising Inductances in Integrated Transformers," in *2022 24th European Conference on Power Electronics and Applications (EPE'22 ECCE Europe)*, 2022: IEEE, pp. 1-10.

[23] S. A. Ansari, J. N. Davidson, and M. P. Foster, "Fully-integrated transformer with asymmetric leakage inductances for a bidirectional resonant converter," in *11th International Conference on Power Electronics, Machines and Drives (PEMD 2022)*, 2022, vol. 2022: IET, pp. 260-265.

[24] S. A. Ansari, J. N. Davidson, and M. P. Foster, "A Design Methodology for a CLLLC Bidirectional Resonant Converter with an Integrated Transformer," in *International Exhibition and Conference for Power Electronics, Intelligent Motion, Renewable Energy and Energy Management, PCIM Europe 2023*, 2023: Mesago PCIM GmbH.

[25] A. Mizani, S. A. Ansari, A. Shoulaie, J. N. Davidson, and M. P. Foster, "Single-active switch high-voltage gain DC–DC converter using a non-coupled inductor," *IET Power Electronics*, vol. 14, no. 3, pp. 492-502, 2021.

[26] D. W. Hart and D. W. Hart, *Power electronics*. McGraw-Hill New York, 2011.

[27] M. N. Undeland, W. P. Robbins, and N. Mohan, "Power electronics," *Converters, Applications, and Design*, 1995.

[28] M. H. Rashid, *Power electronics handbook*. Butterworth-heinemann, 2011.

[29] K. M. Smith and K. M. Smedley, "A comparison of voltage-mode soft-switching methods for PWM converters," *IEEE transactions on Power Electronics*, vol. 12, no. 2, pp. 376-386, 1997.

[30] S. Hui, K. E. Cheng, and S. N. Prakash, "A fully soft-switched extended-period quasi-resonant power-factor-correction circuit," *IEEE transactions on power electronics*, vol. 12, no. 5, pp. 922-930, 1997.

[31] K. Fujiwara and H. Nomura, "A novel lossless passive snubber for soft-switching boost-type converters," *IEEE Transactions on Power Electronics*, vol. 14, no. 6, pp. 1065-1069, 1999.

[32] R. Gurunathan and A. K. Bhat, "A zero-voltage transition boost converter using a zero-voltage switching auxiliary circuit," *IEEE Transactions on Power Electronics*, vol. 17, no. 5, pp. 658-668, 2002.

[33] R. Streit and D. Tollik, "High efficiency telecom rectifier using a novel soft-switched boost-based input current shaper," in *[Proceedings] Thirteenth International Telecommunications Energy Conference-INTELEC 91*, 1991: IEEE, pp. 720-726.
[34] K.-H. Liu, R. Oruganti, and F. C. Lee, "Resonant switches-topologies and characteristics," in *1985 IEEE Power Electronics Specialists Conference*, 1985: IEEE, pp. 106-116.
[35] R. P. Severns and G. Bloom, *Modern DC-to-DC switchmode power converter circuits*. Van Nostrand Reinhold Company, 1985.
[36] Y.-A. Ang, "Modelling, analysis and design of LCLC resonant power converters," University of Sheffield, 2006.
[37] R. L. Steigerwald, "A comparison of half-bridge resonant converter topologies," *IEEE transactions on Power Electronics*, vol. 3, no. 2, pp. 174-182, 1988.
[38] M. M. Jovanović, "Resonant, quasi-resonant, multi-resonant and soft-switching techniques—merits and limitations," *International journal of electronics*, vol. 77, no. 5, pp. 537-554, 1994.
[39] M. K. Kazimierczuk and S. Wang, "Frequency-domain analysis of series resonant converter for continuous conduction mode," *IEEE Transactions on Power Electronics*, vol. 7, no. 2, pp. 270-279, 1992.
[40] M. K. Kazimierczuk, W. Szaraniec, and S. Wang, "Analysis and design of parallel resonant convertor at high Q/sub L," *IEEE transactions on aerospace and electronic systems*, vol. 28, no. 1, pp. 35-50, 1992.
[41] K. Siri, I. Batarseh, and C. Lee, "Frequency response for the conventional parallel resonant converter based on the state-plane diagram," *IEEE Transactions on Circuits and Systems I: Fundamental Theory and Applications*, vol. 40, no. 1, pp. 33-42, 1993.
[42] R. Liu, I. Batarseh, and C. Lee, "Comparison of capacitively and inductively coupled parallel resonant converters," *IEEE transactions on power electronics*, vol. 8, no. 4, pp. 445-454, 1993.
[43] G. Spiazzi and S. Buso, "Effect of a split transformer leakage inductance in the LLC converter with integrated magnetics," in *2013 Brazilian Power Electronics Conference*, 2013: IEEE, pp. 135-140.
[44] A. Kats, G. Ivensky, and S. Ben-Yaakov, "Application of integrated magnetics in resonant converters," in *Proceedings of APEC 97-Applied Power Electronics Conference*, 1997, vol. 2: IEEE, pp. 925-930.
[45] M. K. Kazimierczuk and D. Czarkowski, *Resonant power converters*. John Wiley & Sons, 2012.
[46] S. De Simone, "LLC resonant half-bridge converter design guideline," *STMicroelectronics, Application Note AN2450*, p. 35, 2014.
[47] S. A. Ansari and J. Moghani, "Soft Switching Flyback Inverter for Photovoltaic AC Module Applications," *IET Renewable Power Generation*, vol. 13, no. 13, 2019.
[48] G. Hua and F. C. Lee, "Soft-switching techniques in PWM converters," *IEEE Transactions on Industrial Electronics*, vol. 42, no. 6, pp. 595-603, 1995.
[49] X.-F. Cheng, C. Liu, D. Wang, and Y. Zhang, "State-of-the-art review on soft-switching technologies for non-isolated DC-DC converters," *IEEE Access*, vol. 9, pp. 119235-119249, 2021.
[50] K.-H. Liu, R. Oruganti, and F. C. Lee, "Quasi-resonant converters-topologies and characteristics," *IEEE Transactions on Power electronics*, no. 1, pp. 62-71, 1987.
[51] K.-H. Liu and F. C. Lee, "Zero-voltage switching technique in DC/DC converters," in *1986 17th Annual IEEE Power Electronics Specialists Conference*, 1986: IEEE, pp. 58-70.

[52] F. C. Lee, "High-frequency quasi-resonant converter technologies," *Proceedings of the IEEE,* vol. 76, no. 4, pp. 377-390, 1988.
[53] C.-J. Tseng and C.-L. Chen, "A passive lossless snubber cell for nonisolated PWM DC/DC converters," *IEEE Transactions on Industrial Electronics,* vol. 45, no. 4, pp. 593-601, 1998.
[54] R. T. Li, H. S.-H. Chung, and A. K. Sung, "Passive lossless snubber for boost PFC with minimum voltage and current stress," *IEEE Transactions on Power electronics,* vol. 25, no. 3, pp. 602-613, 2009.
[55] X. Yu, J. Su, S. Guo, S. Zhong, Y. Shi, and J. Lai, "Properties and synthesis of lossless snubbers and passive soft-switching PWM converters," *IEEE Transactions on Power Electronics,* vol. 35, no. 4, pp. 3807-3827, 2019.
[56] B. Wang, T. Q. Zheng, and J. Zhang, "Further reduction of switching loss for the lossless snubber based converters," in *2014 IEEE Energy Conversion Congress and Exposition (ECCE)*, 2014: IEEE, pp. 928-934.
[57] H.-L. Do, "Nonisolated bidirectional zero-voltage-switching DC–DC converter," *IEEE Transactions on Power Electronics,* vol. 26, no. 9, pp. 2563-2569, 2011.
[58] Y. Zhang, X.-F. Cheng, C. Yin, and S. Cheng, "Analysis and research of a soft-switching bidirectional DC–DC converter without auxiliary switches," *IEEE transactions on industrial electronics,* vol. 65, no. 2, pp. 1196-1204, 2017.
[59] M. R. Mohammadi and H. Farzanehfard, "A new family of zero-voltage-transition nonisolated bidirectional converters with simple auxiliary circuit," *IEEE Transactions on Industrial Electronics,* vol. 63, no. 3, pp. 1519-1527, 2015.
[60] G. Hua, C.-S. Leu, Y. Jiang, and F. C. Lee, "Novel zero-voltage-transition PWM converters," *IEEE transactions on Power Electronics,* vol. 9, no. 2, pp. 213-219, 1994.
[61] B. Akın, "An improved ZVT–ZCT PWM DC–DC boost converter with increased efficiency," *IEEE Transactions on Power Electronics,* vol. 29, no. 4, pp. 1919-1926, 2013.
[62] I. Barbi, J. Bolacell, D. C. Martins, and F. B. Libano, "Buck quasi-resonant converter operating at constant frequency: Analysis, design and experimentation," in *20th Annual IEEE Power Electronics Specialists Conference*, 1989: IEEE, pp. 873-880.
[63] M. Jabbari and H. Farzanehfard, "Family of soft-switching resonant DC-DC converters," *IET Power Electronics,* vol. 2, no. 2, pp. 113-124, 2009.
[64] A. Elasser and D. A. Torrey, "Soft switching active snubbers for dc/dc converters," *IEEE Transactions on Power Electronics,* vol. 11, no. 5, pp. 710-722, 1996.
[65] J.-W. Yang and H.-L. Do, "Soft-switching bidirectional DC-DC converter using a lossless active snubber," *IEEE Transactions on Circuits and Systems I: Regular Papers,* vol. 61, no. 5, pp. 1588-1596, 2014.
[66] D.-K. Kwak, S.-H. Lee, and D.-Y. Jung, "A new buck-boost dc/dc converter of high efficiency by soft switching technique," in *2009 IEEE 6th International Power Electronics and Motion Control Conference*, 2009: IEEE, pp. 1295-1299.
[67] T. Yao, C. Nan, and R. Ayyanar, "A new soft-switching topology for switched inductor high gain boost," *IEEE Transactions on Industry Applications,* vol. 54, no. 3, pp. 2449-2458, 2018.
[68] J. Millán, P. Godignon, X. Perpiñà, A. Pérez-Tomás, and J. Rebollo, "A survey of wide bandgap power semiconductor devices," *IEEE transactions on Power Electronics,* vol. 29, no. 5, pp. 2155-2163, 2013.
[69] B. Ozpineci and L. M. Tolbert, "Characterization of SiC Schottky diodes at different temperatures," *IEEE Power Electronics Letters,* vol. 1, no. 2, pp. 54-57, 2003.

[70] N. Kaji, H. Niwa, J. Suda, and T. Kimoto, "Ultrahigh-voltage SiC pin diodes with improved forward characteristics," *IEEE Transactions on Electron Devices,* vol. 62, no. 2, pp. 374-381, 2014.

[71] A. Witulski *et al.*, "Single-event burnout of SiC junction barrier Schottky diode high-voltage power devices," *IEEE Transactions on Nuclear Science,* vol. 65, no. 1, pp. 256-261, 2017.

[72] C. Y. Liangchun, G. T. Dunne, K. S. Matocha, K. P. Cheung, J. S. Suehle, and K. Sheng, "Reliability issues of SiC MOSFETs: A technology for high-temperature environments," *IEEE Transactions on Device and Materials Reliability,* vol. 10, no. 4, pp. 418-426, 2010.

[73] I. Josifović, J. Popović-Gerber, and J. A. Ferreira, "Improving SiC JFET switching behavior under influence of circuit parasitics," *IEEE Transactions on Power Electronics,* vol. 27, no. 8, pp. 3843-3854, 2012.

[74] Y. Wang, Y. Ding, and Y. Yin, "Reliability of Wide Band Gap Power Electronic Semiconductor and Packaging: A Review," *Energies,* vol. 15, no. 18, p. 6670, 2022.

[75] S. Tongay *et al.*, "Graphene/GaN Schottky diodes: Stability at elevated temperatures," *Applied physics letters,* vol. 99, no. 10, p. 102102, 2011.

[76] A. Zhan *et al.*, "Comparison of GaN pin and Schottky rectifier performance," *IEEE Transactions on Electron Devices,* vol. 48, no. 3, pp. 407-411, 2001.

[77] J. Liu *et al.*, "Tuning avalanche path in vertical GaN JFETs by gate driver design," *IEEE Transactions on Power Electronics,* vol. 37, no. 5, pp. 5433-5443, 2021.

[78] W. Huang, T. Khan, and T. Chow, "Enhancement-mode n-channel GaN MOSFETs on p and n-GaN/sapphire substrates," in *2006 IEEE International Symposium on Power Semiconductor Devices and IC's*, 2006: IEEE, pp. 1-4.

[79] J. A. del Alamo and J. Joh, "GaN HEMT reliability," *Microelectronics reliability,* vol. 49, no. 9-11, pp. 1200-1206, 2009.

[80] R. Xie, H. Wang, G. Tang, X. Yang, and K. J. Chen, "An analytical model for false turn-on evaluation of high-voltage enhancement-mode GaN transistor in bridge-leg configuration," *IEEE Transactions on Power Electronics,* vol. 32, no. 8, pp. 6416-6433, 2016.

[81] R. Mitova, R. Ghosh, U. Mhaskar, D. Klikic, M.-X. Wang, and A. Dentella, "Investigations of 600-V GaN HEMT and GaN diode for power converter applications," *IEEE transactions on power electronics,* vol. 29, no. 5, pp. 2441-2452, 2013.

[82] B. Zhao, Q. Song, and W. Liu, "Experimental comparison of isolated bidirectional DC–DC converters based on all-Si and all-SiC power devices for next-generation power conversion application," *IEEE Transactions on Industrial Electronics,* vol. 61, no. 3, pp. 1389-1393, 2013.

[83] A. Taylor, J. Lu, L. Zhu, K. H. Bai, M. McAmmond, and A. Brown, "Comparison of SiC MOSFET-based and GaN HEMT-based high-efficiency high-power-density 7.2 kW EV battery chargers," *IET Power Electronics,* vol. 11, no. 11, pp. 1849-1857, 2018.

[84] N. Keshmiri, D. Wang, B. Agrawal, R. Hou, and A. Emadi, "Current status and future trends of GaN HEMTs in electrified transportation," *IEEE Access,* vol. 8, pp. 70553-70571, 2020.

[85] K. Shirabe *et al.*, "Efficiency comparison between Si-IGBT-based drive and GaN-based drive," *IEEE Transactions on Industry Applications,* vol. 50, no. 1, pp. 566-572, 2013.

[86] A. León-Masich, H. Valderrama-Blavi, J. M. Bosque-Moncusí, and L. Martínez-Salamero, "Efficiency comparison between Si and SiC-based implementations in a high gain DC–DC boost converter," *IET Power Electronics,* vol. 8, no. 6, pp. 869-878, 2015.

[87] D. Han, C. T. Morris, W. Lee, and B. Sarlioglu, "A case study on common mode electromagnetic interference characteristics of GaN HEMT and Si MOSFET power converters for EV/HEVs," *IEEE Transactions on Transportation Electrification,* vol. 3, no. 1, pp. 168-179, 2016.

[88] K. Boutros *et al.*, "Normally-off 5A/1100V GaN-on-silicon device for high voltage applications," in *2009 IEEE International Electron Devices Meeting (IEDM)*, 2009: IEEE, pp. 1-3.

[89] F. Gamand, M. D. Li, and C. Gaquière, "A 10-MHz GaN HEMT DC/DC boost converter for power amplifier applications," *IEEE Transactions on Circuits and Systems II: Express Briefs,* vol. 59, no. 11, pp. 776-779, 2012.

[90] M. Parvez, A. T. Pereira, N. Ertugrul, N. H. Weste, D. Abbott, and S. F. Al-Sarawi, "Wide bandgap DC–DC converter topologies for power applications," *Proceedings of the IEEE,* vol. 109, no. 7, pp. 1253-1275, 2021.

[91] B. Liu, R. Ren, Z. Zhang, B. Guo, F. F. Wang, and D. Costinett, "Impacts of high frequency, high di/dt, dv/dt environment on sensing quality of GaN based converters and their mitigation," *CPSS Transactions on Power Electronics and Applications,* vol. 3, no. 4, pp. 301-312, 2018.

[92] G. Rizzoli, M. Mengoni, L. Zarri, A. Tani, G. Serra, and D. Casadei, "Comparative Experimental Evaluation of Zero-Voltage-Switching Si Inverters and Hard-Switching Si and SiC Inverters," *IEEE Journal of Emerging and Selected Topics in Power Electronics,* vol. 7, no. 1, pp. 515-527, 2019.

[93] H. Mahdi, A. M. Ammar, Y. Nour, and M. A. Andersen, "A class-E-based resonant AC-DC converter with inherent PFC capability," *IEEE Access,* vol. 9, pp. 46664-46673, 2021.

[94] T. Nagashima, X. Wei, T. Suetsugu, M. K. Kazimierczuk, and H. Sekiya, "Waveform equations, output power, and power conversion efficiency for class-E inverter outside nominal operation," *IEEE Transactions on Industrial Electronics,* vol. 61, no. 4, pp. 1799-1810, 2013.

[95] N. J. Dahl, A. M. Ammar, and M. A. Andersen, "Identification of ZVS points and bounded low-loss operating regions in a class-D resonant converter," *IEEE Transactions on Power Electronics,* vol. 36, no. 8, pp. 9511-9520, 2021.

[96] Y. Wang, N. Qi, Y. Guan, C. Cecati, and D. Xu, "A single-stage LED driver based on SEPIC and LLC circuits," *IEEE Transactions on Industrial Electronics,* vol. 64, no. 7, pp. 5766-5776, 2016.

[97] H.-J. Chiu, Y.-K. Lo, T.-P. Lee, S.-C. Mou, and H.-M. Huang, "Design of an RGB LED backlight circuit for liquid crystal display panels," *IEEE Transactions on Industrial electronics,* vol. 56, no. 7, pp. 2793-2795, 2009.

[98] Z. Fang, T. Cai, S. Duan, and C. Chen, "Optimal design methodology for LLC resonant converter in battery charging applications based on time-weighted average efficiency," *IEEE Transactions on Power Electronics,* vol. 30, no. 10, pp. 5469-5483, 2014.

[99] M. Shang, H. Wang, and Q. Cao, "Reconfigurable LLC topology with squeezed frequency span for high-voltage bus-based photovoltaic systems," *IEEE Transactions on Power Electronics,* vol. 33, no. 5, pp. 3688-3692, 2017.

[100] F. M. Spliid, A. M. Ammar, and A. Knott, "Analysis and design of a resonant power converter with a wide input voltage range for AC/DC applications," *IEEE Journal of Emerging and Selected Topics in Power Electronics,* vol. 8, no. 3, pp. 2056-2066, 2019.

[101] A. M. Ammar, F. M. Spliid, Y. Nour, and A. Knott, "Analysis and design of a charge-pump-based resonant AC–DC converter with inherent PFC capability," *IEEE Journal of Emerging and Selected Topics in Power Electronics,* vol. 8, no. 3, pp. 2067-2081, 2020.

[102] Y. Wang, F. Li, Y. Qiu, S. Gao, Y. Guan, and D. Xu, "A single-stage LED driver based on flyback and modified class-E resonant converters with low-voltage stress," *IEEE Transactions on Industrial Electronics,* vol. 66, no. 11, pp. 8463-8473, 2019.

[103] N. J. Dahl, A. M. Ammar, A. Knott, and M. A. Andersen, "An improved linear model for high-frequency class-DE resonant converter using the generalized averaging modeling technique," *IEEE Journal of Emerging and Selected Topics in Power Electronics,* vol. 8, no. 3, pp. 2156-2166, 2019.

[104] C. Ekkaravarodome, K. Jirasereeamornkul, and M. K. Kazimierczuk, "Implementation of a DC-Side Class-DE Low-$\bm {d\upsilon/dt} $ Rectifier as a PFC for Electronic Ballast Application," *IEEE Transactions on Power Electronics,* vol. 29, no. 10, pp. 5486-5497, 2013.

[105] K. Jirasereeamornkul, M. K. Kazimierczuk, I. Boonyaroonate, and K. Chamnongthai, "Single-stage electronic ballast with class-E rectifier as power-factor corrector," *IEEE Transactions on Circuits and Systems I: Regular Papers,* vol. 53, no. 1, pp. 139-148, 2006.

[106] A. K. Bhat, "A resonant converter suitable for 650 V DC bus operation," *IEEE transactions on power electronics,* vol. 6, no. 4, pp. 739-748, 1991.

[107] S. Aldhaher, P. C.-K. Luk, K. E. K. Drissi, and J. F. Whidborne, "High-input-voltage high-frequency class E rectifiers for resonant inductive links," *IEEE Transactions on Power Electronics,* vol. 30, no. 3, pp. 1328-1335, 2014.

[108] Y. Wang, O. Lucia, Z. Zhang, S. Gao, Y. Guan, and D. Xu, "A review of high frequency power converters and related technologies," *IEEE Open Journal of the Industrial Electronics Society,* vol. 1, pp. 247-260, 2020.

[109] J. A. Ferreira and J. A. Roux, "A series resonant converter for arc-striking applications," *IEEE Transactions on Industrial Electronics,* vol. 45, no. 4, pp. 585-592, 1998.

[110] S. Ferdous, M. A. Shoeb, G. Shafiullah, and M. A. M. Oninda, "Parallel resonant converter for battery charging application," in *2019 9th International Conference on Power and Energy Systems (ICPES)*, 2019: IEEE, pp. 1-6.

[111] M. A. Saket, N. Shafiei, and M. Ordonez, "LLC converters with planar transformers: Issues and mitigation," *IEEE Transactions on power electronics,* vol. 32, no. 6, pp. 4524-4542, 2016.

[112] B. Yang, F. C. Lee, A. J. Zhang, and G. Huang, "LLC resonant converter for front end DC/DC conversion," in *APEC. Seventeenth Annual IEEE Applied Power Electronics Conference and Exposition (Cat. No. 02CH37335)*, 2002, vol. 2: IEEE, pp. 1108-1112.

[113] X. Huang, Y. Kong, Z. Ouyang, W. Chen, and S. Lin, "Analysis and comparison of push–pull class-E inverters with magnetic integration for megahertz wireless power transfer," *IEEE Transactions on Power Electronics,* vol. 35, no. 1, pp. 565-577, 2019.

[114] J. Deng, W. Li, S. Li, and C. Mi, "Magnetic integration of LCC compensated resonant converter for inductive power transfer applications," in *2014 IEEE Energy Conversion Congress and Exposition (ECCE)*, 2014: IEEE, pp. 660-667.

[115] Y.-C. Liu, C.-Y. Xiao, C.-C. Huang, P.-C. Chi, and H.-J. Chiu, "Integrated magnetics design for a full-bridge phase-shifted converter," *Energies,* vol. 14, no. 1, p. 183, 2020.

[116] P. Zumel, O. Garcia, J. Cobos, and J. Uceda, "Magnetic integration for interleaved converters," in *Eighteenth Annual IEEE Applied Power Electronics Conference and Exposition, 2003. APEC'03.*, 2003, vol. 2: IEEE, pp. 1143-1149.

[117] Z. Zhang, J. Huang, and Y. Xiao, "GaN-based 1-MHz partial parallel dual active bridge converter with integrated magnetics," *IEEE Transactions on Industrial Electronics,* vol. 68, no. 8, pp. 6729-6738, 2020.

[118] Y. Zhang, D. Xu, K. Mino, and K. Sasagawa, "1MHz-1kW LLC resonant converter with integrated magnetics," in *APEC 07-Twenty-Second Annual IEEE Applied Power Electronics Conference and Exposition*, 2007: IEEE, pp. 955-961.

[119] C. Fei, R. Gadelrab, Q. Li, and F. C. Lee, "High-frequency three-phase interleaved LLC resonant converter with GaN devices and integrated planar magnetics," *IEEE Journal of Emerging and Selected Topics in Power Electronics*, vol. 7, no. 2, pp. 653-663, 2019.

[120] J. Wang *et al.*, "Design of Integrated Magnetic Transformer for High Frequency LLC Converter," in *2020 4th International Conference on HVDC (HVDC)*, 2020: IEEE, pp. 986-991.

[121] S. Stegen and J. Lu, "Structure comparison of high-frequency planar power integrated magnetic circuits," *IEEE transactions on magnetics*, vol. 47, no. 10, pp. 4425-4428, 2011.

[122] Y. Liu, H. G. Wu, J. Zou, Y. Tai, and Z. Ge, "CLL Resonant Converter with Secondary Side Resonant Inductor and Integrated Magnetics," *IEEE Transactions on Power Electronics*, vol. 36, no. 10, pp. 11316 - 11325, 2021.

[123] R. Muhammad, S. Kim, C. Suk, S. Choi, B. Yu, and S. Park, "Integrated Planar Transformer Design of 3-kW Auxiliary Power Module for Electric Vehicles," in *2020 IEEE Energy Conversion Congress and Exposition (ECCE)*, 2020: IEEE, pp. 1239-1243.

[124] S.-Y. Yu, C. Hsiao, and J. Weng, "A High Frequency CLLLC Bi-directional Series Resonant Converter DAB Using an Integrated PCB Winding Transformer," in *2020 IEEE Applied Power Electronics Conference and Exposition (APEC)*, 2020: IEEE, pp. 1074-1080.

[125] M. A. Bakar and K. Bertilsson, "An improved modelling and construction of power transformer for controlled leakage inductance," in *2016 IEEE 16th International Conference on Environment and Electrical Engineering (EEEIC)*, 2016: IEEE, pp. 1-5.

[126] Y. Park, S. Chakraborty, and A. Khaligh, "DAB Converter for EV Onboard Chargers Using Bare-Die SiC MOSFETs and Leakage-Integrated Planar Transformer," *IEEE Transactions on Transportation Electrification*, vol. 8, no. 1, pp. 209-224, 2021.

[127] S. Li, Q. Min, E. Rong, R. Zhang, X. Du, and S. Lu, "A magnetic integration half-turn planar transformer and its analysis for LLC resonant DC-DC converters," *IEEE Access*, vol. 7, pp. 128408-128418, 2019.

[128] Z. Ouyang, W. G. Hurley, and M. A. Andersen, "Improved Analysis and Modeling of Leakage Inductance for Planar Transformers," *IEEE Journal of Emerging and Selected Topics in Power Electronics*, vol. 7, no. 4, pp. 2225-2231, 2018.

[129] Z. Ouyang, J. Zhang, and W. G. Hurley, "Calculation of leakage inductance for high-frequency transformers," *IEEE Transactions on Power Electronics*, vol. 30, no. 10, pp. 5769-5775, 2014.

[130] J. Zhang, Z. Ouyang, M. C. Duffy, M. A. Andersen, and W. G. Hurley, "Leakage inductance calculation for planar transformers with a magnetic shunt," *IEEE Transactions on Industry Applications*, vol. 50, no. 6, pp. 4107-4112, 2014.

[131] W. Liu and J. Van Wyk, "Design of integrated LLCT module for LLC resonant converter," in *Twentieth Annual IEEE Applied Power Electronics Conference and Exposition, 2005. APEC 2005.*, 2005, vol. 1: IEEE, pp. 362-368.

[132] J. Biela and J. W. Kolar, "Analytic model inclusive transformer for resonant converters based on extended fundamental frequency analysis for resonant converter-design and optimization," *IEEJ Transactions on Industry Applications*, vol. 126, no. 5, pp. 568-577, 2006.

[133] M. D'Antonio, S. Chakraborty, and A. Khaligh, "Planar Transformer with Asymmetric Integrated Leakage Inductance Using Horizontal Air Gap," *IEEE Transactions on Power Electronics*, 2021.

[134] M. Li, Z. Ouyang, B. Zhao, and M. A. Andersen, "Analysis and modeling of integrated magnetics for LLC resonant converters," in *IECON 2017-43rd Annual Conference of the IEEE Industrial Electronics Society*, 2017: IEEE, pp. 834-839.

[135] M. Meinhardt, M. Duffy, T. O'Donnell, S. O'Reilly, J. Flannery, and C. O. Mathuna, "New method for integration of resonant inductor and transformer-design, realisation, measurements," in *APEC'99. Fourteenth Annual Applied Power Electronics Conference and Exposition. 1999 Conference Proceedings (Cat. No. 99CH36285)*, 1999, vol. 2: IEEE, pp. 1168-1174.

[136] Y. Park, S. Chakraborty, and A. Khaligh, "A bare-die SiC-based isolated bidirectional DC-DC converter for electric vehicle on-board chargers," in *2020 IEEE Transportation Electrification Conference & Expo (ITEC)*, 2020: IEEE, pp. 49-54.

[137] J. Hu and C. R. Sullivan, "The quasi-distributed gap technique for planar inductors: Design guidelines," in *IAS'97. Conference Record of the 1997 IEEE Industry Applications Conference Thirty-Second IAS Annual Meeting*, 1997, vol. 2: IEEE, pp. 1147-1152.

[138] J. Hu and C. R. Sullivan, "AC resistance of planar power inductors and the quasidistributed gap technique," *IEEE Transactions on Power Electronics*, vol. 16, no. 4, pp. 558-567, 2001.

[139] M. Noah, T. Shirakawa, K. Umetani, J. Imaoka, M. Yamamoto, and E. Hiraki, "Effects of secondary leakage inductance on the LLC resonant converter," *IEEE Transactions on Power Electronics*, vol. 35, no. 1, pp. 835-852, 2019.

[140] H.-S. Choi, "AN4151. Half-bridge LLC resonant converter design using Fairchild Power Switch (FPS)," *Fairchild semiconductor*, 2007.

[141] M. Noah, K. Umetani, M. Yamamoto, and J. Imaoka, "Winding orientation method to minimise the secondary leakage of a gapped transformer utilised in LLC resonant converter," *Electronics Letters*, vol. 54, no. 3, pp. 157-159, 2018.

[142] Y. Zhang, D. Xu, M. Chen, Y. Han, and Z. Du, "LLC resonant converter for 48 V to 0.9 V VRM," in *2004 IEEE 35th Annual Power Electronics Specialists Conference (IEEE Cat. No. 04CH37551)*, 2004, vol. 3: IEEE, pp. 1848-1854.

[143] Y. Zuo, X. Pan, and C. Wang, "A Reconfigurable Bidirectional isolated LLC Resonant Converter for Ultra-Wide Voltage-gain Range applications," *IEEE Transactions on Industrial Electronics*, vol. 69, no. 6, pp. 5713 - 5723, 2021.

[144] Y. Zhang, D. Zhang, J. Li, and H. Zhu, "Bidirectional LCLL Resonant Converter With Wide Output Voltage Range," *IEEE Transactions on Power Electronics*, vol. 35, no. 11, pp. 11813-11826, 2020.

[145] A. Soni and A. K. Dhakar, "Bi-Directional CLLC Resonant Converter with Integrated Planar Transformer for Energy Storage Systems," in *IECON 2020 The 46th Annual Conference of the IEEE Industrial Electronics Society*, 2020: IEEE, pp. 4255-4260.

[146] X. Ma, P. Wang, H. Bi, and Z. Wang, "A Bidirectional LLCL Resonant DC-DC Converter With Reduced Resonant Tank Currents and Reduced Voltage Stress of the Resonant Capacitor," *IEEE Access*, vol. 8, pp. 125549-125564, 2020.

[147] M. Mohammadi, A. Dehbashi, G. B. Gharehpetian, A. Khoshsaadat, and P. Mattavelli, "A Family of Soft-Switching DC–DC Converters With Two Degrees of Freedom," *IEEE Transactions on Industrial Electronics*, vol. 68, no. 10, pp. 9398-9409, 2020.

[148] Z. Fang, Z. Huang, H. Jing, and F. Liu, "Hybrid mode-hopping modulation for LLC resonant converter achieving high efficiency and linear behaviour," *IET Power Electronics*, vol. 13, no. 6, pp. 1153-1162, 2020.

[149] W. Chen, P. Rong, and Z. Lu, "Snubberless bidirectional DC–DC converter with new CLLC resonant tank featuring minimized switching loss," *IEEE Transactions on industrial electronics*, vol. 57, no. 9, pp. 3075-3086, 2009.
[150] Y. Wei, Q. Luo, and A. Mantooth, "Overview of modulation strategies for LLC resonant converter," *IEEE Transactions on Power Electronics*, vol. 35, no. 10, pp. 10423-10443, 2020.
[151] C. W. Tsang, M. P. Foster, D. A. Stone, and D. T. Gladwin, "Analysis and design of LLC resonant converters with capacitor–diode clamp current limiting," *IEEE Transactions on Power Electronics*, vol. 30, no. 3, pp. 1345-1355, 2014.
[152] J.-H. Jung, H.-S. Kim, M.-H. Ryu, and J.-W. Baek, "Design methodology of bidirectional CLLC resonant converter for high-frequency isolation of DC distribution systems," *IEEE Transactions on Power Electronics*, vol. 28, no. 4, pp. 1741-1755, 2012.
[153] Z. U. Zahid, Z. M. Dalala, R. Chen, B. Chen, and J.-S. Lai, "Design of bidirectional DC–DC resonant converter for vehicle-to-grid (V2G) applications," *IEEE Transactions on Transportation Electrification*, vol. 1, no. 3, pp. 232-244, 2015.
[154] J. Min and M. Ordonez, "Bidirectional resonant CLLC charger for wide battery voltage range: Asymmetric parameters methodology," *IEEE Transactions on Power Electronics*, vol. 36, no. 6, pp. 6662-6673, 2020.
[155] M. A. Rezaei, K.-J. Lee, and A. Q. Huang, "A high-efficiency flyback micro-inverter with a new adaptive snubber for photovoltaic applications," *IEEE Transactions on Power Electronics*, vol. 31, no. 1, pp. 318-327, 2015.
[156] S. Arab Ansari, A. R. Mizani, S. Ashouri, and J. Shokrollahi Moghani, "Fault ride-through capability enhancement for microinverter applications," *Journal of Renewable Energy*, vol. 2019, 2019.
[157] D. W. Hart, *Power electronics (series 1)*, 1st ed. New York: USA: McGraw-Hill Education, Feb. 2011.
[158] D. Graovac, M. Purschel, and A. Kiep, "MOSFET power losses calculation using the data-sheet parameters," *Infineon application note*, vol. 1, 2006.
[159] L. Efthymiou *et al.*, "Zero reverse recovery in SiC and GaN Schottky diodes: A comparison," in *2016 28th International Symposium on Power Semiconductor Devices and ICs (ISPSD)*, 2016: IEEE, pp. 71-74.
[160] Micrometals, "Iron Powder Cores for Power Conversion and Line Filter Applications," *Micrometals, February* no. L, 2007.
[161] 650V CoolMOS™ CFDA Superjunction (SJ) MOSFET IPW65R150CFDA [Online] Available: https://www.infineon.com/
[162] Thermal Materials, Aug. 2019 [Online] Available: https://dm.henkel-dam.com/is/content/henkel/lt-8116-brochure-thermal-interface-materials-selection-guidepdf
[163] Mouser Electronics [Online] Available: https://www.mouser.co.uk/
[164] Anglialive [Online] Available: https://www.anglia-live.com/
[165] Pace Components [Online] Available: http://www.pacecomponents.co.uk/
[166] A. Mirzaee, S. Arab Ansari, and J. Shokrollahi Moghani, "Single switch quadratic boost converter with continuous input current for high voltage applications," *International Journal of Circuit Theory and Applications*, vol. 48, no. 4, pp. 587-602, 2020.
[167] Z. Fang, Z. Huang, H. Jing, and F. Liu, "Hybrid mode-hopping modulation for LLC resonant converter achieving high efficiency and linear behaviour," *IET Power Electronics*, vol. 13, no. 6, pp. 1153-1162, 2020.
[168] W. G. Hurley and W. H. Wölfle, *Transformers and inductors for power electronics: theory, design and applications*. John Wiley & Sons, 2013.

[169] S. Tumansk, "Magnetic Materials," in *Handbook of Magnetic Measurements* CRC Press, 2011.
[170] *Magnetics Ferrite Catalog*, Magnetics, 2013. [Online]. Available: www.mag-inc.com.